Advanced lung and liver models for hazard characterization of nanomaterials

Thesis submitted in partial fulfilment of the
requirements for the degree of Philosophiae Doctor

by

Elisabeth Elje

Faculty of Medicine
University of Oslo

Health Effects Laboratory
Department of Environmental Chemistry
NILU – Norwegian Institute for Air Research

2023

UNIVERSITY
OF OSLO

Series of dissertations submitted to the
Faculty of Medicine, University of Oslo

ISBN 978-82-348-0270-6

Cover: UiO.
Print production: Graphic center, University of Oslo.

Summary

Humans are constantly exposed to particles from the surrounding environment, and outdoor air pollution is a major environmental health problem. Human-made nanomaterials (NMs), having particle sizes < 100 nm in at least one dimension, are released into the environment during production and usage, and are of great concern due to the size-related increased reactivity and interaction with biological systems, compared to corresponding bulk materials. After inhalation, some NMs can deposit in the lungs, cross the lung-blood barrier, enter the circulatory system, and reach other target organs, including the liver.

To avoid potential negative health effects of NMs, risk assessment and regulations on the production and use of NMs are needed and require exposure data and toxicity data of NMs. Toxicological studies have traditionally been performed using animal studies (*in vivo*) which have ethical concerns, or by relatively simple cellular-based studies (*in vitro*) with low physiological complexity. To support the risk assessment of an increasing number of NMs, new approach methodologies (NAMs) are being developed for hazard assessment. As a part of this, there is a need for development of new advanced *in vitro* models based on cell cultures in more physiological relevant conditions. Of special importance is the application of these models for genotoxicity testing, to evaluate the ability of the NM to alter the genetic information. Genetic damage can lead to genetic diseases, cancer, or reproductive toxicity, and is a crucial endpoint to include in risk assessment of chemicals, including NMs.

The aim of this work was to contribute to the development of advanced lung and liver models, representing a first-contact and secondary target organ of inhaled NMs, respectively. The performance of the models was compared with each other and to traditional *in vitro* models, to find potential similarities or differences between the models.

Five advanced lung models, representing the conducting airways with bronchial epithelial cells, and the gas-exchange region with alveolar epithelial cells, were constructed with epithelial cells on a permeable membrane allowing medium and nutrient supply from the bottom while keeping the physiological conditions with air on top (at the air-liquid interface, ALI). The cells were cultured alone in monoculture or in coculture with endothelial cells and macrophages. An advanced liver model was constructed with hepatocytes cultured in spheroids; a dense 3D spheroidal organization of cells without adhesion to a substrate, allowing increased cell-to-cell interactions and signaling. Effects on cellular viability and genotoxicity were compared to

traditional *in vitro* models of the same cell type cultured on a flat 2D surface submerged in culture medium.

Differences and similarities were found between the models. After exposure of the lung models to an aerosol of NMs, different responses were seen on viability and DNA damage depending on the cell types included. The advanced monocultures seemed to be more sensitive to NM-induced toxicity compared to traditional monocultured cells immersed in medium without air conditions. A commonly used genotoxicity test for testing of chromosomal damage after NM exposure, the micronucleus test, was for the first time successfully applied to ALI cocultures. In liver models, different or similar responses were seen on viability and DNA damage, where traditional cultures were more sensitive to induced cytotoxicity and advanced models were more sensitive to induced genotoxicity. The comet assay was, for the first time, successfully applied to the HepG2 spheroid model for testing of DNA strand breaks and oxidized base lesions.

In general, this work has shown that the culturing conditions of the cells affect the toxic response to chemicals and NMs. The traditional cultures reflected concentration-dependent responses better, and higher variability was seen in the advanced models. Inter-laboratory reproducibility of the performance of advanced models was investigated, and some limitations of the models were discussed. In conclusion, this work contributed to new knowledge on advanced *in vitro* models by application of genotoxicity testing after NM exposures. The advanced models are promising 3D models for use in genotoxicity studies and can support the hazard and risk assessment of NMs in compliance with the 3R´s for next generation risk assessment.

Samandrag (Summary in Norwegian)

Menneske er kontinuerleg eksponert for partiklar frå omgivnadane, og utandørs luftforureining er eit alvorleg helseproblem. Menneskeskapte nanomaterialar (NM) med partikkelstorleik < 100 nm i minst éin dimensjon vert sleppt ut til miljøet ved produksjon og bruk. Dette er bekymringsverdig på grunn av auka sjanse for interaksjonar med biologiske system, knytta til storleiken av NM, samanlikna med korresponderande bulk-material. Etter innanding kan nokre NM deponere i lungene, krysse lunge-blod-barrieren og komme inn i sirkulasjonssystemet og dermed nå andre sekundære målorgan som leveren.

For å unngå potensielle negative helseeffektar av NM, er det nødvendig med risikovurdering og -regulering av produksjon og bruk av NM, som krever data på eksponering og toksisitet av NM. Toksisitetsstudier har tradisjonelt blitt utført ved bruk av dyreforsøk (*in vivo*) som er tilknytta store etiske bekymringer, eller ved bruk av relativt enkle celle-baserte forsøk (*in vitro*) med liten fysiologisk kompleksitet. Nye tilnærmingsmetodar (engelsk: new approach methodologies, NAMs) vert utvikla for å støtte risikovurdering av eit aukande antal NM. Som ein del av dette, er det eit behov for utvikling av nye avanserte *in vitro*-modellar basert på cellekulturar i meir fysiologiske relevante dyrkingsvilkår. Spesielt viktig er bruk av desse modellane for testing av gentoksisitet, for å vurdere eigenskapane til NM til å endre cellenes genetiske informasjon. Genetisk skade kan føre til genetiske sjukdomar, kreft, eller reproduktiv toksisitet, og er kritisk informasjon å inkludere i risikovurdering av kjemikalie, inkludert NM.

Målet med dette arbeidet var å bidra til utviklinga av avanserte lunge- og levermodellar, som henholdsvis representerer første kontaktorgan og sekundært målorgan for NM. Prestasjonen av modellane vart samanlikna mellom modellane og med tradisjonelle *in vitro*-modellar, for å finne potensielle likheiter og ulikheiter. Effektar på celleviabilitet og gentoksisitet vart analysert etter eksponering for ei gruppe av kjemikaliar og NM.

Fem avanserte lungemodellar som representerer bronkiene og alveolene vart konstruerte med epitel-celler på ein permeabel membran som gir medium- og næringstilførsel frå undersida og samtidig gir fysiologiske forhold med luft på toppen (på luft-væske-sjiktet, engelsk: air-liquid inter-face, ALI). Epitel-cellene vart dyrka åleine i monokultur eller i kokultur med endotel-celler og makrofager. Ein avansert levermodell vart konstruert med hepatocytter dyrka i ein sfæroide; ein tett 3D-sfærisk organisering av celler uten kontakt med ei overflate, som gir auka interaksjonar og signalisering mellom cellene. Effektar på celleviabilitet og gentoksisitet vart

samanlikna mot tradisjonelle in vitro-modellar av same celletype dyrka på ei flat 2D-overflate med medium på toppen.

Forskjellar og fellestrekk vart funne mellom modellane. Etter eksponering av lungemodellane til ein aerosol av NM, vart det målt ulike responsar i viabilitet og DNA-skade avhengig av celletypane som var tilstades. Monokulturane på væske-luft-sjiktet virka å vere meir sensitive for NM-indusert toksisitet samanlikna med tradisjonelle monokulturar. Ein mykje brukt gentoksisitets-test for måling av kromosomskade etter NM-eksponering, mikronukleus-test, vart for første gang brukt på kokulturar på væske-luft-sjiktet. I levermodellane vart det målt ulike eller like responsar på viabilitet og DNA-skade, der tradisjonelle kulturar var meir sensitive til indusert cytotoksisitet og avanserte modellar meir sensitive til indusert gentoksisitet. Komet-testen vart for første gang brukt på HepG2-sfæroidemodellen for testing av DNA-trådbrudd og oksidert skade på DNA-basene.

Dette arbeidet har generelt vist at cellenes dyrkingsvilkår påverkar toksisitetsresponsane til kjemikalie og NM. Dei tradisjonelle modellane viste konsentrasjons-avhengige responsar betre, og høgare variasjon vart målt i dei avanserte modellane. Reproduserbarheit mellom laboratorium vart undersøkt, og noen begrensninger ved modellane vart diskutert. Avslutningsvis, har dette arbeidet bidratt til ny kunnskap om avanserte *in vitro*-modellar, ved bruk av gentoksisitets-testing etter NM-eksponering. Dei avanserte modellane er lovande 3D-modellar for bruk i gentoksisitets-studier og kan støtte fare- og risikovurdering av NM i samsvar med dei 3 R’ane for neste-generasjons risikovurdering.

Acknowledgements

This research project was carried out at NILU – Norwegian Institute for Air Research in the period of 2017 to 2022 and was funded by The Norwegian Research Council. I am very grateful to everyone that made this project a reality and for giving me the opportunity to work on this interesting topic.

I am greatly thankful for the help and encouragement from my main supervisor Elise Rundén-Pran and my co-supervisors Espen Mariussen and Reidun Torp. Thank you for giving me the chance to explore independently and providing guidance when needed, as well as giving valuable feedback and interesting discussions. A special thanks to Espen, for first introducing me to toxicological studies in 2013 and further inspiring me to become a researcher.

A special thank you to Arno Gutleb, Aline Chary and Tommaso Serchi at Luxembourg Institute of Science and Technology (Luxembourg) for your collaboration on the lung model and for inviting us to try the setup and your procedures.

A big thank you to Yvonne Kohl for the collaboration on the liver model, and for welcoming me to Fraunhofer Institute for Biomedical Engineering (Germany) together with Thorsten Knoll, Michelle Hesler and Sarah Spring. I learned a lot from you all and had a wonderful stay.

I would like to thank all co-authors and project collaborators for all your efforts and discussions. Thank you to Catalan Institute of Nanoscience and Nanotechnology (Spain) for providing nanomaterials, Norwegian National Institute of Occupational Health (Norway) for collaboration on lung the model, and Mihaela R. Cimpan at University of Bergen (Norway) for lending us culture medium when all providers were empty.

Thank you to my present and former colleagues at the Health Effects Laboratory – Maria who is always a huge inspiration, Naouale, Iren, Evy, Alexandra, Eleonora, Erin, Tatiana, and Tanima – for helping in the lab and good discussions. Thank you also to my colleagues at the Department of Environmental Chemistry; Aasmund for being a great leader; Morten for teaching me how to prepare samples for silver analysis; and Hilde and Marit for running the instrument. Thank you to all my colleagues at NILU for providing such a friendly and inspiring work environment.

Thank you to all friends and family, and especially Trond and Sofie, for supporting and believing in me throughout the whole process.

Elisabeth Elje,
Kjeller, February 2023

List of publications

This thesis is based upon the following papers, which are referred to in the text by Roman numerals (I-V):

I. Laura M. A. Camassa*, Elisabeth Elje*, Espen Mariussen, Eleonora M. Longhin, Maria Dusinska, Shan Zienolddiny-Narui, Elise Rundén-Pran.
Advanced Respiratory Models for Hazard Assessment of Nanomaterials—Performance of Mono-, Co- and Tricultures.
Nanomaterials, 2022; 12; 2609; doi:10.3390/nano12152609
*Shared first-authorship

II. Elise Rundén-Pran*, Espen Mariussen*, Elisabeth Elje, Aline Chary, Eleonora Marta Longhin, Naouale El Yamani, Maria Dusinska, Arno C. Gutleb, Tommaso Serchi.
Hazard assessment of spherical and rod-shaped silver nanomaterials by an advanced lung model at the air-liquid interface.
(Manuscript)
*Shared first-authorship

III. Elisabeth Elje*, Espen Mariussen, Erin McFadden, Maria Dusinska, Elise Rundén-Pran*.
Different sensitivity of advanced bronchial and alveolar mono- and coculture models for hazard assessment of nanomaterials.
Nanomaterials, 2023; 13; 407; doi:10.3390/nano13030407
*Corresponding authors

IV. Elisabeth Elje, Michelle Hesler, Elise Rundén-Pran, Pascal Mann, Espen Mariussen, Sylvia Wagner, Maria Dusinska, Yvonne Kohl.
The comet assay applied to HepG2 liver spheroids.
Mutat Res Gen Tox En, 2019; 845; 403033; doi:10.1016/j.mrgentox.2019.03.006

V. Elisabeth Elje, Espen Mariussen, Oscar H. Moriones, Neus G. Bastús, Victor Puntes, Yvonne Kohl, Maria Dusinska and Elise Rundén-Pran.

Hepato(Geno)Toxicity Assessment of Nanoparticles in a HepG2 Liver Spheroid Model.
Nanomaterials, 2020; 10; 545; doi:10.3390/nano10030545

Contents

1. Introduction

1.1. Human exposure to air pollution

1.1.1. Particular matter and nanomaterials

Humans are constantly exposed to particles, gases, and microorganisms in the surrounding environment. Both natural and engineered (human-made) particles are found in the ambient air. Outdoor air pollution constitutes a major environmental health problem which was estimated to cause 4.2 million premature deaths worldwide in 2016 [1]. Exposure to fine and ultrafine particulate matter with particle diameters below 2.5 µm (PM2.5) and 1 µm (PM1), respectively, are linked to respiratory and cardiovascular diseases as well as cancers [1].

The production and use of the smallest human-made particles, nanomaterials (NMs) with dimensions < 100 nm in at least one dimension [2,3], are increasing and lead to increased human exposures. NMs of silver (Ag) are some of the most widely used NMs in consumer products, with estimated annual production of 280-635 metric tons in 2021 [4]. From this, approximately 1 % will be released in the air, water, or soil [5,6].

NMs are unique from their bulk counterparts due to smaller dimensions and thus higher relative number of atoms at the surface compared to the inside of the structure, giving properties unique to each material. NMs can be designed to a specific function by fine-tuning the physicochemical characteristics, such as size, shape and aspect ratio, material composition, agglomeration status, solubility, surface area, surface structure and surface charge [7,8] (Fig. 1). Due to the antimicrobial activity, silver NMs are currently applied in water disinfection, everyday household products, textiles, and a range of medical products including wound dressings, surgical instruments, and disinfectants [9,10]. Additionally, silver NMs are also used in electronics, catalysis, and biosensors due to their optical properties [10]. Silver in general has been used for thousands of years, in jewelry, dental alloys, water disinfection, and medical applications including open wound and burn treatments [9,10]. Other frequently used NMs include NMs of titanium dioxide (TiO_2) which is used as a pigment in paint, food, and cosmetics [11], and of zinc oxide (ZnO) which is used in cosmetics due to its UV-blocking properties [12].

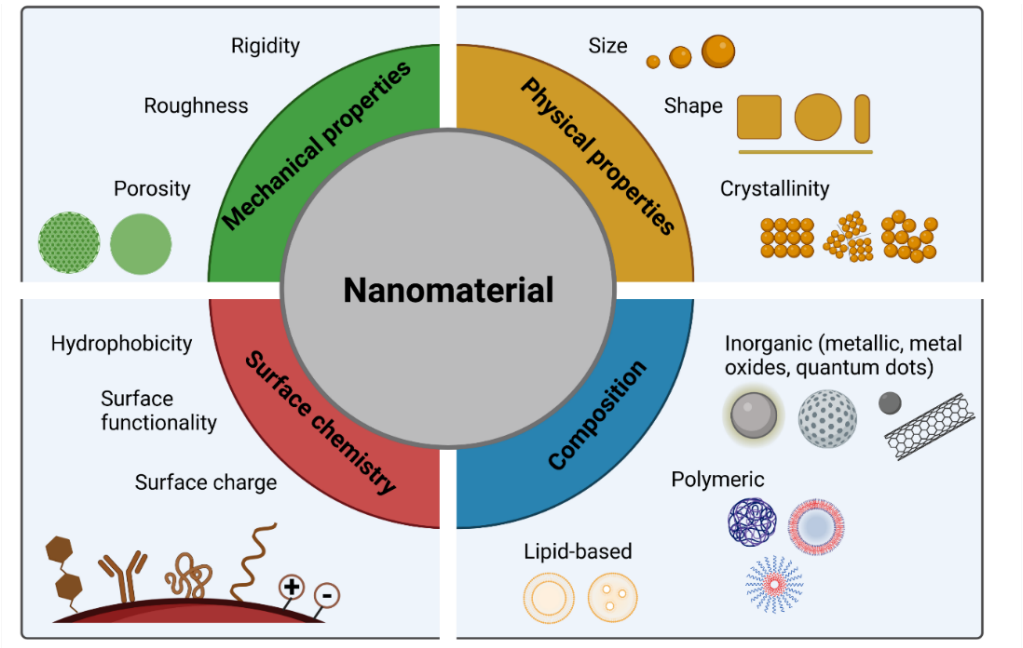

Figure 1: Physicochemical characteristics of nanomaterials, including mechanical properties, physical properties, surface chemistry and material composition. The physicochemical characteristics can be fine-tuned during the production process and will determine the properties of the nanomaterial. Created with BioRender.com.

Consumer products containing NMs may have a long life-cycle including initial synthesis, production, manufacturing, industrial emission, use of the product, product degradation and disposal. Humans can be exposed to NMs during all these phases and states of the NM-containing product [9,10], through several entry routes, including inhalation, oral ingestion, dermal contact, or directly administered through intravenous injection. Exposure to airborne NMs mostly occurs in the workplace, however, widespread consumer exposure via oral ingestion, dermal contact or inhalation is likely to occur [10,13].

1.1.2. Inhalation exposure and the respiratory system

Inhalation is the main human exposure route of airborne particular matter, including NMs, making the respiratory system a first line target organ. The human respiratory system can be divided into two compartments with different main functions (Fig. 2A). In the upper airways, the nasopharyngeal region heats, humidifies and filters the inhaled air. In the lower airways, the tracheobronchial region or conducting airways further humidifies and filters the air and conducts it deeper into the lungs. The most distal bronchiole in the tracheobronchial tree, the

terminal bronchiole, bifurcates (divides) to form respiratory bronchioli containing alveolar ducts terminating in clusters of alveolar sacs. Gas-exchange occurs in the respiratory bronchioli and the alveoli, where oxygen from the inhaled air is exchanged with carbon dioxide in the venous blood in the pulmonary capillaries surrounding the airways [14,15].

The airways contain different cell types sending and receiving signals of importance for the outcome of exposure to pollutants or a toxic insult. In the tracheobronchial region, the main cell types include ciliated cells, mucus-producing serous cells, goblet cells, and basal cells (Fig. 2B). The ciliated and serous cells, together with submucosal glands, contribute to the "mucociliary escalator" where inhaled particles are moved up the airway tree and thereafter swallowed. The population of ciliated and serous cells gradually transit into non-ciliated cuboidal (club) cells in the terminal bronchioli. The club cells are involved in detoxification of toxicants as they have relatively high levels of cytochrome P450 enzymes and produce pulmonary surfactants to reduce the surface tension and maintain the bronchiole structure [15].

In a human adult, the total alveolar area is about 40-80 m^2 containing 300 million alveoli [16]. Gas exchange occurs across the 0.4 μm thick barrier consisting of alveolar epithelial type I cells, alveolar epithelial type II cells, alveolar macrophages, interstitial fluid, and capillary endothelial cells (Fig. 2C). The type I cells cover 90-95 % of the alveolar surface, allows gas exchange, and prevents leakage of fluids across the alveolar wall into the lumen. Type II cells cover only 7% of the alveolar surface, secretes surfactants, and are critical to alveolar repair as they can differentiate to type I cells that cannot replicate [15,17–20].

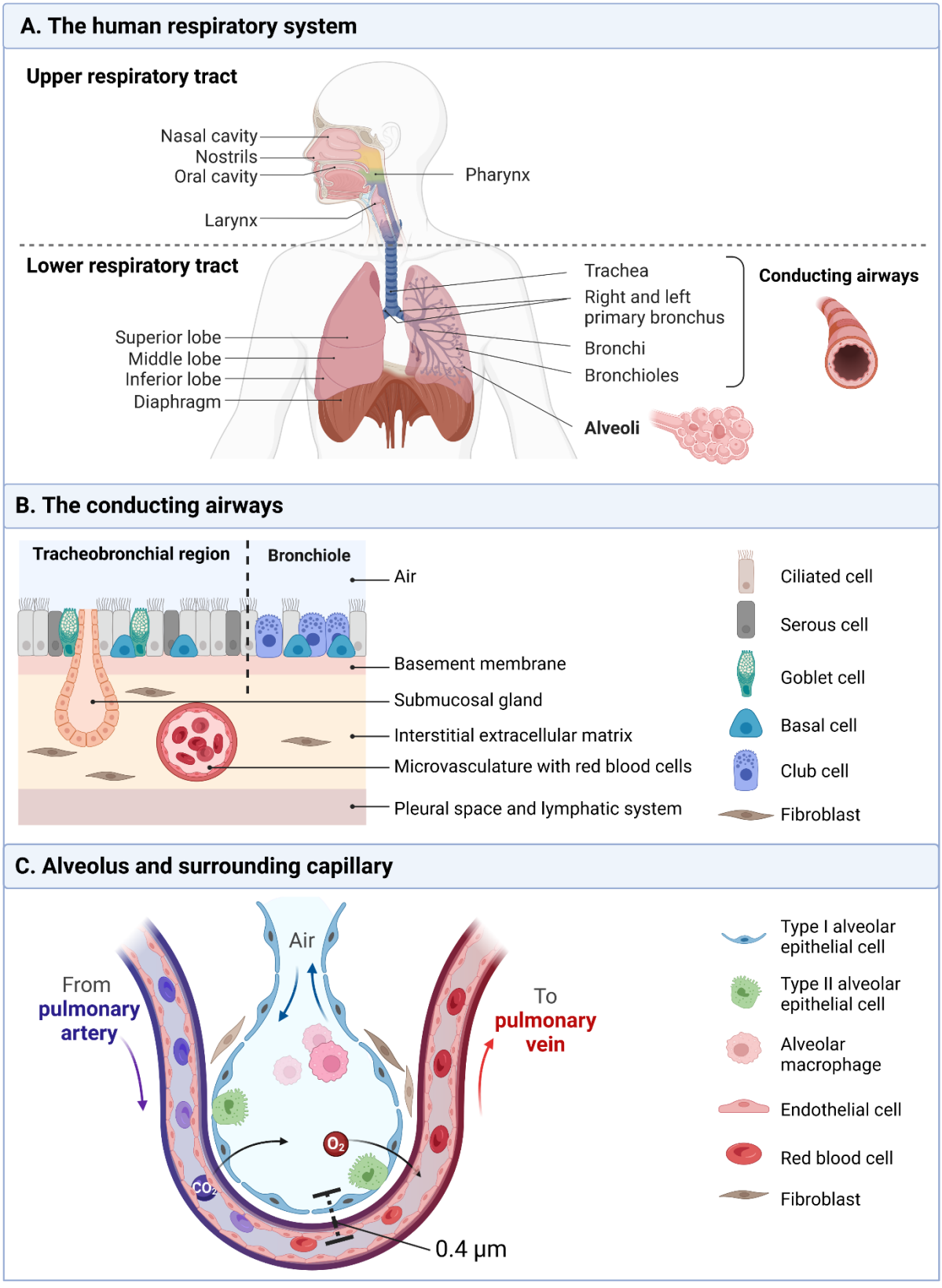

Figure 2: The structure of the human respiratory system. A) The upper and lower respiratory tract. B) The tracheobronchial region of the conducting airways consists of different cell types with submucosal glands. The epithelial cells make a barrier from the air to the blood vessels, pleural space, and

lymphatic system. C) The cells in the alveoli deepest in the lungs make a thin barrier and are in close contact with the capillaries. Gas exchange occur across this lung-blood-barrier. Created with BioRender.com.

1.1.3. Particle deposition in the respiratory system and systemic exposure

Deposition of particles in the respiratory system is dependent on the physicochemical properties of the particles, including charge, density, shape, and size [17,21]. Based on mathematical modeling of single particles, the larger particles have highest deposition in the upper airways and are less likely to penetrate deep in the lungs. PM2.5, PM1 and NMs have significant deposition in all regions. NMs < 5 nm have highest deposition in the upper airways due to fast diffusion while NMs > 5 nm have highest deposition in the alveolar and tracheobronchial regions (Fig. 3 adapted from [17]). *In vivo* studies have confirmed that particles with a smaller agglomerate size have higher deposition in the alveolar region compared to particles with larger agglomerate size [21]. Particles deposit in different locations in the airway system by mechanisms including inertial impaction, gravitational settling, diffusion, interception, and electrostatic interaction [14,17]. For NMs, diffusion is the most relevant deposition mechanism due to displacement of NMs upon collision with air molecules. Electrostatic precipitation occurs only for charged NMs, whereas the other mechanisms are relevant mainly for larger particles [17].

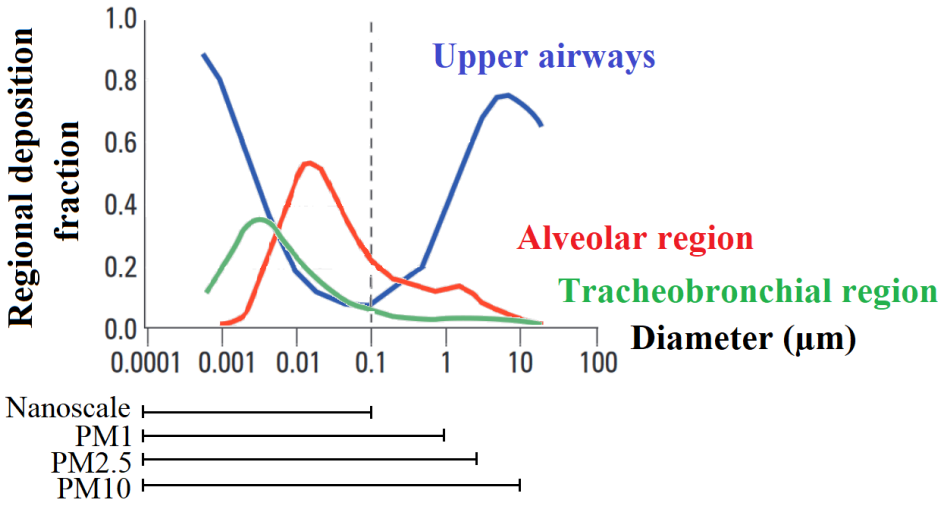

Figure 3: Deposition of particles in the different regions of the human respiratory system. Diameter scales are shown for nanomaterials at the nanoscale, and particular matter with particle diameters below 1, 2.5 and 10 µm (PM1, PM2.5, PM10, respectively). Modified from [17].

When deposited, the NMs can be removed by the "mucociliary escalator" or by clearance mechanisms involving alveolar macrophages, or interact with the respiratory cells and cause local effects. Some NMs may cross the airway epithelium barrier, constituted apically by intercellular tight junctions, and attached basally to a basement membrane composed of extracellular matrix, to enter the pleural space, the lymphatic system, and/or the circulatory system and further reach secondary target organs [15,22–24]. The oxygenated pulmonary blood can potentially contain NMs translocated from the alveoli and is pumped through the heart and transported to the upper body (including the brain), liver, stomach, and intestines (gastrointestinal tract, GI), the lower body, and to the kidneys for cleansing (Fig. 4).

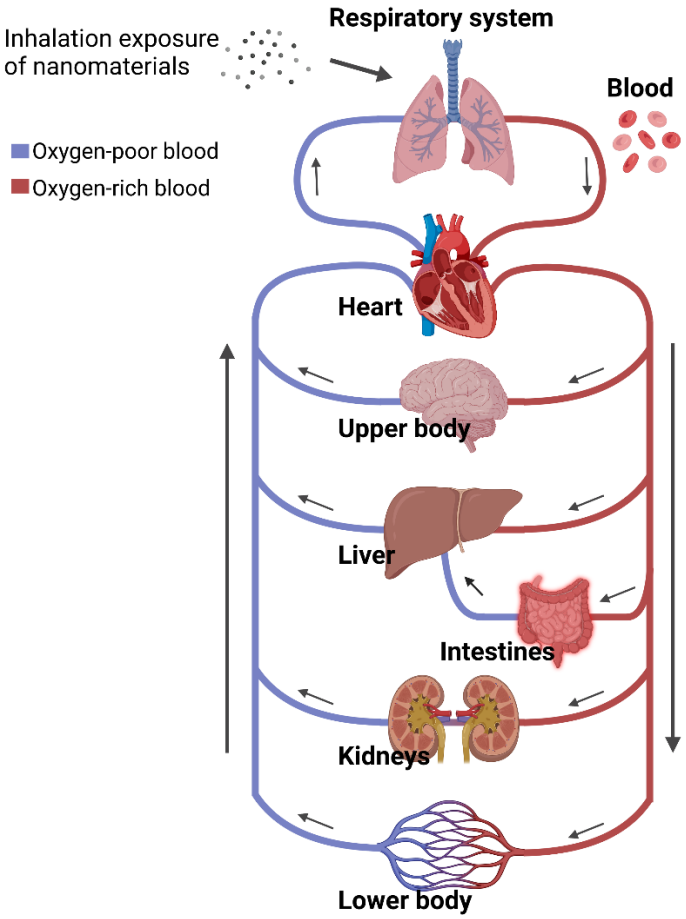

Figure 4: Overview of potential distribution of nanomaterials in the circulatory system after inhalation. Created with BioRender.com.

The liver is an important target for all substances reaching systemic circulation, as it is the main organ for metabolism of exogenous chemical and particles [25]. NMs accumulate in the liver at higher concentrations compared to other organs [26,27]. Blood with contaminants and NMs are distributed from the systemic circulation into the liver, but also directly from the GI tract by the first-pass effect. Toxicants in the GI tract are transported to the liver via the hepatic portal vein to immediately be subjected to biotransformation or excretion. This process reduces the toxicant concentration before reaching the target organ or site. At the same time, it increases the exposure concentration of the liver cells.

A human liver is organized in about one million hexagonal lobules, each with a diameter of approximately 1 mm. The lobules have a central vein in the center, and portal triads at the vertexes, comprising an artery, a vein and a bile duct bundled by connective tissue (Fig. 5A, 4B). The main cell types include hepatocytes, sinusoidal endothelial cells, stellate cells, and Kupffer cells (macrophages), which are organized in sinusoids (Fig. 5C). Blood flows in capillaries through the sinusoids, from the portal vein towards the central vein, along hepatocytes which are joined by tight junctions. The sinusoidal network allows for free transfer of oxygen, nutrients and waste products between the hepatocytes and blood. This results in a spatial biochemical gradient influencing metabolism and gene expression, known as metabolic zonation [28,29].

Around 30-99% of the NMs circulating in the bloodstream will be sequestered by the liver [30]. For medicinal applications, NMs are generally administered intravenously, and typically only 5% are delivered to the target tissue [30]. The remaining NMs are, depending on the size, either sequestered by the liver and spleen or eliminated through the kidneys [25,30].

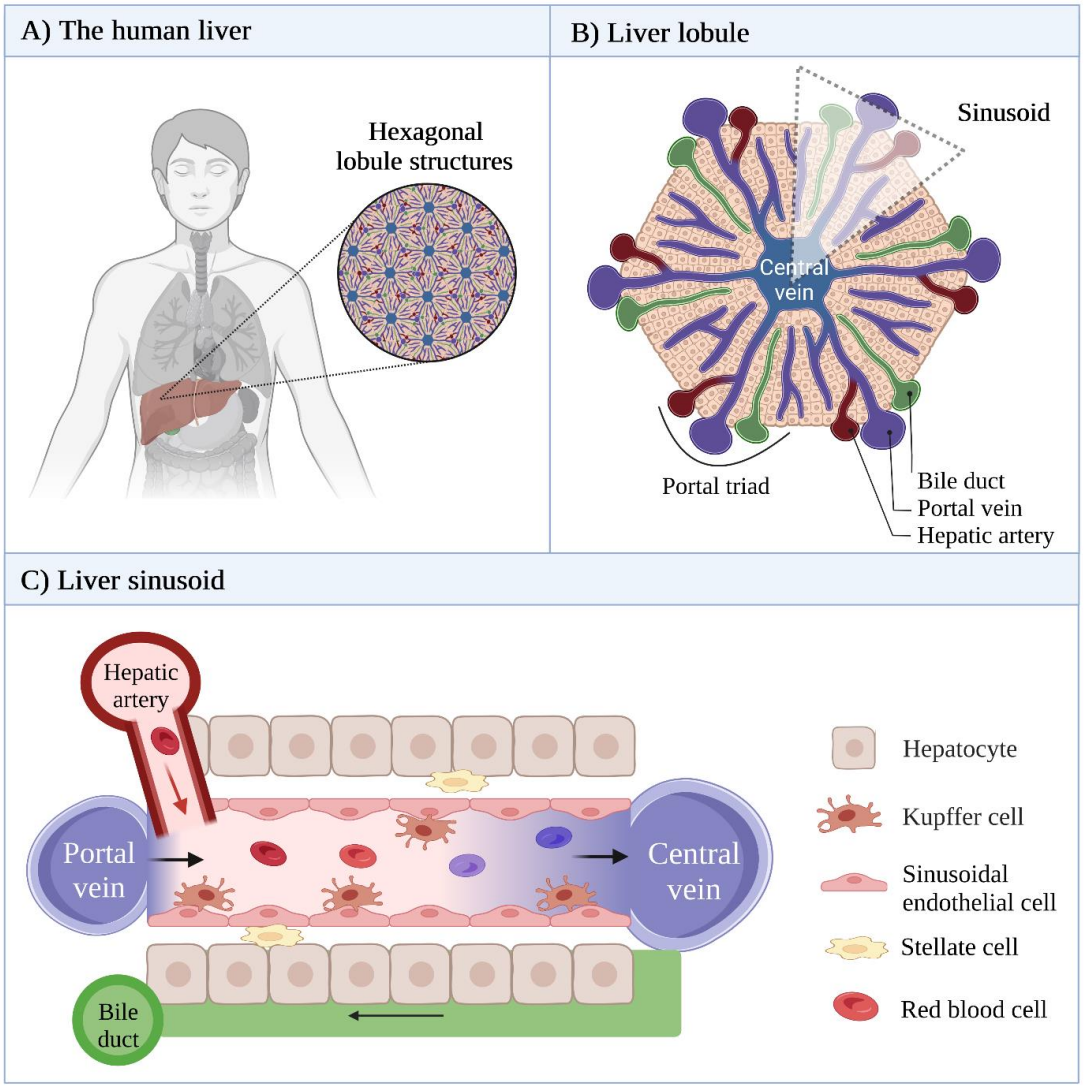

Figure 5: The structure of the human liver. A, B) The liver cells are arranged in hexagonal lobule structures, C) with hepatocytes and other cell types interacting in the sinusoids. Created with BioRender.com.

1.2. Health effects of nanomaterial exposure

Exposure to NMs and interactions with human cells can be beneficial and used for targeting specific cell types or tissues for drug delivery, such as in nanomedicines. However, the interactions may also lead to adverse effects by impairing cellular functions and induce toxicity.

Nanotoxicology is a growing research field focused on identifying toxic responses and mechanisms caused by NM exposure to humans and the environment. Human hazard characterization of NM exposure is essential for proper risk assessment to avoid unintended

adverse effects on human health. Toxicity and bioavailability of a compound (including NMs) to an organism is determined by both the exposure dose/concentration and the compound´s toxicokinetics, which explain the interaction of the compound with the organism. This includes essential parameters such as absorption (uptake into cells or tissues), distribution to tissues or organs, metabolism, including toxification and de-toxification, and excretion or elimination from the organism The toxicokinetics of a compound determine tissue concentration, the length of interaction with the primary or secondary target sites, and half-life in the body [31].

NMs have different toxicokinetic properties compared to corresponding bulk materials, due to the smaller size and higher relative number of atoms at the surface, and thus high reactivity [32]. Uptake of NMs into cells are not only limited to phagocytosis as for larger particles, but also includes vesicle transport pathways or adhesive interaction. Although metabolism of solid NMs may not occur in the same way as for other chemicals, which are normally metabolized to increase or decrease the toxicity of the parent compound, some NMs can dissolve after uptake to cells, leading to hot spots of toxic ions. Of special concern, is the potential bio-persistence of non-degradable NMs which are not excreted, which may cause long-term effects [32]. Accumulation of gold NMs were studied in humans after inhalation exposure. Gold NMs were found to translocate from the lung to the blood. The translocated gold was found to be accumulated in the excised carotid plaque from sites of vascular inflammation in patients with cerebrovascular disease, and the gold NMs showed potential to cause significant biological action to affect the disease process. Some gold was detected in urine up to three months after exposure [22,23].

1.2.1. Hazard characterization by genotoxicity testing

NMs can be hazardous in distinct organs and tissues by different mode of action and key events. Genotoxicity is an adverse endpoint which is crucial to investigate as part of the hazard characterization of all NMs and other chemicals. Genotoxicity describes the property of chemical or physical agents to alter the genetic information. The genetic damage can be repairable or induce permanent changes in the genome. Depending on if the damage occurs in germ or somatic cells, it can cause genetic disease, cancer, or reproductive toxicity [33–36].

An occupational study found higher levels of DNA damage in leukocytes of workers exposed to nanocomposite materials for a long term (18 ± 10 years) compared to a control group. During

the work shift, a further increase in the DNA damage level was induced after acute exposures. Results were dependent on the gender and health status of the workers [37].

NM-induced genotoxicity occurs through primary (either direct or indirect) or secondary mechanisms [35,36]. Some NMs internalized by cells can directly interact with the genetic material and cause physical or chemical damage. This is referred to as direct, primary genotoxicity. Depending on the cell cycle and thus the organizational level of DNA, the NMs can bind to the DNA molecules and interfere with DNA replication or transcription of DNA into RNA, or disturb the mitosis process, leading to formation of micronuclei by chromosome breakage and/or rearrangements (clastogenicity) or numerical chromosome aberrations (aneuploidy) [35,36]. Thus, direct, primary NM-induced genotoxicity can cause DNA damage such as DNA breaks and other DNA lesions, large DNA malformations, or chromosomal damage [35,36].

Indirect, primary NM-induced genotoxicity occurs by affecting intermediate biomolecules that either are involved in normal genome functions or in cell division, causing DNA injury or chromosomal malformations. The key indirect mechanism of primary NM-induced genotoxicity is oxidative stress [36]. Oxidative stress is caused by an imbalance between detoxification mechanisms and reactive metabolites such as reactive oxygen species (ROS), and can lead to DNA injury, damage to lipids, proteins, and other cellular components [38]. Interaction of free radicals with DNA can cause purine or pyrimidine oxidized lesions and strand breaks. If not repaired, it can result in gene mutations and larger chromosomal damages [35].

Secondary genotoxicity is considered to be the main mechanism of genotoxicity of NMs and is mediated by extracellular ROS via the inflammatory responses of immune cells such as macrophages and neutrophils [35,36,39,40]. NMs can activate phagocytes to produce inflammation as an initial defense mechanism involved in clearance of microorganisms or foreign materials. If the clearance of NMs fails, it can cause a chronic immune cell response [35].

1.3. Model systems for nanomaterial hazard assessment

Only a limited number of studies have investigated unintended health effects in human subjects caused by exposure to NMs without any medical component, due to the ethical implications arising from conducting studies on healthy human subjects and potentially toxic NMs. Several

experimental studies on animals (*in vivo*) or cellular systems (*in vitro*) have shown that the interaction between biological environments and the NMs is dependent on the NMs' physicochemical properties [7]. As an example, the shape of NMs influences uptake into cells [41], as well as mutagenic potential [42]. The mutagenic potential of silver NMs has also been shown to be dependent on surface coating and charge [43]. Thus, all toxicological studies on NMs should also include characterization of the physicochemical properties in the applied test system, to ensure we know what we are testing and to be able to compare with other results [10]. Although increasing numbers of studies focus on nanotoxicology, more investigations are required to better understand the responses and toxicity mechanisms following NM exposure [10], using appropriate models and methods to avoid unintended effects on humans and the environment.

1.3.1. *In vivo* vs *in vitro* models

Hazard assessment of NMs and other contaminants are normally performed by *in vivo* or *in vitro* studies. *In vivo* animal studies are highly beneficial to study systemic responses to exposures, however, structural differences to human anatomy are an issue making extrapolation from animals to humans difficult. In addition, there are important ethical considerations to make around animal experiments [44,45]. Thus, there is an ongoing shift in experimental toxicology and pharmacology, towards increased use of *in vitro* models in compliance with the 3 Rs to reduce, replace and refine animal experiments.

In vitro models give reproducible, higher-throughput results, are time- and cost effective, and ethically beneficial, compared to animal studies. They allow utilization of human cells, which might reflect human effects better than rodent models, and enable studies of underlying mechanisms of toxicity under controlled conditions [46–49]. To be used in toxicity assessment, it is critically important that the *in vitro* model reflects the *in vivo* situation as closely as possible. Standard *in vitro* models have several limitations, because of the simplicity of the cellular arrangements. They typically include cells grown in two dimensions on a flat surface with static submerged conditions, without the complexity and structural coordination as seen *in vivo* where cells are growing in three dimensions. This simplified cellular arrangement results in limited intercellular interactions and cell signaling, which is important for cellular effects of the test compound and other stimuli [29,47–49]. The communication between different cell types is not reflected in standard monocultured models, and consequently, they cannot be used to assess the ability of NMs to induce secondary genotoxicity [35].

An important aspect of replacing animal experiments, is the development of new approach methodologies (NAMs). As part of this, there is a need for development of more advanced *in vitro* models better resembling the *in vivo* situation [46–48]. Application of new advanced *in vitro* models with cells arranged in a three-dimensional (3D) structure is likely to better reflect human responses, as this arrangement involves a cell environment where the cells are closer in contact and surrounded by an extracellular matrix [29,50], better resembling tissue and organ structure. Such new advanced models can be used for hazard assessment of any test substance, including NMs and drugs.

Advanced *in vitro* models come in many forms, with cells cultured in mono- or multi-cultures, in planar structures or 3D, with and without scaffolds and/or matrix/hydrogels, and in static or dynamic conditions. Each advanced model has its own requirements for cell types and applications, and thus, all the advanced models have their own advantages and limitations [29,51,52].

Several new *in vitro* models with different states of complexity are being developed. Establishment of a new alternative method starts with development and optimization, followed by validation and eventually regulatory acceptance [53]. From the 7th International Workshop on Genotoxicity Testing in November 2017, it was concluded that the advanced skin models have reached an advanced state of validation after over 10 years of development; while the advanced airway and liver models for genotoxicity assays are at an earlier stage of development [12,50].

For hazard assessment of NMs, the models should be validated for suitability of testing of NMs, as the NMs for example can have limited permeation in hydrogels etc. [28]. This thesis is focused on two main models which are highly relevant for human exposure and applicable for NM testing, namely lung and liver 3D models.

1.3.2. Advanced *in vitro* 3D models of lung and liver

3D lung model at the air-liquid interface

Respiratory cells cultured at the air-liquid interface (ALI), with air on the apical side and a microporous membrane with liquid supplying nutrients on the basal side, is a highly physiological relevant model for lung cells [44,50]. The same principle can be applied for cells from the eye and skin [50]. Lung models at the ALI can be made using immortalized cells, or

primary cells, such as bronchial epithelial cells obtained from bronchial brushings or organ donations of patients [45]. The early version of ALI culture was introduced in the 1970s by Voisin and colleagues, with a culture composed of alveolar macrophages of guinea pigs [19,54]. Although primary cells have high physiological relevance, primary cells may have unstable phenotypes and high inter-donor variations, making the use of immortalized cell lines more reliable. Application of cell lines has many advantages over primary cells, including no inter-donor variations, relatively easy culture procedures and low requirements for manual handling and manipulation, unlimited life span, more stable phenotypes, high availability, and low costs [45]. In the recent years, several studies on nanotoxicity assessment have been published on ALI models prepared from different lung cell lines, including alveolar epithelial A549 cells, bronchial epithelial BEAS-2B or Calu-3 cells [31,44,49,55–63].

In 2009 a model based on A549 cells in combination with controlled exposure to aerosolized gold (Au) and ZnO NMs (abstracts P-186 and P-187 in [64]) was reported. Due to toxicity of NMs being dependent on the physicochemical properties, this needs special attention during exposure. In submerged exposures, the NMs are submerged in the culture medium and thus covered by a biomolecule corona, which are biomolecules covering and evolving in a dynamic manner depending on the NMs' physicochemical properties, the available components in the medium and time [65,66]. When the cells are exposed at the ALI to an aerosol of NMs, the particles are not covered by a biomolecule corona in the same way before being deposited on top of the cells. Thus, ALI exposure of NM aerosols is better mimicking human lung exposure, where the NMs are inhaled in humid air and deposited on the aqueous lining of the lungs, including surfactants or mucus on top of the epithelial cells [44]. Commercially available exposure instruments allow for exposure of NM aerosols (for example VITROCELL® and CULTEX®), in a practical and reproducible manner. In addition, the concentration of NMs delivered to the cells can be directly determined in a much easier manner compared to standard 2D cultures or experiments on rodents [44].

In general, the cellular properties and responses have been shown to change when the cells are cultured and exposed at ALI conditions, compared to traditional submerged conditions. At the ALI, A549 cells produces surfactants, which is one of the physiological functions of this cell type (alveolar epithelial type II) that cannot be seen in submerged conditions [44], and they produce enough surfactants to decrease the surface tension to similar values as in the airways [55].

The sensitivity to induced toxicity can change when cultured in ALI conditions, depending on the NMs and endpoints tested [44]. The sensitivity can also be dependent on the cell type(s) included in the model. The epithelial lung cells can be cultured using a single cell type alone (monoculture) as described for A549 cells, or in a mixture/combination with other cell types (coculture), such as endothelial cells, macrophages, and dendritic cells. This allows for cell signaling and communication between the different cell types, and separate analysis of the cell types at the end of the experiment is possible. For example, in a study by Wang *et al* (2019) different responses were seen in different models after exposure to PM2.5. A549/EA.hy926 cocultures had a stronger inflammatory response than A549 monocultures. No cytotoxicity was seen in the cocultures, measured by the LDH assay, however, when increasing the complexity by adding macrophage-like THP-1 cells, a cytotoxic effect was seen at the highest tested concentration [67]. The addition of immune cells impacts the inflammatory effects by communication and cooperation between the epithelial cells and immune cells [68,69].

To find the most realistic model relevant for human hazard assessment of NMs, further optimization of the model(s) is needed as well as to investigate the impact of different layers of complexity.

3D liver model

There are several methods for culturing liver cell lines in 3D conditions to improve the longevity and differentiation of the cells into enhanced, fully functional hepatocytes in a more physiologically relevant setup [28,48]. Hepatocyte spheroids, or 3D tissues, are formed when the adhesion to the culture substrate is prevented and monodispersed cells are self-organized into a spherical conformation [48,70–72]. Spheroids can be prepared by spontaneous self-assembly in non-adhesive wells under static conditions, with agitation, in microcavities or in hanging drops [29]. Preparation of liver spheroids by hanging drop technique uses the gravitational forces and is a robust, economical, and simple method, with high size reproducibility [29]. This model is shown to recapitulate the liver microenvironment well and facilitates the use of 3D model systems in high-throughput toxicity screening [28].

Spheroids can be formed from either primary cells or cell lines. Use of primary human hepatocytes (PHHs) are considered as the “gold standard” for studying metabolism and toxicity of chemicals [29,48], however, much research has been directed towards using hepatic-derived cell lines instead due to difficulties associated with culturing of PHHs, including de-

differentiation of cells during long-term culture, costs, and inter-donor variation [48]. The human hepatocellular carcinoma cell line HepG2 is one of the most frequently studied cell lines for 2D and 3D hepatotoxicity studies and may represent an alternative to PHHs when cultured in an advanced setup [28]. Compared to HepG2 2D cultures, 3D HepG2 spheroids show enhanced liver-like functionality by formation of bile canalicular-like structures and tight cell-cell interactions [29,48], and high activity of liver-specific functions including albumin, urea synthesis, and CYP expression [73–76].

Hepatocyte spheroids have been applied for toxicity studies with NMs and other chemicals, where different sensitivities of the 3D model have been found in the various studies. HepG2 spheroids were more resistant than 2D cultures to NM-induced cytotoxicity, after exposure of Ag, SiO_2, and ZnO NMs [75]. The micronucleus assay has been applied on HepG2 spheroids for detection of chromosomal damage, showing higher sensitivity of the 3D model than standard 2D model to acute exposures of benzo(a)pyrene and 2-amino-1-methyl-6-phenylimidazo(4,5-b)pyridine [77]. Micronucleus assay has also been applied to HepG2 spheroids after longer-term exposures to TiO_2, ZnO, Ag, $BaSO_4$ and CeO_2 NMs [78,79]. Using a commercially available spheroid model with primary liver cells, the effect of single or repeated exposure of NMs of Ag, ZnO, TiO_2, and multi-walled carbon nanotubes, was investigated. All NMs at high concentrations induced DNA SBs in the spheroidal cells evaluated by comet assay, with Ag and ZnO NMs most potent, and with similar responses as previously reported in a related study on C3A cells which are clonal derivative cells of HepG2 cells [80,81].

1.4. Next generation risk assessment of nanomaterials

Hazard and risk assessment of environmental contaminants is needed for the regulatory bodies to avoid unintended adverse outcomes on human health and environment. Knowledge on both hazard characterization and exposure data are needed for risk assessment. As an increasing number of NMs are produced and used, acquiring this knowledge is challenging. NAMs is an approach to overcome this challenge involved in the so-called next generation risk assessment (NGRA) of NMs. The development of advanced *in vitro* models is part of NAMs, in addition to safe-and-sustainability-by-design approaches, *in silico* modeling by grouping of NMs' physicochemical properties and read across, to assess the risk more easily and realistically. Usage of advanced models, which are more physiological relevant than traditional models and

with medium throughput, will make the risk assessment more relevant and aid to better understand the NMs' behavior and protect the humans and environment.

At present, the development of advanced 3D models is at a relatively early stage. No *in vitro* models for inhalation toxicology, with or without ALI approaches, are currently validated from a regulatory perspective [44]. During the developmental stage, it is important to optimize the model and its reproducibility [53]. For advanced models of lung and liver, the differences in toxic responses compared to traditional models or humans are not yet clear. In addition, limited studies have focused on genotoxicity assessment with the advanced 3D models [28]. In the process of development and validation of these advanced models, the toxicological responses and results should be compared to traditional 2D models, to evaluate potential differences and challenges. Use of the similar endpoints and statistical comparisons will enhance the applicability of the results from such studies [44]. Such model optimization is needed before the advanced models can further be validated against human data and regulated to be used in hazard characterization and risk assessment of NMs.

2. Aims of the study

The main hypothesis of the present study was the following: hazard assessment sensitivity to NM exposure changes when going from standard submerged monocultures to advanced *in vitro* cellular models of lung and liver. Therefore, the overall aim of this thesis was to contribute to the development, optimalization and characterization of advanced *in vitro* models for lung and liver, and more specifically to apply these models for cyto- and genotoxicity testing of NMs and compare the results between the models and with results from standard 2D monoculture models (Fig. 6).

The specific objectives were:

Lung model:

- Establish and characterize advanced alveolar (**Paper I, II**) and bronchial cell models (**Paper III**).
- Compare the cyto- and genotoxic responses in lung cells at the ALI and in submerged monocultures after exposure to two reference Ag NMs with different physicochemical properties (**Paper II**).
- Compare cyto- and genotoxic responses of mono-, co- and triculture lung models at the ALI after reference Ag NM exposure (**Paper I, III**).
- Investigate differences between advanced bronchial and alveolar cell models (**Paper III**).

Liver model:

- Establish and characterize an advanced 3D hepatocyte model (**Paper IV**).
- Compare the cyto- and genotoxicity responses in advanced liver spheroids with 2D monolayers after exposure to chemicals (**Paper IV**).
- Compare the cyto- and genotoxicity responses in liver spheroids and monolayers after exposure to NMs (**Paper V**).

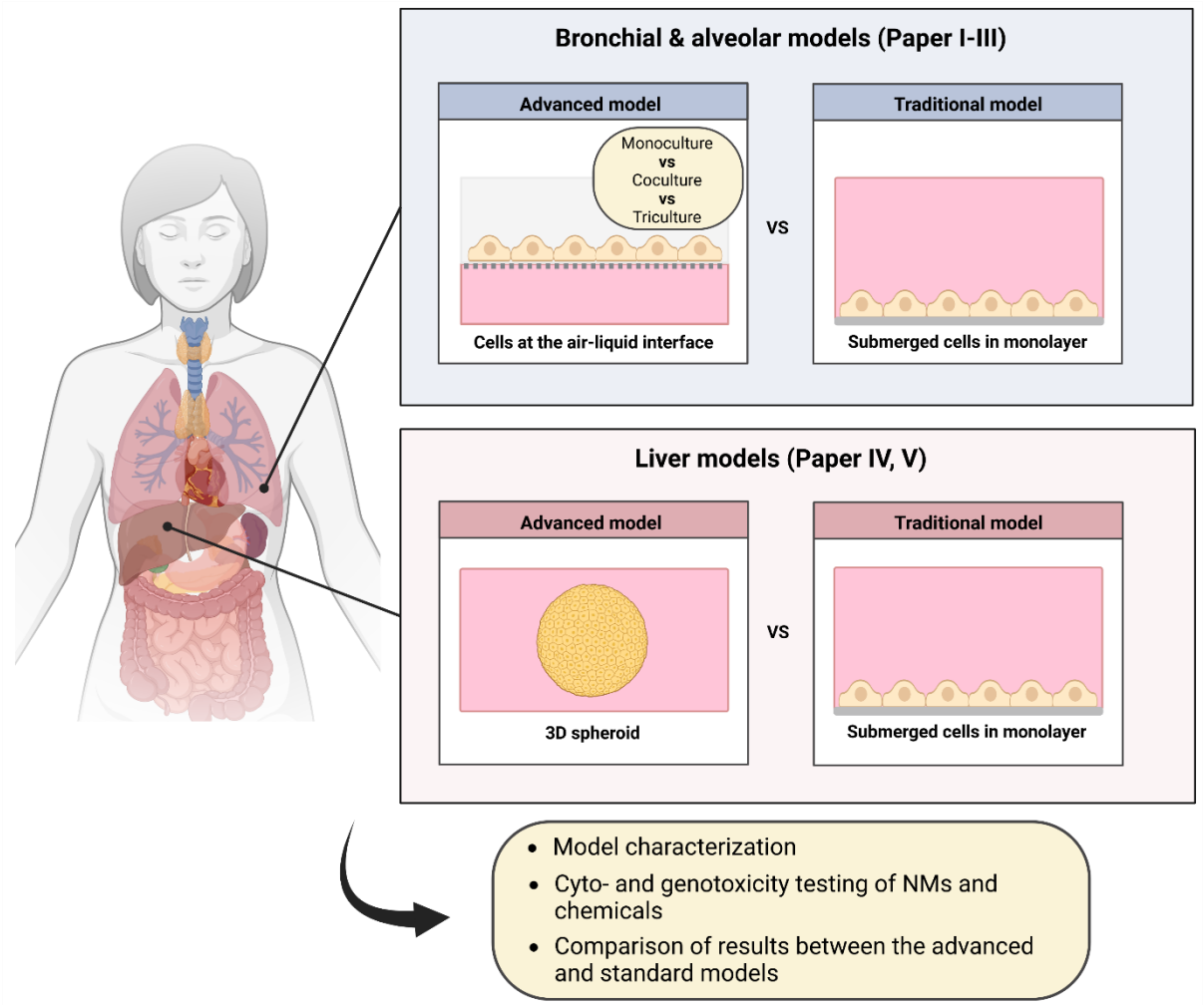

Figure 6: Graphical presentation of the aims of this thesis. Created with BioRender.com.

3. Methodological considerations

This chapter will provide a general description and justification of the most important materials and methods used in this study, which are summarized in Table 1.

Table 1: Overview of the nanomaterials, cell lines, cell culture conditions, exposure systems, and test methods used in this work. ALI: air-liquid interface, MN: micronucleus, NM: nanomaterial, TB: trypan blue, TEM: transmission electron microscopy.

Conditions		Paper				
		I	**II**	**III**	**IV**	**V**
NMs	Ag (NM-300K)	X	X	X	-	X
	Ag (NM-302)	-	X	-	-	-
	TiO_2	-	-	-	-	X
	ZnO (NM-110)	-	-	-	-	X
Cell lines	A549	X	X	X	-	-
	BEAS-2B	-	-	X	-	-
	EA.hy926	X	X	X	-	-
	THP-1	X	-	-	-	-
	HepG2	-	-	-	X	X
Culture model	Traditional 2D monolayer	-	X	X	X	X
	3D spheroid	-	-	-	X	X
	ALI	X	X	X	-	-
	Monoculture	X	X	X	X	X
	Coculture	X	X	X	-	-
	Triculture	X	-	-	-	-
Exposure system	Submerged	-	X	X	X	X
	Aerosol	X	X	X	-	-
Test methods	alamarBlue assay	X	X	X	X	X
	TB exclusion	-	-	X	X	-
	Live/dead staining	-	-	-	X	X
	Comet assay	X	X	X	X	X
	MN assay	-	-	X	-	-
	TEM/confocal (NM uptake)	X	X	-	-	-

3.1. Nanomaterials, dispersions, and physicochemical characterization

Nanomaterials

A group of NMs representing broad applications and high production numbers were selected (Fig. 7). Two silver (Ag) NMs, NM-300K and NM-302, and one zinc oxide (ZnO) NM, NM-110, were selected as well-characterized reference NMs and thus appropriate for benchmarking and development of new model systems. NM-300K and NM-302 were selected based on toxicity seen in our previous studies [42,82], and NM-110 due to its expected toxicity and dissolution in culture medium. Titania NMs were also included as stable non-dissolving particles and were synthesized according to the procedure in **Paper IV** by a collaborating project partner (Catalan Institute of Nanoscience and Nanotechnology (ICN2), Spain).

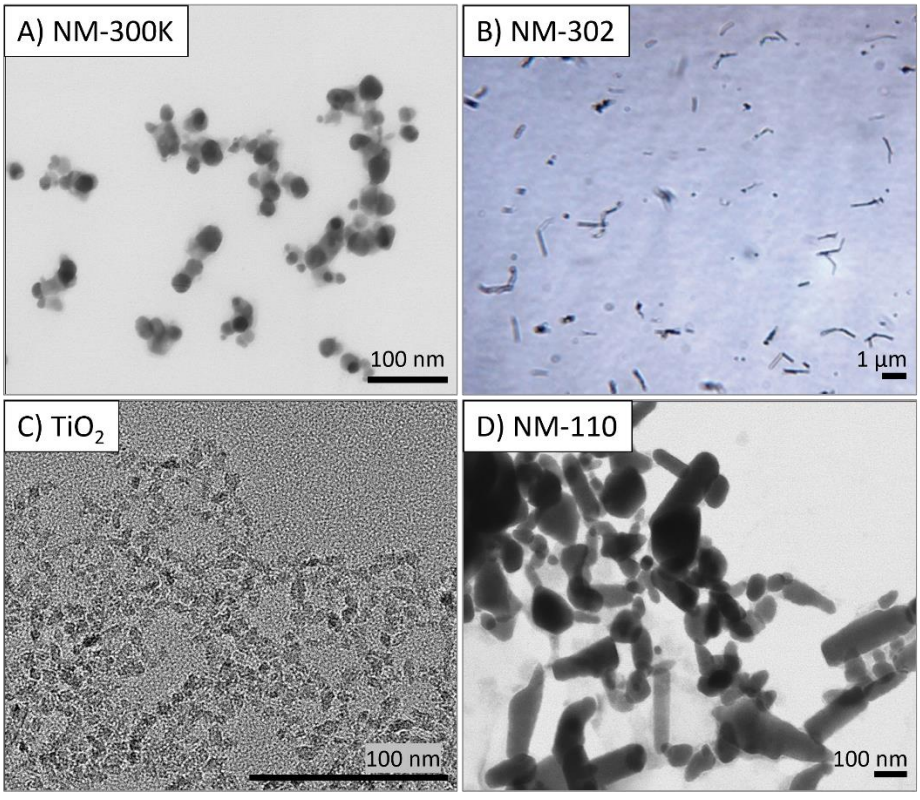

Figure 7: The NMs used within this work. A) Spherical NM-300K, B) rod-shaped NM-302, C) quasi-spherical TiO_2 NMs, and D) irregularly shaped NM-110. Figure A, C, and D with scale bars 100 nm were obtained by electron microscopy as described in ***Paper V****, by Oscar H. Moriones (Catalan Institute of Nanoscience and Nanotechnology (ICN2) and Universitat Autonòma de Barcelona, Spain). Figure B with scale bar 1 µm was obtained by optical microscopy and adapted from* [42].

Nanomaterial dispersion protocol

Nanomaterials are synthesized as powder or in suspension form, and to prepare stable dispersions for use in toxicity studies, sonication may be required. There are several protocols for dispersion of NMs, such as the NANOGENOTOX protocol [83], protocols from the EU-project NanoDefine [84], and the "DeLoid" protocol [85]. The NANOGENOTOX protocol has been validated under several projects, including European Union's FP7 NanoReg, and Horizon 2020 NanoReg2 and PATROLS. This protocol is commonly used for dispersing reference materials from JRC. Briefly explained, the NMs are mixed with water added 0.05 % wt/vol bovine serum albumin (BSA) to a final NM concentration of 2.56 mg/ml and are sonicated on ice with a probe sonicator giving a total of 7056 J ± 103 J per 6 ml volume. The BSA and water solution needs sterile filtration before use, which causes about 28 % loss of BSA. Thus, the final BSA concentration is 0.036 % wt/vol, however, 0.05 % is stated in the procedures [83].

The main principles of the Nanogenotox protocol were followed for NM-300K, NM-302 and NM-110 in this work, to ensure reproducibility of data and comparability between studies. Aerosol exposures in **Paper I-III** required a modification of the dispersion protocol for NM-300K and NM-302 to achieve a higher concentration of the NM dispersion for application in the aerosol system. Some modifications on sonication energy were also performed, and all details can be found in the papers.

TiO_2 NMs synthesized and provided by ICN2 were dispersed according to their own protocol as described in detail in **Paper V**. The NMs were provided in an aqueous dispersion of tetramethylammonium hydroxide (TMAOH) and were mixed directly with serum (1:1 vol/vol) before addition of serum-free medium, with a final proportion of 1:1:9 of NMs, serum and medium, respectively. No sonication was performed.

Characterization of NMs' physicochemical properties

It is necessary to perform characterization of the NMs' physicochemical properties in parallel with toxicity testing, as even small changes in physicochemical properties can cause big changes in toxicity and hazardous potential of the NMs [17], and proper physicochemical characterization is needed to use the toxicity data in grouping and risk assessment of NMs. Some of the most important characteristics are described below and were focused upon in this

work. A summary of the physicochemical characteristics of the NMs is given in Table 5 in the General discussion.

Pristine diameter

The diameter of the synthesized NM, often measured by electron microscopy, x-ray diffraction or atomic force microscopy. The pristine diameter is an intrinsic property of the NM.

Hydrodynamic diameter

Particles dispersed in a liquid will be in constant movement due to Brownian motion. By irradiating the dispersion with a laser beam, the light will be scattered by the particles. The scattered light can be detected over time and analyzed to give information about the hydrodynamic diameter of the particles. The hydrodynamic diameter is the diameter of a sphere with the same diffusion speed as the particle being measured [86] and includes the potential biomolecule corona surrounding the particle. This is the basis for two commonly used methods for hydrodynamic diameter evaluation; dynamic light scattering (DLS) and nanoparticle tracking analysis (NTA).

In a DLS analysis, the scattered light beams will interfere with each other to produce a so-called speckle pattern with light and dark areas due to constructive or destructive wave phase additions. The speckle pattern changes over time as the particles are in constant Brownian motion. Smaller particles move faster, and larger particles move more slowly, which influences the correlation of the detected light scattering over time. By measuring this intensity fluctuation, the particle diffusion coefficient and hydrodynamic diameter can be calculated. DLS is based on an ensemble measurement (signal from the whole sample) and gives an intensity weighted distribution. This can be re-calculated to a number and volume distribution if providing relevant parameters [86].

In NTA, the particles are illuminated by a laser beam, and the scattering objects are observed under a microscope and camera. The trajectories of individual scattering objects are recorded by the camera, operating at approximately 30 frames per seconds, to track the scatter from particles moving under Brownian motion. The trajectories are used to identify the diffusion

coefficient and then the hydrodynamic diameter. NTA provides a particle-by-particle measurement and gives a number-based distribution [87,88].

In both techniques, the hydrodynamic diameter is derived from the particle diffusion coefficient and calculated from the Stokes-Einstein equation. For perfectly monodisperse samples the results from both techniques would be expected to be very similar [88,89].

Zeta potential

Charged particles in suspension attract ions to the particle surface, forming an electrical double layer around each particle. The liquid layer of ions contains two parts; the inner region or Stern layer with strongly bound ions, and the outer diffuse region with less firmly associated ions. The liquid layers will move together with the particle. There is a boundary in the diffuse layer, called the slipping plane, where the ions inside form a stable entity with the particle while the ions outside stay with the bulk dispersant. The electric potential between the particle surface and the dispersing liquid varies with distance from the particle surface. The potential at the slipping plane is the zeta potential. The magnitude of the zeta potential gives an indication of the stability of the colloidal suspension; the particles will repel each other if all particles have a large negative or positive zeta potential, while there will be no force to prevent agglomeration and flocculation if all particles have low zeta potential values [90,91].

The zeta potential can be determined by measuring the particle velocity while the particles are moving in an electric field. The moving particles cause fluctuations to the light beam which passes through the sample cell, and the fluctuation frequency of the scattered light is detected and proportional to the particle velocity [90,91].

Stability

In addition to zeta potential analysis as described above, stability of NMs can be determined by measuring the size distribution over time, which will give indication in changes in the NM dispersion such as aggregation. Particle or colloidal stability can also be analyzed by ultraviolet-visible light spectroscopy (UV-vis). The spectra show which wavelengths of light that are absorbed by the sample. By comparing the spectra of the NMs in different media or at

different time points, the changes/shift in absorbance can be indicative of stability change, aggregation, or presence of protein corona.

Concentration and dissolution

In cases where metal or metal oxide NMs are dissolving, the amounts of dissolved species can be determined by filtering the sample through a 3kDa filter during centrifugation. NMs will remain in the filter, but dissolved species will pass through in the filtrate. The amounts of dissolved species in the filtrate can then be measured by elemental analysis by ICP-MS. By analyzing the total amount of the element of interest in the sample before and after filter centrifugation, the total concentration and the proportion of dissolved species can be determined. Additionally, information on sample impurities can be determined by measuring other elements.

Nanomaterial dosimetry

Nanomaterial concentrations applied for cell exposure are normally expressed as mass, surface area or number of particles, per cell culture volume or area. The relationship between the units depends on the NMs' properties (mass – surface area – number ratio) and cell culture conditions and will typically vary between different culture dishes or plates showing the need for reporting detailed information for facilitation of data comparisons.

In this work, the surface area of most of the NMs was unknown, and the NM concentrations are expressed as NM mass per dish culture area. The NM concentrations in the range of 0.01-100 $\mu g/cm^2$ were applied for cell exposures and were selected based on publications [82,92–94] and discussions from previous projects (for example NanoTEST, NanoReg, Nanosolution). These concentrations are higher than expected in realistic exposure scenarios, which has been estimated to $7.5x10^{-4}$ $\mu g/cm^2$ [69], and instead represent high concentration acute exposures.

The concentration metrics reflects the total mass of NMs per culture area, however, for submerged conditions the delivered concentration to the cells is dependent on the colloidal stability or sedimentation of the NMs in the culture media at the given concentration. For exposures at the ALI (section 3.3), the NMs are directly delivered to the cells and do not need to cross the medium.

3.2. Negative and positive controls

As positive controls, commonly used and commercially available chemicals with known toxic mechanisms were used:

- Colchicine binds to tubulin and inhibits cell division (mitosis) causing reduced proliferation activity [95].
- Chlorpromazine hydrochloride is the hydrochloride salt form of chlorpromazine, which is a traditional antipsychotic drug. It also has other actions and therapeutic uses, for example revealing nausea and vomiting, by blocking the dopamine receptors in the chemical trigger zone of the brain. Chlorpromazine is widely distributed in the body after intake, with metabolism in the liver to >100 metabolites, and is over time excreted in urine and feces. Chlorpromazine can induce liver cholestasis and hepatic necrosis; thus, it can be toxic to the liver [96,97].
- Methyl methanesulfonate (MMS) is a DNA alkylating agent commonly used as a model compound in genotoxicity studies. It methylates guanine to 7-methylguanine and adenine to 3-methyladenine, causing base mispairing and replication blocks, respectively [98,99]. This leads to DNA SBs, chromosome breaks, micronucleus formation and finally cell death [100,101].
- Hydrogen peroxide (H_2O_2) is a commonly used oxidant agent in the comet assay. H_2O_2 crosses the plasma membrane through aquaporins (water channels), enters the nucleus and generates hydroxyl free radicals (OH•) by reactions with iron or copper ions. The OH• attacks the sugar residue of the DNA backbone, leading to base loss and single SBs [102–104].
- Mitomycin-C is a cross-linking agent causing DNA adducts and DNA inter-strand and intra-strand cross-links by alkylation of guanine residues [105].

For submerged experiments, negative control was cell culture medium without any test substances. For experiments with ALI cultures, an incubator control received the same treatment as the other samples except for the aerosol exposure and was the main negative control. An additional negative control for aerosol exposure, receiving exposure to PBS without NMs, was included in **Paper I** and **III**. In **Paper II**, incubator control was included only in comet assay and not in the alamarBlue assay.

Solvent control was included for the NMs (**Paper I-III, V**) and the positive control chemicals in characterization of the HepG2 spheroids (**Paper IV**). For NMs, the solvent control was the dispersion media of NMs prepared in the same manner as the NMs equivalent to the highest tested concentration or a range of concentrations. For chlorpromazine hydrochloride and colchicine, sterile water at equivalent concentration was used as solvent control. For MMS, DMSO in PBS at equivalent concentrations was used as solvent control. No solvent control was used for H_2O_2 and mitomycin-C.

3.3. Advanced and standard cell culture models

Cell lines and culture medium

Use of human cells (cell lines or primary cells) is a great advantage of *in vitro* models for studying toxicity, compared to *in vivo* animal studies. Five human cell lines were used in this work:

- Alveolar carcinoma cells, A549: Epithelial cells isolated from the lung tissue of a 58-year-old Caucasian male with lung cancer [106,107]. The cells are derived from adenocarcinoma, representing type II pneumocytes, and are accepted and commonly used as a model cell line in nanotoxicology [55,69].
- Bronchial epithelial cells, BEAS-2B: Epithelial cells isolated from normal human bronchial epithelium from non-cancerous individuals [108].
- Endothelial cells, EA.hy926: Established by fusing primary human umbilical vein cells with a thioguanine-resistant clone of A549 by exposure to polyethylene glycol (PEG) [109,110].
- Monocytes, THP-1: Monocytes isolated from peripheral blood from an acute monocytic leukemia patient. This cell line can be differentiated to macrophage-like cells [111,112].
- Hepatocellular carcinoma cells, HepG2: Cells with epithelial-like morphology, isolated from a hepatocellular carcinoma of a 15-year-old Caucasian male with lung cancer [113].

Each cell type was cultured in its own cell culture medium, either Dulbecco's Modified Eagle's Medium DMEM (A549, HepG2), Roswell Park Memorial Institute RPMI (THP-1), or LHC-9 (BEAS-2B). DMEM and RPMI media were supplemented with fetal bovine serum (FBS) and antibiotics (penicillin-streptomycin). For use with THP-1 cells, the serum was heat-inactivated in order to inactivate components of the complement system in the serum. The described culture details above are for experiments performed at NILU, and some differences were seen in protocols for cell culture at the collaborating laboratories. Cell cultures of all cell models (described below) were imaged in daily cell culture work with a standard inverted microscope, to confirm cell density, growth, and morphology similar to what is stated by the provider.

Cell culture models and nanomaterial exposure

Cells can be cultured in different arrangements and localizations. Standard cell cultures include cells cultured in 2D arrangements on a flat culture surface, submerged in medium on the apical side. In some cases, special coating is necessary to ensure appropriate contact between the cells and the surface. More advanced cultures include the use of scaffolds, gels (extracellular matrix), hanging cultures, ultra-low attachment plates, or/and permeable membranes, and with cells in mono- or coculture with other cell types. Following, exposure to test substance can be performed in different ways, in submerged or aerosolized conditions, for different time lengths including acute, chronic, spiked, repeated exposure (time), and with different concentrations (low, high). The following culture types were included in this work (Fig. 8):

- Submerged cells: Monoculture of cells at the bottom of a flat dish or plate. Submerged exposure to chemicals or NMs dispersed in cell culture medium in static conditions for 3 and 24h before end-point analysis.
- Air-liquid interface: Culture of lung cells on porous membrane inserts, with the basolateral side of the cells and membrane submerged in medium, and the apical side at the ALI. Exposure to NMs in VITROCELL® Cloud system with AeronebLab nebulizer (Fig. 9), and incubation for 20-24h before end-point analysis. Positive control exposure was performed via the basolateral medium.
    - Monoculture: Monoculture of lung epithelial cells at the apical side of a porous membrane, at the ALI. No cells on the basolateral side of the membrane.
    - Coculture: Monoculture of lung epithelial cells at the apical side and monoculture of endothelial cells at the basolateral side of a porous membrane.

- Triculture: Coculture of lung epithelial cells and macrophages at the apical side and monoculture of endothelial cells at the basolateral side of a porous membrane.

- Spheroid: Monoculture of cells growing in a hanging drop at the bottom-side of a petri-dish lid. The cells form a spheroid due to gravitational forces. After some days the spheroid is transferred to a cell culture plate with a cell-repellent coating (ultra-low attachment, ULA) to facilitate spheroid formation, with additional medium and convenient handling. Formation of spheroids directly in the ULA plates is also possible, however, a low reproducibility of shape in initial experiments were observed and this was not continued. Spheroids are exposed in the well, submerged, for 24h before end-point analysis.

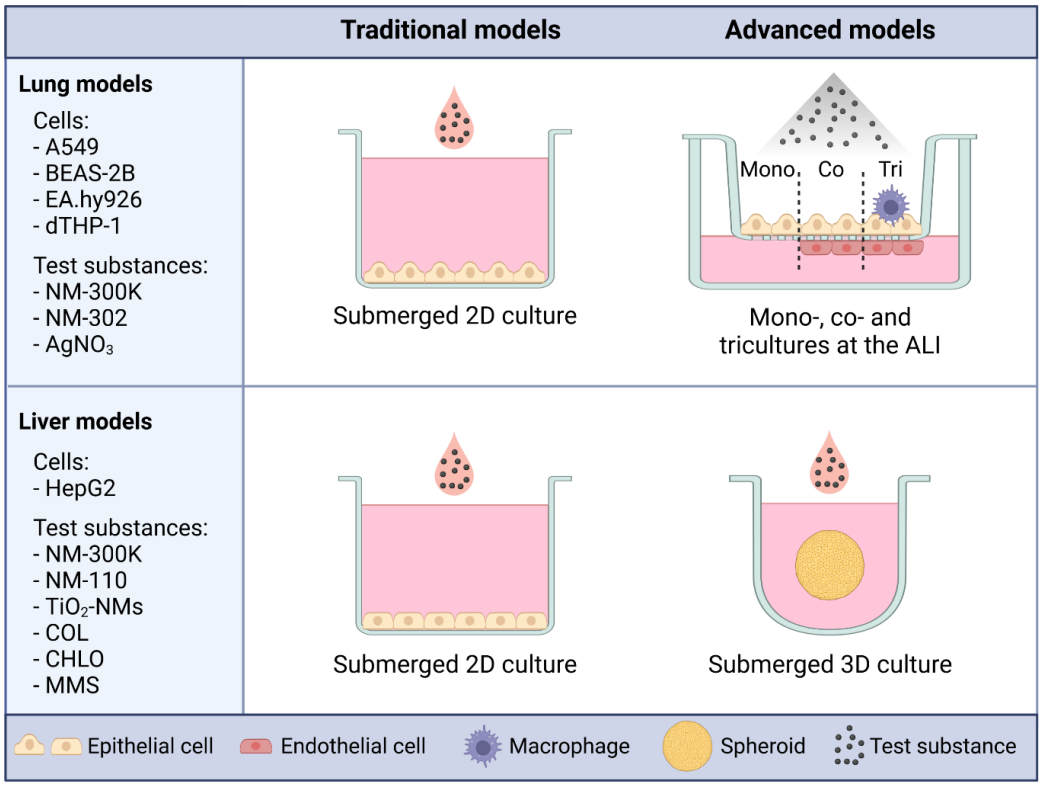

Figure 8: Cell culture models and exposure methods used in this work. Illustration, size not to scale. ALI: air-liquid interface; COL: colchicine; CHLO: chlorpromazine hydrochloride; MMS: methyl methanesulfonate. Created with BioRender.com.

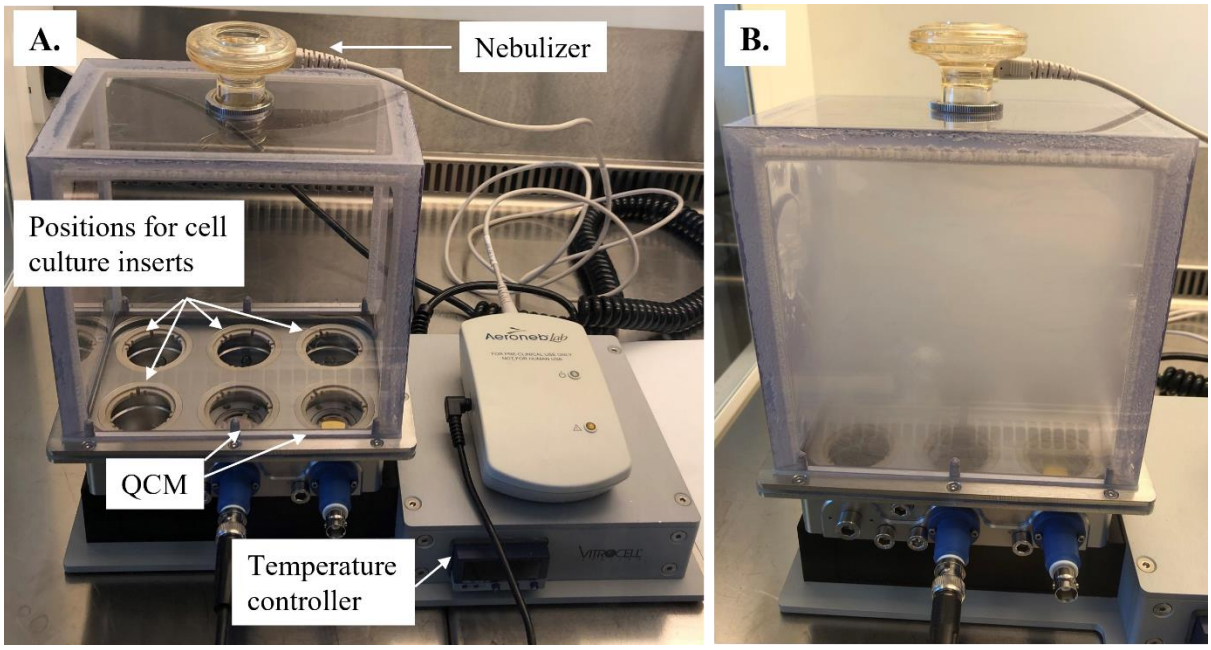

Figure 9: VITROCELL® Cloud 6, with A) AeronebLab nebulizer, in total six positions for cell culture inserts and/or quartz crystal microbalance(s) (QCM), and a temperature controller. B) A cloud of phosphate buffered saline is formed in the chamber after nebulization.

3.4. Cytotoxicity testing of NMs

Cell viability and cytotoxicity of cell cultures can be investigated by different methods and assays, which measure loss of some cellular or intercellular structure or functions. Typical assays include:

- Trypan blue exclusion test: Staining of cells with permeable plasma membranes in blue, thus, the viability can be determined by microscopy investigation [114].
- alamarBlue assay: In living cells, the non-fluorescent resazurin which is the active ingredient in alamarBlue solution, is reduced to a highly fluorescent compound resorufin. Thus, the assay detects metabolically active cells and is used for the quantitative analysis of cell viability and proliferation. The results are normalized to the negative control sample [115,116].
- Lactate dehydrogenase (LDH) assay: LDH assay is a colorimetric assay for quantification of extracellular LDH, which is a stable cytoplasmic enzyme that is rapidly released into the surrounding cell culture medium upon damage of the plasma membrane. This occurs in cells undergoing apoptosis, necrosis, and other forms of cellular damage. In the LDH assay, LDH catalyzes lactate to pyruvate and produces

NADH, and NADH reduces a yellow tetrazolium salt into a red dye. The absorbance is determined and is directly proportional to the amount of LDH in the culture [117,118].

- Staining of live/dead cells: Staining with live cell markers and evaluating the viability by fluorescence microscopy or flow cytometry. Fluorescein diacetate (FDA) is a cell-permeant esterase substrate, which is hydrolyzed by intracellular esterases to yield fluorescein which can be detected by its fluorescence. Thus, intracellular detection of fluorescein measures both enzymatic activity for activation of the fluorescence and cell-membrane integrity [119]. Propidium iodide (PI) is permeant only in dead cells and is used as a fluorescent nuclear and chromosome stain which binds to DNA by intercalating between the bases with little or no sequence preference [120]. Evaluation of live/dead cells in the intact spheroids and cells in the microfluidic cartridge was performed using a confocal microscope. The confocal microscope is constructed to study a narrow section of the sample at the time, giving a detailed and high resolved image of the sample. Several scans will give detailed information about the differences in depth. For spheroids we were only able to scan about 150 µm deep into the spheroid, mainly on the outer region. Laser and imaging settings were optimized, using the same settings for all samples within each experiment. Separate control samples were included to control for fluorescence detection in correct channel.

Cytotoxicity testing should always be performed as part of all genotoxicity testing strategies, to avoid potential false positive effects in the genotoxicity assays. Positive results in genotoxicity testing may not always be due to genotoxicity but can instead represent an indirect effect of general cellular toxicity. Thus, cytotoxicity testing is needed to identify an appropriate concentration range for the genotoxicity testing, to avoid reporting of false positive results [121,122].

3.5. Genotoxicity testing of NMs

Genotoxicity is a critical endpoint in hazard and risk assessment of NMs, chemicals and environmental contaminants. Information on genotoxicity is crucial information for risk assessment of NMs performed by regulatory bodies and it is recommended to follow the OECD test guidelines whenever possible. Information on *in vitro* genotoxic mechanisms and effect level gives an indication on the possible genotoxicity and the carcinogenicity ability of the

compound. Positive genotoxicity results in standard 2D models indicate a need for the genotoxic endpoints to be investigated by read across to *in vivo* studies with similar materials, or a need for genotoxicity studies to be performed *in vivo* [123]. Possibly can advanced 3D models replace the needs for *in vivo* studies in future.

In vitro genotoxicity assays are commonly used in combination as a test battery to detect damage at different levels of the genome:

DNA damage

The comet assay, or alkaline single cell gel electrophoresis, has been strongly recommended for regulatory purposes and is the most common test for detecting DNA damage after NM exposure [9,36,114,123], although there is no OECD test guideline for the *in vitro* comet assay yet. The comet assay requires a low quantity of sample and is a sensitive and cost-effective method for the identification of DNA strand breaks and oxidized or alkylated base lesions [123–130]. This can be an early prediction of the mutagenic and carcinogenic potential of the compound [131,132].

In comet assay, the cells are embedded in agarose on a microscope slide and lysed to remain only DNA as series of supercoiled loops. Then alkaline conditions are introduced to let the DNA unwind before running the electrophoresis, where the negatively charged DNA migrates towards the anode. DNA strands with break(s) will migrate further in the gel, due to relaxed supercoiling allowing the loop to extend under the electrophoretic field, forming shapes appearing as comets by staining and microscopic investigations (Fig. 10). The comet head represents the former nucleus, and the loops of DNA moving out of the DNA are in the tail. The comets are scored to give % DNA in tail (between 0 and 100), which is nearly linearly proportional to the number of breaks [36,114].

Oxidized or alkylated DNA bases, which can be formed by genotoxic agents but also in oxidative stress with excess presence of ROS, can be detected in the comet assay by using a modified version of the procedure. Oxidized or alkylated bases can be detected by incubation of samples directly after lysis with lesion-specific endonucleases, such as endonuclease III and formamidopyrimidine DNA glycosylase (Fpg) that recognize oxidized pyrimidines and purines respectively [36,43,125]. These endonucleases will repair the damage but leave a break in the strand, which normally will be repaired in a living cell but not in the assay. Thus, the sample

with oxidized damage and enzyme treatment will have an increase in level of SBs. The oxidized damage can be measured as the net value: % DNA in tail of sample without enzyme treatment subtracted from % DNA in tail of sample with enzyme treatment.

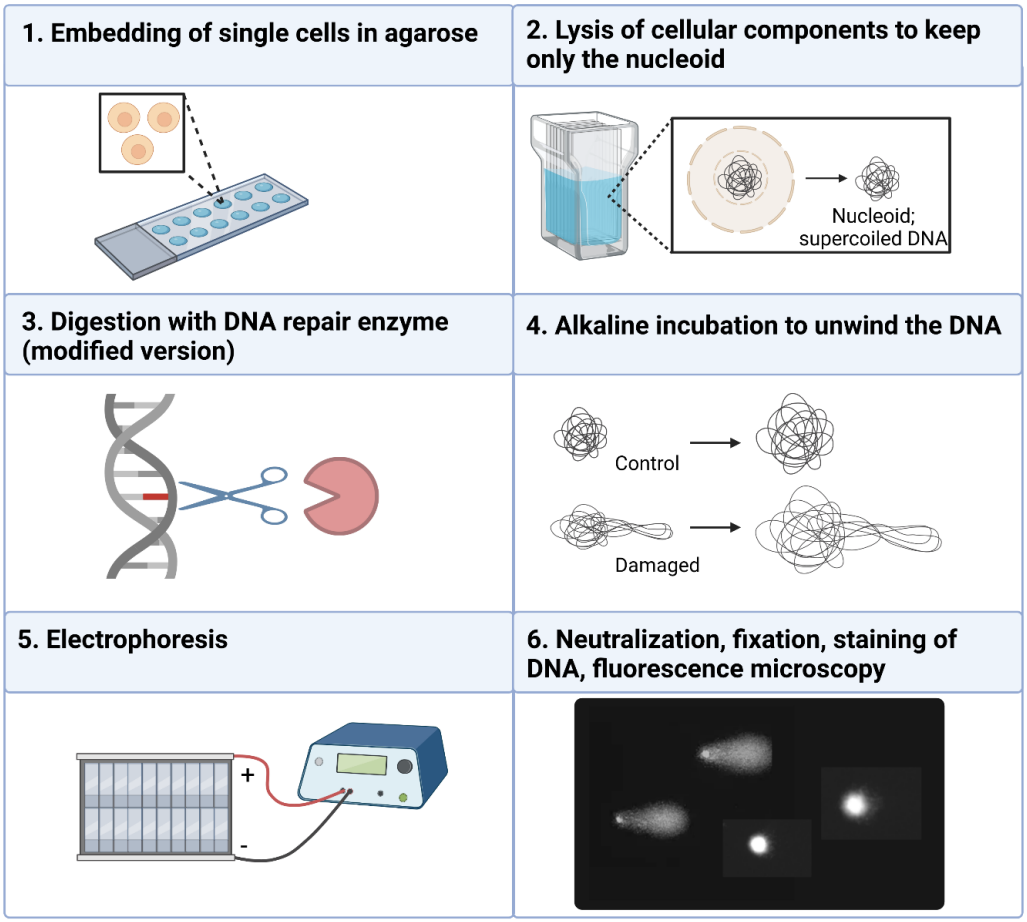

Figure 10: Principle of comet assay, modified from [122]. *Created with BioRender.com.*

Chromosomal damage

Chromosomal damage in mammalian cells *in vitro* can reliably be measured by the cytokines-blocked micronucleus test (OECD test guideline 487). In micronucleus test the ability of the NMs or other test substance to induce structural chromosome damage (clastogenic effect) or numerical chromosome alterations (aneugenic effect) is measured [114].

During mitosis, fragments of chromosome or chromatid, or whole chromosomes can be excluded from the nuclei of daughter cells and will form single or multiple micronuclei in the cytoplasm. The micronuclei can be detected by microscopic examination after DNA staining. The cytokinesis can be blocked by addition of cytochalasin B, which inhibits actin assembly,

and lead to formation of binucleated cells. This will allow scoring of cells that have completed mitosis during or after treatment [114], and investigation of chromosomal damage (Fig. 11).

In this work, a (semi-)automatic fluorescence microscopy system (Metasystems) was used for micronuclei evaluation. Camera and imaging settings were optimized, using the same settings for image collection of all samples within each experiment. The classifier was constructed to identify and image the cells with the 10x objective using specific settings for size etc., and score them in three categories: mononucleate cells, binucleated cells, and binucleated cells with micronuclei. Then, all binucleated cell images were checked manually to confirm/change category. All suspected micronuclei were checked using a 40x objective. Slides were coded to avoid scoring bias.

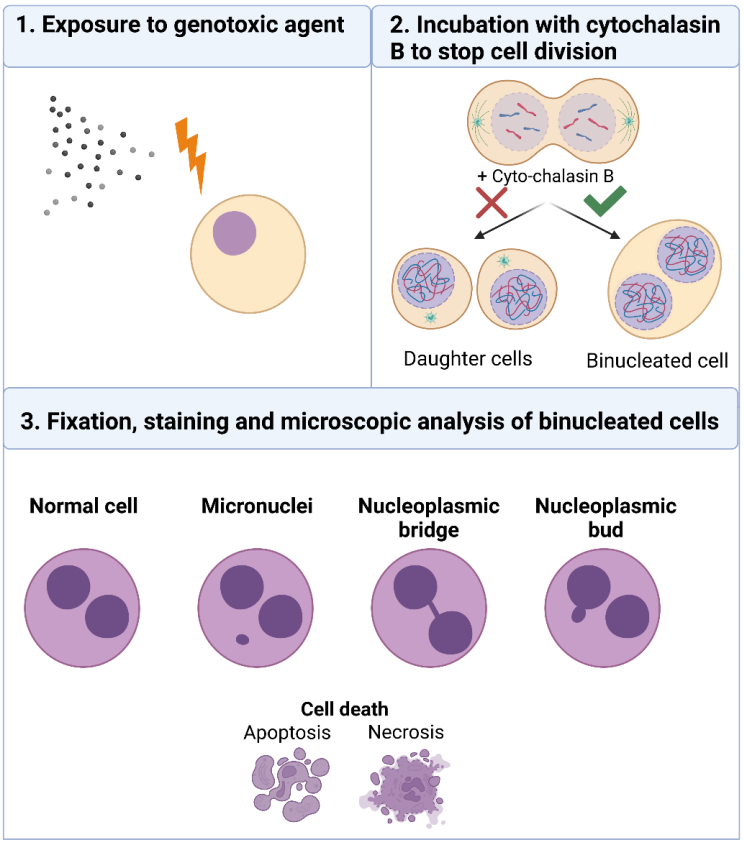

Figure 11: Principle of the cytokinesis-block micronucleus assay. Created with BioRender.com.

Gene mutations

Mammalian gene mutation tests measure mutations at a specific locus, for example the HPRT (hypo-zanthine phosphoribosyltransferase) or TK (thymidine kinase) genes, according to the

OECD test guidelines 476 and 490, respectively. The assays require specific cell types, which makes the assays incompatible with investigations on NMs' hazard potential on specific organs. Thus, investigation of gene mutations was not included in this work.

3.6. Statistical analysis

Results are presented as mean value with standard deviation, calculated from *n* independent biological repeats/experiments (each with a specified number of technical repeats), unless otherwise explained. Mathematical calculations were conducted in Windows Excel, and statistical analysis was performed in GraphPad/Prism. Most of the tests were performed by one-way ANOVA with multiple comparisons Dunnett, compared to the negative control. Level of significance was set to $p < 0.05$. The same statistical tests were performed in traditional and advanced models of each type (lung or liver).

4. Summary of papers and results

4.1. Main results of Paper I

Advanced respiratory models for hazard assessment of nanomaterials – performance of mono-, co- and tricultures

The three cell lines were identified at the intended locations in the tricultures, with epithelial A549 and macrophage-like dTHP-1 cells in apical side and endothelial EA.hy926 cells in the basolateral side of the permeable membrane. The dTHP-1 cells were observed with variable densities and morphologies, in between or on top of the A549 cells, with a ratio of 8-39 A549 cells per dTHP-1 cells similarly to the lungs *in vivo* (10:1 ratio of pneumocytes and macrophages). Some tight junctions were identified between A549 cells, however, the culture models did not form a complete barrier as both fluorescein sodium salt and Ag from NM-300K were identified in the basolateral culture medium.

The cellular viability after NM-300K exposure was compared between mono-, co- and tricultures in two laboratories, and the results changed by adding complexity when introducing several cell types. In monocultures, NM-300K at 10 μg/cm^2 (nominal conc.) induced a strong reduction in the relative viability of A549 cells compared to the untreated control. At the same exposure concentration in co- and tricultures, a slight non-statistically significant reduction in viability of apical and basolateral cells was seen compared to the PBS control sample, which also had reduced relative viability, indicating a higher sensitivity of the co- and tricultures to air exposure or sample manipulation compared to the monocultures.

No significant increase in DNA damage (SBs or oxidized lesions) was seen after NM-300K exposure in the apical cells in either of the models. A high increase in DNA SBs was seen in EA.hy926 cells from cocultures after exposure at the highest concentration of NM-300K.

Although no significant effects were seen on viability or DNA damage levels of tricultures, uptake analysis showed that single particles (5-20 nm) or small aggregates (about 100 nm) appeared to be internalized in lamellar bodies, vesicles specialized in cell surfactant production, in the apical cells. No NMs were found in the endothelial cells.

4.2. Main results of Paper II

Hazard assessment of spherical and rod-shaped silver nanomaterials by an advanced lung model at the air-liquid interface

In this paper, the effect of two Ag NMs (NM-300K and NM-302) were compared to each other after exposure of A549 and EA.hy926 cocultured at the ALI, using a slightly different procedure from **Paper I**, and monocultured in traditional submerged cultures.

Exposure of A549/EA.hy926 cocultured at the ALI to NM-300K induced a concentration-dependent reduction in cell viability in both A549 and EA.hy926 cells. In contrast, NM-302 exposure only affected the EA.hy926 cells which were indirectly exposed. No significant increase in IL-8 level, effect on cell layer integrity, or translocation of Nrf2 (important mediator in the antioxidant defense mechanisms) was found after exposure.

Similar results on viability as for ALI cocultures were found for submerged monocultured cells. Higher toxicity was measured of NM-300K than NM-302, with similar results in both cell types after short (3 h) exposure and with EA.hy926 cells being slightly more sensitive after long (24 h) exposure. $AgNO_3$ induced stronger reduction in viability than both NMs, with higher sensitivity of EA.hy926 cells than A549 cells. This indicates that the measured effect of the NMs might be related to dissolution or ion release.

Increased level of DNA SBs was measured only in A549 cells after exposure to the highest NM-300K concentration. However, at this concentration the exposure was also cytotoxic, with cell viability below the cut-off for use for comet assay (≤ 60 %). No increase in oxidized base lesions was found.

In submerged A549 cultures, NM-300K exposure was genotoxic after 3h and 24h and increase in oxidized base lesions was detected after 24h exposure. No genotoxic effect of NM-302 was seen. Genotoxic effects of the NMs on submerged monocultured EA.hy926 were not tested.

4.3. Main results of Paper III

Different sensitivity of advanced bronchial and alveolar mono- and coculture models for hazard assessment of nanomaterials

An advanced bronchial model was established and compared to the alveolar mono- and cocultures from **Paper I**.

Cell growth, confluency and permeability in the advanced models changed when going from mono- to coculture of bronchial BEAS-2B cells with EA.hy926 cells.

The effect of NM-300K was dependent on the cell types and culture models. The cellular viability of both BEAS-2B and A549 cells in monocultures was reduced after NM-300K exposure at the highest tested concentration (10 μg/cm^2), but not when each of the cells were cocultured with EA.hy926 cells. A trend towards increased levels of IL-8 was found after NM-300K exposure of all models, and an increase in IL-8 was seen also after PBS exposure.

NM-300K induced DNA damage in BEAS-2B cells in monoculture and also in EA.hy926 cells from coculture, however, only when in coculture with A549 cells and not with BEAS-2B cells.

The cytokinesis-block micronucleus assay was applied to NM exposed cells from mono- and cocultures at the ALI, as one of the first studies to our knowledge. No effect of NM-300K was seen on micronuclei induction, in neither of the models.

This study indicates that the four advanced models based on BEAS-2B, A549 and EA.hy926 cells have different characteristics, and that the sensitivity of the cells to NM-300K exposure is dependent on the culture conditions.

4.4. Main results of Paper IV

The comet assay applied to HepG2 liver spheroids

The preparation of an advanced HepG2 spheroid liver model was established in two independent laboratories and characterized before used for toxicological studies. Spheroids with initial 2500 live cells were growing to a dense structure with more than 35.000 live cells per spheroid at the day of exposure to test substances. A necrotic core was observed and reflected in the average viability of 79 %. The spheroid size increased up to 800 µm in a reproducible manner, as shown by the inter-laboratory comparison.

Differences were found in the metabolic status of the spheroids and corresponding monolayers. Spheroids had lower levels of albumin compared to 2D cultures, possibly related to the late time point of sampling or large spheroid size.

After 24 h exposure to chlorpromazine hydrochloride and methyl MMS, reduced relative viability was seen in both 2D and 3D cultures, with higher sensitivity of 2D cultures.

The comet assay was successfully applied to HepG2 spheroids for the first time to our knowledge. Background levels of DNA SBs in HepG2 cells from spheroids were similar to that of monocultures. Spheroids were more sensitive to MMS exposure (24 h) than 2D cultures, with higher levels of DNA SBs and SBs + Fpg compared to 2D cultures.

H_2O_2 exposure of 2D and 3D cultures showed that the 2D cultures were more sensitive to induction of SBs than 3D cultures, likely related to limited exposure of cells in the spheroid interior and possibility of repair during sample preparations. The opposite trend was seen with 3D cultured cells, being more sensitive than 2D if exposed after embedded into gels, which ensures exposure of all cells and limited time for repair.

These results show that the HepG2 spheroid model can be successfully applied for genotoxicity testing by the comet assay and represent a promising advanced *in vitro* model for hazard assessment of chemicals.

4.5. Main results of Paper V

Hepato(geno)toxicity assessment of nanoparticles in a HepG2 liver spheroid model

The spheroid model established in **Paper IV** was exposed to NM-300K, NM-110, and TiO_2 NMs for 24h and applied for cyto- and genotoxicity studies, in parallel with monolayer cultures. The cellular viability and DNA damage of HepG2 cells in 2D and 3D cultures were affected by 24h exposure to NM-300K and NM-110. The effects of the NMs on viability of 2D cultures were compared to their corresponding salt solutions, silver nitrate $AgNO_3$ and zinc chloride $ZnCl_2$.

After exposure to NM-300K and $AgNO_3$, the viability measured by alamarBlue assay decreased in a concentration-related manner in 2D cultures. The EC_{50} value of $AgNO_3$ was lower than that of NM-300K, showing higher toxicity of the salt solution than the NMs in this test system. In 3D cultures, the decrease in viability after NM-300K exposure was not statistically significant. However, most cells on the spheroid surface were identified as dead by fluorescent staining in confocal microscopy after exposure to the highest concentration of NM-300K.

In both 2D and 3D cultures, the viability measured by alamarBlue assay decreased in a concentration-related manner after NM-110 exposure, giving EC_{50} values in the same range as each other and as for $ZnCl_2$ exposure to 2D cultures.

An apparent trend with concentration-dependent increase in level of DNA SBs was seen after exposure to NM-300K and NM-110 in both 2D and 3D cultures. The effect was statistically significant only in 2D cultures and at cytotoxic concentrations (<60 % viability). No effect on viability or DNA damage was seen after exposure of 2D and 3D cultures to TiO_2 NMs.

Combined, these results show that the spheroids and monolayers can give different or similar responses, depending on the different test substances.

4.6. Comparisons of the toxicity responses of different cell models

The responses of the applied cell models after exposure to the test substances were summarized to give a better overview of the major observations from the performed works.

In Table 2, all EC_{50} values from traditional cell models and advanced liver models were summarized. In Table 3, all cytotoxicity results on ALI cultures from **Paper I-III** were summarized. EC_{50} values for advanced lung models are not applicable due to use of only two exposure concentrations. In Table 4, the main results from comet assay were summarized. The responses were classified as positive (+) if the effect was statistically significant compared to the negative control at non-cytotoxic concentration(s), potentially positive ((+)) if the effect was statistically significant compared to the negative control at cytotoxic concentrations only, and negative (-) if no statistically significant effect compared to the negative control was found.

Table 2: Summarized EC_{50} values after 24 hours exposure of NMs and chemicals in all cell types tested. EC_{50}: effective concentration giving 50 % reduction in viability, reported as mean with standard deviation (SD) calculated from at least n=3 independent experiments. For nanomaterials, the unit is mass per area of the 2D culture plate. For NM-300K in A549 cells, result is shown as mean with standard error of the mean and not SD.

Model		**Lung model**			**Liver model**	
		Traditional			**Traditional**	**Advanced**
Cell line		A549	BEAS-2B	EA.hy926	HepG2	HepG2
EC_{50} ($\mu g/cm^2$) of NMs and corresponding salts	**NM-300K**	37 ± 15	16.4 ± 6.0	22.5 ± 8.2	3.8	>30
	NM-110	-	-	-	10.1	16.2
	TiO_2 NMs	-	-	-	>75	>75
	NM-302	57.9 ± 4.9	-	27.4 ± 4.0	-	-
	$AgNO_3$	5.0 ± 1.5	-	2.8 ± 0.7	0.8	-
	$ZnCl_2$	-	-	-	8.4	-
EC_{50} (µM) of chemicals	**COL**	-	-	-	>750	>750
	CHLO	-	-	-	93	227
	MMS	-	-	-	417	>750
Paper		**II**	**III**	**II**	**IV, V**	**IV, V**

*Table 3: Summarized results from alamarBlue assay after NM-300K exposure to cell cultures at the air-liquid interface using the VITROCELL® Cloud System in different laboratories. Results are presented as mean relative viability with standard deviation, normalized to incubator control (**Paper I, III**) or control with BSA-water and PBS exposure. Control: exposure to PBS (**Paper I, III**) or exposure to BSA-water and PBS (**Paper II**). Low/High: lower and higher NM-300K concentrations applied in ALI system, about 1 and 10 µg/cm^2, respectively. BSA: bovine serum albumin, PBS: phosphate buffered saline.*

Model and sample		**Relative cell viability (%)**					
Alveolar model		**Apical side - A549**			**Basal side - EA.hy926**		
		Paper I lab 1	**Paper I lab 2**	**Paper II**	**Paper I lab 1**	**Paper I lab 2**	**Paper II**
Monoculture	Control	93 ± 23	93 ± 26				
	Low	72 ± 13	81 ± 18				
	High	59 ± 26	25 ± 7				
Coculture	Control	62 ± 22	77 ± 15	100 ± 0	69 ± 19	93 ± 52	100 ± 0
	Low	57 ± 20	75 ± 21	93 ± 3	67 ± 21	92 ± 16	76 ± 8
	High	59 ± 29	51 ± 27	54 ± 1	68 ± 21	70 ± 41	66 ± 6
Alveolar model		**Apical side - A549 and dTHP-1**			**Basal side - EA.hy926**		
		Paper I lab 1	**Paper I lab 1**	**Paper II**	**Paper I lab 1**	**Paper I lab 2**	**Paper II**
Triculture	Control	68 ± 12	85 ± 26		86 ± 15	108 ± 8	
	Low	67 ± 19	74 ± 26		93 ± 21	101 ± 10	
	High	51 ± 18	66 ± 23		66 ± 18	90 ± 18	
Bronchial model		**Apical side - BEAS-2B**			**Basal side - EA.hy926**		
		Paper III			**Paper III**		
Monoculture	Control	91 ± 9					
	Low	92 ± 15					
	High	57 ± 2					
Coculture	Control	67 ± 17			94 ± 10		
	Low	85 ± 21			81 ± 34		
	High	60 ± 8			100 ± 9		

Table 4: Summarized results on genotoxicity evaluated by the comet assay (DNA strand breaks (SBs)) in the specified cell lines after 24 hours exposure. Positive response is indicated by +, positive response at cytotoxic concentrations only is indicated by (+), and negative response is indicated by -. In cases where several models have positive result (in horizontal lines only), an extra + is indicated to the model with strongest response. For triculture, results on A549 represent mixture of A549 and dTHP-1 cells. H_2O_2 exposure was performed on single cells embedded in gels (5 min, 4°C).

Model	**Cell types**	**Test substance**	**Traditional model**	**Advanced model**			**Paper**
			Monoculture	**Monoculture**	**Coculture**	**Triculture**	
Lung (alveolar)	A549	NM-300K		-	-	-	I
		NM-300K	+		(+)		II
		NM-302	-		-		II
	EA.hy926	NM-300K			+	-	I
		NM-300K			-		II
		NM-302			-		II
Lung (bronchial)	BEAS-2B	NM-300K	(+)	+	-		III
		H_2O_2	+	++	+++		III
	EA.hy926	NM-300K			-		III
		H_2O_2	+		++		III
Liver	HepG2	NM-300K	(+)	-			V
		NM-110	(+)	-			V
		TiO_2 NMs	-	-			V
		MMS	+	++			IV
		H_2O_2	+	++			IV

5. General discussion

This work focused upon the establishment and characterization of advanced *in vitro* models of lung and liver, and their use in hazard assessment of NMs. Published protocols on lung and liver advanced models differ when it comes to type of cell lines, cell densities, droplet volumes (for spheroids), culture medium, and culture conditions and durations. Thus, to find the most optimal *in vitro* model for human hazard assessment, it is of interest to compare the different models and their reproducibility/reliability in different laboratories. The reproducibility of NM-induced effects on viability in lung cells at the ALI with three levels of complexities was compared in two independent laboratories. Similarly, the reproducibility of liver spheroid preparation and cultivation was compared in two independent laboratories, giving reproducible results. The suitability of these advanced models for toxicity studies of NMs, with focus on genotoxicity studies, was investigated, and the advanced models were found to give some differences in responses compared to traditional cell culture models. Although some challenges with use of advanced models for regulatory purposes are needed to be solved, the development of lung models at the ALI and liver spheroids combined with genotoxicity assessment is in-line with the 3R concept and supports the ongoing effort to implement NAMs and *in vitro* models with realistic *in vivo*-conditions for regulatory purposes.

5.1. Toxicity responses in advanced and traditional models

We wanted to compare the cyto- and genotoxicity responses, induced by chemicals or reference NMs, of the different advanced models to each other and to corresponding traditional models.

As expected, the relative cell viability of monocultured traditional cell cultures decreased after 24h exposure to most of the test substances, with the toxicity being dependent on both the test substances and cell lines (Table 2). All cell lines in traditional culture were exposed to NM-300K, where HepG2 was the most sensitive cell line, followed by BEAS-2B, EA.hy926, and A549, and with HepG2 spheroids showing least sensitivity (Table 2). Monocultured A549 and BEAS-2B cells at the ALI had similar or stronger decrease in viability after NM-300K exposure compared to submerged cells (**Paper I, II, III**). Comparing the viability results from all exposures, the advanced lung model had higher or similar sensitivity as the traditional model, while the advanced liver model had lower or similar sensitivity as the traditional model.

Cocultures are generally considered as physiologically more relevant for *in vivo* or human modeling of the respiratory system than monocultures as a more realistic complexity is

introduced. When going from mono- to cocultures (**Paper I and III**) and further to tricultures (**Paper I**), changes occurred in the properties of the model and the sensitivity to a toxic exposure. Going from mono- to cocultures, the barrier integrity of the model changed. In A549 models, the coculture seemed to be more permeable to Ag from the NM-300K compared to monocultures. In BEAS-2B models, higher permeation was seen and thus weaker barrier integrity, compared to the A549 models. BEAS-2B cocultures appeared to have higher permeation than the BEAS-2B monocultures (**Paper III**).

The viability of both alveolar and bronchial monocultures was reduced after exposure to NM-300K. However, by introducing endothelial cells the apical cells seemed to be unaffected to the NM-300K exposure, compared to the PBS control. Apical cells of both coculture types, as well as of alveolar tricultures, were affected by the PBS control. The responses of the endothelial cells seemed to be dependent on the cocultured cell type, as they were affected by PBS only when in coculture or triculture with A549, but not in coculture with BEAS-2B (Table 3, **Paper I, III**).

Genotoxicity testing by the comet assay showed some differences between the models (Table 4). NM-300K induced DNA SBs in both traditional submerged A549 and BEAS-2B cells, however, for BEAS-2B SBs were seen only at cytotoxic concentrations. In advanced models, a genotoxic effect was seen in BEAS-2B in monoculture but not in coculture, and no significant effect was seen in the alveolar models. It should be noted that the analysis of triculture apical cells in **Paper I** was performed on a mixture (coculture) of both A549 and dTHP1 cells, and further experiments may be needed to determine if this may have influenced the results. Similarly to the epithelial cells, the genotoxic response of EA.hy926 cells in coculture or triculture models seemed to depend on the other cell types. A genotoxic effect of NM-300K was seen when in coculture with A549 only, and not with BEAS-2B nor in triculture with A549/dTHP1.

Paper IV was the first study to apply the comet assay to HepG2 spheroids, showing a higher sensitivity to MMS exposure of the HepG2 spheroids compared to the traditional 2D model. Shortly after, Stampar et al (2019) published a work where they applied the comet assay to HepG2 spheroids prepared by a different technique, and in consistence with our paper, they found an improved sensitivity of the HepG2 spheroids over 2D cultures for detection of genotoxicity [133]. In **Paper V** we found that the advanced liver models had similar or less

sensitive responses to the tested NMs (Table 4), suggesting that the model's response and sensitivity may be dependent on the type of test substance, possibly related to the NMs' physicochemical properties and uptake in the spheroids.

Interesting differences in genotoxic response between the models were seen when using the positive control chemical, H_2O_2, with exposure to single cells in gels. The cells from the advanced models were more sensitive to the induced DNA damage than cells from standard 2D models, and this was seen for both BEAS-2B and EA.hy926 in the bronchial models (**Paper III**) and for HepG2 cells from the liver model (**Paper IV**). In the H_2O_2 experiments there was limited or no time for DNA strand repair, in contrast to the other exposures where repair can occur during cell harvest and embedding in gels. DNA repair is a major cellular defense mechanism against DNA damage, and the DNA damage is fixed in the genome only when the DNA repair capacity is exceeded [134]. The cells in these lung and liver advanced models are cultured at higher confluency and density than in corresponding traditional models, and this may affect the replication rates and potentially the DNA repair and other processes in the cells. Further investigations are needed to determine if the repair activity and capacity are different between the models.

For investigation of chromosomal damage, the MN assay is frequently used, and is a required test method in a genotoxicity testing strategy from a regulatory point of view. The MN assay has already been applied in several studies in the advanced liver model [28,77,79,135]. Limited studies are available on the micronucleus assay in combination with advanced human lung models at the ALI, especially in cocultures. At the time of writing, only six publications on the topic are available, applying the micronucleus assay to A549 monocultures [136], BEAS-2B monocultures [137] or primary nasal epithelial cells [138–141]. To our knowledge, **Paper III** is the first study applying micronucleus test to A549 and BEAS-2B cocultures at the ALI. No effect of NM-300K on micronuclei induction was found in either of the cell types in the advanced lung models. These results are in contrast to the genotoxic effect detected in other studies on BEAS-2B in standard 2D conditions [142,143], and further studies are needed to investigate potential differences between the advanced and submerged models. After exposure to the mutagenic control chemical mitomycin-C, a significant induction of micronuclei was seen in BEAS-2B cells and A549 cells in both mono- and cocultures, showing the successful performance of the test system. The response of the endothelial cells to mitomycin-C was significant only when in coculture with BEAS-2B cells and not with A549, and further investigations are needed to determine the reasons for this. Nevertheless, although some

modifications are needed for further optimalization of the protocol, these results show that the MN assay successfully can be applied to both mono- and cocultures at the ALI and supports the development of advanced models (**Paper III**).

5.2. Reproducibility of advanced models' performance in different laboratories

The reproducibility of the NM-induced cytotoxicity in alveolar lung cells at the ALI, in mono-, co- or tricultures in two laboratories, was investigated in **Paper I**. In general, similar trends were seen although the strength of the responses was different and dependent on the treatment type. The toxic response of exposure to NM-300K was more pronounced in Lab 2 than in Lab 1, possibly due to differences in physicochemical properties of the NM (discussed in section 5.3.).

In **Paper II**, a similar protocol for coculture model as in **Paper I** was applied. In **Paper II**, a stronger effect of NM-300K was found on both the apical and basal cells compared to the effect detected in both of the laboratories in **Paper I** (Table 3). It is likely that the difference in sensitivity to NM exposure is dependent on both the culture properties and the applied concentrations of the NMs. Between the laboratories, there may be variations in both nominal and deposited NM concentrations, which will influence the results of the experiments. Exposure to a toxic chemical with a more reliable effect compared to NMs being dependent on physicochemical properties, as well as more detailed characterization of cell numbers and barrier integrity in all laboratories, could have given further insights into the differences between the cultures prepared in the three laboratories.

The seeding and cultivation of HepG2 spheroids were performed in two independent laboratories. Although the HepG2 cells were from different providers and cultivated in different cell culture media, the spheroids were giving reproducible sizes indicating the use of a robust protocol (**Paper IV**). Further, after exposure of both spheroids and monolayers to three chemicals the viability was compared in the laboratories. A more pronounced effect of the chemicals was found by the alamarBlue assay in Lab 1 than by flow cytometry in Lab 2. The different results were most likely caused by unintended removal of damaged or dead cells during the washing steps before analysis, which impacted the measured viability in the flow cytometry but not in the AB assay due to different assay principles (**Paper IV**). Thus, to better understand the reproducible behavior of the cell models in further experiments, either the same assays should be used, or the protocols should be optimized.

Other studies on A549 cells at the air-liquid interface or liver spheroids report high reproducibility [144–146]. Barosova et al (2021) concludes that the use of cells, reagents, and other consumables from the same providers, as well as detailed standard operating procedures (SOPs) and training of personnel, are critical to obtain reproducible results across independent laboratories [146].

5.3. Challenges to resolve to improve the quality of studies on advanced models

The work in this thesis has gained new insight into the characteristics and responses of the lung and liver models. However, as identified in this work and as pointed out in literature, some challenges need to be considered in further investigations and use of the advanced models. These are addressed below.

Human handling of advanced models – sensitivity and variations

Advanced models are complex and thus more vulnerable to variabilities in performance to human handling. In **Paper I-V** we observed that there seems to be more variability between the technical and biological replica in advanced models compared to standard 2D models. Thus, there is a need for adequate training and highly detailed SOPs to ensure minimum variability in the results caused by the operator so that the variations reflect the biological effects.

The procedure for preparing spheroids in hanging drops (**Paper IV** and **V**) is similar to other studies [77,79,135,147]. Uniform spheroids were produced by using relatively low costs and equipment needs. In recent studies, spheroids have been seeded directly in the lid of normal plates coated with agarose, allowing for centrifugation of spheroids to the well instead of manual transfer [79,135]. This reduces the need for manual handling prone to errors, as well as it reduces the costs and increases the throughput. The spheroids can also be seeded directly in the wells of the spheroid plate without first being seeded as hanging drops, however, our preliminary experiments resulted in non-uniform sizes, in contrast to in literature [133].

Viability of cells and availability of nutrients

In advanced models such as spheroids and multi-layers of cells, the cells have uneven access to the culture medium with supply of critical nutrients and oxygen. This may affect the cellular

viability of advanced models and are in contrast to the more homogenous distribution of cells in traditional 2D cultures.

In spheroids, transport of nutrients, effective oxygenation, and waste removal occur through diffusion or zonation. This results in limited oxygen and nutrient diffusion towards the core, in combination with an accumulation of waste. Consequently, three zones are formed: the proliferating cell zone (towards the surface), the quiescent viable cell zone, and a necrotic core in the middle [28]. Similar metabolic zonation occurs in the *in vivo* liver as well, however, the complex vascular structures ensure sufficient nutrient supply and waste removal [148]. The development of the necrotic core in spheroids is dependent on the cultivation time (age), cell type and 3D conformation including size. A small necrotic core was seen in our spheroids with a spheroid diameter of 800 µm. The culture conditions (including the number of seeded cells, medium change, and cultivation duration) were selected based on initial experiments with multiple conditions (**Paper IV**). After one week in culture, all spheroids had a diameter above 300 µm which has been reported to be the lower limit for development of a necrotic core [48].

The presence of a necrotic core can be beneficial in cancer research, where the zones resemble the cellular heterogeneity of solid *in vivo* tumors, however, it is an undesirable characteristic in genetic toxicology where the model should recapitulate an *in vivo*-like liver microenvironment [149]. In **Paper IV** and **V**, all cells from the spheroid were pooled, but the core and rim of the spheroid can also be separated using other protocols [150]. Further improvements of the protocol for preparation and cultivation of the spheroid are needed to increase the longevity which is limited by the progression of necrosis.

In ALI cultures with multiple cell layers, such as co- or tricultures on permeable membranes, the apical cells have less contact with the culture medium compared to the endothelial cells or when in monoculture. There may also be a higher number of cells in total than in monocultures, such as seen for BEAS-2B cells (**Paper III**), influencing the amount of nutrients per cell. These differences between co- or tricultures and monocultures may explain the dry spots occasionally seen in the apical side of the ALI cultures (**Paper III**) and the increased sensitivity of co- and tricultures to buffer exposure (**Paper I, III**). It may also be related to the increased sensitivity of the BEAS-2B cells from cocultures to H_2O_2 exposure compared to monocultures (**Paper III**). The mono- and cocultured BEAS-2B cells were cultured in different media, however, we found no effect of medium type on viability or H_2O_2 sensitivity in BEAS-2B cells, and further investigations are needed to determine the reasons for the different H_2O_2 sensitivity (**Paper**

III). Nevertheless, using the appropriate medium is important and as there is no culture medium commercially available for cocultures of epithelial and endothelial cells, the medium should be optimized for each model to ensure appropriate cultivation conditions.

Models that stay viable over long periods of time are needed for further research on advanced models, moving further from acute exposures that have been used in this thesis, to long-term exposures at lower concentrations. The HepG2 spheroids had a stable size and circularity measured for 21 days (**Paper IV**). Although the full longevity of the advanced models was not investigated in this work, other studies have showed that both HepG2 spheroids [78] and lung cultures at the ALI can be cultured for long term exposures [56,58]. This supports further investigations on the HepG2 spheroids and alveolar and bronchial ALI models, for long term exposures at concentrations relevant for occupational exposures.

The use of reference nanomaterials and characterization of physicochemical properties

The use of reference NMs is highly useful to ensure comparability with other studies. In total four different NMs were used in this work (Table 5), with three of them being reference materials (NM-300K, NM-302 and NM-110). From these, NM-300K was the only NM used in both the liver and lung models and the physicochemical properties were measured in several laboratories (**Paper I-III, V**). As explained above, NM-300K induced variable responses in the alveolar cocultures in three laboratories, and this may be related to differences in the cultures. Another explanation may be that these differences are related to small differences in the NMs' physicochemical properties. Differences were seen in the hydrodynamic diameter of NM-300K measured in the two laboratories of **Paper I** and in the other studies (Table 5). The spectroscopic stability analysis of NM-300K indicated that there were not enough BSA proteins available in the stock dispersion to cover all Ag NMs completely, leading to agglomeration of the NMs (**Paper V**). By increasing the concentration of Ag while keeping the BSA concentration the same as in **Paper V**, we observed more agglomeration, in **Paper I** lab 1 and **Paper III**. However, this we did not see in **Paper I** lab 2, where the size was instead the same as measured at lower concentration (**Paper V**).

*Table 5: Physicochemical characterization of the four NMs applied in **Paper I-III** and **V**. PD: pristine diameter, Concentration: nominal concentration of stock dispersions (A and B), Dissolution: <3 kDa fraction in stock dispersion compared to measured total concentration (**Paper I**) or in culture medium compared to the nominal total concentration (**Paper V**), HD: hydrodynamic diameter in laboratory 1 and 2 measured by NTA or DLS, NTA: nanoparticle tracking analysis, DLS: dynamic light scattering, PDI: polydispersive index, a.u.: arbitrary unit, ZP: zeta potential.*

Nanomaterial	**NM-300K**				**NM-302**	**NM-110**	**TiO_2**
Paper	**I**	**II**	**III**	**V**	**I**	**V**	**V**
PD (nm)	<20 [151]				50x3000 [42,152,153]	147 ± 149 [154]	5.5 ± 1.0
Polymorph				Metallic	Metallic	Zincite	Anatase
Morphology				Sphere	Wires, particles [42]	Variable	Quasi-sphere
Concentration (mg/ml)	10	A: 24 B: 2.56	10	2.56	A: 14 B: 2.56	2.56	0.455
Dissolution (%)	3.6			<1		3-23	
HD (nm), NTA		A: 50 ± 4 B: 65 ± 11			A: 244 ± 8 B: 168 ± 34		
HD (nm), DLS	**1:** 130.7 ± 23.2 **2:** 57.5 ± 5.7		149.3 ± 42.5	54.2 ± 3.48		378.8 ± 21.5	193.6 ± 6.2
PDI (a.u.)	**1**: 0.380 ± 0.037 **2**: 0.343 ± 0.067		0.331 ± 0.062	0.364 ± 0.023		0.199 ± 0.046	0.262 ± 0.013
ZP (mV)	-17.1 ± 2.8	B: -22.65	-17.1 ± 2.8	-9.84 ± 3.94	B: 0.57	-15.8 ± 0.70	-16.1 ± 1.80

The dispersion and stability of the NMs may be linked to the sonication process, as the sonication was performed to properly disperse the NMs by acoustic energy. Temperature increase was avoided by keeping the dispersion on ice during sonication. The sonication energy may affect the resulting hydrodynamic diameter [155]. In this case, no obvious relationship between hydrodynamic diameter and estimated delivered energy or time was found for NM-300K (Fig. 12). The different physicochemical properties between the laboratories point to the importance of using a highly detailed dispersion protocol for reference NMs which is important for reliable results.

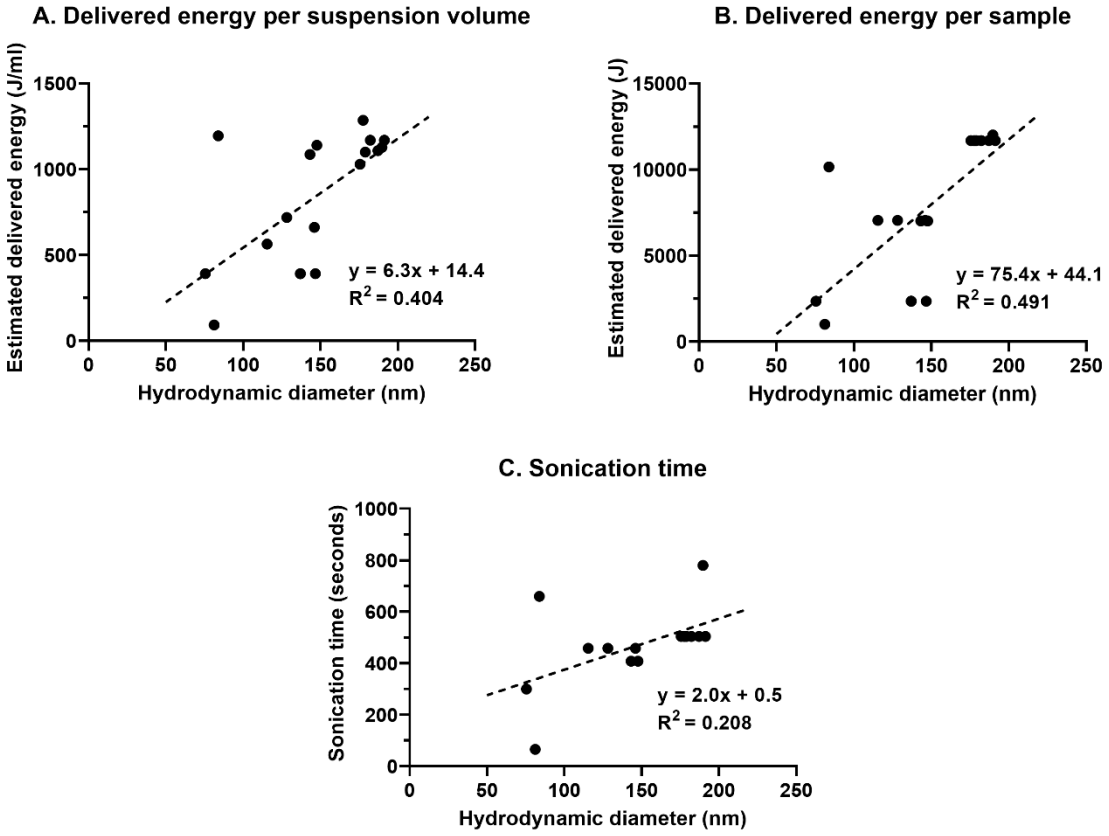

Figure 12: Relationship between hydrodynamic diameter of NM-300K (x-axis) and estimated delivered energy per suspension volume (A), estimated delivered energy per sample (B), and sonication time (C) (y-axis). No linear relationship was seen between hydrodynamic diameter and any of the other parameters. Data obtained at NILU from a total of 18 stock dispersions from ***Paper I, III****, and additional unpublished data (Elje, 2022).*

Characterization of NMs in the exposure system

Control of NMs' physicochemical properties are important for understanding the link to toxicity and the usefulness of the results. This is important both in stock dispersion and in culture medium or other exposure system. In **Paper I-III**, the characterization of the NMs was performed before nebulization and usage in the Cloud system. Preliminary experiments collecting NMs deposited in PBS in a petri dish on top of the Cloud base followed by size measurement by DLS, showed a similar hydrodynamic diameter before and after nebulization and deposition in the cloud system (details not shown). In contrast, when submerged in LHC-9 medium for submerged experiments, the size increased (**Paper III**). If the size of NMs

without culture medium remains the same before and after nebulization, it allows for better control of the exposure, which is a great benefit for the ALI models.

Avoiding interference between the nanomaterial and the test system

Avoiding interference between the test substance and the test method, caused by a high adsorption capacity and optical activity of some NMs, is crucial to avoid reporting false negative or positive results. This is a general challenge for both traditional and advanced cell models. Sufficient control samples should be included to control for potential interference. In this work, potential interference of NMs and the following test methods was tested, and no interference was found for alamarBlue (**Paper I-III**), comet assay (**Paper I, V**), and ELISA (**Paper III**). Interference was detected between NM-300K and the LDH assay, as also seen in other studies on Ag [59,156], and the results on LDH assay were excluded from the **Paper I** due to this issue. In LAL endotoxin test, no endotoxins were detected in the NM-300K dispersions at low concentrations, however, at higher concentrations the NMs interfered with the read-out of the assay due to an absorbance peak of NM-300K at similar wavelength as the measurement wavelength in the assay (**Paper II**). As no endotoxins were found by the HEK endotoxin test (**Paper I**), it is likely that there were no endotoxins present in the samples. No interference control was included for micronucleus assay or cell counting with trypan blue, which is a limitation of the study design and should be improved for further studies.

Dosimetry in traditional vs advanced models

The concentration or number of NMs located in close enough proximity to interact with the cells, will depend on the experiment design as well as the NMs' physicochemical properties. During submerged exposure, the NMs may remain in a stable colloidal dispersion or sediment in the dish (Fig. 13), which is likely to have occurred with NM-300K at high concentrations due to agglomeration. The colloidal stability or sedimentation will highly influence the number of NMs available for cell-NM interaction. A strong advantage of using cultures at the ALI for NM experiments, is the deposition of NMs directly on the apical side of the culture which is without medium. This deposited concentration can be measured in semi-real time by use of microbalances (quartz crystal microbalance) or by elemental analysis which was performed in **Paper I** and **III**. When comparing results between exposure at the ALI and submerged, it is

most relevant to use the concentrations directly delivered to the cells. In this work, the deposited NM concentration in the submerged cultures was not measured and the total applied concentration was used. It should also be noted that in ALI exposures only the apical cells will be directly exposed while the basolateral cells are indirectly exposed.

The behavior of NMs in submerged cultures may also be influenced by the applied culture dish type, as NMs can stick to the walls [49] and may also be influenced by the coating of the dish. In **Paper V**, where the toxic responses of three NMs were compared between HepG2 spheroids and submerged cultures, different culture plates were used. Due to the ultra-low attachment coating of the spheroid plates, the spheroids do not attach to the surface and "swims" in the middle of the well. However, without cells present, NM-300K was also observed to be located mainly in the middle of the well (Elje, unpublished results, 2022). Depending on the NM concentration and interaction with the coating, the concentration delivered to the spheroid surface may either be increased, if centered around the spheroid, or decreased if sedimentation occurs (Fig 12). In addition, in the spheroidal cultures only the cells on the surface are directly exposed, in contrast to 2D cultures where all cells are exposed to the NMs. As there are many variables affecting the delivered concentrations of NMs to the cells, it was important to keep the applied concentration the same. HepG2 spheroids and 2D cultures were exposed in 100 µl media with NMs, giving the same final concentrations (mass per volume) in the wells. Use of 100 µl exposure media has been applied also for other studies with HepG2 spheroids [79,135]. Submerged experiments with lung cells (A549, BEAS-2B, EA.hy926) were performed in 200 µl media, thus giving a half mass per volume concentration but the same mass per culture surface area concentration when compared to exposures for liver models.

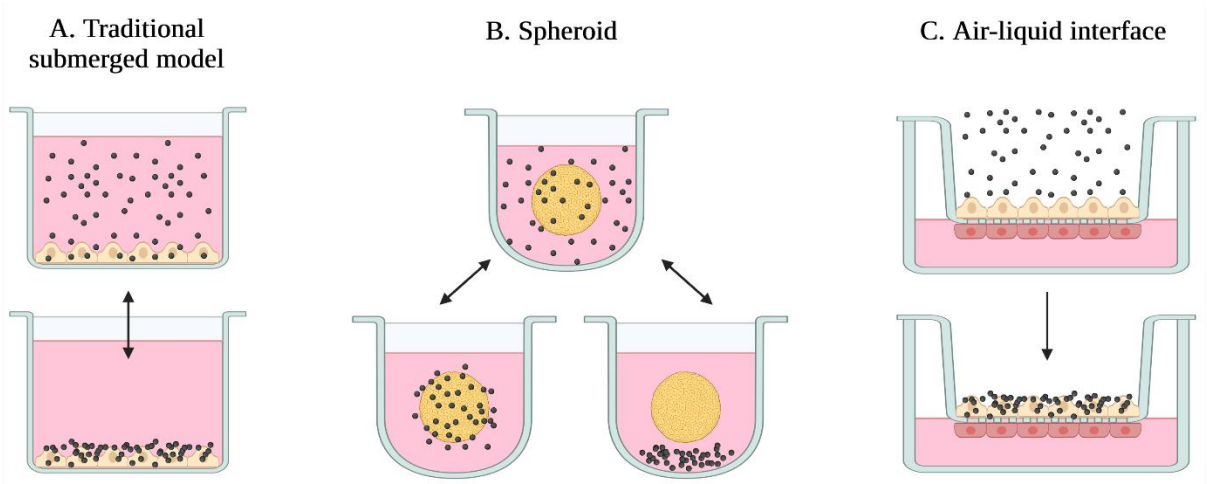

Figure 13: Potential fates of the nanomaterials (black dots) in cell culture systems, affecting the delivered nanomaterial concentration to the cells, in A) submerged 2D cultures, B) submerged spheroid cultures, and C) air-liquid interface (ALI) cultures. Illustration not to scale. Created with BioRender.com.

6. Future perspectives

6.1. Further developments of the advanced models

Lung cultures with dynamic forces of breathing

With every inhalation and exhalation, the lungs are changing its volume by stretching the tissues in addition to be exposed to changing air pressures. This is not reflected in the models of this thesis, as the culture plates and inserts have relatively high stiffness. By simulating breathing patterns, by use of mechanically tunable substrates for cell culture, the experimental conditions could be even more realistic to the human scenario [157–159].

Coculture spheroids

Coculture of hepatocytes and other liver cells would increase the physiological relevance of the spheroid model and could possibly change the sensitivity to NM or chemical exposures. Coculture of HepG2 and macrophage-like cells, dTHP-1, was tested at variable HepG2:dTHP-1 cells ratios in spheroid plates. Preliminary results showed that the dTHP-1 cells were able to form spheroids alone, although after longer incubation times than for HepG2. The coculture spheroids had similar shape and size as HepG2 spheroids, with the macrophage-like cells spread in the spheroid identified by fluorescent labeling (Fig. 14A). Other studies on liver spheroids with HepG2 and additional cells, including coculture with Kupffer cells [28] and tricultures with EA.hy926 cells and stellate cells [160], show different metabolic viability and sensitivity compared to spheroid monocultures.

Microfluidic systems and body-on-chip

To further increase the physiological relevance of an *in vitro* model, the cell culture model can be cultured under a dynamic flow of culture medium (or other physiological solution) to simulate shear forces and *in vivo*-like conditions, in contrast to the traditional static culture media conditions. This normally occurs in miniaturized microfluidic systems, often referred to as organ-on-chip systems, or body-on-chip systems if different cell types are integrated. During the last two decades, a lot of developments have been made within microfluidics for cell

culturing, giving highly beneficial and physiologically relevant culture models with integrated sensors providing real-time results of cellular responses.

Such a microfluidic platform/device was developed within the HISENTS project and described in Kohl *et al* 2021. HepG2 and A549 cells were cultured attached to a porous membrane submerged in culture medium on both sides, in separate microfluidic circuits with dynamic flow of culture medium. The viability of both cell lines and DNA damage levels of HepG2 were similar as were seen in traditional submerged cultures. Different models can be combined in the same medium circuit, moving towards the body-on-chip concept, as demonstrated with HepG2 and kidney (TH-1) cells [161].

Combination of lung and liver models in the microfluidic platform would enhance the relevance of the submerged monolayer models. By exposing the lung cells in the microfluidic platform to for example NM-300K, and indirectly exposing the HepG2 through conditioned medium, the responses could be compared to effects in monocultured cells under static conditions (**Paper I, V**). We have performed preliminary experiments on HepG2 cells under dynamic conditions, with 24 h exposure to NM-300K before evaluation of viability and DNA damage (Fig. 14B). Although the effect of NM-300K on DNA damage was not statistically significantly different from the control, it was similar to the static conditions in **Paper V**.

Miniaturization of advanced models and culturing under dynamic flow of medium or other biological fluids, is an interesting and highly relevant step forward for the advanced models. Preliminary experiments were conducted with A549 cells at the ALI under dynamic conditions, in a microfluidic vessel with an open reservoir on top and dynamic flow of medium below the cells. The cells were exposure to aerosolized MMS which induced DNA damage as evaluated by the comet assay. We observed high inter-experimental variation, which may be caused by leakage of medium through the chip membrane (Elje, unpublished results). For further experiments on ALI models in microfluidic systems, the design of the system should allow control of pressure from the medium to the cells to ensure reproducible conditions.

Preliminary experiments were conducted also with HepG2 spheroids inside a microfluidic vessel. However, the spheroids attached to the membrane and lost their initial shape. Seeding and culture of spheroids inside microfluidic systems require further optimization such as different dimensions of the system, because of the larger size and the need for retaining the shape of the advanced model.

Additional toxicity assays

Most of the cytotoxicity assays used in this study requires the treatment to be stopped, which limits the use of the sample for other endpoints measurements. A good alternative, or supplement, could be to measure the trans-epithelial electrical resistance (TEER) across the cell layer(s). TEER is a real-time, non-invasive quantitative technique to measure the integrity of tight junction dynamics in cell culture models of endothelial and epithelial monolayers. TEER measurements are generally performed by measuring ohmic resistance or impedance across a wide spectrum of frequencies, of cells in static or dynamic conditions [162,163]. TEER measurements are commonly integrated in an organ-/body-on-chip setup [161,162] and have also been used in ALI cultures [58,60,67]. Inclusion of TEER measurements in the ALI experimental setup could increase the throughput and give valuable insights into the model performances and mechanisms of NM-induced toxicity.

Comet assay is the most widely used genotoxicity assay for *in vitro* toxicity experiments with NMs. Another genotoxicity assay, the novel γH2AX assay, measures DNA double strand breaks by analyzing the phosphorylation of the H2AX histone using specific antibodies [123]. Thus, γH2AX is a biomarker for DNA double strand breaks with relatively high specificity and sensitivity [36,164], and this can be detected by different methods (western blot, ELISA, flow cytometry or microscopy). This assay was tested on ALI cultures giving promising preliminary results (Fig. 14C), using a similar protocol as previously published on cells at the ALI [165]. The assay can also be applied to spheroids after cutting to thin slices.

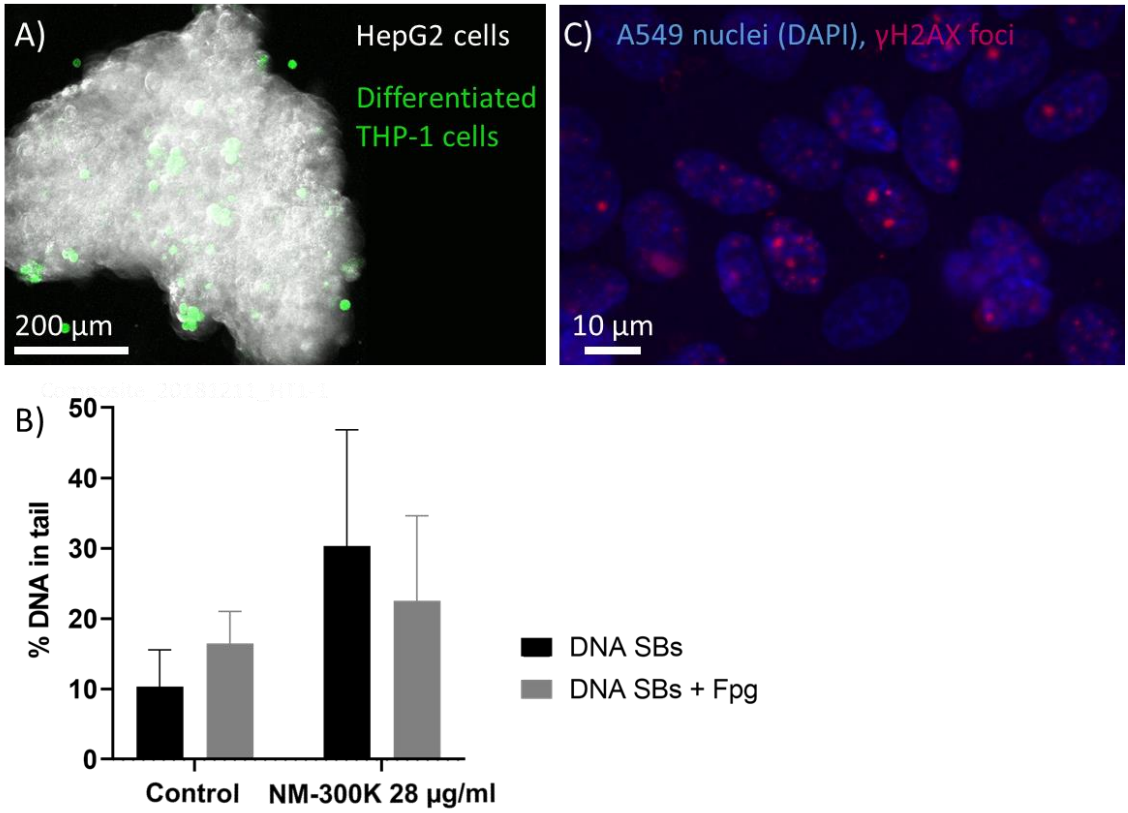

Figure 14: Preliminary results of A) coculture spheroid of HepG2 cells (in white) and differentiated THP-1 cells (in green), B) DNA damage levels in HepG2 cells induced by NM-300K in a dynamic exposure system, C) detection of DNA double strand breaks in A549 cells at the air-liquid interface by γH2AX assay.

6.2. Implementation of the advanced models in next generation risk assessment

For advanced lung and liver models together with other NAMs to be used in NGRA by regulatory bodies, the use of the models for toxicity testing should be approved as OECD test guidelines, as this will ensure optimal and reproducible conditions. The process of implementation of alternative test methods can be divided into three main parts; 1) development, optimization, and standardization of new model protocols, 2) validation across laboratories and against *in vivo* animal or human data, and 3) regulatory approval resulting in an OECD test guideline [53]. For advanced lung and liver models, further work is first needed at the first phase where the work in this thesis contributes.

As seen in this work, the sensitivity of the advanced models to toxic compounds and NMs seems to be dependent on both cell types and culturing conditions, and protocols should be harmonized across laboratories to ensure reproducible results and robust SOPs. In this harmonization process, it should also be further explored how strict the SOPs need to be in

order to ensure proper sensitivity of the models without being highly biased by operator/human handling. Additionally, further studies should investigate how complex the models have to be, as higher complexity also may cause higher costs and variations.

To replace all animal studies with NAMs in the future, it will be necessary to combine multiple sources of information and contribute to NGRA by integrated approaches to testing and assessment (IATA). Multiple advanced *in vitro* models may be needed. Each model would need its own set of criteria optimized for a specific endpoint. Traditional submerged monolayer cultures may be beneficial for cytotoxicity screening approaches to identify environmental contaminants and NMs to apply for further investigations by use of advanced models.

7. Concluding remarks

This thesis presents advanced *in vitro* models of the lung and liver, with characterization of the models, application in cyto- and genotoxicity studies with NMs, and comparisons between the models and to traditional culture models.

The following were the main conclusions regarding lung model:

- The model characterization showed that cell growth and permeability were dependent on both cell types (alveolar or bronchial) and culture models (mono- or coculture).
- Lung cells at the ALI were compatible with cyto- and genotoxicity testing after NM exposure, and mono-, co- and tricultures were successfully applied for the comet and micronucleus assays.
- The cyto- and genotoxicity responses induced by Ag NMs were dependent on both cell types (alveolar or bronchial) and culture model (mono-, co-, triculture, submerged).
- The reproducibility of the toxicity responses in ALI cultures was tested in different laboratories and gave some differences in the sensitivity, showing the importance of use of harmonized protocols.

The following were the main conclusions regarding liver model:

- The liver model was established in two laboratories, with reproducible results on size development.
- HepG2 spheroids were compatible with genotoxicity testing of chemicals and NMs and were successfully applied for the comet assay for the first time.
- The response of HepG2 cells to a toxic insult was dependent on the culture conditions (2D or 3D culture).

General conclusions:

Human responses and toxicity mechanisms to NM or chemical exposure are complex. The advanced models may be physiologically more relevant to humans than traditional models, but have some limitations, including higher variability due to the complexness. The model for a

specific question should be carefully selected with the limitations considered in the experimental design and results interpretation. The following is suggested:

- Studies on particle exposures should be performed at the ALI for both cytotoxicity and genotoxicity studies. In this way, the cultures are more representative for the physiological conditions in the human respiratory system, and the exposure is more realistic with better control, without the influence of culture medium on the physicochemical properties of the NMs such as in traditional submerged exposures.
- Monocultures at the ALI may be most beneficial for cytotoxicity screening purposes due to their higher sensitivity to NM exposures compared to co- and triculture models. Monocultures could together with co- and tricultures be used for more detailed investigations including genotoxicity studies by the comet and micronucleus assays.
- Traditional 2D liver models can be beneficial for cytotoxicity screening as they reflected concentration-dependent responses better than advanced models. Advanced 3D models are more useful for genotoxicity studies and detailed investigations due to their higher sensitivity.

Abbreviations

2D	Two-dimensional
3D	Three-dimensional
ALI	Air-liquid interface
BSA	Bovine serum albumin
DLS	Dynamic light scattering
MN	Micronucleus
NAMs	New approach methodologies
NGRA	Next generation risk assessment
NM	Nanomaterial
NTA	Nanoparticle tracking analysis
SB	Strand break
PBS	Phosphate buffered saline
ZP	Zeta potential

List of figures and tables

Figures

Tables

Author contributions

Paper I

- Investigation: nanomaterial dispersion and size characterization, Ag analysis, cytotoxicity testing, genotoxicity testing, confocal imaging (Fig. 2), deposition and permeation experiments
- Data analysis
- Visualization
- Contributed to writing of original draft
- Revision and editing of manuscript

Paper II

- Investigation: nanomaterial dispersion, cytotoxicity testing, genotoxicity testing
- Data analysis
- Visualization
- Contributed to writing of original draft
- Revision and editing of manuscript

Paper III

- Conceptualization
- Investigation: nanomaterial dispersion and characterization, mono- and coculture experiments (model characterization, alamarBlue, comet assay, micronucleus test), submerged experiments with NM-300K (alamarBlue, comet assay), Ag permeation experiments, sample digestion before elemental analysis
- Data analysis
- Visualization
- Writing of original draft
- Revision and editing of manuscript

Paper IV

- Investigation: size analysis and cell counting over time (Fig 2A, 3), cell exposure, alamarBlue assay, comet assay, confocal imaging
- Data analysis
- Visualization
- Writing of original draft
- Revision and editing of manuscript

Paper V

- Conceptualization
- Investigation: nanomaterial dispersion, dissolution analysis, cell exposure, cytotoxicity testing, genotoxicity testing, confocal imaging
- Data analysis
- Visualization
- Writing of original draft
- Revision and editing of manuscript

References

1. World Health Organization. *Ambient (outdoor) air pollution*. https://www.who.int/en/news-room/fact-sheets/detail/ambient-(outdoor)-air-quality-and-health (accessed 2022-09-06).

2. European Commission. Commission Recommendation of 18 October 2011 on the Definition of Nanomaterial - 2011/696/EU. *Official Journal of the European Union* **2011**, 38–40.

3. Bonner, J. C. Nanotoxicology. In *Molecular and Biochemical Toxicology*; Wiley-Blackwell, 2018.

4. Janković, N. Z.; Plata, D. L. Engineered Nanomaterials in the Context of Global Element Cycles. *Environ Sci Nano* **2019**, *6* (9), 2697–2711. https://doi.org/10.1039/c9en00322c.

5. Kaegi, R.; Voegelin, A.; Ort, C.; Sinnet, B.; Thalmann, B.; Krismer, J.; Hagendorfer, H.; Elumelu, M.; Mueller, E. Fate and Transformation of Silver Nanoparticles in Urban Wastewater Systems. *Water Res* **2013**, *47* (12), 3866–3877. https://doi.org/10.1016/j.watres.2012.11.060.

6. Giese, B.; Klaessig, F.; Park, B.; Kaegi, R.; Steinfeldt, M.; Wigger, H.; von Gleich, A.; Gottschalk, F. Risks, Release and Concentrations of Engineered Nanomaterial in the Environment. *Sci Rep* **2018**, *8* (1), 1–18. https://doi.org/10.1038/s41598-018-19275-4.

7. Nel, A.; Xia, T.; Mädler, L.; Li, N. Toxic Potential of Materials at the Nanolevel. *Science (1979)* **2006**, *311* (5761), 622–627. https://doi.org/10.1126/science.1114397.

8. Allouni, Z. E.; Høl, P. J.; Cauqui, M. A.; Gjerdet, N. R.; Cimpan, M. R. Role of Physicochemical Characteristics in the Uptake of TiO 2 Nanoparticles by Fibroblasts. *Toxicology in Vitro* **2012**, *26* (3), 469–479. https://doi.org/10.1016/j.tiv.2012.01.019.

9. Rodriguez-Garraus, A.; Azqueta, A.; Vettorazzi, A.; López de Cerain, A. Genotoxicity of Silver Nanoparticles. *Nanomaterials* **2020**, *10* (2), 251. https://doi.org/10.3390/nano10020251.

10. Ferdous, Z.; Nemmar, A. Health Impact of Silver Nanoparticles: A Review of the Biodistribution and Toxicity Following Various Routes of Exposure. *Int J Mol Sci* **2020**, *21* (7), 2375. https://doi.org/10.3390/ijms21072375.

11. Weir, A.; Westerhoff, P.; Fabricius, L.; Hristovski, K.; von Goetz, N. Titanium Dioxide Nanoparticles in Food and Personal Care Products. *Environ Sci Technol* **2012**, *46* (4), 2242–2250. https://doi.org/10.1021/es204168d.

12. Vaseem, M.; Umar, A.; Hahn, Y. ZnO Nanoparticles: Growth, Properties, and Application. In *Metal Oxide Nanostructures and Their Applications*; Umar, A., Hahn, Y., Eds.; American Scientific Publishers: Valencia, CA, USA, 2010; Vol. 5, pp 1–36.

13. de Matteis, V. Exposure to Inorganic Nanoparticles: Routes of Entry, Immune Response, Biodistribution and In Vitro/In Vivo Toxicity Evaluation. *Toxics* **2017**, *5* (4), 29. https://doi.org/10.3390/toxics5040029.

14. Rostami, A. A. Computational Modeling of Aerosol Deposition in Respiratory Tract: A Review. *Inhalation Toxicology*. Taylor & Francis February 2009, pp 262–290. https://doi.org/10.1080/08958370802448987.

15. Bonner, J. C. Molecular Mechanisms of Respiratory Toxicity. In *Molecular and Biochemical Toxicology*; Smart, R. C., Hodgson, E., Eds.; Wiley, 2018.

16. Weibel, E. R.; Gomez, D. M. *Architecture of the Human Lung*; 1962; Vol. 137.

17. Oberdörster, G.; Oberdörster, E.; Oberdörster, J. Nanotoxicology: An Emerging Discipline Evolving from Studies of Ultrafine Particles. *Environ Health Perspect* **2005**, *113* (7), 823–839. https://doi.org/10.1289/ehp.7339.

18. Binns, C. *Introduction to Nanoscience and Nanotechnology*; John Wiley and Sons: Hoboken, NJ, USA, 2010. https://doi.org/10.1002/9780470618837.

19. Paur, H. R.; Cassee, F. R.; Teeguarden, J.; Fissan, H.; Diabate, S.; Aufderheide, M.; Kreyling, W. G.; Hänninen, O.; Kasper, G.; Riediker, M.; Rothen-Rutishauser, B.; Schmid, O. In-Vitro Cell Exposure

Studies for the Assessment of Nanoparticle Toxicity in the Lung-A Dialog between Aerosol Science and Biology. *J Aerosol Sci* **2011**, *42* (10), 668–692. https://doi.org/10.1016/j.jaerosci.2011.06.005.

20. Tsuda, A.; Gehr, P. *Nanoparticles in the Lung : Environmental Exposure and Drug Delivery*, 1st ed.; CRC Press, 2015.

21. Braakhuis, H. M.; Park, M. V. D. Z.; Gosens, I.; de Jong, W. H.; Cassee, F. R. Physicochemical Characteristics of Nanomaterials That Affect Pulmonary Inflammation. *Particle and Fibre Toxicology 2014 11:1* **2014**, *11* (1), 1–25. https://doi.org/10.1186/1743-8977-11-18.

22. Miller, M. R.; Raftis, J. B.; Langrish, J. P.; McLean, S. G.; Samutrtai, P.; Connell, S. P.; Wilson, S.; Vesey, A. T.; Fokkens, P. H. B.; Boere, A. J. F.; Krystek, P.; Campbell, C. J.; Hadoke, P. W. F.; Donaldson, K.; Cassee, F. R.; Newby, D. E.; Duffin, R.; Mills, N. L. Inhaled Nanoparticles Accumulate at Sites of Vascular Disease. *ACS Nano* **2017**, *11* (5), 4542–4552. https://doi.org/10.1021/acsnano.6b08551.

23. Miller, M. R.; Raftis, J. B.; Langrish, J. P.; McLean, S. G.; Samutrtai, P.; Connell, S. P.; Wilson, S.; Vesey, A. T.; Fokkens, P. H. B.; Boere, A. J. F.; Krystek, P.; Campbell, C. J.; Hadoke, P. W. F.; Donaldson, K.; Cassee, F. R.; Newby, D. E.; Duffin, R.; Mills, N. L. Correction to: Inhaled Nanoparticles Accumulate at Sites of Vascular Disease (ACS Nano (2017) 11:5 (4542-4552) DOI: 10.1021/Acsnano.6b08551). *ACS Nano*. American Chemical Society October 24, 2017, pp 10623–10624. https://doi.org/10.1021/acsnano.7b06327.

24. Raftis, J. B.; Miller, M. R. Nanoparticle Translocation and Multi-Organ Toxicity: A Particularly Small Problem. *Nano Today* **2019**, *26*, 8–12. https://doi.org/10.1016/j.nantod.2019.03.010.

25. Klaassen, C. D.; Watkins III, J. B. *Casarett & Doull's Essentials of Toxicology*, 2nd ed.; McGraw-Hill Education, 2010.

26. Johnston, H. J.; Hutchison, G.; Christensen, F. M.; Peters, S.; Hankin, S.; Stone, V. A Review of the in Vivo and in Vitro Toxicity of Silver and Gold Particulates: Particle Attributes and Biological Mechanisms Responsible for the Observed Toxicity. *Critical Reviews in Toxicology*. Taylor & Francis April 2010, pp 328–346. https://doi.org/10.3109/10408440903453074.

27. Sharma, V.; Singh, P.; Pandey, A. K.; Dhawan, A. Induction of Oxidative Stress, DNA Damage and Apoptosis in Mouse Liver after Sub-Acute Oral Exposure to Zinc Oxide Nanoparticles. *Mutat Res Genet Toxicol Environ Mutagen* **2012**, *745* (1–2), 84–91. https://doi.org/10.1016/j.mrgentox.2011.12.009.

28. Llwellyn, S. v.; Niemeijer, M.; Nymark, P.; Moné, M. J.; van de Water, B.; Conway, G. E.; Jenkins, G. J. S.; Doak, S. H. In Vitro Three-Dimensional Liver Models for Nanomaterial DNA Damage Assessment. *Small* **2021**, *17*, 2006055. https://doi.org/10.1002/smll.202006055.

29. Godoy, P.; Hewitt, N. J.; Albrecht, U.; Andersen, M. E.; Ansari, N.; Bhattacharya, S.; Bode, J. G.; Bolleyn, J.; Borner, C.; Böttger, J.; Braeuning, A.; Budinsky, R. A.; Burkhardt, B.; Cameron, N. R.; Camussi, G.; Cho, C. S.; Choi, Y. J.; Craig Rowlands, J.; Dahmen, U.; Damm, G.; Dirsch, O.; Donato, M. T.; Dong, J.; Dooley, S.; Drasdo, D.; Eakins, R.; Ferreira, K. S.; Fonsato, V.; Fraczek, J.; Gebhardt, R.; Gibson, A.; Glanemann, M.; Goldring, C. E. P.; Gómez-Lechón, M. J.; Groothuis, G. M. M.; Gustavsson, L.; Guyot, C.; Hallifax, D.; Hammad, S.; Hayward, A.; Häussinger, D.; Hellerbrand, C.; Hewitt, P.; Hoehme, S.; Holzhütter, H. G.; Houston, J. B.; Hrach, J.; Ito, K.; Jaeschke, H.; Keitel, V.; Kelm, J. M.; Kevin Park, B.; Kordes, C.; Kullak-Ublick, G. A.; Lecluyse, E. L.; Lu, P.; Luebke-Wheeler, J.; Lutz, A.; Maltman, D. J.; Matz-Soja, M.; McMullen, P.; Merfort, I.; Messner, S.; Meyer, C.; Mwinyi, J.; Naisbitt, D. J.; Nussler, A. K.; Olinga, P.; Pampaloni, F.; Pi, J.; Pluta, L.; Przyborski, S. A.; Ramachandran, A.; Rogiers, V.; Rowe, C.; Schelcher, C.; Schmich, K.; Schwarz, M.; Singh, B.; Stelzer, E. H. K.; Stieger, B.; Stöber, R.; Sugiyama, Y.; Tetta, C.; Thasler, W. E.; Vanhaecke, T.; Vinken, M.; Weiss, T. S.; Widera, A.; Woods, C. G.; Xu, J. J.; Yarborough, K. M.; Hengstler, J. G. Recent Advances in 2D and 3D in Vitro Systems Using Primary Hepatocytes, Alternative Hepatocyte Sources and Non-Parenchymal Liver Cells and Their Use in Investigating Mechanisms of Hepatotoxicity, Cell Signaling and ADME. *Archives of Toxicology*. Springer August 23, 2013, pp 1315–1530. https://doi.org/10.1007/s00204-013-1078-5.

30. Zhang, Y. N.; Poon, W.; Tavares, A. J.; McGilvray, I. D.; Chan, W. C. W. Nanoparticle–Liver Interactions: Cellular Uptake and Hepatobiliary Elimination. *Journal of Controlled Release* **2016**, *240*, 332–348. https://doi.org/10.1016/j.jconrel.2016.01.020.

31. Müller, L.; Gasser, M.; Raemy, D. O.; Herzog, F.; Brandenberger, C.; Schmid, O.; Gehr, P.; Rothen-Rutishauser, B.; Clift, M. J. D. Realistic Exposure Methods for Investigating the Interaction of Nanoparticles with the Lung at the Air-Liquid Interface In Vitro. *Insciences Journal* **2011**, 30–64. https://doi.org/10.5640/insc.010130.

32. Colognato, R.; Park, M. V. D. Z.; Wick, P.; de Jong, W. H. Interaction with the Human Body. In *Adverse effects of engineered nanomaterials : exposure, toxicology, and impact on human health*; Fadeel, B., Pietroiusti, A., Shvedova, A. A., Eds.; Academic Press, 2012.

33. Doak, S. H.; Dusinska, M. NanoGenotoxicology: Present and the Future. *Mutagenesis* **2017**, *32* (1), 1–4. https://doi.org/10.1093/mutage/gew066.

34. Dusinska, M.; Tran, L. NanoTEST in a Nutshell. *Nanotoxicology*. Informa Healthcare May 1, 2015, pp 1–4. https://doi.org/10.3109/17435390.2014.991774.

35. Kohl, Y.; Rundén-Pran, E.; Mariussen, E.; Hesler, M.; el Yamani, N.; Longhin, E. M.; Dusinska, M. Genotoxicity of Nanomaterials: Advanced In Vitro Models and High Throughput Methods for Human Hazard Assessment—A Review. *Nanomaterials* **2020**, *10* (10), 1911. https://doi.org/10.3390/nano10101911.

36. Dusinska, M.; Tulinska, J.; el Yamani, N.; Kuricova, M.; Liskova, A.; Rollerova, E.; Rundén-Pran, E.; Smolkova, B. Immunotoxicity, Genotoxicity and Epigenetic Toxicity of Nanomaterials: New Strategies for Toxicity Testing? *Food and Chemical Toxicology* **2017**, *109*, 797–811. https://doi.org/10.1016/j.fct.2017.08.030.

37. Novotna, B.; Pelclova, D.; Rossnerova, A.; Zdimal, V.; Ondracek, J.; Lischkova, L.; Vlckova, S.; Fenclova, Z.; Klusackova, P.; Zavodna, T.; Topinka, J.; Komarc, M.; Dvorackova, S.; Rossner, P. The Genotoxic Effects in the Leukocytes of Workers Handling Nanocomposite Materials. *Mutagenesis* **2020**, *35* (4), 331–340. https://doi.org/10.1093/MUTAGE/GEAA016.

38. MacKenzie, E. L.; Tsuji, Y. Reactive Metabolites, Reactive Oxygen Species (ROS) and Toxicity. In *Molecular and biochemical toxicology*; Smart, R. C., Hodgson, E., Eds.; Wiley-Blackwell, 2018.

39. Stone, V.; Johnston, H.; Schins, R. P. F. Development of in Vitro Systems for Nanotoxicology: Methodological Considerations in Vitro Methods for Nanotoxicology. *Critical Reviews in Toxicology*. Taylor & Francis 2009, pp 613–626. https://doi.org/10.1080/10408440903120975.

40. Magdolenova, Z.; Collins, A.; Kumar, A.; Dhawan, A.; Stone, V.; Dusinska, M. Mechanisms of Genotoxicity. A Review of in Vitro and in Vivo Studies with Engineered Nanoparticles. *Nanotoxicology*. Taylor & Francis May 2014, pp 233–278. https://doi.org/10.3109/17435390.2013.773464.

41. Albanese, A.; Tang, P. S.; Chan, W. C. W. The Effect of Nanoparticle Size, Shape, and Surface Chemistry on Biological Systems. *Annu Rev Biomed Eng* **2012**, *14* (1), 1–16. https://doi.org/10.1146/annurev-bioeng-071811-150124.

42. Gábelová, A.; el Yamani, N.; Alonso, T. I.; Buliaková, B.; Srančíková, A.; Bábelová, A.; Pran, E. R.; Fjellsbø, L. M.; Elje, E.; Yazdani, M.; Silva, M. J.; Dušinská, M. Fibrous Shape Underlies the Mutagenic and Carcinogenic Potential of Nanosilver While Surface Chemistry Affects the Biosafety of Iron Oxide Nanoparticles. *Mutagenesis* **2017**, *32* (1), 193–202. https://doi.org/10.1093/mutage/gew045.

43. Huk, A.; Izak-Nau, E.; el Yamani, N.; Uggerud, H.; Vadset, M.; Zasonska, B.; Duschl, A.; Dusinska, M. Impact of Nanosilver on Various DNA Lesions and HPRT Gene Mutations - Effects of Charge and Surface Coating. *Part Fibre Toxicol* **2015**, *12* (1), 25. https://doi.org/10.1186/s12989-015-0100-x.

44. Lacroix, G.; Koch, W.; Ritter, D.; Gutleb, A. C.; Larsen, S. T.; Loret, T.; Zanetti, F.; Constant, S.; Chortarea, S.; Rothen-Rutishauser, B.; Hiemstra, P. S.; Frejafon, E.; Hubert, P.; Gribaldo, L.; Kearns, P.; Aublant, J. M.; Diabaté, S.; Weiss, C.; de Groot, A.; Kooter, I. Air-Liquid Interface in Vitro Models for Respiratory Toxicology Research: Consensus Workshop and Recommendations. *Appl In Vitro Toxicol* **2018**, *4* (2), 91–106. https://doi.org/10.1089/aivt.2017.0034.

45. Yaqub, N.; Wayne, G.; Birchall, M.; Song, W. Recent Advances in Human Respiratory Epithelium Models for Drug Discovery. *Biotechnology Advances*. Elsevier Inc. January 1, 2022, p 107832. https://doi.org/10.1016/j.biotechadv.2021.107832.

46. Bale, S. S.; Vernetti, L.; Senutovitch, N.; Jindal, R.; Hegde, M.; Gough, A.; McCarty, W. J.; Bakan, A.; Bhushan, A.; Shun, T. Y.; Golberg, I.; DeBiasio, R.; Usta, O. B.; Taylor, D. L.; Yarmush, M. L. In Vitro Platforms for Evaluating Liver Toxicity. *Exp Biol Med* **2014**, *239* (9), 1180–1191. https://doi.org/10.1177/1535370214531872.

47. Evans, S. J.; Clift, M. J. D.; Singh, N.; de Oliveira Mallia, J.; Burgum, M.; Wills, J. W.; Wilkinson, T. S.; Jenkins, G. J. S.; Doak, S. H. Critical Review of the Current and Future Challenges Associated with Advanced *in Vitro* Systems towards the Study of Nanoparticle (Secondary) Genotoxicity. *Mutagenesis* **2017**, *32* (1), 233–241. https://doi.org/10.1093/mutage/gew054.

48. Kyffin, J. A.; Sharma, P.; Leedale, J.; Colley, H. E.; Murdoch, C.; Mistry, P.; Webb, S. D. Impact of Cell Types and Culture Methods on the Functionality of in Vitro Liver Systems – A Review of Cell Systems for Hepatotoxicity Assessment. *Toxicology in Vitro*. Elsevier Ltd April 1, 2018, pp 262–275. https://doi.org/10.1016/j.tiv.2018.01.023.

49. Upadhyay, S.; Palmberg, L. Air-Liquid Interface: Relevant In Vitro Models for Investigating Air Pollutant-Induced Pulmonary Toxicity. *Toxicological Sciences* **2018**, *164* (1), 21–30. https://doi.org/10.1093/toxsci/kfy053.

50. Pfuhler, S.; van Benthem, J.; Curren, R.; Doak, S. H.; Dusinska, M.; Hayashi, M.; Heflich, R. H.; Kidd, D.; Kirkland, D.; Luan, Y.; Ouedraogo, G.; Reisinger, K.; Sofuni, T.; van Acker, F.; Yang, Y.; Corvi, R. Use of in Vitro 3D Tissue Models in Genotoxicity Testing: Strategic Fit, Validation Status and Way Forward. Report of the Working Group from the 7th International Workshop on Genotoxicity Testing (IWGT). *Mutat Res Genet Toxicol Environ Mutagen* **2020**, *850–851*, 503135. https://doi.org/10.1016/j.mrgentox.2020.503135.

51. Breslin, S.; O'Driscoll, L. Three-Dimensional Cell Culture: The Missing Link in Drug Discovery. *Drug Discovery Today*. Elsevier Current Trends March 1, 2013, pp 240–249. https://doi.org/10.1016/j.drudis.2012.10.003.

52. Astashkina, A.; Grainger, D. W. Critical Analysis of 3-D Organoid in Vitro Cell Culture Models for High-Throughput Drug Candidate Toxicity Assessments. *Advanced Drug Delivery Reviews*. Elsevier April 20, 2014, pp 1–18. https://doi.org/10.1016/j.addr.2014.02.008.

53. Bas, A.; Burns, N.; Gulotta, A.; Junker, J.; Drasler, B.; Lehner, R.; Aicher, L.; Constant, S.; Petri-Fink, A.; Rothen-Rutishauser, B. Understanding the Development, Standardization, and Validation Process of Alternative In Vitro Test Methods for Regulatory Approval from a Researcher Perspective. *Small* **2021**, *17* (15), 2006027. https://doi.org/10.1002/smll.202006027.

54. Voisin, C.; Aerts, C.; Jakubczak, E.; Tonnel, A. B. LA CULTURE CELLULAIRE EN PHASE GAZEUSE. UN NOUVEAU MODELE EXPERIMENTAL D'ETUDE IN VITRO DES ACTIVITE DES MACROPHAGES ALVEOLAIRES. *Clinical Respiratory Physiology* **1977**, *13* (1), 69–82.

55. Rothen-Rutishauser, B.; Blank, F.; Mühlfeld, C.; Gehr, P. In Vitro Models of the Human Epithelial Airway Barrier to Study the Toxic Potential of Particulate Matter. *http://dx.doi.org.ezproxy.uio.no/10.1517/17425255.4.8.1075* **2008**, *4* (8), 1075–1089. https://doi.org/10.1517/17425255.4.8.1075.

56. Braakhuis, H. M.; He, R.; Vandebriel, R. J.; Gremmer, E. R.; Zwart, E.; Vermeulen, J. P.; Fokkens, P.; Boere, J.; Gosens, I.; Cassee, F. R. An Air-Liquid Interface Bronchial Epithelial Model for Realistic, Repeated Inhalation Exposure to Airborne Particles for Toxicity Testing. *JoVE (Journal of Visualized Experiments)* **2020**, *2020* (159), e61210. https://doi.org/10.3791/61210.

57. Herzog, F.; Clift, M. J. D.; Piccapietra, F.; Behra, R.; Schmid, O.; Petri-Fink, A.; Rothen-Rutishauser, B. Exposure of Silver-Nanoparticles and Silver-Ions to Lung Cells in Vitro at the Air-Liquid Interface. *Part Fibre Toxicol* **2013**, *10* (1), 1–14. https://doi.org/10.1186/1743-8977-10-11/FIGURES/6.

58. He, R. W.; Braakhuis, H. M.; Vandebriel, R. J.; Staal, Y. C. M.; Gremmer, E. R.; Fokkens, P. H. B.; Kemp, C.; Vermeulen, J.; Westerink, R. H. S.; Cassee, F. R. Optimization of an Air-Liquid Interface in Vitro Cell Co-Culture Model to Estimate the Hazard of Aerosol Exposures. *J Aerosol Sci* **2021**, *153*. https://doi.org/10.1016/J.JAEROSCI.2020.105703.

59. Fizeşan, I.; Cambier, S.; Moschini, E.; Chary, A.; Nelissen, I.; Ziebel, J.; Audinot, J. N.; Wirtz, T.; Kruszewski, M.; Pop, A.; Kiss, B.; Serchi, T.; Loghin, F.; Gutleb, A. C. In Vitro Exposure of a 3D-

Tetraculture Representative for the Alveolar Barrier at the Air-Liquid Interface to Silver Particles and Nanowires. *Part Fibre Toxicol* **2019**, *16* (1), 1–21. https://doi.org/10.1186/S12989-019-0297-1/FIGURES/13.

60. Klein, S. G.; Serchi, T.; Hoffmann, L.; Blömeke, B.; Gutleb, A. C. An Improved 3D Tetraculture System Mimicking the Cellular Organisation at the Alveolar Barrier to Study the Potential Toxic Effects of Particles on the Lung. *Part Fibre Toxicol* **2013**, *10* (1), 31. https://doi.org/10.1186/1743-8977-10-31.

61. Klein, S. G.; Cambier, S.; Hennen, J.; Legay, S.; Serchi, T.; Nelissen, I.; Chary, A.; Moschini, E.; Krein, A.; Blömeke, B.; Gutleb, A. C. Endothelial Responses of the Alveolar Barrier in Vitro in a Dose-Controlled Exposure to Diesel Exhaust Particulate Matter. *Part Fibre Toxicol* **2017**, *14* (1), 1–17. https://doi.org/10.1186/S12989-017-0186-4/TABLES/5.

62. Rothen-Rutishauser, B. M.; Kiama, S. C.; Gehr, P. A Three-Dimensional Cellular Model of the Human Respiratory Tract to Study the Interaction with Particles. *Am J Respir Cell Mol Biol* **2005**, *32* (4), 281–289. https://doi.org/10.1165/rcmb.2004-0187OC.

63. Kaur, K.; Mohammadpour, R.; Ghandehari, H.; Reilly, C. A.; Paine, R.; Kelly, K. E. Effect of Combustion Particle Morphology on Biological Responses in a Co-Culture of Human Lung and Macrophage Cells. *Atmos Environ* **2022**, *284*, 119194. https://doi.org/10.1016/J.ATMOSENV.2022.119194.

64. Poster Abstracts. *J Aerosol Med Pulm Drug Deliv* **2009**, *22* (2), 173–208. https://doi.org/10.1089/jamp.2008.00a3.

65. Westmeier, D.; Stauber, R. H.; Docter, D. The Concept of Bio-Corona in Modulating the Toxicity of Engineered Nanomaterials (ENM). *Toxicol Appl Pharmacol* **2016**, *299*, 53–57. https://doi.org/10.1016/j.taap.2015.11.008.

66. Nel, A. E.; Mädler, L.; Velegol, D.; Xia, T.; Hoek, E. M. V.; Somasundaran, P.; Klaessig, F.; Castranova, V.; Thompson, M. Understanding Biophysicochemical Interactions at the Nano–Bio Interface. *Nature Materials 2009 8:7* **2009**, *8* (7), 543–557. https://doi.org/10.1038/nmat2442.

67. Wang, G.; Zhang, X.; Liu, X.; Zheng, J.; Chen, R.; Kan, H. Ambient Fine Particulate Matter Induce Toxicity in Lung Epithelial-Endothelial Co-Culture Models. *Toxicol Lett* **2019**, *301*, 133–145. https://doi.org/10.1016/J.TOXLET.2018.11.010.

68. Blank, F.; Rothen-Rutishauser, B.; Gehr, P. Dendritic Cells and Macrophages Form a Transepithelial Network against Foreign Particulate Antigens. *https://doi.org/10.1165/rcmb.2006-0234OC* **2012**, *36* (6), 669–677. https://doi.org/10.1165/RCMB.2006-0234OC.

69. Paur, H. R.; Cassee, F. R.; Teeguarden, J.; Fissan, H.; Diabate, S.; Aufderheide, M.; Kreyling, W. G.; Hänninen, O.; Kasper, G.; Riediker, M.; Rothen-Rutishauser, B.; Schmid, O. In-Vitro Cell Exposure Studies for the Assessment of Nanoparticle Toxicity in the Lung—A Dialog between Aerosol Science and Biology. *J Aerosol Sci* **2011**, *42* (10), 668–692. https://doi.org/10.1016/J.JAEROSCI.2011.06.005.

70. Kelm, J. M.; Fussenegger, M. Microscale Tissue Engineering Using Gravity-Enforced Cell Assembly. *Trends in Biotechnology*. Elsevier Current Trends April 1, 2004, pp 195–202. https://doi.org/10.1016/j.tibtech.2004.02.002.

71. Kelm, J. M.; Timmins, N. E.; Brown, C. J.; Fussenegger, M.; Nielsen, L. K. Method for Generation of Homogeneous Multicellular Tumor Spheroids Applicable to a Wide Variety of Cell Types. *Biotechnol Bioeng* **2003**, *83* (2), 173–180. https://doi.org/10.1002/bit.10655.

72. Kelm, J. M.; Djonov, V.; Ittner, L. M.; Fluri, D.; Born, W.; Hoerstrup, S. P.; Fussenegger, M. Design of Custom-Shaped Vascularized Tissues Using Microtissue Spheroids as Minimal Building Units. *Tissue Eng* **2006**, *12* (8), 2151–2160. https://doi.org/10.1089/ten.2006.12.2151.

73. Hurrell, T.; Ellero, A. A.; Masso, Z. F.; Cromarty, A. D. Characterization and Reproducibility of HepG2 Hanging Drop Spheroids Toxicology in Vitro. *Toxicology in Vitro* **2018**, *50*, 86–94. https://doi.org/10.1016/j.tiv.2018.02.013.

74. Chang, T. T.; Hughes-Fulford, M. Monolayer and Spheroid Culture of Human Liver Hepatocellular Carcinoma Cell Line Cells Demonstrate Distinct Global Gene Expression Patterns and Functional Phenotypes. *Tissue Eng Part A* **2009**, *15* (3), 559–567. https://doi.org/10.1089/ten.tea.2007.0434.

75. Dubiak-Szepietowska, M.; Karczmarczyk, A.; Jönsson-Niedziółka, M.; Winckler, T.; Feller, K. H. Development of Complex-Shaped Liver Multicellular Spheroids as a Human-Based Model for Nanoparticle Toxicity Assessment in Vitro. *Toxicol Appl Pharmacol* **2016**, *294*, 78–85. https://doi.org/10.1016/j.taap.2016.01.016.

76. Fleddermann, J.; Susewind, J.; Peuschel, H.; Koch, M.; Tavernaro, I.; Kraegeloh, A. Distribution of SiO2 Nanoparticles in 3D Liver Microtissues. *Int J Nanomedicine* **2019**, *Volume 14*, 1411–1431. https://doi.org/10.2147/IJN.S189888.

77. Shah, U. K.; Mallia, J. de O.; Singh, N.; Chapman, K. E.; Doak, S. H.; Jenkins, G. J. S. A Three-Dimensional in Vitro HepG2 Cells Liver Spheroid Model for Genotoxicity Studies. *Mutat Res Genet Toxicol Environ Mutagen* **2018**, *825*, 51–58. https://doi.org/10.1016/j.mrgentox.2017.12.005.

78. Llewellyn, S. v.; Conway, G. E.; Zanoni, I.; Jørgensen, A. K.; Shah, U. K.; Seleci, D. A.; Keller, J. G.; Kim, J. W.; Wohlleben, W.; Jensen, K. A.; Costa, A.; Jenkins, G. J. S.; Clift, M. J. D.; Doak, S. H. Understanding the Impact of More Realistic Low-Dose, Prolonged Engineered Nanomaterial Exposure on Genotoxicity Using 3D Models of the Human Liver. *J Nanobiotechnology* **2021**, *19* (1), 193. https://doi.org/10.1186/s12951-021-00938-w.

79. Conway, G. E.; Shah, U.-K.; Llewellyn, S.; Cervena, T.; Evans, S. J.; al Ali, A. S.; Jenkins, G. J.; Clift, M. J. D.; Doak, S. H. Adaptation of the *in Vitro* Micronucleus Assay for Genotoxicity Testing Using 3D Liver Models Supporting Longer-Term Exposure Durations. *Mutagenesis* **2020**, *35* (4), 319–330. https://doi.org/10.1093/mutage/geaa018.

80. Kermanizadeh, A.; Løhr, M.; Roursgaard, M.; Messner, S.; Gunness, P.; Kelm, J. M.; Møller, P.; Stone, V.; Loft, S. Hepatic Toxicology Following Single and Multiple Exposure of Engineered Nanomaterials Utilising a Novel Primary Human 3D Liver Microtissue Model. *Part Fibre Toxicol* **2014**, *11* (1), 56. https://doi.org/10.1186/s12989-014-0056-2.

81. Kermanizadeh, A.; Gaiser, B. K.; Hutchison, G. R.; Stone, V. An in Vitro Liver Model - Assessing Oxidative Stress and Genotoxicity Following Exposure of Hepatocytes to a Panel of Engineered Nanomaterials. *Part Fibre Toxicol* **2012**, *9* (1), 28. https://doi.org/10.1186/1743-8977-9-28.

82. el Yamani, N.; Collins, A. R.; Rundén-Pran, E.; Fjellsbø, L. M.; Shaposhnikov, S.; Zielonddiny, S.; Dusinska, M. *In Vitro* Genotoxicity Testing of Four Reference Metal Nanomaterials, Titanium Dioxide, Zinc Oxide, Cerium Oxide and Silver: Towards Reliable Hazard Assessment. *Mutagenesis* **2017**, *32* (1), 117–126. https://doi.org/10.1093/mutage/gew060.

83. Jensen, K. A.; Clausen, P. A.; Birkedal, R.; Kembouche, Y.; Christiansen, E.; Jacobsen, N. R.; Levin, M.; Koponen, I.; Wallin, H.; de Temmerman, P.-J.; Mast, J.; Guiot, C.; Spalla, O.; Motzkus, C.; Shivachev, B.; Rousset, D.; Witschger, O. *Towards a Method for Detecting the Potential Genotoxicity of Nanomaterials. Deliverable 3. Final Protocol for Producing Suitable Manufactured Nanomaterial Exposure Media. The Generic NANOGENOTOX Dispersion Protocol. Standard Operating Procedure (SOP) and Background Documentation.* https://www.anses.fr/en/system/files/nanogenotox_deliverable_5.pdf (accessed 2022-06-17).

84. European Commission; Joint Research Centre; Mech, A.; Rauscher, H.; Rasmussen, K.; et al. *The NanoDefine methods manual. Part 3, Standard operating procedures (SOPs) - Publications Office of the European Union*. https://op.europa.eu/en/publication-detail/-/publication/b8bf4c68-4246-11ea-9099-01aa75ed71a1/language-en/format-PDF/source-search (accessed 2022-09-09).

85. Deloid, G. M.; Cohen, J. M.; Pyrgiotakis, G.; Demokritou, P. Preparation, Characterization, and in Vitro Dosimetry of Dispersed, Engineered Nanomaterials. *Nat Protoc* **2017**, *12* (2), 355–371. https://doi.org/10.1038/nprot.2016.172.

86. Malvern Panalytical. *An Introduction to Dynamic Light Scattering (DLS)*. https://www.malvernpanalytical.com/en/learn/knowledge-center/technical-notes/TN101104DynamicLightScatteringIntroduction (accessed 2022-06-01).

87. Malvern Panalytical. *Nanoparticle Tracking Analysis NTA*. https://www.malvernpanalytical.com/en/products/technology/light-scattering/nanoparticle-tracking-analysis (accessed 2022-06-01).

88. Nobbmann, U. *NTA or DLS? - Materials Talks*. https://www.materials-talks.com/nta-or-dls/ (accessed 2022-06-01).

89. Malvern Panalytical. *Synergy of complementary nanomaterial characterization techniques: NTA+DLS*. https://www.malvernpanalytical.com/en/learn/knowledge-center/whitepapers/WP161122NTA-DLSComplementaryNanoCharacterization.html (accessed 2022-06-01).

90. Malvern Panalytical. *Zetasizer Advance Series User Guide*. https://www.malvernpanalytical.com/en/learn/knowledge-center/user-manuals/MAN0592EN (accessed 2022-06-01).

91. Malvern Panalytical. *Zeta potential - An introduction in 30 minutes*. https://www.malvernpanalytical.com/en/learn/knowledge-center/technical-notes/TN101104ZetaPotentialIntroduction (accessed 2022-06-01).

92. Magdolenova, Z.; Drlickova, M.; Henjum, K.; Rundén-Pran, E.; Tulinska, J.; Bilanicova, D.; Pojana, G.; Kazimirova, A.; Barancokova, M.; Kuricova, M.; Liskova, A.; Staruchova, M.; Ciampor, F.; Vavra, I.; Lorenzo, Y.; Collins, A.; Rinna, A.; Fjellsbo, L.; Volkovova, K.; Marcomini, A.; Amiry-Moghaddam, M.; Dusinska, M. Coating-Dependent Induction of Cytotoxicity and Genotoxicity of Iron Oxide Nanoparticles. *http://dx.doi.org/10.3109/17435390.2013.847505* **2015**, *9* (S1), 44–56. https://doi.org/10.3109/17435390.2013.847505.

93. Cowie, H.; Magdolenova, Z.; Saunders, M.; Drlickova, M.; Correia Carreira, S.; Halamoda Kenzaoi, B.; Gombau, L.; Guadagnini, R.; Lorenzo, Y.; Walker, L.; Fjellsbo, L. M.; Huk, A.; Rinna, A.; Tran, L.; Volkovova, K.; Boland, S.; Juillerat-Jeanneret, L.; Marano, F.; Collins, A. R.; Dusinska, M. Suitability of Human and Mammalian Cells of Different Origin for the Assessment of Genotoxicity of Metal and Polymeric Engineered Nanoparticles. *http://dx.doi.org/10.3109/17435390.2014.940407* **2015**, *9* (S1), 57–65. https://doi.org/10.3109/17435390.2014.940407.

94. Guadagnini, R.; Moreau, K.; Hussain, S.; Marano, F.; Boland, S. Toxicity Evaluation of Engineered Nanoparticles for Medical Applications Using Pulmonary Epithelial Cells. *http://dx.doi.org/10.3109/17435390.2013.855830* **2015**, *9* (S1), 25–32. https://doi.org/10.3109/17435390.2013.855830.

95. Finkelstein, Y.; Aks, S. E.; Hutson, J. R.; Juurlink, D. N.; Nguyen, P.; Dubnov-Raz, G.; Pollak, U.; Koren, G.; Bentur, Y. Colchicine Poisoning: The Dark Side of an Ancient Drug. *Clinical Toxicology*. Taylor & Francis June 2010, pp 407–414. https://doi.org/10.3109/15563650.2010.495348.

96. PubChem. *Chlorpromazine hydrochloride | C17H20Cl2N2S*. https://pubchem.ncbi.nlm.nih.gov/compound/Chlorpromazine-hydrochloride (accessed 2022-09-07).

97. Buchweitz, J. P.; Ganey, P. E.; Bursian, S. J.; Roth, R. A. Underlying Endotoxemia Augments Toxic Responses to Chlorpromazine: Is There a Relationship to Drug Idiosyncrasy? *Journal of Pharmacology and Experimental Therapeutics* **2002**, *300* (2), 460–467. https://doi.org/10.1124/jpet.300.2.460.

98. Lundin, C.; North, M.; Erixon, K.; Walters, K.; Jenssen, D.; Goldman, A. S. H.; Helleday, T. Methyl Methanesulfonate (MMS) Produces Heat-Labile DNA Damage but No Detectable in Vivo DNA Double-Strand Breaks. *Nucleic Acids Res* **2005**, *33* (12), 3799–3811. https://doi.org/10.1093/nar/gki681.

99. Beranek, D. T. Distribution of Methyl and Ethyl Adducts Following Alkylation with Monofunctional Alkylating Agents. *Mutation Research - Fundamental and Molecular Mechanisms of Mutagenesis* **1990**, *231* (1), 11–30. https://doi.org/10.1016/0027-5107(90)90173-2.

100. Lee, M. Y.; Kim, M. A.; Kim, H. J.; Bae, Y. S.; Park, J. I.; Kwak, J. Y.; Chung, J. H.; Yun, J. Alkylating Agent Methyl Methanesulfonate (MMS) Induces a Wave of Global Protein Hyperacetylation: Implications in Cancer Cell Death. *Biochem Biophys Res Commun* **2007**, *360* (2), 483–489. https://doi.org/10.1016/j.bbrc.2007.06.084.

101. Wyatt, M. D.; Pittman, D. L. Methylating Agents and DNA Repair Responses: Methylated Bases and Sources of Strand Breaks. *Chemical Research in Toxicology*. American Chemical Society December 2006, pp 1580–1594. https://doi.org/10.1021/tx060164e.

102. Rhaese, H. J.; Freese, E. Chemical Analysis of DNA Alterations. I. Base Liberation and Backbone Breakage of DNA and Oligodeoxyadenylic Acid Induced by Hydrogen Peroxide and Hydroxylamine.

BBA Section Nucleic Acids And Protein Synthesis **1968**, *155* (2), 476–490. https://doi.org/10.1016/0005-2787(68)90193-7.

103. Halliwell, B.; Aruoma, O. I. DNA Damage by Oxygen-Derived Species Its Mechanism and Measurement in Mammalian Systems. *FEBS Lett* **1991**, *281* (1–2), 9–19. https://doi.org/10.1016/0014-5793(91)80347-6.

104. Hudecová, A.; Hašplová, K.; Miadoková, E.; Magdolenová, Z.; Rinna, A.; Collins, A. R.; Gálová, E.; Vaculčíková, D.; Gregáň, F.; Dušinská, M. *Gentiana Asclepiadea* Protects Human Cells against Oxidation DNA Lesions. *Cell Biochem Funct* **2012**, *30* (2), 101–107. https://doi.org/10.1002/cbf.1822.

105. Brüsehafer, K.; Rees, B. J.; Manshian, B. B.; Doherty, A. T.; O'Donovan, M. R.; Doak, S. H.; Jenkins, G. J. S. Chromosome Breakage Induced by the Genotoxic Agents Mitomycin C and Cytosine Arabinoside Is Concentration and P53 Dependent. *Toxicological Sciences* **2014**, *140* (1), 94–102. https://doi.org/10.1093/toxsci/kfu058.

106. ATCC. *A549*. https://www.atcc.org/products/ccl-185 (accessed 2022-06-01).

107. Lieber, M.; Todaro, G.; Smith, B.; Szakal, A.; Nelson-Rees, W. A Continuous Tumor-Cell Line from a Human Lung Carcinoma with Properties of Type II Alveolar Epithelial Cells. *Int J Cancer* **1976**, *17* (1), 62–70. https://doi.org/10.1002/ijc.2910170110.

108. ATCC. *BEAS-2B*. https://www.atcc.org/products/crl-9609 (accessed 2022-06-01).

109. ATCC. *EA.hy926*. https://www.atcc.org/products/crl-2922 (accessed 2022-06-01).

110. Suggs, J. E.; Madden, M. C.; Friedman, M.; Edgell, C. J. S. Prostacyclin Expression by a Continuous Human Cell Line Derived from Vascular Endothelium. *Blood* **1986**, *68* (4), 825–829. https://doi.org/10.1182/blood.v68.4.825.825.

111. ATCC. *THP-1*. https://www.atcc.org/products/tib-202 (accessed 2022-06-01).

112. Tsuchiya, S.; Yamabe, M.; Yamaguchi, Y.; Kobayashi, Y.; Konno, T.; Tada, K. Establishment and Characterization of a Human Acute Monocytic Leukemia Cell Line (THP-1). *Int J Cancer* **1980**, *26* (2), 171–176. https://doi.org/10.1002/ijc.2910260208.

113. ATCC. *HepG2*. https://www.atcc.org/products/hb-8065 (accessed 2022-06-01).

114. Dusinska, M.; Mariussen, E.; Rundén-Pran, E.; Hudecova, A. M.; Elje, E.; Kazimirova, A.; el Yamani, N.; Dommershausen, N.; Tharmann, J.; Fieblinger, D.; Herzberg, F.; Luch, A.; Haase, A. In Vitro Approaches for Assessing the Genotoxicity of Nanomaterials. In *Methods in Molecular Biology*; Humana Press Inc., 2019; Vol. 1894, pp 83–122. https://doi.org/10.1007/978-1-4939-8916-4_6.

115. Ansar Ahmed, S.; Gogal, R. M.; Walsh, J. E. A New Rapid and Simple Non-Radioactive Assay to Monitor and Determine the Proliferation of Lymphocytes: An Alternative to [3H]Thymidine Incorporation Assay. *J Immunol Methods* **1994**, *170* (2), 211–224. https://doi.org/10.1016/0022-1759(94)90396-4.

116. Longhin, E. M.; el Yamani, N.; Rundén-Pran, E.; Dusinska, M. The Alamar Blue Assay in the Context of Safety Testing of Nanomaterials. *Frontiers in Toxicology* **1AD**, *0*, 113. https://doi.org/10.3389/FTOX.2022.981701.

117. Kumar, P.; Nagarajan, A.; Uchil, P. D. Analysis of Cell Viability by the Lactate Dehydrogenase Assay. *Cold Spring Harb Protoc* **2018**, *2018* (6), 465–468. https://doi.org/10.1101/pdb.prot095497.

118. invitrogen; ThermoFisher Scientific. *CyQUANT™ LDH Cytotoxicity Assay MAN0018500*; 2019. https://www.thermofisher.com/document-connect/document-connect.html?url=https://assets.thermofisher.com/TFS-Assets%2FLSG%2Fmanuals%2FMAN0018500_CyQUANT-LDH-Cytotoxicity-Assay-Kit_PI.pdf (accessed 2022-06-02).

119. ThermoFisher Scientific. *Fluorescein Diacetate (FDA)*. https://www.thermofisher.com/order/catalog/product/F1303 (accessed 2022-06-02).

120. invitrogen; ThermoFisher Scientific. *Propidium Iodide Nucleic Acid Stain*; 2006. https://www.thermofisher.com/document-connect/document-

connect.html?url=https://assets.thermofisher.com/TFS-Assets%2FLSG%2Fmanuals%2Fmp01304.pdf (accessed 2022-06-02).

121. Azqueta, A.; Stopper, H.; Zegura, B.; Dusinska, M.; Møller, P. Do Cytotoxicity and Cell Death Cause False Positive Results in the in Vitro Comet Assay? *Mutation Research/Genetic Toxicology and Environmental Mutagenesis* **2022**, *881*, 503520. https://doi.org/10.1016/J.MRGENTOX.2022.503520.

122. el Yamani, N.; Rundén-Pran, E.; Collins, A. R.; Longhin, E. M.; Elje, E.; Hoet, P.; Vinković Vrček, I.; Doak, S. H.; Fessard, V.; Dusinska, M. The Miniaturized Enzyme-Modified Comet Assay for Genotoxicity Testing of Nanomaterials. *Frontiers in Toxicology* **2022**, *0*, 125. https://doi.org/10.3389/FTOX.2022.986318.

123. Gottardo, S.; Crutzen, H.; Jantunen, P. NANoREG Framework for the Safety Assessment of Nanomaterials - EUR 28550 EN. European Union March 2017. https://doi.org/10.2760/245972.

124. Collins, A. R. The Use of Bacterial Repair Endonucleases in the Comet Assay. In *Methods in Molecular Biology*; Humana Press Inc., 2017; Vol. 1641, pp 173–184. https://doi.org/10.1007/978-1-4939-7172-5_9.

125. Dušinská, M.; Collins, A. Detection of Oxidised Purines and UV-Induced Photoproducts in DNA of Single Cells, by Inclusion of Lesion-Specific Enzymes in the Comet Assay. *Alternatives to Laboratory Animals* **1996**, *24* (3), 405–411. https://doi.org/10.1177/026119299602400315.

126. Dusinska, M.; Collins, A. R. The Comet Assay in Human Biomonitoring: Gene-Environment Interactions. *Mutagenesis*. Oxford Academic May 1, 2008, pp 191–205. https://doi.org/10.1093/mutage/gen007.

127. Collins, A. R.; Annangi, B.; Rubio, L.; Marcos, R.; Dorn, M.; Merker, C.; Estrela-Lopis, I.; Cimpan, M. R.; Ibrahim, M.; Cimpan, E.; Ostermann, M.; Sauter, A.; el Yamani, N.; Shaposhnikov, S.; Chevillard, S.; Paget, V.; Grall, R.; Delic, J.; de-Cerio, F. G.; Suarez-Merino, B.; Fessard, V.; Hogeveen, K. N.; Fjellsbø, L. M.; Pran, E. R.; Brzicova, T.; Topinka, J.; Silva, M. J.; Leite, P. E.; Ribeiro, A. R.; Granjeiro, J. M.; Grafström, R.; Prina-Mello, A.; Dusinska, M. High Throughput Toxicity Screening and Intracellular Detection of Nanomaterials. *WIREs Nanomedicine and Nanobiotechnology* **2017**, *9* (1), e1413. https://doi.org/10.1002/wnan.1413.

128. Boiteux, S.; O'Connor, T. R.; Lederer, F.; Gouyette, A.; Laval, J. Homogeneous Escherichia Coli FPG Protein. A DNA Glycosylase Which Excises Imidazole Ring-Opened Purines and Nicks DNA at Apurinic/Apyrimidinic Sites. *Journal of Biological Chemistry* **1990**, *265* (7), 3916–3922. https://doi.org/10.1016/s0021-9258(19)39680-2.

129. Boiteux, S.; Laval, J.; Gajewski, E.; Dizdaroglu, M. Substrate Specificity of the Escherichia Coli Fpg Protein Formamidopyrimidine-DNA Glycosylase: Excision of Purine Lesions in DNA Produced by Ionizing Radiation or Photosensitization. *Biochemistry* **1992**, *31* (1), 106–110. https://doi.org/10.1021/bi00116a016.

130. Speit, G.; Schütz, P.; Bonzheim, I.; Trenz, K.; Hoffmann, H. Sensitivity of the FPG Protein towards Alkylation Damage in the Comet Assay. *Toxicol Lett* **2004**, *146* (2), 151–158. https://doi.org/10.1016/j.toxlet.2003.09.010.

131. Kang, S. H.; Kwon, J. Y.; Lee, J. K.; Seo, Y. R. Recent Advances in In Vivo Genotoxicity Testing: Prediction of Carcinogenic Potential Using Comet and Micronucleus Assay in Animal Models. *J Cancer Prev* **2013**, *18* (4), 277–288. https://doi.org/10.15430/jcp.2013.18.4.277.

132. Hong, Y. hee; Jeon, H. L.; Ko, K. Y.; Kim, J.; Yi, J. S.; Ahn, I.; Kim, T. S.; Lee, J. K. Assessment of the Predictive Capacity of the Optimized in Vitro Comet Assay Using HepG2 Cells. *Mutat Res Genet Toxicol Environ Mutagen* **2018**, *827*, 59–67. https://doi.org/10.1016/j.mrgentox.2018.01.010.

133. Štampar, M.; Tomc, J.; Filipič, M.; Žegura, B. Development of in Vitro 3D Cell Model from Hepatocellular Carcinoma (HepG2) Cell Line and Its Application for Genotoxicity Testing. *Arch Toxicol* **2019**, *93* (11), 3321–3333. https://doi.org/10.1007/S00204-019-02576-6/FIGURES/6.

134. Wang, Z. DNA Damage and Mutagenesis. In *Molecular and Biochemical Toxicology*; Smart, R. C., Hodgson, E., Eds.; Wiley, 2017.

135. Llewellyn, S. v.; Conway, G. E.; Shah, U. K.; Evans, S. J.; Jenkins, G. J. S.; Clift, M. J. D.; Doak, S. H. Advanced 3D Liver Models for In Vitro Genotoxicity Testing Following Long-Term Nanomaterial Exposure. *JoVE (Journal of Visualized Experiments)* **2020**, *2020* (160), e61141. https://doi.org/10.3791/61141.

136. Binder, S.; Cao, X.; Bauer, S.; Rastak, N.; Kuhn, E.; Dragan, G. C.; Monsé, C.; Ferron, G.; Breuer, D.; Oeder, S.; Karg, E.; Sklorz, M.; di Bucchianico, S.; Zimmermann, R. In Vitro Genotoxicity of Dibutyl Phthalate on A549 Lung Cells at Air–Liquid Interface in Exposure Concentrations Relevant at Workplaces. *Environ Mol Mutagen* **2021**, *62* (9), 490–501. https://doi.org/10.1002/EM.22464.

137. Platel, A.; Privat, K.; Talahari, S.; Delobel, A.; Dourdin, G.; Gateau, E.; Simar, S.; Saleh, Y.; Sotty, J.; Antherieu, S.; Canivet, L.; Alleman, L. Y.; Perdrix, E.; Garçon, G.; Denayer, F. O.; lo Guidice, J. M.; Nesslany, F. Study of in Vitro and in Vivo Genotoxic Effects of Air Pollution Fine (PM2.5-0.18) and Quasi-Ultrafine (PM0.18) Particles on Lung Models. *Science of The Total Environment* **2020**, *711*, 134666. https://doi.org/10.1016/J.SCITOTENV.2019.134666.

138. Koehler, C.; Ginzkey, C.; Friehs, G.; Hackenberg, S.; Froelich, K.; Scherzed, A.; Burghartz, M.; Kessler, M.; Kleinsasser, N. Aspects of Nitrogen Dioxide Toxicity in Environmental Urban Concentrations in Human Nasal Epithelium. *Toxicol Appl Pharmacol* **2010**, *245* (2), 219–225. https://doi.org/10.1016/J.TAAP.2010.03.003.

139. Koehler, C.; Ginzkey, C.; Friehs, G.; Hackenberg, S.; Froelich, K.; Scherzed, A.; Burghartz, M.; Kessler, M.; Kleinsasser, N. Ex Vivo Toxicity of Nitrogen Dioxide in Human Nasal Epithelium at the WHO Defined 1-h Limit Value. *Toxicol Lett* **2011**, *207* (1), 89–95. https://doi.org/10.1016/J.TOXLET.2011.08.004.

140. Koehler, C.; Thielen, S.; Ginzkey, C.; Hackenberg, S.; Scherzed, A.; Burghartz, M.; Paulus, M.; Hagen, R.; Kleinsasser, N. H. Nitrogen Dioxide Is Genotoxic in Urban Concentrations. *http://dx.doi.org/10.3109/08958378.2013.788104* **2013**, *25* (6), 341–347. https://doi.org/10.3109/08958378.2013.788104.

141. Wiest, F.; Scherzad, A.; Ickrath, P.; Poier, N.; Hackenberg, S.; Kleinsasser, N. Studies on Toxicity and Inflammatory Reactions Induced by E-Cigarettes: In Vitro Exposure of Human Nasal Mucosa Cells to Propylene Glycol at the Air–Liquid Interface. *HNO* **2021**, *69* (12), 952–960. https://doi.org/10.1007/S00106-021-00998-2/FIGURES/3.

142. García-Rodríguez, A.; Kazantseva, L.; Vila, L.; Rubio, L.; Velázquez, A.; Ramírez, M. J.; Marcos, R.; Hernández, A. Micronuclei Detection by Flow Cytometry as a High-Throughput Approach for the Genotoxicity Testing of Nanomaterials. *Nanomaterials 2019, Vol. 9, Page 1677* **2019**, *9* (12), 1677. https://doi.org/10.3390/NANO9121677.

143. Cervena, T.; Rossnerova, A.; Zavodna, T.; Sikorova, J.; Vrbova, K.; Milcova, A.; Topinka, J.; Rossner, P. Testing Strategies of the In Vitro Micronucleus Assay for the Genotoxicity Assessment of Nanomaterials in BEAS-2B Cells. *Nanomaterials 2021, Vol. 11, Page 1929* **2021**, *11* (8), 1929. https://doi.org/10.3390/NANO11081929.

144. Steinritz, D.; Möhle, N.; Pohl, C.; Papritz, M.; Stenger, B.; Schmidt, A.; Kirkpatrick, C. J.; Thiermann, H.; Vogel, R.; Hoffmann, S.; Aufderheide, M. Use of the Cultex® Radial Flow System as an in Vitro Exposure Method to Assess Acute Pulmonary Toxicity of Fine Dusts and Nanoparticles with Special Focus on the Intra- and Inter-Laboratory Reproducibility. *Chem Biol Interact* **2013**, *206* (3), 479–490. https://doi.org/10.1016/J.CBI.2013.05.001.

145. Bell, C. C.; Dankers, A. C. A.; Lauschke, V. M.; Sison-Young, R.; Jenkins, R.; Rowe, C.; Goldring, C. E.; Park, K.; Regan, S. L.; Walker, T.; Schofield, C.; Baze, A.; Foster, A. J.; Williams, D. P.; van de Ven, A. W. M.; Jacobs, F.; van Houdt, J.; Lähteenmäki, T.; Snoeys, J.; Juhila, S.; Richert, L.; Ingelman-Sundberg, M. Comparison of Hepatic 2D Sandwich Cultures and 3D Spheroids for Long-Term Toxicity Applications: A Multicenter Study. *Toxicological Sciences* **2018**, *162* (2), 655–666. https://doi.org/10.1093/TOXSCI/KFX289.

146. Barosova, H.; Meldrum, K.; Karakocak, B. B.; Balog, S.; Doak, S. H.; Petri-Fink, A.; Clift, M. J. D.; Rothen-Rutishauser, B. Inter-Laboratory Variability of A549 Epithelial Cells Grown under Submerged and Air-Liquid Interface Conditions. *Toxicology in Vitro* **2021**, *75*, 105178. https://doi.org/10.1016/J.TIV.2021.105178.

147. Shah, U. K.; Mallia, J. de O.; Singh, N.; Chapman, K. E.; Doak, S. H.; Jenkins, G. J. S. A Three-Dimensional in Vitro HepG2 Cells Liver Spheroid Model for Genotoxicity Studies. *Mutation Research/Genetic Toxicology and Environmental Mutagenesis* **2018**, *825*, 51–58. https://doi.org/10.1016/J.MRGENTOX.2017.12.005.

148. van Grunsven, L. A. 3D in Vitro Models of Liver Fibrosis. *Adv Drug Deliv Rev* **2017**, *121*, 133–146. https://doi.org/10.1016/J.ADDR.2017.07.004.

149. Štampar, M.; Breznik, B.; Filipič, M.; Žegura, B. Characterization of In Vitro 3D Cell Model Developed from Human Hepatocellular Carcinoma (HepG2) Cell Line. *Cells 2020, Vol. 9, Page 2557* **2020**, *9* (12), 2557. https://doi.org/10.3390/CELLS9122557.

150. Frandsen, H. S.; Štampar, M.; Vej-Nielsen, J. M.; Žegura, B.; Rogowska-Wrzesinska, A. Method to Disassemble Spheroids into Core and Rim for Downstream Applications Such as Flow Cytometry, Comet Assay, Transcriptomics, Proteomics, and Lipidomics. In *Next Generation Culture Platforms for Reliable In Vitro Models: Methods and Protocols*; Brevini, T. A. L., Fazeli, A., Turksen, K., Eds.; Humana Press. Methods in Molecular Biology, 2021; Vol. 2273, pp 173–188. https://doi.org/10.1007/978-1-0716-1246-0_12.

151. Klein, C. L.; Comero, S.; Stahlmecke, B.; Romazanov, J.; Kuhlbusch, T. A. J.; Doren, E. van; De, P.-J.; Mast, T. J.; Wick, P.; Krug, H.; Locoro, G.; Hund-Rinke, K.; Kördel, W.; Friedrichs, S.; Maier, G.; Werner, J.; Gawlik, B. M. NM-Series of Representative Manufactured Nanomaterials NM-300 Silver Characterisation, Stability, Homogeneity. **2011**. https://doi.org/10.2788/23079.

152. Fraunhofer IME. NM-302 Nano-Silver Elongated Rods, Material Information Sheet, Version 12. 2017.

153. Fraunhofer IME. NM-302 Nano-Silver Elongated Rods, Material Information Sheet, Version 1. 2012.

154. Singh, C.; Friedrichs, S.; Levin, M.; Birkedal, R.; Jensen, K.; Pojana, G.; Wohlleben, W.; Schulte, S.; Wiench, K.; Turney, T.; Koulaeva, D.; Marshall, D.; Hund-Rinke, K.; Koerdel, W.; van Doren, E.; de Temmerman, P.; Abi Daoud Francisco, M.; Mast, J.; Gibson, P.; Koeber, R.; Linsinger, T.; Klein, C. NM-Series of Representative Manufactured Nanomaterials - Zinc Oxide NM-110, NM-111, NM-112, NM-113: Characterisation and Test Item Preparation. *EUR 25066 EN*. Publications Office of the European Union: Luxembourg 2011. https://doi.org/10.2787/55008.

155. Cohen, J. M.; Beltran-Huarac, J.; Pyrgiotakis, G.; Demokritou, P. Effective Delivery of Sonication Energy to Fast Settling and Agglomerating Nanomaterial Suspensions for Cellular Studies: Implications for Stability, Particle Kinetics, Dosimetry and Toxicity. *NanoImpact* **2018**, *10*, 81–86. https://doi.org/10.1016/J.IMPACT.2017.12.002.

156. Oh, S. J.; Kim, H.; Liu, Y.; Han, H. K.; Kwon, K.; Chang, K. H.; Park, K.; Kim, Y.; Shim, K.; An, S. S. A.; Lee, M. Y. Incompatibility of Silver Nanoparticles with Lactate Dehydrogenase Leakage Assay for Cellular Viability Test Is Attributed to Protein Binding and Reactive Oxygen Species Generation. *Toxicol Lett* **2014**, *225* (3), 422–432. https://doi.org/10.1016/J.TOXLET.2014.01.015.

157. Huh, D.; Matthews, B. D.; Mammoto, A.; Montoya-Zavala, M.; Yuan Hsin, H.; Ingber, D. E. Reconstituting Organ-Level Lung Functions on a Chip. *Science (1979)* **2010**, *328* (5986), 1662–1668. https://doi.org/10.1126/science.1188302.

158. Schürch, D.; Vanhecke, D.; Clift, M. J. D.; Raemy, D.; de Aberasturi, D. J.; Parak, W. J.; Gehr, P.; Petri-Fink, A.; Rothen-Rutishauser, B. Modeling Nanoparticle-Alveolar Epithelial Cell Interactions under Breathing Conditions Using Captive Bubble Surfactometry. *Langmuir* **2014**, *30* (17), 4924–4932. https://doi.org/10.1021/la500307q.

159. Sengupta, A.; Roldan, N.; Kiener, M.; Froment, L.; Raggi, G.; Imler, T.; de Maddalena, L.; Rapet, A.; May, T.; Carius, P.; Schneider-Daum, N.; Lehr, C.-M.; Kruithof-de Julio, M.; Geiser, T.; Marti, T. M.; Stucki, J. D.; Hobi, N.; Guenat, O. T. A New Immortalized Human Alveolar Epithelial Cell Model to Study Lung Injury and Toxicity on a Breathing Lung-On-Chip System. *Frontiers in Toxicology* **2022**, *0*, 68. https://doi.org/10.3389/FTOX.2022.840606.

160. Ma, X.; Sun, J.; Ye, Y.; Ji, J.; Sun, X. Application of Triple Co-Cultured Cell Spheroid Model for Exploring Hepatotoxicity and Metabolic Pathway of AFB1. *Science of The Total Environment* **2022**, *807*, 150840. https://doi.org/10.1016/J.SCITOTENV.2021.150840.

161. Kohl, Y.; Biehl, M.; Spring, S.; Hesler, M.; Ogourtsov, V.; Todorovic, M.; Owen, J.; Elje, E.; Kopecka, K.; Moriones, O. H.; Bastús, N. G.; Simon, P.; Dubaj, T.; Rundén-Pran, E.; Puntes, V.; William, N.; von Briesen, H.; Wagner, S.; Kapur, N.; Mariussen, E.; Nelson, A.; Gabelova, A.; Dusinska, M.; Velten, T.; Knoll, T. Microfluidic In Vitro Platform for (Nano)Safety and (Nano)Drug Efficiency Screening. *Small* **2021**, *17* (15), 2006012. https://doi.org/10.1002/SMLL.202006012.

162. Henry, O. Y. F.; Villenave, R.; Cronce, M. J.; Leineweber, W. D.; Benz, M. A.; Ingber, D. E. Organs-on-Chips with Integrated Electrodes for Trans-Epithelial Electrical Resistance (TEER) Measurements of Human Epithelial Barrier Function. *Lab Chip* **2017**, *17* (13), 2264–2271. https://doi.org/10.1039/c7lc00155j.

163. Srinivasan, B.; Kolli, A. R.; Esch, M. B.; Abaci, H. E.; Shuler, M. L.; Hickman, J. J. TEER Measurement Techniques for In Vitro Barrier Model Systems. *Journal of Laboratory Automation*. SAGE Publications Inc. April 1, 2015, pp 107–126. https://doi.org/10.1177/2211068214561025.

164. Kuo, L. J.; Yang, L.-X. γ-H2AX - A Novel Biomarker for DNA Double-Strand Breaks. *In Vivo (Brooklyn)* **2008**, *22* (3).

165. Zhang, S.; Chen, H.; Wang, A.; Liu, Y.; Hou, H.; Hu, Q. Genotoxicity Evaluation of Carbon Monoxide and 1,3-Butadiene Using a New Joint Technology: The in Vitro ΓH2AX HCS Assay Combined with Air–Liquid Interface System. *Toxicol Mech Methods* **2019**, *29* (1), 1–7. https://doi.org/10.1080/15376516.2018.1477897.

I

nanomaterials

MDPI

Article

Advanced Respiratory Models for Hazard Assessment of Nanomaterials—Performance of Mono-, Co- and Tricultures

Laura Maria Azzurra Camassa [1,†], Elisabeth Elje [2,3,†], Espen Mariussen [2,4], Eleonora Marta Longhin [2], Maria Dusinska [2], Shan Zienolddiny-Narui [1,*] and Elise Rundén-Pran [2,*]

1 National Institute of Occupational Health in Norway, 0033 Oslo, Norway; laura.camassa@stami.no
2 NILU—Norwegian Institute for Air Research, 2027 Kjeller, Norway; eel@nilu.no (E.E.); espen.mariussen@fhi.no (E.M.); eml@nilu.no (E.M.L.); mdu@nilu.no (M.D.)
3 Institute of Basic Medical Sciences, Department of Molecular Medicine, University of Oslo, 0372 Oslo, Norway
4 Norwegian Institute of Public Health, FHI, 0456 Oslo, Norway
* Correspondence: shan.narui@stami.no (S.Z.-N.); erp@nilu.no (E.R.-P.); Tel.: +47-2319-5284 (S.Z.-N.); +47-6389-8237 (E.R.-P.)
† These authors contributed equally to this work.

Abstract: Advanced in vitro models are needed to support next-generation risk assessment (NGRA), moving from hazard assessment based mainly on animal studies to the application of new alternative methods (NAMs). Advanced models must be tested for hazard assessment of nanomaterials (NMs). The aim of this study was to perform an interlaboratory trial across two laboratories to test the robustness of and optimize a 3D lung model of human epithelial A549 cells cultivated at the air–liquid interface (ALI). Potential change in sensitivity in hazard identification when adding complexity, going from monocultures to co- and tricultures, was tested by including human endothelial cells EA.hy926 and differentiated monocytes dTHP-1. All models were exposed to NM-300K in an aerosol exposure system (VITROCELL® cloud-chamber). Cyto- and genotoxicity were measured by AlamarBlue and comet assay. Cellular uptake was investigated with transmission electron microscopy. The models were characterized by confocal microscopy and barrier function tested. We demonstrated that this advanced lung model is applicable for hazard assessment of NMs. The results point to a change in sensitivity of the model by adding complexity and to the importance of detailed protocols for robustness and reproducibility of advanced in vitro models.

Keywords: 3D lung model; air–liquid interface; nanotoxicology; NM-300K; tricultures

Citation: Camassa, L.M.A.; Elje, E.; Mariussen, E.; Longhin, E.M.; Dusinska, M.; Zienolddiny-Narui, S.; Rundén-Pran, E. Advanced Respiratory Models for Hazard Assessment of Nanomaterials—Performance of Mono-, Co- and Tricultures. *Nanomaterials* **2022**, *12*, 2609. https://doi.org/10.3390/nano12152609

Academic Editor: Javier Jiménez-Lamana

Received: 29 June 2022
Accepted: 26 July 2022
Published: 29 July 2022

1. Introduction

The exponential rise in production and use of NMs is increasing the risk of human and environmental exposure. Upon inhalation of particulate and chemical environmental pollutants, the respiratory system is the first-line target for adverse health effects [1,2]. This is emphasizing the importance of developing and validating advanced respiratory models for hazard identification and characterization of NMs to ensure safe use and reduced concern for public health. Development of new alternative methods (NAMs), including advanced three-dimensional (3D) in vitro models, are needed for next-generation human hazard and risk assessment, moving from in vivo animal experiments towards in vitro testing and in silico modeling, in compliance with the 3R principle to reduce, replace and refine animal experiments and as part of an integrated approach to testing and assessment (IATA) for regulatory use of in vitro data.

A large fraction of the NMs (diameter $\leq$ 100 nm) has been shown to deposit in the alveolar region of the lungs [3,4]. The interaction of the reactive NMs with the large surface area of the lungs is of importance for cellular uptake, and thus for the local and systemic effects [5]. Both environmental and engineered NMs have been shown to induce adverse health effects, such as pulmonary, cardiovascular, neurological, and reproductive

disorders [6–8]. A direct association between exposure to diesel exhaust particles (DEPs) in exhaust fumes and lung cancer has been demonstrated [9–12]. Engineered NMs, (e.g., metallic nanoparticles, quantum dots, carbon nanotubes) have also been shown to cause toxicity after inhalation exposure [13–15]. At the cellular level, NMs can provoke oxidative stress, inflammatory responses, and/or genotoxicity. These molecular events play key roles in the development of adverse health effects of NMs [16].

The potential hazardous health effect of inhaled NMs depends on the interaction of deposited nanoparticles at the lung surface with the cells of the air–blood barrier [3,17–20]. Most of the pulmonary in vitro studies have been conducted using cell lines in submerged conditions, which is far from the in vivo situation. Additionally, the cell medium can influence the status and the properties of the NMs [21–23]. Therefore, it is important to establish robust and optimized in vitro models closer to the real-life inhalation exposure situation that can give a more realistic judgment regarding the hazardous potential of compounds, including particulate matters and NMs [24].

Closer to the scenario in vivo is the exposure of cells at the air–liquid interface (ALI), where cells cultivated on porous membranes are in direct contact with the air on one side and cell culture media on the other [9,25–28]. The aim of this work was to test for potential change in sensitivity for toxic insults when going from mono- to tricultures, and to test the robustness of and optimize an advanced 3D lung model in combination with an aerosol exposure system (VITROCELL® cloud-chamber), to feature the air–blood barrier in the alveoli of the lower respiratory tract by performing and an interlaboratory trial across two laboratories. This advanced respiratory model, closer to the in vivo situation, can be used to study pulmonary processes and responses and as a valuable tool for hazard identification and characterization of NMs and environmental pollutants in the lungs after inhalation exposure.

We included in the model several human cell lines relevant for lung exposure, to advance from standard 2Ds to 3D cell cultures. We compared the response and sensitivity of mono-, co-, and tricultures of human lung epithelial cells (A549), endothelial cells (EA.hy926), and human differentiated monocytes (dTHP-1), respectively, after exposure in a VITROCELL® cloud-chamber, to the JRC repository silver NMs NM-300K. Moreover, we aimed to establish a harmonized protocol and experimental design by performing an interlaboratory trial across two laboratories to strengthen the robustness of this advanced respiratory model for future applications for toxicity testing of NMs exposure.

2. Materials and Methods

2.1. Cell Cultures

The same batch of the cells were used for the inter-laboratory comparison studies performed at Laboratory 1 (NILU) and Laboratory 2 (STAMI). The human alveolar type II lung epithelial A549 [29], monocytic THP-1 [30], and endothelial EA.hy926 cells [31] were purchased from the American Type Culture Collection (ATCC, Manassas, VA, USA). The cell lines were cultured in DMEM or RPMI supplemented with 9–10% fetal bovine serum (FBS, product no. 26140079, ThermoFisher Scientific, Oslo, Norway; FBS, ultra-low endotoxin product no: S009Y20008, Biowest, vwr, Oslo, Norway) and 1% penicillin/streptomycin (Pen-Strep, product no. 15070063, ThermoFisher Scientific) (Table S1) and maintained in an incubator with humidified atmosphere at 5% CO_2 and at 37 °C. A549 and EA.hy926 cells were cultured at a density of approximately 1.3×10^4 cells/cm^2 in vented cell culture flasks. The cells were sub-cultured twice a week by dry trypsinization (0.25% for 2–4 min at 37 °C). THP-1 cells were maintained in suspension at a density of 3–9 $\times 10^5$ cells/mL for a maximum of 6–8 weeks.

For differentiation of THP-1 from monocytes to macrophage-like cells, phorbol-12-myristat-13 acetate (PMA, Sigma-Aldrich, St. Louis, MI, USA, product no. P8139, EU) was prepared as a stock solution (1 mg/mL) in DMSO. The stock solution was diluted in Milli-Q (MQ) to 10 µg/mL, and aliquots were kept at −20 °C in the dark. PMA at 20 ng/mL was added to undifferentiated THP-1 cells for 3 days. Differentiated THP-1 cells

(dTHP-1) were cultured for 48 h in RPMI complete medium. Mature macrophages were evaluated by upregulation of the marker CD11b [32] by confocal laser scanning microscopy (LSM) (Section 2.10). dTHP-1 cells were harvested by incubation with 5 mL Accutase® (Merck, Rahway, NJ, USA) for 10–15 min. In some cases, cell scraping was necessary in addition to Accutase® incubation to detach the cells. Accutase® was neutralized by adding complete cell culture medium. The cell suspension was centrifuged at 200× *g* for 5 min and resuspended in fresh complete medium.

A549, EA.hy926, and THP-1 were used at passages (P) 2–25, 3–19, and 3–15, respectively. Detailed information on passage numbers for each cell type is shown in Table S2. All cell lines were tested regularly for mycoplasma contamination.

2.2. Advanced In Vitro 3D Lung Models

Monocultures of A549, cocultures of A549 + EA.hy926, and tricultures of A549 + EA.hy926 + dTHP-1 (Figure 1) were seeded at specified concentrations (Table S3) on inserts of polyethylene terephthalate (PET) with 1 µm pore size and with a surface area of 4.2 cm^2 (Falcon, BD Biosciences, San Jose, CA, USA) or 4.5 cm^2 (Millicell, Merck). The choice of inserts with 1 µm pore size was to allow for spatial interaction between the cell types and at the same time to create compartmentalization between the cells. Mono-, co-, and tricultures were cultured in submerged conditions in 6-well plates (Falcon, BD Biosciences) for 48 h to let the cells grow to confluency. The cultures were transferred to ALI conditions by removing the apical medium and placed in the incubator for 24 h before exposure to the VITROCELL® cloud system.

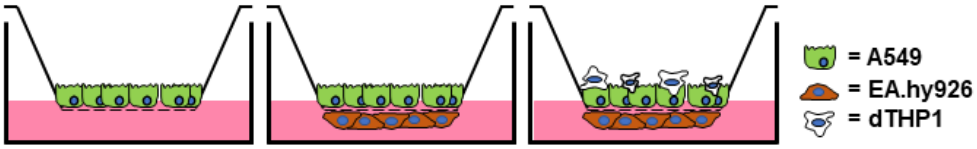

Figure 1. Scheme of mono-, co-, and triculture lung models of A549, EA.hy926, and differentiated THP-1 (dTHP-1) cells cultivated at the air–liquid interface (ALI) on membrane inserts.

2.2.1. Monocultures of A549

A549 cells were seeded at the density of 1.1 × 10^5 cells/cm^2 on the apical side of the cell insert in a 6-well plate, with 1 mL medium at the apical side and 3 mL medium at the basolateral side. The cells were incubated for 48 h before the basolateral medium was replaced by 1.5 mL fresh culture medium, and the apical medium was carefully removed to place the cells in ALI conditions before exposure.

2.2.2. Cocultures of A549 and EA.hy926

EA.hy926 cells were seeded at the density of 1.1 × 10^5 cell/cm^2 on the basolateral side of cell inserts and placed in the incubator for 4 h. The inserts were then turned and placed inside of a 6-well plate with 3 mL of medium/well. A549 cells were seeded on top of the membrane insert in 1 mL medium, as described for monocultures.

2.2.3. Tricultures of A549, EA.hy926 and dTHP-1

Tricultures were prepared as described for cocultures, but with inclusion of dTHP-1 cells. After 48 h incubation of the cocultures, the apical medium was removed. dTHP-1 cells were seeded at the density of 1.1–2.2 × 10^5 cell/cm^2 (4.9–10 × 10^5 cells/insert) in 1 mL medium on top of the A549 cell layer. The same number of cells was seeded for all inserts within each experiment. After 4 h incubation, the basolateral medium was replaced by 1.5 mL fresh medium, and the apical medium was carefully aspirated to remove non-attached dTHP-1 cells and to place the cells in ALI conditions for 24 h.

2.3. NM-300K Dispersion and Characterization

2.3.1. NM-300K Nanoparticles (Ag NMs)

The JRC Repository NM NM-300K and its dispersant NM-300K DIS were purchased from Fraunhofer IME, Germany. NM-300K are engineered spherical silver NMs with pristine size < 20 nm [33] and were chosen as a reference NM based on our previous work, including the work in NanoREG, showing toxicity of these NMs [34–36]. NM-300K DIS is a colloidal dispersion medium of deionized water (85%) containing 7% stabilizing agent (ammonium nitrate) and 8% emulsifiers (4% Polyoxyethylene Glycerol Trioleate and 4% Polyoxyethylene Sorbitan Monolaurate, Tween 20). NM-300K has a nominal silver concentration of 10% (*w*/*w*) [33]. The same batch of NM-300K was used by both laboratories.

2.3.2. NM-300K Dispersion

A stock dispersion of NM-300K at nominal concentration 10 mg Ag/mL was sonicated in a solution of 0.05% bovine serum albumin (BSA) and MQ water to avoid agglomeration of silver particles, following the NANOGENOTOX protocol [37] with modifications. The dispersion was sonicated on ice and thereafter kept on ice for 10 min before use. At Lab 1, the sonication was conducted using a Labsonic®P sonicator and a 3 mm probe (product no 853 5124, Sartorius Stedim Biotech, Göttingen, Germany) at 50% amplitude for 5 min (100% cycle), or with a Q500 sonicator and a 3 or 6 mm microtip probe (Qsonica L.L.C, Newtown, PA, USA) at 30–35% amplitude for 7–8 min. At Lab 2, the sonication was conducted using a 400-Watt Branson Sonifier S-450D (Branson Ultrasonis Corp., Danbury, CT, USA) equipped with a standard 13 mm disruptor horn (Model number: 101-147-037), for 5 min and 10% amplitude. The sonicators were calibrated to give a delivered energy of 390–1090 J/mL of NM dispersion. The dispersion medium NM-300K DIS solvent control was prepared using the same procedure as for stock dispersion of NM-300K. For cell exposure at the lowest concentration, NM-300K stock was diluted in phosphate-buffered saline (PBS) without $CaCl_2/MgCl_2$.

2.3.3. Dynamic Light Scattering Analysis of NM-300K

The hydrodynamic size and size distribution of NM-300K stock dispersion and diluted dispersion (in PBS) was measured at both laboratories using dynamic light scattering (DLS). The stock and diluted dispersions were diluted 1:100 in ultrapure water, mixed by pipetting, transferred to a disposable cuvette (DTS0012), and placed in the Zetasizer. At Lab 1 a Zetasizer Ultra Red (Malvern Panalytical Ltd., Malvern, UK) was used, with 3–5 measurements with automatic number of sub-runs at a fixed measurements angle of 174.4°. At Lab 2 a Zetasizer Nano ZS (Malvern Panalytical Ltd.) was used, with 3 measurements with 11 sub-runs at a fixed measurements angle of 173°. Analysis was performed at 25 °C with 120 s equilibration time, automatic attenuation, and no pause between repeats. Data were processed in the ZS Explorer software (Lab 1) or Zetasizer Nano software (Lab 2), using general purpose model, refractive index 1.59, and absorption 0.01. Results were presented as Z-average (Z-ave) which is the intensity weighted mean hydrodynamic size of the ensemble collection of particles, the polydispersity index (PDI), and hydrodynamic diameter (by intensity) of individual peaks in the size distributions.

Zeta potential (ZP) was also measured. The dispersion was diluted at 1:100 in ultrapure water, transferred to a disposable folded capillary cell (DTS1070) pre-wetted with ethanol and water, and placed in the Zetasizer Ultra Red. The ZP was measured by mixed mode measurement phase analysis light scattering (M3-PALS) at 25 °C.

For testing the stability of the NMs in different buffer solutions (PBS with and without $CaCl_2/MgCl_2$, HBSS with and without $CaCl_2/MgCl_2$, DMEM D6046 with no supplements), the dispersion was diluted 1:10 in the different buffers and further diluted 1:10 in ultrapure water, before size analysis by DLS in Zetasizer Ultra Red as described above.

2.3.4. Analysis of Total and Dissolved Ag

The concentration of total and dissolved Ag species in the NM-300K stock dispersion (10 mg/mL) was measured by inductively coupled plasma mass spectrometry (ICP-MS). Directly after preparation, 0.5 mL of the stock dispersion was transferred to an Eppendorf tube and stored at room temperature (RT) until further processing for analysis of total Ag content. In parallel, directly after preparation, 1 mL of the NM-300K stock dispersion was transferred to Amicon Ultra centrifugal filter (3 kDa) unit tubes (Millipore, product no UFC900324) [36,38]. The filter was preconditioned with ultrapure water at 3900 g for 30 min before use. To separate Ag-NMs and dissolved Ag species, the samples were centrifuged at 3900 g for 45 min. Ultrapure water was used as control. The dissolved Ag in the filtrate (<3 kDa fraction) was stored at RT until further processing (Section 2.6). The proportion of dissolved Ag was calculated by dividing the measured Ag in the ultracentrifuged samples by the measured total Ag in the stock dispersion. The total Ag was measured from 7 independent experiments, each with one stock dispersion (n = 7), and the dissolved fraction was measured from two independent experiments, each with one dissolved fraction (n = 2).

2.3.5. Endotoxin Testing of NM-300K

The NM-300K and NM-300K DIS were tested for possible endotoxin content with two different methods: HEK293 colorimetric test (InvivoGen) and the Limus Amebocyte Lysate (LAL Kinetic QCL) test.

HEK293 Endotoxin Test

The human embryonic kidney (HEK) 293 cell line endotoxin colorimetric test is based on the ability of the HEK293 toll-like receptor (TLR) 2 and TLR 4 transfected cells to recognize lipoteichoic acid (LTA) and lipopolysaccharide (LPS), respectively, from gram-negative bacteria (lipid A). These cells are engineered to be extremely sensitive to TLR-receptor agonists and further activation of the NF-κB pathway. HEK293 hTRL2 and hTLR4 cells co-express the NF-κB-inducible reporter gene secreted embryonic alkaline phosphatase (SEAP). The presence of the agonists LPS or LTA, starting as low as 0.03 ng/mL, will activate the HEK293 TLR2 and TLR4 receptors, respectively, and further the NF-κB pathway. NF-κB activation can be quantified using the dye HEK-Blue™Detection and reading the absorbance (OD) at 650 nm. The measured absorbance is directly proportional to the endotoxin concentration in the solution, where one endotoxin unit/mL (EU/mL) equals approximately 0.1 ng endotoxin/mL of solution.

Cells and reagents for the HEK293 endotoxin colorimetric test were purchased from InvivoGen. HEK293 hTLRnull, hTLR2, and hTLR4 cells were grown and maintained in DMEM high glucose, 10% FBS, and the antibiotics 10U penicillin/streptomycin (Gibco, Waltham, MA, USA) and Normocin (InvivoGen). Zeocin (InvivoGen) was additionally added to the cell medium for HEK293 hTLRnull, and HEK-Blue selection antibiotics (InvivoGen) were added to the cell medium for the maintenance of HEK293 hTRL2 and hTRL4 cells. HEK293 hTLRnull, hTLR2, and hTLR4 cell lines were exposed to NM-300K at concentrations of 1 μg/mL and 10 μg/mL for 24 h. Four replica exposures were conducted for each cell line. Cell viability was examined with the AlamarBlue assay as described in Section S1.2. (Supplementary Materials). The absorbance was measured using a Spectrometer Gen 5 microplate data acquisition system and quantified using the analysis software (BioTek, Winooski, VT, USA). HEK293 hTLRnull cells were used as a negative control.

Limulus Amebocyte Lysate (LAL Kinetic QCL) Endotoxin Test

The LAL chromogenic endotoxin test (Lonza, EU) is based on a reaction between gram-negative bacterial endotoxin present in the analysis sample and a pro-enzyme, pro-factor C. The activation of the enzyme releases p-nitroaniline (pNA) from a synthetic substrate, producing a yellow color. The time required before the appearance of the yellow color is inversely proportional to the amount of endotoxin present. The yellow color from pNA

is measured photometrically at 405 nm throughout the incubation period (30 min). NM-300K was tested for endotoxin with the LAL test at Lab 2, at the concentration of 0.5 and 50 μg/mL following the kit protocol. The concentration of endotoxin was calculated from its reaction time by comparison to a standard curve made by *E. coli* endotoxin. The LAL colorimetric test is extremely sensitive and detects as little as 0.1 EU/mL (approx. 0.01 ng endotoxin per mL).

2.4. Cell Exposure

The commercially available VITROCELL® 6 Cloud System (VITROCELL® Systems GmbH, Waldkirch, Germany) was used to expose the cells to NM-300K and controls. The system is equipped with an Aerogen Pro® vibrating membrane nebulizer, which generates a dense cloud of droplets with a median aerodynamic diameter of 4–6 μm that are deposited at the bottom of the exposure chamber (area 145 cm^2) [39] and is maintained at 37 °C in a laminar flow hood.

Transwell inserts with mono-, co- or tricultures were transferred to the VITROCELL® 6 Cloud system, which was filled with an 18 mL cell culture medium/well to let the basolateral side of the insert be in contact with medium. A total volume of 300 μL (2 × 150 μL) of 10 mg/mL and 1 mg/mL of NM-300K dispersion was nebulized, to obtain, respectively, a nominal deposition concentration of 10 $\mu g/cm^2$ and 1 $\mu g/cm^2$ for exposure of the cells. See Supplementary Materials (S1.3.) for calculations on nominal deposition concentration. The same volume was used for exposure with the negative control PBS w/o $CaCl_2/MgCl_2$ and the solvent control NM-300K DIS. Exposures were performed in the same order in each experiment (PBS, NM-300K DIS, NM-300K 1 mg/mL, NM-300K 10 mg/mL) to avoid cross-over of solutions to the samples. Between each exposure, the nebulizer was rinsed with PBS, and the outlet and the box were wiped with a tissue. The plate was also wiped with tissue with ethanol between each exposure. The same nebulizer was used for all experiments at each laboratory, and was rinsed with PBS for several minutes, and wiped with a tissue between experiments.

For experiments performed at Lab 1, the nebulizer was rinsed with 150 μL PBS directly after the exposure to make sure a minimum of the NM dispersion was left in the nebulizer. Thus, the cultures were exposed to total volume of 300 μL sample and 150 μL PBS.

The cloud was allowed to settle (5–8 min) before the box was opened and the inserts transferred to new plates with a 1.5 mL fresh culture medium. Unexposed cultures (incubator control) were also transferred to new plate with fresh culture medium. The cultures were placed in the incubator for 24 h before processing for further analysis.

To defy the suitable control buffer in the experiment, cell cultures were exposed to several aerosolized buffer solutions. The buffer solutions of interest were PBS without $CaCl_2/MgCl_2$ (D8537 Sigma), PBS with $CaCl_2/MgCl_2$ (D8662 Sigma), Hank's balanced salt solution (HBSS) without $CaCl_2/MgCl_2$ (14175-046 Gibco), HBSS with $CaCl_2/MgCl_2$ (14025-050 Gibco), and DMEM D6046 without supplements. Exposure of cell inserts to buffer solutions was performed using 3 × 150 μL buffer solution. The cloud settled for 8 min before the box was opened and the inserts were transferred to new culture plates with 1.5 mL fresh culture medium. The cultures were placed in the incubator for 24 h before processed for further analysis. Between exposures, the nebulizer was rinsed using the next buffer to test, with the order PBS without $CaCl_2/MgCl_2$, PBS with $CaCl_2/MgCl_2$, HBSS without $CaCl_2/MgCl_2$, HBSS with $CaCl_2/MgCl_2$, and DMEM without serum.

2.5. Deposition Efficiency and Barrier Integrity

2.5.1. Fluorescein Measurements

To measure deposition efficiency in the VITROCELL® cloud system, a fluorescent water-soluble fluorescein sodium salt (product no. 46960, CAS 518-47-8, BioReagent, Sigma-Aldrich) was used. At Lab 1, transwell inserts with 1 mL PBS were exposed to 150 μL aerosolized fluorescein (10 μg/mL). Aliquots of the PBS-fluorescein solution were transferred to a black 96-well plate for reading of fluorescence in a microplate reader at

excitation 480 nm and emission 525 nm. The amount of fluorescein in each sample was quantified from a seven-point standard curve (0.625–100 ng/mL). Background fluorescence from the cell culture medium was subtracted from the measurements. The deposited fluorescein concentration per area was calculated by dividing the total amount of fluorescein in each sample by the area of the insert. The deposition efficiency of fluorescein in the VITROCELL® system was calculated by dividing the deposited fluorescein (μg/cm^2) by the maximum deposition per total area (1.5 μg/145 cm^2), multiplied by 100%. This protocol for determination of deposition efficiency was similar to the VITROCELL® protocol [40–42] that was used at Lab 2, where 200 μL of 15 μg/mL fluorescein in PBS was applied.

In parallel with deposition efficiency analysis, the cellular barrier integrity was investigated by measuring the break-through of fluorescein to the basolateral side of the cocultures. Cocultures of A549 and EA.hy926 were exposed at ALI to 150 μL aerosolized fluorescein (10 μg/mL). After incubation overnight, aliquots of the cell culture medium from the basolateral compartments were transferred to a black 96-well plate, with a standard curve, for fluorescence reading, as described above. Background fluorescence from the cell culture medium was subtracted from the measurements. The proportion of fluorescein transferred to the basolateral side of the membrane was calculated by dividing the amount recovered in the cell culture medium at the basolateral side of the membrane by the total deposition of fluorescein.

The deposition efficiency of the nebulizer used in the experiment was measured with 3 independent experiments, and the results were used to determine the required volumes and concentrations of NM-300K to obtain the nominal concentrations.

2.5.2. ICP-MS Analysis of Ag

The amount of NM-300K deposited on the cells (mono- and cocultures) was quantified by ICP-MS to obtain precise information on the Ag amount delivered to the cells, and to determine the amount of Ag crossing the cellular barriers during exposure.

For deposition measurements, the well of the VITROCELL® plate was filled with 10 mL PBS, ensuring no contact between the insert and the liquid, but keeping the system humid. NM-300K was nebulized as explained above for exposure of cells (Section 2.4) onto cell-free inserts, which after exposure were dried overnight in a 6-well plate (RT in the dark). The next day, the porous membrane filter was removed from the insert walls using scalpel and tweezer and transferred to a 5 mL Eppendorf tube. Blank, unexposed filters were included as control. The filters were stored in dark conditions at RT before further processing (Section 2.6). Deposition of NM-300K was calculated by dividing the total Ag amounts per filter by the membrane area. For the lower concentration, 2 independent experiments with each 2 inserts were used for the lower concentration, and 4 independent experiments with each 2–3 inserts for the higher.

The amount of Ag crossing the cellular barrier was also measured by collecting the basolateral medium into an Eppendorf tube, which was stored at RT before further processing. Results were calculated from 3 independent experiments (n = 3) each with 1–2 inserts (except for monocultures lower concentration where n = 2 experiments). Medium was also collected from dry, cell-free inserts with deposited NM-300K, incubated with 1.5 mL medium (DMEM D6046) below the insert for 24 h, to determine the maximum transfer of Ag through the insert (n = 2 independent experiments each with 1 insert). The relative amount of Ag crossing the cellular barrier was calculated by dividing the transferred Ag amount by the total deposited Ag.

2.6. Elemental Analysis of NM-300K by ICP-MS

The amount of Ag was measured by ICP-MS in liquid solutions (NM dispersions, water, cell culture media) and in filters from transwell inserts. Liquid samples were vortexed vigorously for at least 10 s before use. Approximately 0.25 g solution or complete filters were transferred to a Teflon container (18 mL) and subjected to microwave-assisted digestion with concentrated ultrapure distilled nitric acid mixed with ultrapure deionized MQ-water

(2 mL water and 1 mL nitric acid). The samples were digested in an UltraCLAVE single reaction chamber microwave oven (Milestone, Italy) according to a 60 min stepwise heating program, with a hold time for maximum temperature (250 °C) at 15 min. The samples were allowed to cool down to RT in their vessels after digestion, before being transferred to 10 mL test tubes (VWR, polycarbonate) and diluted with deionized ultrapure water to a final volume of approximately 10 mL. Two blank samples, containing only ultrapure water and nitric acid, and one reference material were included in each digestion run. The reference material Oyster Tissue (1566b) from National Institute of Standards and Technology (NIST) containing 0.666 ± 0.009 μg/g Ag, was subjected to similar microwave-assisted digestion to assess the recovery of Ag. Mean recovery of Ag in the NIST Oyster Tissue was 0.642 ± 0.010 μg/g. The samples were analyzed for ^{107}Ag by ICP-MS type Agilent 7700x (Agilent, Santa Clara, CA, USA), using the method accredited according to requirements of NS-EN/IEC 17025 (NILU-U-110).

2.7. Cytotoxicity Testing by the AlamarBlue Assay

Cytotoxicity was measured by the colorimetric assay AlamarBlue (AB) after 22–24 h exposure. This fluorometric assay is based on measuring cell viability by cellular reduction of the cell permeable, non-toxic dye resazurin into fluorescent resorufin in metabolically active cells. The fluorescence intensity is proportional to the number of living cells. The inserts were added to medium containing 10% *v*/*v* AB solution (Sigma-Aldrich) (1 mL on apical side, 1.5 mL on basolateral side) and incubated for 1–1.5 h. The plates were swirled gently to ensure proper mixing of the solution before aliquots of 40 μL or 100 μL (constant volumes within experiment) were taken from both compartments and transferred into a 96-well plate to measure the fluorescence intensity (ex.530 nm, em.590 nm). Blank values (medium with 10% *v*/*v* AB solution without cells) were subtracted from the measured fluorescence intensities. Cell viability was measured relative to unexposed incubator control (set to 100%). A minimum number of 3 independent experiments were performed with single or duplicate cell cultures. The inserts were not washed with PBS after exposure before addition of AB-medium, to minimize the loss of damaged/dead cells in the sample.

Control for interference between the NM-300K and read-out of the assay was included: cell-free inserts exposed to NM-300K were added 1 mL medium containing 10% *v*/*v* AB solution on the apical side and incubated for 1–1.5 h. Aliquots for fluorescence reading were performed as described above. Fluorescence intensity was compared to blank values (AB solution without NMs), and no differences were found (results not shown).

2.8. Genotoxicity Testing by the Comet Assay

The miniaturized 12-gel enzyme-modified version of the comet assay was performed to determine DNA damage (strand breaks, SBs) and oxidized base lesions, as described previously [35,43,44]. The first step was to harvest/collect the cells from the cell culture inserts. Directly after performing the AB assay, the cell cultures were washed twice with PBS (1 mL on apical side, 2 mL on basolateral side). The cells were wet trypsinized for 3–5 min in the incubator. For monocultures, 200–300 μL trypsin (0.25%, Sigma) was added to the apical side (dry basolateral side) and gently mixed after incubation to ensure proper disaggregation of the cell layer, before addition of 1 mL cell culture media for neutralization. For cocultures and tricultures, 200–300 μL trypsin (0.25%) was used on the apical side, while 1.5 mL trypsin (0.05%, Sigma) was used on the basolateral side of the membrane. The trypsin on the apical side was neutralized by 1 mL medium and on the basolateral side with 3 mL. The cells were resuspended by gently pipetting and transferred to Eppendorf tubes.

The cell suspensions were diluted in cell culture media to give approximately 200.000 cells/mL. Aliquots of the cell suspension were mixed 1:4 with low melting point agarose (0.8% *w*/*v*, Sigma-Aldrich, 37 °C) to a final agarose concentration of 0.64% *w*/*v*. Minigels (10 μL) with approximately 400 cells were made on cooled microscopic slides pre-coated with 0.5% standard melting point agarose (Sigma-Aldrich), with a maximum

of 12 gels per slide. Slides were placed in Coplin jars and submerged in lysis solution (2.5 M NaCl, 0.1 M EDTA, 10 mM Tris, 1% *v*/*v* Triton X-100, pH 10, 4 °C) for 1–3 days. As a positive control for DNA strand breaks (SBs), separate slides were submerged in 100 µM H_2O_2 (in PBS, 4 °C) for 5 min, rinsed twice with PBS for 2 min, and then submerged in a separate Coplin jar with lysis solution.

For detection of oxidized or alkylated bases, the modified comet assay was used with the bacterial repair enzyme formamidopyrimidine DNA glycosylase (Fpg, gift from NorGenoTech, Oslo, Norway), which converts oxidized or alkylated bases to SBs [45]. After lysis, separate slides with cells embedded in gels were washed twice for 8 min in buffer F (40 mM HEPES, 0.1 M KCl, 0.5 mM EDTA, 0.2 mg/mL BSA, pH 8, 4 °C), added Fpg diluted in buffer F (final 60.000 × dilution), and covered with a polyethylene foil before incubation at 37 °C for 30 min in a humid box. Positive control for function of Fpg was performed regularly in the laboratory, by using a photosensitizer Ro 19-8022 (kindly provided by Hoffmann La Roche, Switzerland) with light to induce oxidized purines, mainly 8-oxoG, which is detected by the Fpg [46–48]. A549 cells were exposed to the photosensitizer Ro 19–8022 (2 µM) and irradiated with visible light (30 cm distance from cells, 250 W) on ice for 4 min, before embedding into gels. The positive control gave expected response based on historical controls (>20% DNA in tail for net Fpg).

The slides were placed in a horizontal tank submerged in electrophoresis solution (0.3 M NaOH, 1 mM EDTA, pH > 13, 4 °C) to let the DNA unwind for 20 min. Electrophoresis was run for 20 min at 25 V (1.25 V/cm, around 350 mA, Consort EV202, 4 °C). The gels were neutralized for 5 min in PBS and dH_2O and dried horizontally overnight.

For quantification of DNA SBs, the gels were stained with SYBR gold (1:2000, Sigma-Aldrich), covered with a coverslip, and imaged in Leica DMI 6000 B (Leica Microsystems) equipped with a SYBR®photographic filter (Thermo Fischer Scientific). Comets of relaxed loops of DNA, withdrawn from the nuclei when subjection of DNA to the electrophoretic field after introducing breaks in the DNA, were scored using the software Comet assay IV 4.3.1 (Perceptive Instruments, Bury St Edmunds, UK). Median DNA tail intensity, proportional to the number of SBs, was calculated from 50 comets per gel as a measure of DNA SBs. Medians were averaged from 2–6 gels per cell culture. A total of 3–5 independent experiments were performed with single or duplicate exposure wells per experiment.

Control for possible interference between the NM-300K and analysis of comets was included. A sample of A549 control cells was mixed directly with NM-300K suspended in cell culture medium (140 µg/mL), just before embedding with LMP-agarose. The slides were handled in parallel with the other slides, as described above. The results from A549 cells analyzed with NM-300K present were compared to A549 control cells.

2.9. Uptake Analysis by Transmission Electron Microscopy

Engulfing of NM-300K by cells on the apical side of the insert (A549 and macrophage-like cells) was investigated by transmission electron microscopy (TEM). At 24 h after ALI exposure with 0.5 µg/cm^2 NM-300K, the cells were washed twice with PBS, fixed with 2.5% glutaraldehyde in PBS for 20 min, washed with PBS, and postfixed with 1% OsO_4 solution for 1 h. The cells were dehydrated in a series of ethanol with increasing concentrations and embedded in Epon–Durcupan resin. After polymerization for 72 h at 56 °C, ultrathin sections were cut at 70–80 nm using a Leica Reichert Ultracut Ultratome and Diatome knife and collected on 200 mesh size copper grids. Sections were contrasted with 2% uranyl acetate for 4 min and rinsed in MQ water. Contrast in lead citrate was avoided not to create deposition and interference during the microscopical investigation. Sections were examined with a Tecnai-12 transmission electron microscope operated at 80 kV.

2.10. Immunofluorescence and Confocal Microscopy

2.10.1. Antibodies Staining

At 24 h postexposure, unexposed and ALI exposed tricultures were washed in PBS and fixed with a solution of 4% paraformaldehyde (PFA) in PBS for 15 min at RT.

The membranes were removed from the plastic holder with a blade and kept in a 1:10 solution of fixative and PBS. The cells were permeabilized with a solution of 0.01% Triton-X 100 in PBS for 10 min. Unspecific epitopes were saturated in 2% BSA in PBS for 30 min. Cells were incubated overnight in a humidified chamber with primary antibodies directed toward cell markers specific to the air–blood barrier (Table S4). The primary antibodies were diluted in 2% BSA in PBS. The membranes were washed in PBS and incubated with secondary antibodies conjugated to a fluorescent probe (Table S4). Cells were stained with the nuclear staining DAPI for 5 min, washed in PBS and mounted on a microscopy slide with a mounting medium solution (Invitrogen), and covered with a coverslip. The cells were examined with a confocal Zeiss L-10 inverted microscope.

2.10.2. Staining with Live Cell Markers

To identify differentiated THP-1 cells in tricultures, dTHP-1 cells were stained with CellTracker Green CMFDA (CTG, Invitrogen) which is a non-toxic dye that remains in the cell for 3–6 generations. dTHP-1 cells were incubated with 10 μM CTG in serum-free medium for 30 min, washed twice with PBS, before detached and seeded on top of the A549 cells on the apical side of the transwell insert. For tricultures, plasma membranes were stained with CellMask Deep Red Plasma Membrane Stain (Invitrogen), 1:750 dilution in serum-free medium for 15 min at 37 °C.

The cells were then washed in PBS and fixed in 4% formaldehyde for 15 min at RT. The transwell inserts were rinsed again with PBS and processed by carefully detaching the membrane with cells from the plastic walls. The membranes were then mounted between two glass coverslips with the mounting medium ProLong Gold Antifade Reagent with DAPI (Cell signaling Technology) for nuclei counterstaining. The samples were left to dry overnight at RT in the dark and later stored at 4 °C in the dark. Confocal microscopy was performed using a Zeiss LSM 700 (lasers 405, 488, and 639 nm; objective 40x). Image acquisition and processing were performed with the Zeiss Software ZEN. Z-stack acquisition was performed with 27–44 μm thickness, with 44 images for each stack.

The cell densities of A549 and dTHP-1 were estimated by manually counting the number of cells per image and dividing with the image area. The densities were compared to the seeding densities, and the A549 to dTHP-1 ratio was also calculated. A549 analysis was performed on 6 samples with a total of 25 images (2–10 images/sample) within three independent experiments (n = 3). dTHP-1 analysis was performed on 4 samples with a total of 17 images (2–10 images/sample) within two independent experiments (n = 2), with seeding densities 0.82–1.67 $\times$ 10^5 cells/cm^2. EA.hy926 cells were not counted.

2.11. Statistical Analysis

Results are presented as mean with standard deviation (SD) of at least 3 independent experiments (n = 3) with 1–2 replica inserts unless otherwise stated. Statistical analysis of AB and comet assay results was performed by comparing the mean of each sample to the mean of negative control (inserts exposed to PBS), by one-way ANOVA with multiple comparisons and post-test Dunnet using GraphPad Prism version 9.3.1 for Windows, GraphPad Software, San Diego, CA, USA. Level of significance was set to $p < 0.05$.

3. Results

3.1. Characterization of the Advanced 3D Lung Model

The orthogonal confocal pictures of the triculture model (Figure 2) show A549 (Figure 2a,c–e) and EA.hy926 cells (Figure 2b) growing at opposite sides of a transwell transparent membrane inserts, with cell membranes in red stained with cell mask red and nuclei in blue stained with DAPI. The A549 and EA.hy926 cells were evenly distributed on the membranes; however, some spots with fewer cells were also observed. A549 had a density of about 3.8 $\times$ 10^5 cells/cm^2 (SD: 0.3 $\times$ 10^5 cells/cm^2, n = 3). The dTHP-1 cells were located on the apical side of the transwell insert (in green), on top of the A549 cells. The dTHP-1 cells had a variable density and morphology (Figure 2c–e). Approximately

30% of the dTHP-1 cells seemed to be necrotic or damaged with irregular structures, although this was highly variable between images and samples. The proportion of dTHP-1 cells adhering and remaining in the culture compared to the seeded number of cells was estimated to be 25–38% (n = 2) by microscopic evaluation. The ratio between A549 and dTHP-1 cells in the tricultures was estimated to be 8–39 A549 cells per dTHP-1 cell (n = 3).

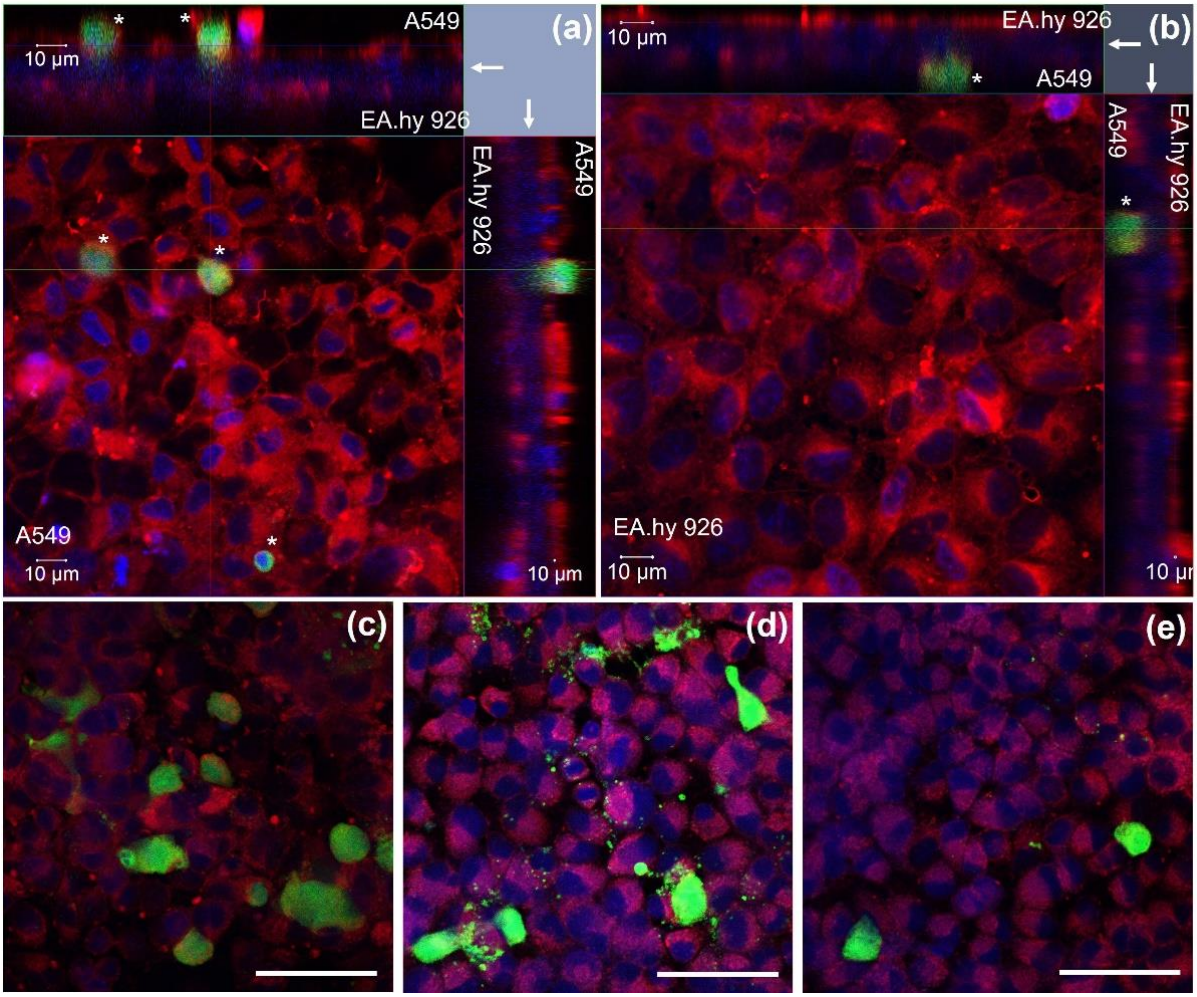

Figure 2. Triculture model investigated by confocal microscopy. (**a**,**b**) Z-stack image series (2D x-y view and respective side views) showing the distribution of A549, EA.hy926, and dTHP-1 (*, green) cells on the opposite sides of a transwell insert (arrow). (**a**) The 2D x-y view from the A549 and dTHP-1 side (z-stack thickness 44.5 µm). (**b**) The 2D x-y view from the EA.hy926 side (z-stack thickness 27.5 µm). (**c**–**e**) dTHP-1 cells in different morphologies on top of the A549 cells. Red: cellular membranes stained with Cell Mask red dye, blue: nuclei counterstained with DAPI, green: dTHP-1 cells stained with Cell tracker green dye. Magnification: 40×. Scale bar 10 µm (**a**,**b**) and 50 µm (**c**–**e**). dTHP-1: differentiated THP-1.

TEM analyses of tricultures showed cells compartmentalized in the apical and in the basolateral side of the insert with a 1 µm pore size (Figure 3a). EA.hy926 endothelial cells were localized at the bottom of the cell insert and the alveolar type II A549 cell on the upper side (Figure 3a). Cells that resemble the round morphology of THP-1 were seen on top of the epithelial A549 cells (Figure 3b), which were recognized by the presence of small microvilli (arrows) and lamellar bodies (LM). To further characterize the triculture lung model, dTHP-1 cells were stained with the mature macrophage marker CD11b (Figure 3c). The formation of tight junctions between A549 cells was visualized by labeling of ZO-1

protein in the cell membrane using LSM (Figure 3c). Distorted ZO-1 protein was found in the A549 cytoplasm (Figure 3c).

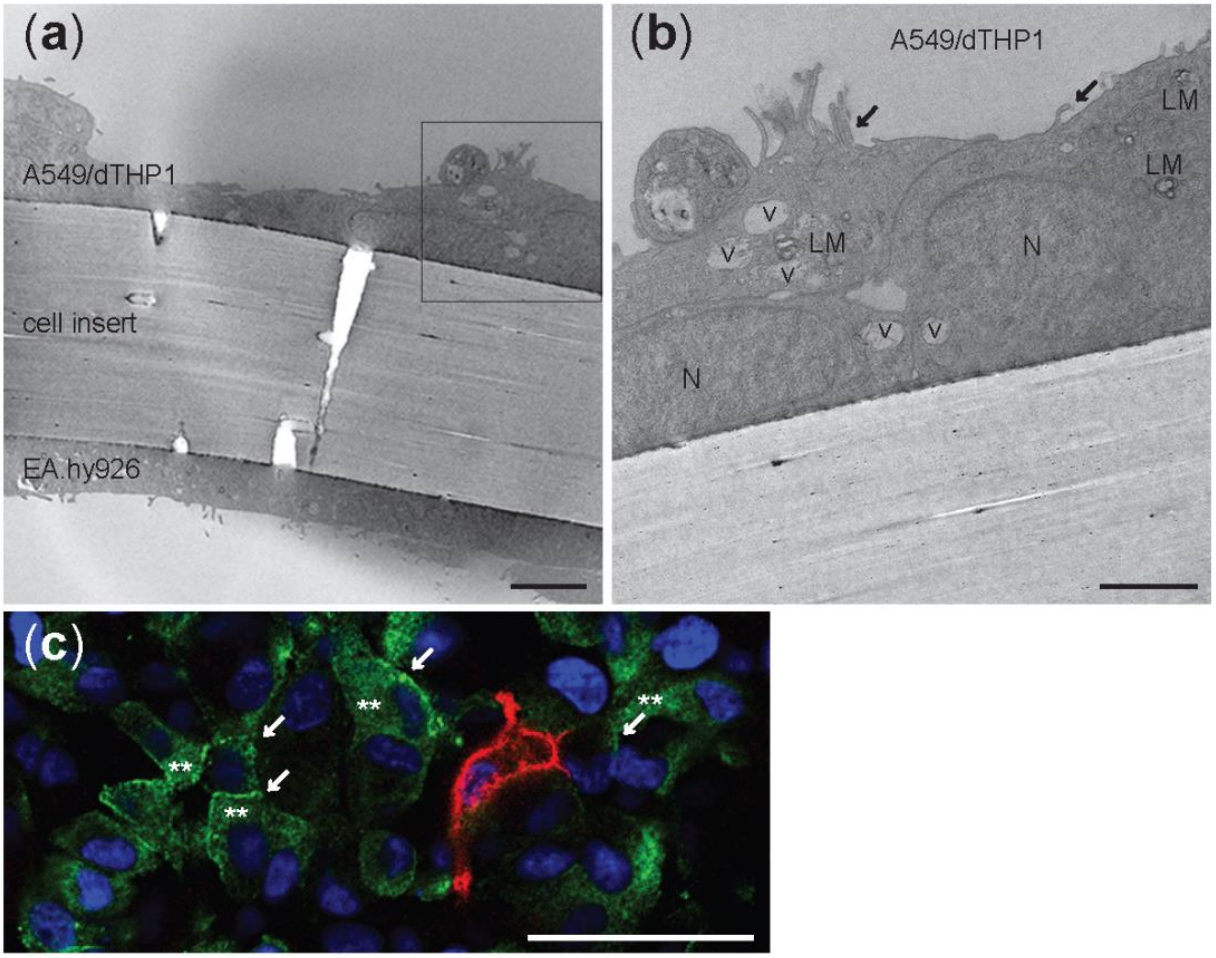

Figure 3. Transmission electron microscopy micrographs (**a**,**b**) and confocal picture © of unexposed triculture with A549 and dTHP-1 cells at the apical side and EA.hy926 cells at the basolateral side of a cell insert with 1 μm pore size membrane. LM: lamellar bodies; v: vesicles; N: nuclei; black arrows: microvilli. (**a**) Scale bar: 5 μm. (**b**) Scale bar: 1 μm. (**c**) Confocal image of the apical side. A549 were stained with ZO-1 antibody (green) and differentiated THP-1 with CD11b (red). White arrows: tight junctions. **: cytoplasmic ZO-1. Nuclei are stained in blue (DAPI). Scale bar: 50 μm; Magnification: 40×.

3.2. Characterization of AgNM-300K

The stock dispersions were characterized by Ag content (total and <3 kDa fraction), endotoxin content, hydrodynamic diameter, and zeta potential (Table S5 and S1.2). The concentration of Ag in the stock dispersion was measured by ICP-MS to be 7.2 mg/mL ± 0.9 mg/mL (n = 7), which was lower than the expected nominal concentration of 10 mg/mL. A small amount of Ag (1.9 ng/mL ± 1.3 ng/mL, n = 3) was measured also in the dispersant control (NM-300K DIS). The amount of dissolved Ag in the dispersion, defined as <3 kDa fraction, was measured to be about 3.6% (n = 2). The NM-300K and NM-300K DIS stock dispersions were confirmed to be endotoxin-free by both HEK293 and LAL assays, being <1 EU/mL and <0.1 EU/mL, respectively (S1.2 and Figure S1).

The hydrodynamic diameter of NM-300K, measured by DLS, was found to be polydisperse with a Z-ave of 130.7 nm ± 23.2 nm with PDI of 0.380 ± 0.037 measured at Lab 1, and a Z-ave of 57.5 nm ± 5.7 nm with PDI of 0.343 ± 0.067 measured at Lab 2 (Table S5).

The hydrodynamic size of the NMs measured by Lab 1 was in general higher than at Lab 2, while the PDI was nearly the same in the dispersions from both laboratories, indicating a moderately polydisperse distribution type. The dispersions showed 2–3 peaks, where about 95% of the particles (by intensity) were in the peak of 202 nm ± 39 nm (Lab 1) or 89 nm ± 13 nm (Lab 2). The other peaks, with less intensity, were similar between both laboratories with NM diameters measured to be 5–18 nm and 1600–4600 nm, the latter peak indicating some aggregation (Table S6). The dispersions had a ZP of −17.1 ± 2.8 mV, indicating the high stability of Ag NMs in the stock dispersions (Table S5).

The size distribution of the diluted dispersion applied for cloud exposure was confirmed to be similar to the stock dispersion (Table S6). The hydrodynamic diameter of the Ag NMs was measured in other buffer solutions and was found to be similar in all solutions (Table S7).

3.3. Deposition of Fluorescein and Ag in the Cloud System and Permeation through the Cell Barrier

Mean deposition efficiency of fluorescein reaching the surface of the cells after exposure in the VITROCELL® cloud system was very consistent between the labs and calculated to 53.0% (±2.2% SD) at Lab 1 and 52.9% (±1.5% SD) at Lab 2.

The amount of Ag NMs deposited on cell culture inserts was measured by ICP-MS analysis to be 0.83 μg/cm^2 and 6.02 μg/cm^2, for low and high concentration, which is lower than the respective nominal concentrations 1 and 10 μg/cm^2 (Table 1). Compared to the applied concentration, this results in a deposition efficiency of Ag of 41–56%. No Ag was detected in the blank samples (culture insert membrane without deposition).

Table 1. Deposition and permeation of Ag in mono- and cocultures exposed to an aerosol of NM-300K. Control was exposed to NM-300K DIS. Results are presented as mean with SD. Deposition was measured in 2 or 4 independent experiments with 2–3 replica inserts in each experiment. Permeation was measured in 2–3 independent experiments, each with 1–2 replica inserts. Maximum permeation of NM-300K at high concentration through empty inserts was 7% (11 μM, *n* = 2). * Control was insert membranes without Ag deposition. LOD, limit of detection; SD, standard deviation.

	Unit	Solvent Control	Low Concentration	High Concentration
Nominal deposited concentration	μg/cm^2	0	1	10
Measured deposited concentration	μg/cm^2	<LOD *	0.83 ± 0.05 (*n* = 2)	6.02 ± 0.84 (*n* = 4)
Deposition efficiency	% of nebulized	-	56 (*n* = 2)	41 (*n* = 4)
Permeation of Ag through monoculture cell model	μM (% of deposited)	0.069 ± 0.025 (*n* = 2)	1.9 ± 0.56 (*n* = 2) (8%)	14.5 ± 1.4 (*n* = 3) (9%)
Permeation of Ag through coculture cell model	μM (% of deposited)	0.030 ± 0.017 (*n* = 2)	3.3 ± 0.5 (*n* = 2) (14%)	15.4 ± 1.2 (*n* = 2) (9%)

After 24 h exposure of mono- and cocultures, a substantial amount of Ag was found on the basolateral side of the membrane, showing a permeation of Ag through the cell layers. For monocultures, the permeation was about 8% for the lower and 9% for the highest concentration of Ag NMs, corresponding to around 2 and 15 μM Ag in the basolateral media, respectively. For cocultures, the permeation was similar to monocultures for the highest concentration, but enhanced to about 14%, corresponding to 3 μM, for the lowest concentration. The maximum permeation of Ag through empty inserts without cells was estimated to be 11 μM or 7% of the high concentration, under the experimental conditions, which is at similar levels as for the mono- and coculture cell models. However, a very small amount of Ag (<0.1 μM) was in some experiments found also in the basolateral media of solvent control cells exposed to NM-300K DIS (dispersion media).

Permeation of fluorescein was in addition, measured in the coculture of A549 and EA.hy926 showing that approximately 18% of the deposited fluorescein passed through the cell barrier and was recovered on the basolateral side of the membrane separating the two cell lines in the coculture model (Figure 4). No significant differences between the treatments were observed.

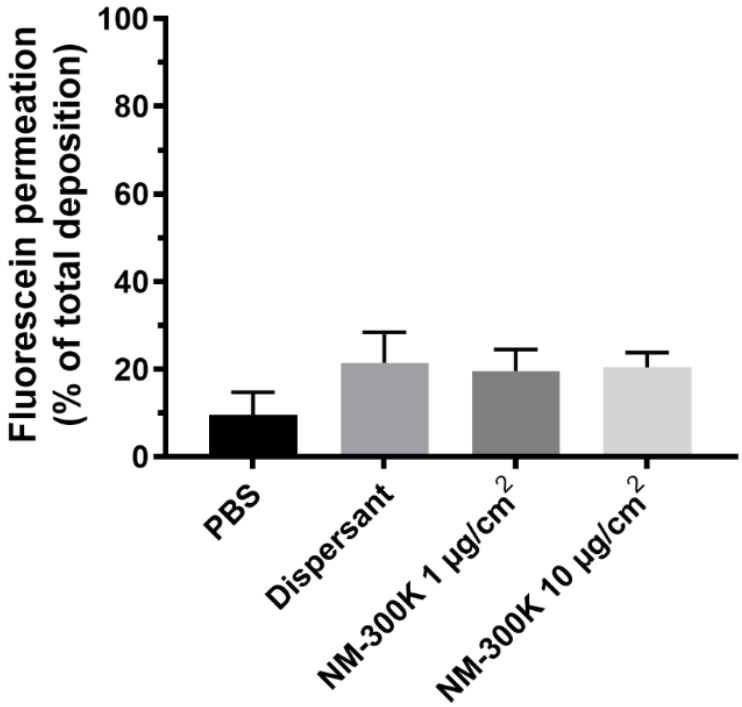

Figure 4. Permeation of fluorescein through the cellular layers. Shown is mean recovery of fluorescein ± SD in the basolateral compartment relative to the total deposition of fluorescein at the apical side of the membrane after exposure of cocultures in the cloud system to phosphate buffered saline (PBS), dispersant NM-300K DIS, or NM-300K at 1 or 10 µg/cm^2. The results are based on 4 technical replicates in $n = 3$ independent experiments. No statistically significant difference was seen between PBS treatment and the other samples, analyzed by ordinary one-way ANOVA with multiple comparisons, post-test Dunnett's, $p > 0.05$. SD: standard deviation.

3.4. Cell Viability

The cell viability of mono-, co-, and tricultures was measured at 20–24 h after NM-300K exposure using AB assay. The cell viability is presented relative to unexposed incubator control (NC), set to 100%. NM-300K exposure at the highest concentration significantly reduced cell viability in the monocultures compared to the PBS exposure control (Table 2 and Figure 5). A nonstatistical reduction in cell viability was seen in both the apical and basolateral cells in co- and tricultures after exposure to NM-300K at the highest concentration, and in Lab 2 also for the low concentration in tricultures, compared to the PBS exposed control. PBS exposure slightly reduced the viability of the apical cells in co- and tricultures in both labs; however, the effect was statistically significant only for tricultures in Lab 1. Cell viability after NM-300K DIS exposure was similar to in the PBS-exposed cells. No interference between NM-300K and read-out of the AB assay was found in cell-free inserts with NM-300K and AB solution (results not shown).

Table 2. Cell viability (%) relative to incubator control (set to 100%) measured by the AlamarBlue assay after exposure of monocultures, cocultures, and tricultures of A549, EA.hy926, and dTHP-1 cells to NM-300K (1 and 10 μg/cm^2) or control solutions (PBS, dispersant (NM-300K DIS)) at the air–liquid interface (ALI). Results are presented as mean with standard deviation from a total of n = 6–9 (Lab 1), n = 3 (Lab 2) for monocultures, for cocultures n = 4–5 (Lab 1), n = 3 (Lab 2), and for tricultures n = 4 independent experiments with each 1–2 replica cell culture inserts, corresponding to results in Figure 5. Statistically significant differences compared to PBS or NC incubator controls were analyzed by one-way ANOVA with multiple comparisons post-test Dunnett's and are indicated by [a] $p < 0.5$ compared to PBS, and [b] $p < 0.05$ compared to NC. NC: negative control, PBS: phosphate buffered saline, dTHP-1: differentiated THP-1 cells.

		Relative Cell Viability (%)					
		Monoculture		Coculture		Triculture	
Cells	Treatment	Lab 1	Lab 2	Lab 1	Lab 2	Lab 1	Lab 2
A549/ A549- dTHP-1	NC	100 ± 0	100 ± 0	100 ± 0	100 ± 0	100 ± 0 [a]	100 ± 0
	PBS	93 ± 23	93 ± 26	62 ± 22	77 ± 15	68 ± 12 [b]	85 ± 26
	Dispersant	82 ± 17	81 ± 28	74 ± 25	80 ± 8	56 ± 17 [b]	87 ± 24
	Ag 1 μg/cm^2	73 ± 13 [b]	81 ± 18	58 ± 20 [b]	75 ± 21	67 ± 19 [b]	74 ± 26
	Ag 10 μg/cm^2	59 ± 26 [ab]	25 ± 8 [ab]	59 ± 29 [b]	51 ± 28 [b]	51 ± 19 [b]	66 ± 23
EA.hy926	NC			100 ± 0	100 ± 0	100 ± 0	100 ± 0
	PBS			69 ± 19	93 ± 52	86 ± 15	108 ± 8
	Dispersant			71 ± 21	94 ± 9	78 ± 15	96 ± 21
	Ag 1 μg/cm^2			67 ± 21 [b]	92 ± 16	94 ± 21	101 ± 10
	Ag 10 μg/cm^2			68 ± 21 [b]	70 ± 41	66 ± 18	90 ± 18

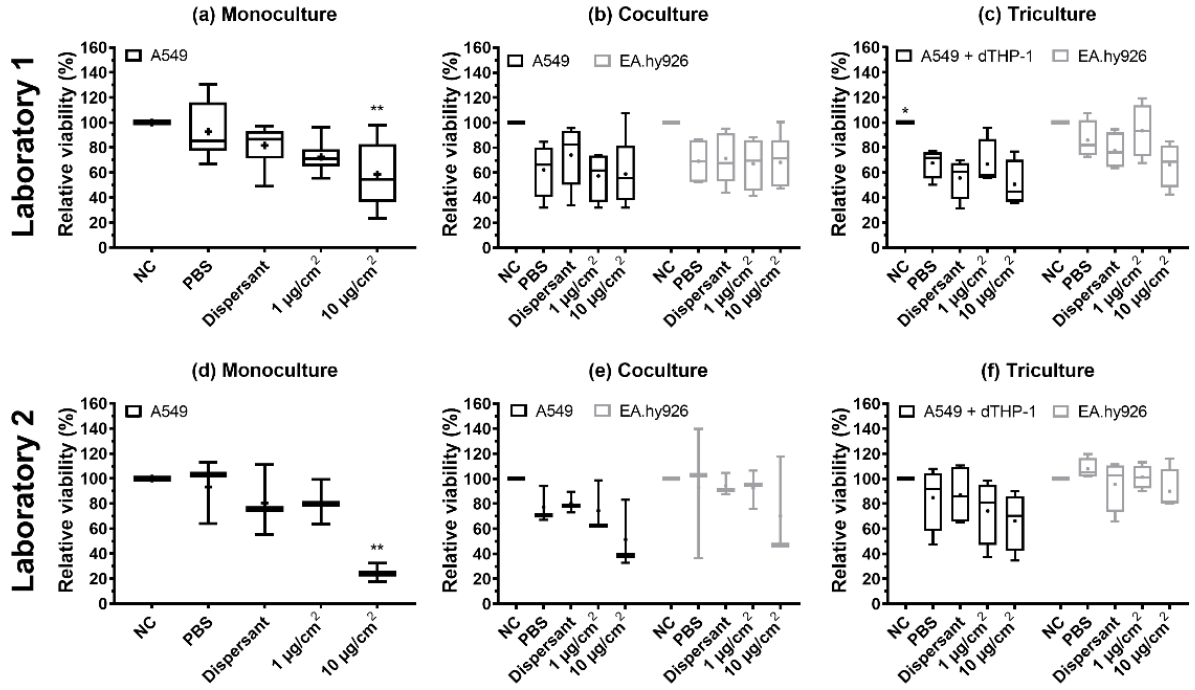

Figure 5. Relative viability measured by the AlamarBlue assay after exposure of monocultures (**a**,**d**), cocultures (**b**,**e**), and tricultures (**c**,**f**) of A549, EA.hy926, and dTHP-1 cells to NM-300K and control solutions at the air–liquid interface (ALI). Experiments were performed at Lab 1 (**a**–**c**) and Lab 2 (**d**–**f**)

for comparison. A reduction in viability was seen after exposure to control solutions and NM-300K at ALI. Results are normalized against negative incubator control (NC, set to 100%) and presented as boxplots with mean (+), median/50th percentile (line), 25th and 75th percentiles (box), and minimum and maximum values (whiskers). A total of (**a**) n = 6–9, (**b**) n = 4–5, (**c**) n = 4, (**d**,**e**) n = 3, and (**f**) n = 4 independent experiments with each 1–2 replica cell culture inserts were performed. Statistically significant differences compared to PBS control were analyzed by ordinary one-way ANOVA with multiple comparisons post-test Dunnett´s, and are indicated by * $p < 0.5$, ** $p < 0.1$. NC: negative control (incubator control), PBS: phosphate buffered saline, dispersant: NM-300K dispersion medium (NM-300K DIS); dTHP-1, differentiated THP-1 cells.

The effect on cell viability of different buffer solutions, PBS, PBS added $CaCl_2/MgCl_2$ (PBS+), HBSS, HBSS added $CaCl_2/MgCl_2$ (HBSS+), and DMEM cell culture medium, was investigated by exposure to cocultures of A549 and EA.hy926 at the ALI. The viability of the A549 cells was reduced compared to the incubator control, NC, for all buffer solutions tested (Figure S2). The viability of EA.hy926 cells was also reduced after exposure to the buffers, but to a lower extent than for the A549 cells. The A549 cells had the highest relative viability after exposure to PBS and HBSS+, while the EA.hy926 had the highest relative viability after exposure to HBSS and HBSS+. No statistically significant differences were found in the relative viability of cultures exposed to PBS compared to the other buffers.

3.5. Genotoxicity (DNA Strand Breaks and Oxidized Base Lesions)

DNA SBs and oxidized base lesions (SBs + Fpg) were measured by the enzyme-modified version of the comet assay. NM-300K induced a statistically significant increase in SBs and SBs + Fpg, measured as % DNA intensity in the tail, in the EA.hy926 cells in the cocultures at the highest concentration (with 80% DNA in tail, $p < 0.001$), compared to the two negative controls (NC, PBS). However, a slight, non-significant increase in both SBs and SBs + Fpg was seen in all models after NM-300K exposure (Figure 6). The effect of dispersant media NM-300K DIS was similar to NC (not shown). A rather high background level of damage was seen in the controls in the cocultures (NC, PBS, dispersant). The positive control for DNA SBs, H_2O_2, gave the expected response based on historical control (>80% SBs) (not shown). No interference between NM-300K and the performance of the comet assay was seen (results not shown).

3.6. Cellular Uptake of NM-300K

Uptake and intracellular localization of NM-300K was investigated by confocal microscopy and TEM after exposure to the ALI. The apical side of tricultures was investigated by confocal microscopy in unexposed cultures (Figure 7a) and after exposure to NM-300K at 10 $\mu g/cm^2$ (Figure 7b,c). A549 cells were in higher number in the control culture (Figure 7a), and they all seemed to express pro-surfactant protein C. Rather few stained dTHP-1 cells were found. In the Ag-exposed cultures (Figure 7b), A549 cells appeared to be damaged and dTHP-1 cells highly expressed CD11b and had the appearance of activated macrophages. The phase contrast image in combination with fluorescent markers shows NMs agglomerates or aggregates in contact with A549 and dTHP-1 cells, and likely a macrophage engulfing NM-300K in the cytoplasm (Figure 7c).

Electron micrographs of the apical side of triculture are shown in Figure 8. In the cytoplasm of alveolar type II cells A549, vesicles specialized in the production of cell surfactant, called lamellar bodies (LMs), were recognized. Strong electron dense LMs and multivesicular bodies (MVB) [49] were identified in the A549 cells exposed to NM-300K, but not in unexposed tricultures (Figure 8). NM-300K appeared to be localized inside of LMs vesicles as single particles (5–20 nm) or in a small aggregate of about 100 nm (Figure 8d). No NM-300K particles were found in the endothelial cells (data not shown).

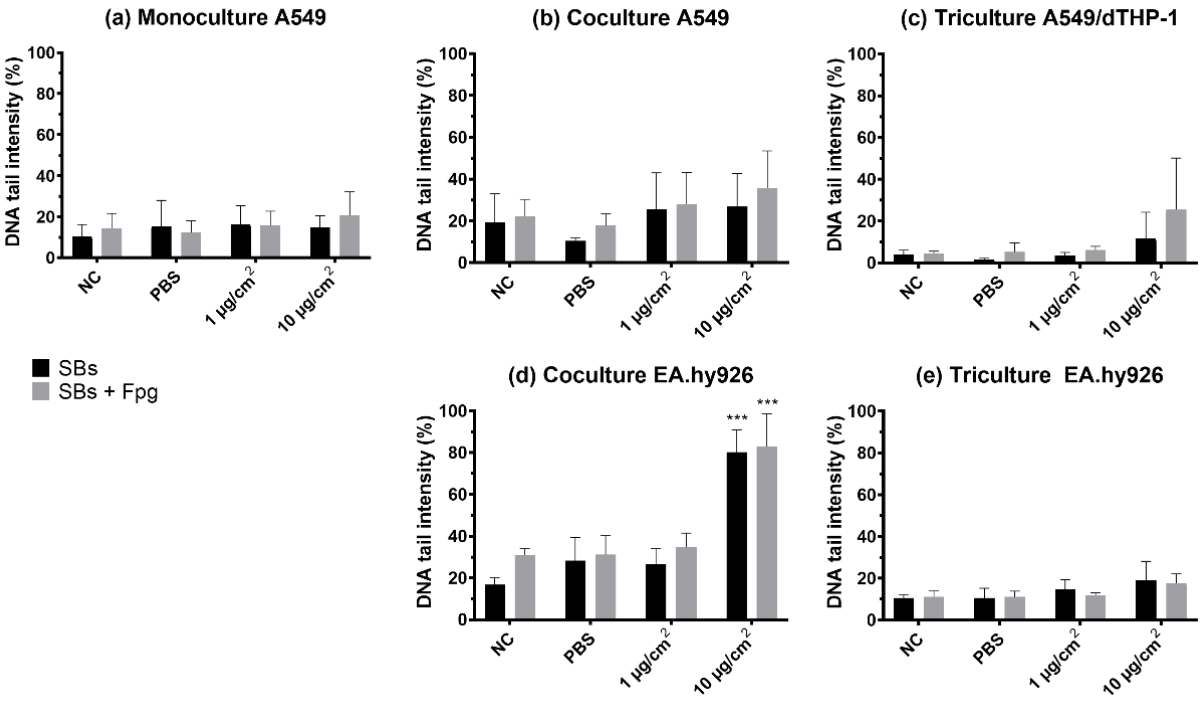

Figure 6. DNA strand breaks and oxidized DNA lesions, measured as DNA tail intensity, by the comet assay with Fpg in cells exposed at the air–liquid interface (ALI) to NM-300K. Cells were cultured as (**a**) monocultures, (**b**,**d**) cocultures, and (**c**,**e**) tricultures. Results are presented as mean of median ± SD of (**a**) n = 3–5, (**b**–**e**) n = 3 independent experiments. From each experiment, the median DNA tail intensity (%) was calculated from 50 cells per 2–6 gels from 1–2 cell culture inserts. Significantly different effects on DNA damage compared to PBS control were analyzed by ordinary one-way ANOVA followed by Dunnett's post-hoc test (*** $p < 0.001$). SBs: strand breaks, NC: negative control, PBS: phosphate buffered saline, SD: standard deviation.

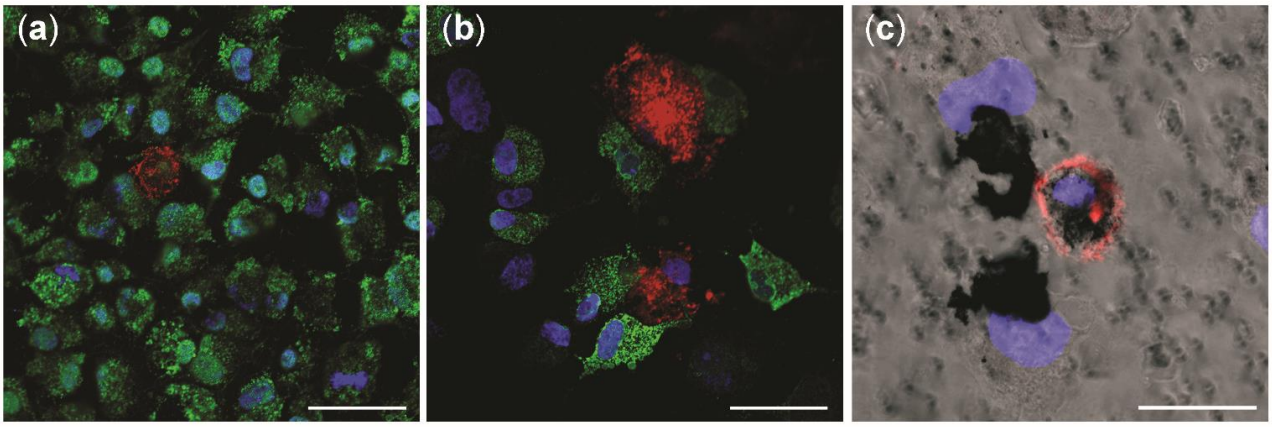

Figure 7. Confocal microscopy investigation of tricultures with and without NM-300K exposure. Confocal pictures show the apical side of triculture model in (**a**) negative incubator control, and (**b**,**c**) after exposure to NM-300K at 10 µg/cm^2. A549 cells were stained with pro-surfactant protein C (green) and dTHP-1 are marked with CD11b (red). DNA is stained with DAPI (blue). (**c**) Phase contrast picture combined with immunofluorescence staining. (**a**–**c**) Magnification: 40×. Scale bar: 50 µm (**a**,**b**); 20 µm (**c**).

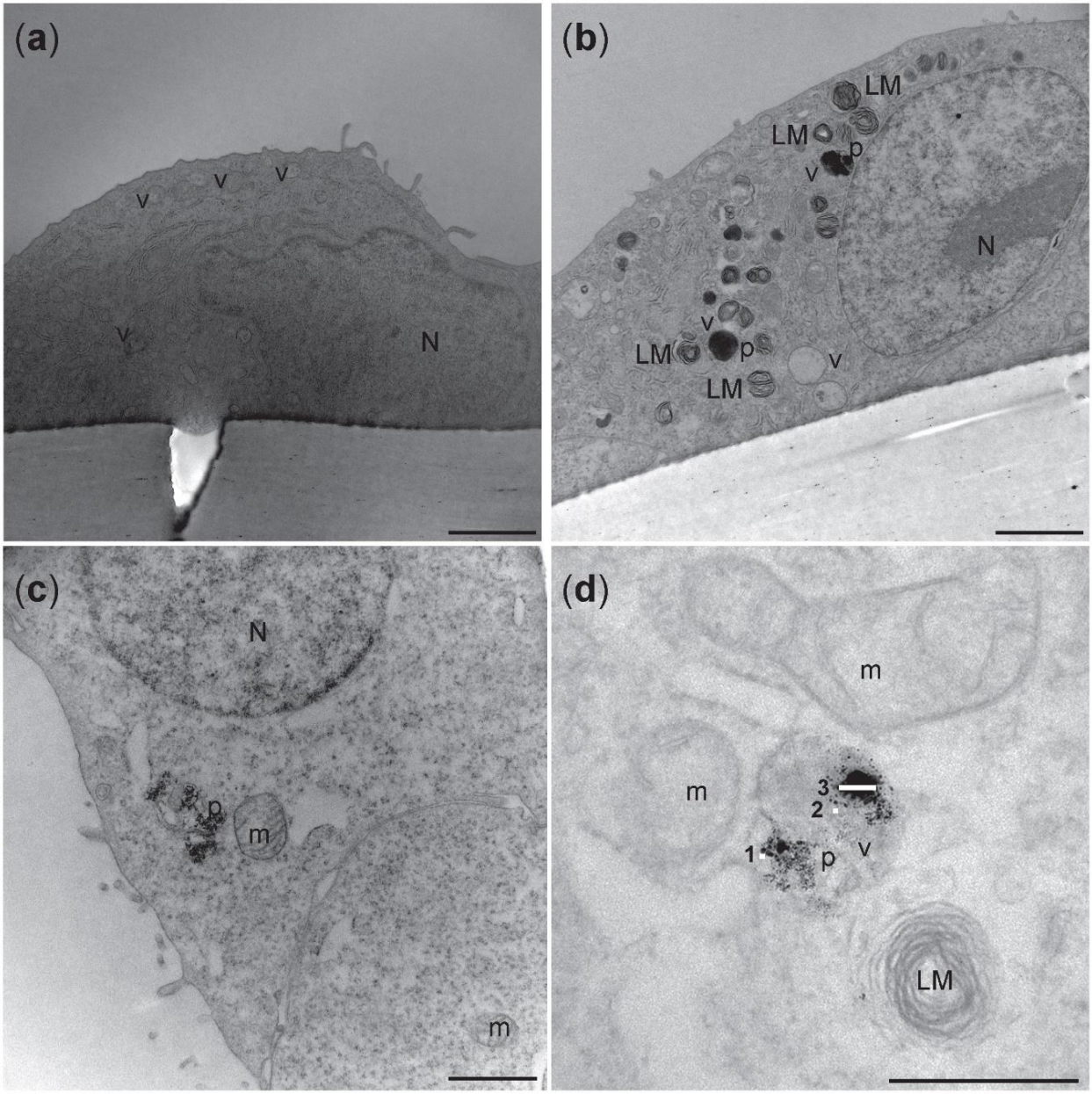

Figure 8. Representative transmission electron micrographs of A549 cells on the apical side of the triculture model. (**a**) Unexposed cells from incubator control (NC) showed no electron dense vacuoles. (**b**) Electron dense vacuoles-like structure and lamellar bodies were seen in cells exposed to NM-300K 10 μg/cm^2. (**c**,**d**) Higher magnification of the cells exposed to NM-300K 10 μg/cm^2 showed that NM-300K were found in the cell cytoplasm (**c**) or inside of a vacuole (**d**). (**d**) NM-300K were found as single particles (5–20 nm) (1,2) or in small aggregate of 100 nm (3). Scalebar: 2 μm (**a**,**b**); 1 μm (**c**); 500 nm (**d**). N: nucleus, LM: lamellar bodies, v: vacuoles-like structure, p: NM-300K nanoparticles, m: mitochondria.

4. Discussion

This study aimed at testing the robustness and sensitivity, characterizing, and optimizing an advanced respiratory model built on human alveolar epithelial A549 cells and evaluating its response to aerosol exposure of silver NM-300K. In more detail, we compared the responses of A549 cells cultured at the ALI in monoculture, in coculture with EA.hy926

cells, and in triculture with EA.hy926 cells and dTHP-1, and performed an interlaboratory trial across two laboratories.

The A549 cell line is an alveolar epithelial type II cell line derived from the human lung adenocarcinoma [29]. This is currently the best characterized and used model of alveolar epithelia in in vitro studies [24,50,51]. A549 cells can partly mimic the property of the alveolar epithelium and are suitable to be used at ALI and in the VITROCELL® exposure system. These cells are of alveolar origin, in contrast to alternative bronchial cell lines such as BEAS-2B, HBEC, and Calu-3.

In the alveolus, the epithelium is in close contact with the capillary endothelium. Endothelial cells are considered a secondary target for inhaled NMs, such as diesel exhaust particulate matters [52,53], and endothelial cell dysfunction is central in adverse cardiovascular disorders, including atherosclerosis, myocardial infarction, and stroke [54]. We used the lung adenocarcinoma-derived endothelial EA.hy926 cells [55,56], as they are closer to the air–blood barrier in vivo situation and thus more relevant than alternative cell lines such as HMEC-1 and hTERT-HDMEC [57–59].

Lung macrophages are, along with alveolar epithelial cells, the first line of defense against inhaled particles. They can express a wide range of pro- and anti-inflammatory cytokines and play a role in cellular uptake and internalization of particles [60,61]. We saw, by confocal microscopy, the presence of NM-300K inside dTHP-1 cells, which are commonly used macrophage cells [62,63] that are easy to cultivate and commonly used in ALI models [25,26,64–66]. In the alveolar model proposed by Klein et al. [25,52], the cell ratio between A549 and dTHP-1 does not correspond to the in situ situation where the number of macrophages is ten times less than alveolar epithelial cells [67]. We used an initial ratio of 2–4x A549/dTHP-1 cells (when at confluency), as some cells were removed during the medium removal or damaged during the detaching procedure before the seeding. Thus, the actual ratio of dTHP-1: A549 was much lower. The morphology of dTHP-1 cells was in our triculture model found to be variable and some of the cells seemed to be damaged or necrotic. The differential viability of the dTHP-1 cells in the tricultures can also be related to the culture conditions where dTHP-1 and A549 cells were sharing the same space, as well as the cell culture media composition in the tricultures, consisting of a mix of culture media optimized for each of the cell lines.

Confocal and electron microscopy confirmed that the presence and localization of all the cell types in the tricultures, with A549 and dTHP-1 cells in the apical compartment and EA.hy926 in the basolateral side of the cell culture insert. A549 and EA.hy926 cells were confluent, although some small holes or less cell dense areas could be observed, which may lead to the increased permeation of substances as shown by the permeation of fluorescein to the basolateral side of the cocultures (Figure 4). Tight junctions between the cells were seen. After 4 days in the culture, tight junction proteins were found to a large extent in the cytoplasm and to some extent in the plasma membrane of A549 cells in the triculture model. Enhanced barrier function can be obtained by extending the culturing period, as A549 cells in monocultures were expressing transcript of ZO-1 protein after two weeks at ALI [68–70]. Previous work by Rothen-Rutishauser et al. showed that epithelial alveolar cells formed adherent junctions and peripheral tight junctions at day 7 in culture [62,69–71].

When cultured in the incubator, our mono-, co-, and tricultures were moist and covered with a shiny film (results not shown). This was likely surfactant produced by the A549 cells, that were found to express surfactant proteins such as surfactant protein C [22,25,68]. Both barrier function and surfactant production may be related to cell batch, and this can influence the results, sensitivity, and reproducibility of the data obtained with the model [72,73].

Mimicking inhalation exposure in in vitro models is challenging, and the characterization of both the cell culture model and exposure system is necessary. Most of the in vitro inhalation studies have been conducted with cells in submerged conditions, which is not reflecting the air–blood barrier in the lungs. Further, the cell medium can influence the properties of the NMs and thereby give a non-realistic judgment regarding the

hazardous potential of NMs and other compounds. Enhanced predictiveness for human effects after inhalation exposure is likely to be obtained with cells cultivated at the ALI, and multicellular models are better mirroring organ-like structures. Thus, to compare sensitivity to NM exposure when adding complexity to the ALI model, mono-, co-, and tricultures were exposed in the VITROCELL® system, where the NM suspension or control solution is nebulized to generate an aerosol which over a few minutes deposits onto the cells. The deposited concentrations of Ag in the VITROCELL® system were found to be 0.8 μg/cm^2 and 6.0 μg/cm^2, which was lower than expected. We measured by ICP-MS an Ag content of the stock concentration of NM-300K at 7.2 mg/mL, which was lower than the nominal concentration at 10 mg/mL The presence of 3.6% dissolved species in the stock dispersion was as expected [36,38,74] and the very low concentration of Ag (1.8 ng/mL) found in the dispersion media was likely caused by contamination during preparation/sonication. The deposition of Ag was measured only at Lab 1; however, as the deposition efficiency of Ag was like that of fluorescein, and the same protocols were used, it is likely that the results would be similar in both laboratories. Quartz crystal microbalance (QCM) has been reported as a precise and sensitive device for quasi-real-time NM dosimetry for the VITROCELL® system [39]. We experienced high inter-experimental variations with the QCM (results not shown) and thus used other methods for the determination of NM deposition. The uptake of NM-300K after aerosol exposure was shown in both A549 and dTHP-1 cells on the apical side. It has been demonstrated that alveolar type II cells can internalize NMs [4]. Ag NMs also appeared inside of dTHP-1 cells, recognizable by the absence of lamellar bodies (LMs). The internalization of silver nanoparticles in A549 and THP1 cells has previously been shown in several investigations [75,76]. LMs are typical of the epithelial alveolar type II cells, and the electron micrographs showed the presence of LMs in A549 cells. Several studies reported an altered quantity of LMs in A549 cells after NMs exposure [60,77,78]. Ag-NMs were internalized in dTHP-1 cells as single particles, and as agglomerates up to 100 nm size (Figure 8d). By confocal microscopy analysis, dTHP-1 cells appeared to have a phagosome-like morphology typical of activated macrophages [79]. Moreover, we observed that the dTHP-1 cells exposed to the highest NM concentration phagocytosed particles which were visible inside of their cytoplasm.

NM-300K was chosen as the test substance for characterization of the different models due to known cytotoxic properties [33,35], and the NM-300K stock dispersion was found to be endotoxin-free, measured by both LAL and HEK293 assays. The large surface area and other surface properties of NMs make them susceptible to endotoxin contamination during the synthesis process. Endotoxin contamination may bias the results of toxicity testing by false positive or negative results if not controlled for [80].

The cellular viability of the lung cells was affected by NM-300K exposure, but also by buffer exposure. Viability was reduced after NM-300K exposure at the highest concentration in monoculture ($p < 0.01$), while in cocultures and tricultures no significant decrease in cell viability was observed. The effect on viability caused by NM-300K was strongest at Lab 2, which may be related to the measured smaller diameter of the NMs used for exposure of the cells. The NM sizes were relatively constant for all dispersions within each laboratory, both measured in stock dispersion and in stock dispersion diluted in physiological buffers. All dispersions showed, by DLS measurements, multiple peaks for the size distribution of the NMs in the dispersion, but the dispersed NMs prepared at Lab 1 were larger than those prepared at Lab 2. To test if the difference in size was related to the two different DLS instruments, three dispersions prepared at Lab 1 were tested in both laboratories, but no significant differences were found (results not shown). This points to the importance of measuring the size, size distribution, and stability of all dispersions used for exposure of cells and toxicity measurements, as the toxic effect is strongly dependent upon physicochemical properties, such as size, of the NMs. In the AB results from both laboratories, we saw higher inter-experimental variation compared to studies with A549 cells in submerged conditions [35,73], which may be related to the complexity of the ALI cultures and the experimental conditions. However, the effect seen on the viability of

A549 monocultures after NM-300K exposure at the highest concentration was similar to submerged experiments with A549 [35].

The monocultures were more sensitive to the induction of cytotoxicity by NM-300K compared with the more complex models. However, the control exposure with PBS and HBSS with and without $CaCl_2$ and $MgCl_2$ reduced the viability of the apical cells in both co- and tricultures, but not in monocultures. This effect was strongest in Lab 1. The high sensitivity of the co- and tricultures to aerosol exposure in general needs to be investigated further. The effects of PBS exposure on the cell viability of the A549 cells could be influenced by less contact with the basolateral media due to the introduction of EA.hy926 cells. High confluency of the EA.hy926 cells would limit more strongly the access of the A549 cells to the basolateral media and constitute an important factor to be aware of for the preparation of the most optimal ALI model. The use of PBS diluted in water (1:10) can be an option to improve the viability of the cells in the negative control (Figure S2), as this will reduce the salts deposited on top of the cells when the water evaporates, while still making a dense aerosol [26]. The choice of solvent will also depend on the solubility of the test particles. Exposure to PBS did not induce an increase in DNA damage; however, the highest concentration of NM-300K induced DNA SBs in EA.hy926 cells in cocultures. In tricultures, no effect of NM-300K was seen on DNA damage in EA.hy926 cells. This might be linked to the potential uptake of NMs by the dTHP-1 cells as previously shown [75,81] making the material less available for cell exposure. One can even speculate if the exposed THP1 cells trigger an inflammatory reaction that can promote DNA repair [82]. The cocultures also had a slightly higher background level of DNA damage compared with mono- and tricultures.

The effect seen on the EA.hy926 cells in cocultures can be caused by signals from the apical side or from the permeation of Ag ions or Ag particles through the cell culture barrier into the basolateral side. In the coculture model, around 3 μM and 15 μM Ag for the lower and higher concentration, respectively, was measured in the basolateral medium after exposure, and it is unknown if this was in form of Ag NMs or dissolved species. Reduced viability and increased DNA damage have previously been reported after exposure to Ag NMs in standard submerged cell cultures [83–86] at concentrations in the same range as the dissolved Ag we detected. The permeation of Ag was lower than that of fluorescein in the cocultures of A549 and EA.hy926 cells, which was expected as fluorescein is a water-soluble molecule. Permeation of Ag NMs or dissolved species into the basolateral medium is more likely to be limited by cell adhesion/uptake or protein binding on cells on either side of the membrane, as Ag has low solubility in physiological medium and high affinity to thiol groups [87–89]. The maximum permeation of Ag through empty inserts without cells was estimated to be around 20%, showing that a substantial amount of the Ag (NMs or dissolved species) was remaining in the apical side or in the insert pores.

Interference between the tested NM and the assay is commonly seen with metallic NMs. No interference was found between NM-300K and the AB and comet assays (results not shown). In contrast, interference of NM-300K with the lactate dehydrogenase (LDH) assay was found after analysis of the basolateral medium of the exposed ALI cultures (results not shown), in line with previously reported data [26,90].

5. Conclusions

The advanced 3D lung model with aerosol exposure at the ALI in the VITROCELL® Cloud chamber was shown to be a promising in vitro model for hazard identification and characterization of NMs in relation to inhalation exposure. Thus, this work is supporting the ongoing effort to implement NAMs and advanced in vitro methods for regulatory purposes and to replace animal studies, in compliance with the 3Rs. This respiratory model was shown to be compatible with different endpoints—cytotoxicity by the AlamarBlue assay and genotoxicity by the enzyme-modified version of the comet assay. NM-300K at the highest concentration tested was shown to be cytotoxic in the monocultures, and induced DNA strand breaks and oxidized base lesions in the EA.hy926 cells in cocultures. No interference of NM-300K with the AlamarBlue and comet assay was detected; however,

interference was detected for the LDH assay. Ag NMs were found to be taken up by the A549 and THP-1 cells, and the deposition efficiency of Ag was measured by ICP-MS to be 41–56%, which is comparable to the deposition efficiency of fluorescein (53%). A549 cells were found to express surfactant protein, as well as tight junctions. However, the barrier was not complete, as Ag was found in the basolateral medium, at a comparable level for both mono- and cocultures, and fluorescein in a substantial amount in the cocultures. Adding complexity to the model, going from monocultures of lung epithelial cells to cocultures with endothelial cells or tricultures by further adding immune cells, changed the sensitivity for exposure to both NM-300K and PBS. This points to the importance of the development and characterization of advanced multicellular in vitro models when moving from monolayer cultures of human cells into 3D and from one type of cell into advanced culture containing several cell types relevant to the organ of interest, as sensitivity and effects can change. There will always be a question about which is the best model to predict human effects. The application of human cells is considered to be advantageous, and advanced 3D models, which are closer to tissue and organ structure, should be more reliable for toxicity testing in vitro for human hazard assessment. More complex models are more challenging to work with and will introduce more variation in the data, as expected and shown by our inter-laboratory comparison study. Thus, detailed and optimized protocols are important to increase reproducibility and robustness. For NGRA, models that are well tested, robust, characterized, and standardized for validation are needed. We, therefore, performed an interlaboratory trial across two labs to characterize the advanced models, test their robustness, and optimize the protocol, and showed that adding realistic complexity by including several cell types changed the outcome of the toxicity testing.

Supplementary Materials: The following supporting information can be downloaded at: https://www.mdpi.com/article/10.3390/nano12152609/s1, Figure S1: HEK293 test; Figure S2: Relative viability of cocultures after buffer exposure; Table S1: Cell types and cell media with supplements used for mono-, co-, and tricultures; Table S2: Passage numbers; Table S3: Cell seeding densities; Table S4: Antibodies and staining for confocal microscopy; Table S5: Characterization of NM-300K dispersions; Table S6: Size distribution of NM-300K diluted 1:100 in ultrapure H_2O; Table S7: Size distribution of NM-300K diluted 1:100–1:10 in PBS; Table S8: Characterization of hydrodynamic diameter by DLS of NM-300K in different buffers.

Author Contributions: Preparation of first draft: L.M.A.C. and E.E. (equal contribution); data analysis and figure preparation: L.M.A.C. and E.E. (equal contribution), E.M., E.M.L. and E.R.-P.; experimental work: L.M.A.C., E.E., E.M. and E.M.L.; manuscript revision: L.M.A.C., E.E., E.M., E.M.L., M.D., S.Z.-N. and E.R.-P.; supervision: E.M., M.D., S.Z.-N. and E.R.-P.; conceptualization: E.M., S.Z.-N., E.R.-P. and M.D. All authors have read and agreed to the published version of the manuscript.

Funding: The work was financially supported by the Norwegian Research council projects NanoBioReal (grant no. 288768) and PhD project (E.E.) (272412/F40), by H2020 project RiskGONE (grant no. 8144259) and TWINALT (grant no. 952404—H2020-WIDESPREAD-2020-5) and by TEPCAN project granted in the Programme "Applied research" under the Norwegian Financial Mechanisms 2014—2021/POLNOR 2019 (EEA and Norway Grants), Thematic areas: Welfare, health and care (NCBR Funding No. NOR/POLNOR/TEPCAN/0057/2019-00).

Data Availability Statement: Data are available from the researchers on request.

Acknowledgments: The authors would like to thank Erin McFadden (NILU), Kristine Haugen Anmarkrud, and Fikirte Debebe Zegeye (STAMI) for technical assistance, Marit Vadset (NILU) for performing ICP-MS analysis, NorGenoTech AS (Norway) for providing the Fpg, and Hoffmann La Roche (Switzerland) for providing the Ro 19-8022. Mahmood Amiry-Moghaddam and Mina Martine Frey (University of Oslo) are greatly acknowledged for their expertise and excellent technical assistance, respectively.

Conflicts of Interest: The authors declare no conflict of interest.

References

1. Jud, C.; Clift, M.J.; Petri-Fink, A.; Rothen-Rutishauser, B. Nanomaterials and the human lung: What is known and what must be deciphered to realise their potential advantages? *Swiss Med. Wkly.* **2013**, *143*, w13758. [CrossRef] [PubMed]
2. Kendall, M.; Holgate, S. Health impact and toxicological effects of nanomaterials in the lung. *Respirology* **2012**, *17*, 743–758. [CrossRef]
3. Rissler, J.; Gudmundsson, A.; Nicklasson, H.; Swietlicki, E.; Wollmer, P.; Londahl, J. Deposition efficiency of inhaled particles (15–5000 nm) related to breathing pattern and lung function: An experimental study in healthy children and adults. *Part. Fibre Toxicol.* **2017**, *14*, 10. [CrossRef] [PubMed]
4. Griese, M.; Reinhardt, D. Smaller sized particles are preferentially taken up by alveolar type II pneumocytes. *J. Drug Target.* **1998**, *5*, 471–479. [CrossRef] [PubMed]
5. Frohlich, E.; Mercuri, A.; Wu, S.; Salar-Behzadi, S. Measurements of Deposition, Lung Surface Area and Lung Fluid for Simulation of Inhaled Compounds. *Front. Pharmacol.* **2016**, *7*, 181. [CrossRef] [PubMed]
6. Boyes, W.K.; van Thriel, C. Neurotoxicology of Nanomaterials. *Chem. Res. Toxicol.* **2020**, *33*, 1121–1144. [CrossRef] [PubMed]
7. Malakar, A.; Kanel, S.R.; Ray, C.; Snow, D.D.; Nadagouda, M.N. Nanomaterials in the environment, human exposure pathway, and health effects: A review. *Sci. Total Environ.* **2021**, *759*, 143470. [CrossRef]
8. Donaldson, K.; Stone, V.; Tran, C.L.; Kreyling, W.; Borm, P.J. Nanotoxicology. *Occup. Environ. Med.* **2004**, *61*, 727–728. [CrossRef]
9. Fizesan, I.; Chary, A.; Cambier, S.; Moschini, E.; Serchi, T.; Nelissen, I.; Kiss, B.; Pop, A.; Loghin, F.; Gutleb, A.C. Responsiveness assessment of a 3D tetra-culture alveolar model exposed to diesel exhaust particulate matter. *Toxicol. In Vitro* **2018**, *53*, 67–79. [CrossRef]
10. Kampa, M.; Castanas, E. Human health effects of air pollution. *Environ. Pollut.* **2008**, *151*, 362–367. [CrossRef]
11. Silverman, D.T. Diesel Exhaust and Lung Cancer-Aftermath of Becoming an IARC Group 1 Carcinogen. *Am. J. Epidemiol.* **2018**, *187*, 1149–1152. [CrossRef] [PubMed]
12. Lee, J.W.; Lee, H.J.; Lee, Y.J.; Lim, Y.B.; Sim, W.J.; Jang, J.H.; Heo, H.R.; Lim, H.J.; Jung, J.W.; Kim, J.S. Determination of Genotoxicity Attributed to Diesel Exhaust Particles in Normal Human Embryonic Lung Cell (WI-38) Line. *Biomolecules* **2021**, *11*, 291. [CrossRef]
13. Simko, M.; Mattsson, M.O. Risks from accidental exposures to engineered nanoparticles and neurological health effects: A critical review. *Part. Fibre Toxicol.* **2010**, *7*, 42. [CrossRef] [PubMed]
14. Simeonova, P.P.; Erdely, A. Engineered nanoparticle respiratory exposure and potential risks for cardiovascular toxicity: Predictive tests and biomarkers. *Inhal. Toxicol.* **2009**, *21* (Suppl. 1), 68–73. [CrossRef]
15. Johnston, H.; Pojana, G.; Zuin, S.; Jacobsen, N.R.; Moller, P.; Loft, S.; Semmler-Behnke, M.; McGuiness, C.; Balharry, D.; Marcomini, A.; et al. Engineered nanomaterial risk. Lessons learnt from completed nanotoxicology studies: Potential solutions to current and future challenges. *Crit. Rev. Toxicol.* **2013**, *43*, 1–20. [CrossRef] [PubMed]
16. Liu, L.; Kong, L. Research progress on the carcinogenicity of metal nanomaterials. *J. Appl. Toxicol.* **2021**, *41*, 1334–1344. [CrossRef]
17. Kim, C.S. Deposition of aerosol particles in human lungs: In Vivo measurement and modelling. *Biomarkers* **2009**, *14* (Suppl. 1), 54–58. [CrossRef] [PubMed]
18. Oberdorster, G. Significance of particle parameters in the evaluation of exposure-dose-response relationships of inhaled particles. *Inhal. Toxicol.* **1996**, *8*, 73–89. [CrossRef]
19. Cassee, F.R.; Muijser, H.; Duistermaat, E.; Freijer, J.J.; Geerse, K.B.; Marijnissen, J.C.; Arts, J.H. Particle size-dependent total mass deposition in lungs determines inhalation toxicity of cadmium chloride aerosols in rats. Application of a multiple path dosimetry model. *Arch. Toxicol.* **2002**, *76*, 277–286. [CrossRef]
20. Schmid, O.; Moller, W.; Semmler-Behnke, M.; Ferron, G.A.; Karg, E.; Lipka, J.; Schulz, H.; Kreyling, W.G.; Stoeger, T. Dosimetry and toxicology of inhaled ultrafine particles. *Biomarkers* **2009**, *14* (Suppl. 1), 67–73. [CrossRef]
21. Joris, F.; Manshian, B.B.; Peynshaert, K.; De Smedt, S.C.; Braeckmans, K.; Soenen, S.J. Assessing nanoparticle toxicity in cell-based assays: Influence of cell culture parameters and optimized models for bridging the in vitro-in vivo gap. *Chem. Soc. Rev.* **2013**, *42*, 8339–8359. [CrossRef] [PubMed]
22. Lenz, A.G.; Karg, E.; Brendel, E.; Hinze-Heyn, H.; Maier, K.L.; Eickelberg, O.; Stoeger, T.; Schmid, O. Inflammatory and oxidative stress responses of an alveolar epithelial cell line to airborne zinc oxide nanoparticles at the air-liquid interface: A comparison with conventional, submerged cell-culture conditions. *Biomed. Res. Int.* **2013**, *2013*, 652632. [CrossRef] [PubMed]
23. Precupas, A.; Gheorghe, D.; Botea-Petcu, A.; Leonties, A.R.; Sandu, R.; Popa, V.T.; Mariussen, E.; Naouale, E.Y.; Runden-Pran, E.; Dumit, V.; et al. Thermodynamic Parameters at Bio-Nano Interface and Nanomaterial Toxicity: A Case Study on BSA Interaction with ZnO, SiO_2, and TiO_2. *Chem. Res. Toxicol.* **2020**, *33*, 2054–2071. [CrossRef] [PubMed]
24. Upadhyay, S.; Palmberg, L. Air-Liquid Interface: Relevant In Vitro Models for Investigating Air Pollutant-Induced Pulmonary Toxicity. *Toxicol. Sci.* **2018**, *164*, 21–30. [CrossRef] [PubMed]
25. Klein, S.G.; Serchi, T.; Hoffmann, L.; Blomeke, B.; Gutleb, A.C. An improved 3D tetraculture system mimicking the cellular organisation at the alveolar barrier to study the potential toxic effects of particles on the lung. *Part. Fibre Toxicol.* **2013**, *10*, 31. [CrossRef]
26. Fizesan, I.; Cambier, S.; Moschini, E.; Chary, A.; Nelissen, I.; Ziebel, J.; Audinot, J.N.; Wirtz, T.; Kruszewski, M.; Pop, A.; et al. In vitro exposure of a 3D-tetraculture representative for the alveolar barrier at the air-liquid interface to silver particles and nanowires. *Part. Fibre Toxicol.* **2019**, *16*, 14. [CrossRef]

27. Chary, A.; Serchi, T.; Moschini, E.; Hennen, J.; Cambier, S.; Ezendam, J.; Blomeke, B.; Gutleb, A.C. An in vitro coculture system for the detection of sensitization following aerosol exposure. *ALTEX* **2019**, *36*, 403–418. [CrossRef]
28. Paur, H.-R.; Cassee, F.R.; Teeguarden, J.; Fissan, H.; Diabate, S.; Aufderheide, M.; Kreyling, W.G.; Hänninen, O.; Kasper, G.; Riediker, M.; et al. In-vitro cell exposure studies for the assessment of nanoparticle toxicity in the lung—A dialog between aerosol science and biology. *J. Aerosol. Sci.* **2011**, *42*, 668–692. [CrossRef]
29. Lieber, M.; Smith, B.; Szakal, A.; Nelson-Rees, W.; Todaro, G. A continuous tumor-cell line from a human lung carcinoma with properties of type II alveolar epithelial cells. *Int. J. Cancer* **1976**, *17*, 62–70. [CrossRef]
30. Tsuchiya, S.; Yamabe, M.; Yamaguchi, Y.; Kobayashi, Y.; Konno, T.; Tada, K. Establishment and characterization of a human acute monocytic leukemia cell line (THP-1). *Int. J. Cancer* **1980**, *26*, 171–176. [CrossRef]
31. Suggs, J.E.; Madden, M.C.; Friedman, M.; Edgell, C.J. Prostacyclin expression by a continuous human cell line derived from vascular endothelium. *Blood* **1986**, *68*, 825–829. [CrossRef]
32. Schwende, H.; Fitzke, E.; Ambs, P.; Dieter, P. Differences in the state of differentiation of THP-1 cells induced by phorbol ester and 1,25-dihydroxyvitamin D3. *J. Leukoc. Biol.* **1996**, *59*, 555–561. [CrossRef]
33. Klein, C.L.; Comero, S.; Stahlmecke, B.; Romazanov, J.; Kuhlbusch, T.A.J.; Van Doren, E.; Linsinger, T. *NM-Series of Representative Manufactured Nanomaterials: NM-300 Silver Characterisation, Stability, Homogeneity*; Publications Office of the European Union: Luxembourg, 2011.
34. Gabelova, A.; El Yamani, N.; Alonso, T.I.; Buliakova, B.; Srancikova, A.; Babelova, A.; Pran, E.R.; Fjellsbo, L.M.; Elje, E.; Yazdani, M.; et al. Fibrous shape underlies the mutagenic and carcinogenic potential of nanosilver while surface chemistry affects the biosafety of iron oxide nanoparticles. *Mutagenesis* **2017**, *32*, 193–202. [CrossRef]
35. El Yamani, N.; Collins, A.R.; Runden-Pran, E.; Fjellsbo, L.M.; Shaposhnikov, S.; Zienolddiny, S.; Dusinska, M. In vitro genotoxicity testing of four reference metal nanomaterials, titanium dioxide, zinc oxide, cerium oxide and silver: Towards reliable hazard assessment. *Mutagenesis* **2017**, *32*, 117–126. [CrossRef]
36. Elje, E.; Mariussen, E.; Moriones, O.H.; Bastus, N.G.; Puntes, V.; Kohl, Y.; Dusinska, M.; Runden-Pran, E. Hepato(Geno)Toxicity Assessment of Nanoparticles in a HepG2 Liver Spheroid Model. *Nanomaterials* **2020**, *10*, 545. [CrossRef]
37. Jensen, K.; Kembouche, Y.; Christiansen, E.; Jacobsen, N.; Wallin, H.; Guiot, C. The generic NANOGENOTOX dispersion protocol. *Stand. Oper. Proced. Backgr. Doc. Final Protoc. Prod. Suitable Manuf. Nanomater. Expo. Media* **2011**. Available online: https://docplayer.net/31130766-Final-protocol-for-producing-suitable-manufactured-nanomaterial-exposure-media-web-report-the-generic-nanogenotox-dispersion-protocol.html (accessed on 29 June 2022).
38. Kleiven, M.; Rossbach, L.M.; Gallego-Urrea, J.A.; Brede, D.A.; Oughton, D.H.; Coutris, C. Characterizing the behavior, uptake, and toxicity of NM300K silver nanoparticles in Caenorhabditis elegans. *Environ. Toxicol. Chem.* **2018**, *37*, 1799–1810. [CrossRef]
39. Ding, Y.; Weindl, P.; Lenz, A.G.; Mayer, P.; Krebs, T.; Schmid, O. Quartz crystal microbalances (QCM) are suitable for real-time dosimetry in nanotoxicological studies using VITROCELL(R)Cloud cell exposure systems. *Part. Fibre Toxicol.* **2020**, *17*, 44. [CrossRef]
40. Lenz, A.G.; Stoeger, T.; Cei, D.; Schmidmeir, M.; Semren, N.; Burgstaller, G.; Lentner, B.; Eickelberg, O.; Meiners, S.; Schmid, O. Efficient bioactive delivery of aerosolized drugs to human pulmonary epithelial cells cultured in air-liquid interface conditions. *Am. J. Respir. Cell Mol. Biol.* **2014**, *51*, 526–535. [CrossRef]
41. Mülhopt, S.; Diabaté, S.; Krebs, T.; Weiss, C.; Paur, H.-R. Lung toxicity determination by in vitro exposure at the air liquid interface with an integrated online dose measurement. *J. Phys. Conf. Ser.* **2009**, *170*, 012008. [CrossRef]
42. Ding, Y.; Weindl, P.; Wimmer, C.; Mayer, P.; Krebs, T.; Schmid, O. *Characterization of the Air-Liquid Interface Cell Exposure (ALICE-CLOUD) System for In-Vitro Toxicological Studies of Engineered Nanomaterials (ENMs)*; European Aerosol Conference (EAC): Zürich, Switzerland, 2017.
43. Dusinska, M.; Costa, S.; Collins, A. Introduction to hCOMET special issue, 'Comet assay in vitro'. *Mutat. Res. Genet. Toxicol. Environ. Mutagen.* **2019**, *845*, 403071. [CrossRef]
44. Elje, E.; Hesler, M.; Runden-Pran, E.; Mann, P.; Mariussen, E.; Wagner, S.; Dusinska, M.; Kohl, Y. The comet assay applied to HepG2 liver spheroids. *Mutat. Res. Genet. Toxicol. Environ. Mutagen.* **2019**, *845*, 403033. [CrossRef]
45. Collins, A. The Use of Bacterial Repair Endonucleases in the Comet Assay. *Methods Mol. Biol.* **2011**, *691*, 137–147. [CrossRef]
46. Azqueta, A.; Slyskova, J.; Langie, S.A.; O'Neill Gaivao, I.; Collins, A. Comet assay to measure DNA repair: Approach and applications. *Front. Genet.* **2014**, *5*, 288. [CrossRef]
47. Azqueta, A.; Ladeira, C.; Giovannelli, L.; Boutet-Robinet, E.; Bonassi, S.; Neri, M.; Gajski, G.; Duthie, S.; Del Bo, C.; Riso, P.; et al. Application of the comet assay in human biomonitoring: An hCOMET perspective. *Mutat. Res. Rev. Mutat. Res.* **2020**, *783*, 108288. [CrossRef]
48. Collins, A.R.; Annangi, B.; Rubio, L.; Marcos, R.; Dorn, M.; Merker, C.; Estrela-Lopis, I.; Cimpan, M.R.; Ibrahim, M.; Cimpan, E.; et al. High throughput toxicity screening and intracellular detection of nanomaterials. *Wiley Interdiscip. Rev. Nanomed. Nanobiotechnol.* **2017**, *9*, e1413. [CrossRef]
49. Kononenko, V.; Erman, A.; Petan, T.; Krizaj, I.; Kralj, S.; Makovec, D.; Drobne, D. Harmful at non-cytotoxic concentrations: SiO_2-SPIONs affect surfactant metabolism and lamellar body biogenesis in A549 human alveolar epithelial cells. *Nanotoxicology* **2017**, *11*, 419–429. [CrossRef]
50. Foster, K.A.; Oster, C.G.; Mayer, M.M.; Avery, M.L.; Audus, K.L. Characterization of the A549 cell line as a type II pulmonary epithelial cell model for drug metabolism. *Exp. Cell Res.* **1998**, *243*, 359–366. [CrossRef]

51. Bisig, C.; Voss, C.; Petri-Fink, A.; Rothen-Rutishauser, B. The crux of positive controls-Pro-inflammatory responses in lung cell models. *Toxicol. In Vitro* **2019**, *54*, 189–193. [CrossRef]
52. Klein, S.G.; Cambier, S.; Hennen, J.; Legay, S.; Serchi, T.; Nelissen, I.; Chary, A.; Moschini, E.; Krein, A.; Blomeke, B.; et al. Endothelial responses of the alveolar barrier in vitro in a dose-controlled exposure to diesel exhaust particulate matter. *Part. Fibre Toxicol.* **2017**, *14*, 7. [CrossRef]
53. Campen, M.J. Vascular endothelium as a target of diesel particulate matter-associated toxicants. *Arch. Toxicol.* **2012**, *86*, 517–518. [CrossRef] [PubMed]
54. Araujo, J.A.; Nel, A.E. Particulate matter and atherosclerosis: Role of particle size, composition and oxidative stress. *Part. Fibre Toxicol.* **2009**, *6*, 24. [CrossRef] [PubMed]
55. Ahn, K.; Pan, S.; Beningo, K.; Hupe, D. A permanent human cell line (EA.hy926) preserves the characteristics of endothelin converting enzyme from primary human umbilical vein endothelial cells. *Life Sci.* **1995**, *56*, 2331–2341. [CrossRef]
56. Ahn, K.; Pan, S.M.; Zientek, M.A.; Guy, P.M.; Sisneros, A.M. Characterization of endothelin converting enzyme from intact cells of a permanent human endothelial cell line, EA.hy926. *Biochem. Mol. Biol. Int.* **1996**, *39*, 573–580. [CrossRef]
57. Bouis, D.; Hospers, G.A.; Meijer, C.; Molema, G.; Mulder, N.H. Endothelium in vitro: A review of human vascular endothelial cell lines for blood vessel-related research. *Angiogenesis* **2001**, *4*, 91–102. [CrossRef]
58. Yang, J.; Chang, E.; Cherry, A.M.; Bangs, C.D.; Oei, Y.; Bodnar, A.; Bronstein, A.; Chiu, C.P.; Herron, G.S. Human endothelial cell life extension by telomerase expression. *J. Biol. Chem.* **1999**, *274*, 26141–26148. [CrossRef]
59. Ades, E.W.; Candal, F.J.; Swerlick, R.A.; George, V.G.; Summers, S.; Bosse, D.C.; Lawley, T.J. HMEC-1: Establishment of an immortalized human microvascular endothelial cell line. *J. Investig. Dermatol.* **1992**, *99*, 683–690. [CrossRef]
60. Wang, M.; Petersen, N.O. Lipid-coated gold nanoparticles promote lamellar body formation in A549 cells. *Biochim. Biophys Acta* **2013**, *1831*, 1089–1097. [CrossRef]
61. Lehnert, B.E. Pulmonary and thoracic macrophage subpopulations and clearance of particles from the lung. *Environ. Health Perspect.* **1992**, *97*, 17–46. [CrossRef]
62. Rothen-Rutishauser, B.; Mueller, L.; Blank, F.; Brandenberger, C.; Muehlfeld, C.; Gehr, P. A newly developed in vitro model of the human epithelial airway barrier to study the toxic potential of nanoparticles. *ALTEX* **2008**, *25*, 191–196. [CrossRef]
63. Qin, Z. The use of THP-1 cells as a model for mimicking the function and regulation of monocytes and macrophages in the vasculature. *Atherosclerosis* **2012**, *221*, 2–11. [CrossRef]
64. Loret, T.; Peyret, E.; Dubreuil, M.; Aguerre-Chariol, O.; Bressot, C.; le Bihan, O.; Amodeo, T.; Trouiller, B.; Braun, A.; Egles, C.; et al. Air-liquid interface exposure to aerosols of poorly soluble nanomaterials induces different biological activation levels compared to exposure to suspensions. *Part. Fibre Toxicol.* **2016**, *13*, 58. [CrossRef]
65. Barosova, H.; Karakocak, B.B.; Septiadi, D.; Petri-Fink, A.; Stone, V.; Rothen-Rutishauser, B. An In Vitro Lung System to Assess the Proinflammatory Hazard of Carbon Nanotube Aerosols. *Int. J. Mol. Sci.* **2020**, *21*, 5335. [CrossRef]
66. Wang, G.; Zhang, X.; Liu, X.; Zheng, J.; Chen, R.; Kan, H. Ambient fine particulate matter induce toxicity in lung epithelial-endothelial co-culture models. *Toxicol. Lett.* **2019**, *301*, 133–145. [CrossRef]
67. Alfaro-Moreno, E.; Nawrot, T.S.; Vanaudenaerde, B.M.; Hoylaerts, M.F.; Vanoirbeek, J.A.; Nemery, B.; Hoet, P.H. Co-cultures of multiple cell types mimic pulmonary cell communication in response to urban PM10. *Eur. Respir. J.* **2008**, *32*, 1184–1194. [CrossRef]
68. Wu, J.; Wang, Y.; Liu, G.; Jia, Y.; Yang, J.; Shi, J.; Dong, J.; Wei, J.; Liu, X. Characterization of air-liquid interface culture of A549 alveolar epithelial cells. *Braz. J. Med. Biol. Res.* **2017**, *51*, e6950. [CrossRef]
69. Rothen-Rutishauser, B.M.; Kiama, S.G.; Gehr, P. A three-dimensional cellular model of the human respiratory tract to study the interaction with particles. *Am. J. Respir. Cell Mol. Biol.* **2005**, *32*, 281–289. [CrossRef]
70. Rothen-Rutishauser, B.; Blank, F.; Muhlfeld, C.; Gehr, P. In vitro models of the human epithelial airway barrier to study the toxic potential of particulate matter. *Expert Opin. Drug Metab. Toxicol.* **2008**, *4*, 1075–1089. [CrossRef]
71. Elbert, K.J.; Schafer, U.F.; Schafers, H.J.; Kim, K.J.; Lee, V.H.; Lehr, C.M. Monolayers of human alveolar epithelial cells in primary culture for pulmonary absorption and transport studies. *Pharm. Res.* **1999**, *16*, 601–608. [CrossRef]
72. He, R.W.; Braakhuis, H.M.; Vandebriel, R.J.; Staal, Y.C.M.; Gremmer, E.R.; Fokkens, P.H.B.; Kemp, C.; Vermeulen, J.; Westerink, R.H.S.; Cassee, F.R. Optimization of an air-liquid interface in vitro cell co-culture model to estimate the hazard of aerosol exposures. *J. Aerosol. Sci.* **2021**, *153*, 105703. [CrossRef]
73. Barosova, H.; Meldrum, K.; Karakocak, B.B.; Balog, S.; Doak, S.H.; Petri-Fink, A.; Clift, M.J.D.; Rothen-Rutishauser, B. Inter-laboratory variability of A549 epithelial cells grown under submerged and air-liquid interface conditions. *Toxicol. In Vitro* **2021**, *75*, 105178. [CrossRef]
74. Köser, J.; Engelke, M.; Hoppe, M.; Nogowski, A.; Filser, J.; Thöming, J. Predictability of silver nanoparticle speciation and toxicity in ecotoxicological media. *Environ. Sci. Nano* **2017**, *4*, 1470–1483. [CrossRef]
75. Lankoff, A.; Sandberg, W.J.; Wegierek-Ciuk, A.; Lisowska, H.; Refsnes, M.; Sartowska, B.; Schwarze, P.E.; Meczynska-Wielgosz, S.; Wojewodzka, M.; Kruszewski, M. The effect of agglomeration state of silver and titanium dioxide nanoparticles on cellular response of HepG2, A549 and THP-1 cells. *Toxicol. Lett.* **2012**, *208*, 197–213. [CrossRef]
76. Cronholm, P.; Karlsson, H.L.; Hedberg, J.; Lowe, T.A.; Winnberg, L.; Elihn, K.; Wallinder, I.O.; Möller, L. Intracellular uptake and toxicity of Ag and CuO nanoparticles: A comparison between nanoparticles and their corresponding metal ions. *Small* **2013**, *9*, 970–982. [CrossRef]

77. Esposito, V.; Lucariello, A.; Savarese, L.; Cinelli, M.P.; Ferraraccio, F.; Bianco, A.; De Luca, A.; Mazzarella, G. Morphology changes in human lung epithelial cells after exposure to diesel exhaust micron sub particles (PM(1).(0)) and pollen allergens. *Environ. Pollut.* **2012**, *171*, 162–167. [CrossRef]
78. Davoren, M.; Herzog, E.; Casey, A.; Cottineau, B.; Chambers, G.; Byrne, H.J.; Lyng, F.M. In vitro toxicity evaluation of single walled carbon nanotubes on human A549 lung cells. *Toxicol. In Vitro* **2007**, *21*, 438–448. [CrossRef]
79. Mosser, D.M.; Edwards, J.P. Exploring the full spectrum of macrophage activation. *Nat. Rev. Immunol.* **2008**, *8*, 958–969. [CrossRef]
80. Oostingh, G.J.; Casals, E.; Italiani, P.; Colognato, R.; Stritzinger, R.; Ponti, J.; Pfaller, T.; Kohl, Y.; Ooms, D.; Favilli, F.; et al. Problems and challenges in the development and validation of human cell-based assays to determine nanoparticle-induced immunomodulatory effects. *Part. Fibre Toxicol.* **2011**, *8*, 8. [CrossRef]
81. Meindl, C.; Öhlinger, K.; Zrim, V.; Steinkogler, T.; Froehlich, E. Screening for Effects of Inhaled Nanoparticles in Cell Culture Models for Prolonged Exposure. *Nanomaterials* **2021**, *11*, 606. [CrossRef]
82. Centurione, L.; Aiello, F.B. DNA Repair and Cytokines: TGF-β, IL-6, and Thrombopoietin as Different Biomarkers of Radioresistance. *Front. Oncol.* **2016**, *6*, 175. [CrossRef]
83. Bobyk, L.; Tarantini, A.; Béal, D.; Veronesi, G.; Kieffer, I.; Motellier, S.; Valsami-Jones, E.; Lynch, I.; Jouneau, P.-H.; Pernet-Gallay, K.; et al. Toxicity and chemical transformation of silver nanoparticles in A549 lung cells: Dose-rate-dependent genotoxic impact. *Environ. Sci. Nano* **2021**, *8*, 806–821. [CrossRef]
84. Huk, A.; Izak-Nau, E.; El Yamani, N.; Uggerud, H.; Vadset, M.; Zasonska, B.; Duschl, A.; Dusinska, M. Impact of nanosilver on various DNA lesions and HPRT gene mutations-effects of charge and surface coating. *Part. Fibre Toxicol.* **2015**, *12*, 25. [CrossRef] [PubMed]
85. González-Vega, J.G.; García-Ramos, J.C.; Chavez-Santoscoy, R.A.; Castillo-Quiñones, J.E.; Arellano-Garcia, M.E.; Toledano-Magaña, Y. Lung Models to Evaluate Silver Nanoparticles' Toxicity and Their Impact on Human Health. *Nanomaterials* **2022**, *12*, 2316. [CrossRef] [PubMed]
86. Gutleb, A.C. Potential of In Vitro Methods for Mechanistic Studies of Particulate Matter–Induced Cardiopulmonary Toxicity. *Crit. Rev. Environ. Sci. Technol.* **2011**, *41*, 1971–2002. [CrossRef]
87. Le Ouay, B.; Stellacci, F. Antibacterial activity of silver nanoparticles: A surface science insight. *Nano Today* **2015**, *10*, 339–354. [CrossRef]
88. Behra, R.; Sigg, L.; Clift, M.J.; Herzog, F.; Minghetti, M.; Johnston, B.; Petri-Fink, A.; Rothen-Rutishauser, B. Bioavailability of silver nanoparticles and ions: From a chemical and biochemical perspective. *J. R. Soc. Interface* **2013**, *10*, 20130396. [CrossRef]
89. Bell, R.A.; Kramer, J.R. Structural chemistry and geochemistry of silver-sulfur compounds: Critical review. *Environ. Toxicol. Chem.* **1999**, *18*, 9–22. [CrossRef]
90. Oh, S.J.; Kim, H.; Liu, Y.; Han, H.K.; Kwon, K.; Chang, K.H.; Park, K.; Kim, Y.; Shim, K.; An, S.S.; et al. Incompatibility of silver nanoparticles with lactate dehydrogenase leakage assay for cellular viability test is attributed to protein binding and reactive oxygen species generation. *Toxicol. Lett.* **2014**, *225*, 422–432. [CrossRef]

Supplementary Materials

Advanced Respiratory Models for Hazard Assessment of Nanomaterials—Performance of Mono-, Co- and Tricultures

Laura Maria Azzurra Camassa [1,†], Elisabeth Elje [2,3,†], Espen Mariussen [2,4‡], Eleonora Marta Longhin [2], Maria Dusinska [2], Shan Zienolddiny-Narui [1,*] and Elise Rundén-Pran [2,*]

[1] National Institute of Occupational Health in Norway, 0033 Oslo, Norway; laura.camassa@stami.no
[2] NILU—Norwegian Institute for Air Research, 2027 Kjeller, Norway; eel@nilu.no (E.E.); espen.mariussen@fhi.no (E.M.); eml@nilu.no (E.M.L.); mdu@nilu.no (M.D.)
[3] Institute of Basic Medical Sciences, Department of Molecular Medicine, University of Oslo, 0372 Oslo, Norway
[4] Norwegian Institute of Public Health, FHI, 0456 Oslo, Norway
* Correspondence: shan.narui@stami.no (S.Z.-N.); erp@nilu.no (E.R.-P.); Tel.: +47-2319-5284 (S.Z.-N.); Tel.: +47-6389-8237 (E.R.-P.)
† These authors contributed equally to this work.
‡ Present address.

S1.1. Cell cultures

The formulation of the different types of culture medium is summarized in Table S1. The passage numbers used for cells in different culture models are summarized in Table S2, and the density of the cell types in Table S3.

Table S1. Cell types and cell media with supplements used for mono-, co- and tricultures. DMEM: Dulbecco's Modified Eagle's Medium. FBS: Fetal bovine serum, hiFBS: heat inactivated FBS (56°C, 30 min), pen/strep: penicillin-streptomycin. RPMI: Roswell Park Memorial Institute Medium. 1% pen-strep equals 100 U/mL penicillin and 100 µg/mL streptomycin. % given as v/v.

Cell Type	**Cell Media Lab 1**	**Cell Media Lab 2**
	Monoculture	
A549 epithelial (ATCC® CCL-185™)	DMEM (Sigma, D6046) + 9% FBS + 1% pen/strep	DMEM low glucose (Gibco 31885023) + 10% hiFBS + 1% pen/strep
EA.hy926 endothelial (ATCC® CRL2922™)	DMEM high glucose with pyruvate and L glutamine (Gibco 11995-065) + 9% FBS + 1% pen/strep	DMEM high glucose (Gibco 11965-092) + 10% hiFBS + 1% pen/strep
THP-1 monocytes (ATCC® TIB-202™)	RPMI1640 (Gibco, A1049101-01) + 9% hiFBS + 1% pen/strep	RPMI1640 (Gibco, A1049101-01) + 10% hiFBS + 1% pen/strep
	Coculture/Triculture	
Coculture: A549/EA.hy926 and *Triculture:* A549/EA.hy926/dTHP-1	*Apical side:* DMEM low glucose + 9% FBS + 1% pen/strep *Basolateral side:* DMEM high glucose + 9% FBS + 1% pen/strep *ALI conditions basolateral side:* 72 % DMEM high glucose + 18 % DMEM low glucose + 9% FBS + 1% pen/strep	*Apical side:* DMEM low glucose + 10% hiFBS + 1% pen/strep *Basolateral side:* DMEM high glucose + 10% hiFBS + 1% pen/strep *ALI conditions basolateral side:* 72 % DMEM high glucose + 18 % DMEM low glucose + 10% hiFBS + 1% pen/strep

Table S2. Passage numbers of cells applied in the experiments.

		Monoculture	**Coculture**	**Triculture**
A549	Lab 1	4, 5, 6, 9, 13, 15	2, 5, 9, 11, 12, 13, 15	13, 16, 19, 21
	Lab 2	5, 7, 9, 11	13, 15, 17	19, 21, 23, 25
EA.hy926	Lab 1	-	3, 5, 7, 8, 9, 10, 12	3, 14, 16, 19
	Lab 2	-	5, 7, 9, 11	13, 15, 17, 19
THP-1	Lab 1	-	-	6, 9, 12, 15
	Lab 2	-	-	5, 8, 11, 14

Table S3. Cell seeding densities in advanced lung models on PET 1 μm transwell inserts (BD Biosciences, Millipore, Falcon). Constant cell densities were used within each experiment. PET: polyethylene terephthalate.

Cell type	Seeding density (cells/cm²)		
	Monoculture	Coculture	Triculture
A549	1.1×10^5	1.1×10^5	1.1×10^5
EA.hy926	-	1.1×10^5	1.1×10^5
dTHP-1	-	-	$1.1\text{-}2.2 \times 10^5$

Table S4. Antibodies and staining for confocal microscopy.

		Supplier	Dilution
Primary antibodies	**Host species**		
Anti- Prosurfactant Protein C antibody	rabbit	ab90716 Abcam	1:250
Anti- Zonula Occludens 1 (ZO-1)	rabbit	61-7300 Life technologies	1:250
Anti- Cd11b	mouse	AM32402PU-N-Origene	1:200
Secondary antibodies			
Donkey anti-Rabbit IgG (H+L) Highly Cross-Adsorbed Secondary Antibody, Alexa Fluor 488		Life technologies	1:1000
Donkey anti-Mouse IgG (H+L) highly cross-adsorbed secondary antibody, Alexa Fluor 596		Life technologies	1:1000
Nuclei staining			
DAPI		Sigma	1:1000

S1.2. NM-300K endotoxin testing

The HEK endotoxin assay can detect as low as 0.01 EU/mL of endotoxin. A 1 unit/mL of endotoxin (EU/mL) is equal approximately 0.1 ng endotoxin/mL of solution. When HEK293 transfected with hTLR2 and hTLR4 were exposed to NM-300K at a concentration of 1 and 10 μg/mL (Fig. S1), they released less than 1 unit/mL of endotoxin (EU/mL). This value is comparable with the HEK293 hTLRnull used as a negative control. On the contrary, HEK293 hTLR2 and hTLR4, showed an extremely high concentration of endotoxin released (positive control) when exposed to their respective agonists LTA and LPS (Fig. S1, left). Higher dosage of NM-300K is not vital for HEK 293 cells (data not shown). HEK293 TLRnull, HEK293 hTLR2 and hTLR4 viability was measured by AB assay for validation of the assay (Fig. S1, right). HEK293 cell viability was affected by transfection of the hTLR2 and hTLR4 but this was independent of the chosen concentrations of NM-300K. Relative viability (%) was measured by AlamarBlue. The fluorescence intensity is proportional to the number of living cells. Cells were incubated with a volume of 200 μL/well of respective medium containing 10 % v/v AB solution (Sigma-Aldrich) at 37°C and 5% CO_2 for 1-1.5 h. Four replica wells were included per condition. Aliquots of 100 μL were taken from each well and transferred into a new 96 well plate to measure the fluorescence intensity (ex.530 nm, em.590 nm). HEK293, HEK293 hTLR2 and hTLR4 cells

viability was not influenced by 1 and 10 μg/mL NM-300K. A decrease in cell viability appears to be dependent by the different cell medium composition more than the exposure to NMs.

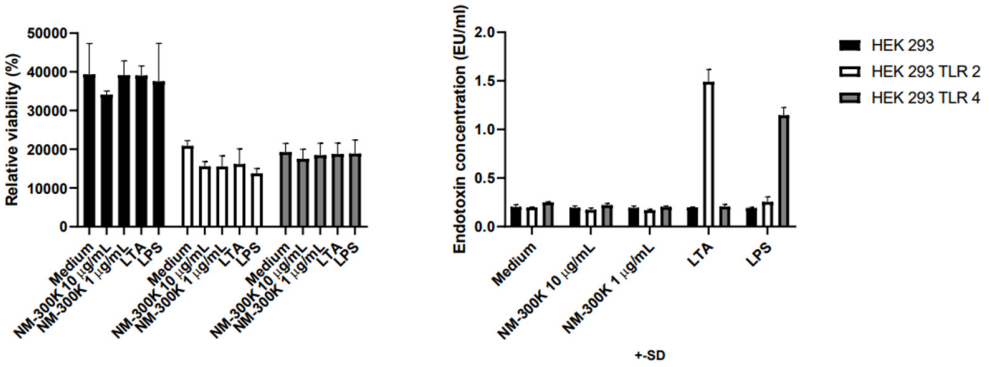

Figure S1. HEK293 AlamarBlue (AB) and endotoxin test 24 hours postexposure with NM-300K. (Left) AB assay: HEK293, HEK293 hTLR2 and hTLR4 cell viability was not influenced by 1 and 10 μg/mL NM-300K. (Right) Exposure with NM-300K did not show any relevant endotoxin concentration (EU/mL) at a concentration of 1 and 10 μg/mL. Endotoxin level followed by exposure showed a level comparable to the negative control cells (hTLRnull). Note the response of HEK293 hTLR2 and hTLR4 when exposed to their respective agonist LTA and LPS. Results are presented as mean with standard deviation of 4 replica samples.

NM-300K nanoparticles at the concentration of 0.5 and 50 μg/mL was also examined for endotoxins with LAL kinetic QCL endotoxin chromogenic test (Lonza). LAL assay is extremely sensitive and detect as little as 0.1 EU/mL (approx. 0.01 ng endotoxin per mL). No considerable endotoxin concentration was detected in any of the nanoparticles and dispersing medium analysed.

NM-300K has a yellow-brown colour with absorbance peak at about 410 nm (Elje et al 2020) and is likely to interfere with the LAL assay when tested at high concentrations, as the assay includes absorbance reading at 405 nm. Our results are at low concentrations, thus, endotoxin contamination cannot be completely excluded, as the sample could be too diluted and below the sensitivity of the test.

S1.3. Calculation of nominal concentrations for exposure in the VITROCELL® system

The deposition efficiency in the VITROCELL® system was estimated to 50 % in preliminary experiments (results not shown). This was used for calculation of nominal concentrations of NM-300K according to the formulas below.

Stock concentration, undiluted = C_{stock} = 10 mg/mL = 10 000 μg/mL
Stock concentration, diluted = $C_{diluted}$ = 1 mg/mL = 1000 μg/mL
Nebulizing volume of sample = V_{sample} = 300 μL
Total deposition area = A_{total} = 145 cm^2 [39]
Deposition efficiency (DE) = 50 % (preliminary experiments)
Nominal concentration low = $C_{nominal\ low}$

Nominal concentration high = $C_{nominal\ high}$

$$C_{nominal\ low} = \frac{C_{diluted} \times V_{sample}}{A_{total}} \times DE = \frac{1000\ \frac{\mu g}{ml} \times 0{,}3\ ml}{145\ cm^2} \times 0{,}50 = 1{,}03\ \mu g/cm^2$$

$$C_{nominal\ high} = \frac{C_{stock} \times V_{sample}}{A_{total}} \times DE = \frac{10000\ \frac{\mu g}{ml} \times 0{,}3\ ml}{145\ cm^2} \times 0{,}50 = 10{,}34\ \mu g/cm^2$$

S1.4. Characterization of NM-300K

The Ag concentration of NM-300K was measured by ICP-MS at Lab 1, and the size distribution of NM-300K was measured by DLS at both laboratories. A summary of the overall characterization is given in Table S5. DLS results per sample and laboratory are summarized in Tables S6 and S7 showing the average size of stock dispersion and diluted dispersion (in PBS), respectively. The size of NM-300K was similar in stock dispersion and after dilution in PBS. For stock dispersions prepared at Lab 1, one dispersion had a smaller size compared to the others. No relationship was found between mean diameter and delivered energy during sonication (results not shown) and is not believed to be the explanation for differences in Z-ave.

Table S5. Characterization of NM-300K dispersions. Measurements of NM-300K stock dispersion with nominal concentration 10 mg/mL performed at Lab 1 and Lab 2. Ag content in stock was measured by ICP-MS. The dispersion was diluted 1:100 in pure water for size (by intensity) and ZP analysis. Presented are mean values with SD from three independent experiments (n=3), except for Ag concentration where n=7 and n=2, and Z-ave (Lab 1) where n=9. DLS: dynamic light scattering, Z-ave: average hydrodynamic diameter, PDI: polydispersity index, ZP: zeta potential, ICP-MS: inductively coupled plasma mass spectrometry.

		Lab 1	**Lab 2**
Ag content (mg/mL)	**Ag concentration**	7.20 ± 0.87 (n=7)	**-**
	Ag < 3 kDa fraction	0.29 ± 0.01 (n=2) 3.6 % ± 0.1 %	-
DLS	**Z-ave (nm)**	130.7 ± 23.2	57.5 ± 5.7
	PDI	0.380 ± 0.037	0.343 ± 0.067
	ZP (mV)	-17.1 ± 2.8	-

Tab S6: Size distribution of NM-300K diluted 1:100 in ultrapure H_2O, measured by DLS (by intensity) in two laboratories. A Zetasizer Ultra Red with measurement angle 174.4° was used at Lab 1, and a Zetasizer Nano ZS with measurement angle 173° was used at Lab 2. Results are average of 3-5 steps per sample. The stock ID corresponds to Supplementary table 5.

Laboratory	**Stock ID**	**Z-Ave**	**PdI**	**Main peak**	**Smaller peak**	**Larger peak**	**Main peak**	**Smaller peak**	**Larger peak**
		nm	a.u.	nm	nm	nm	%	%	%
Lab 1	Stock1	75.6	0.442	108.4	5.1	4353.0	92.9	1.8	5.3
Lab 1	Stock2	146.7	0.413	216.8		4570.0	96.9		3.1
Lab 1	Stock3	137.0	0.387	227.0	6.5		99.6	0.4	
Lab 1	Stock4	136.9	0.402	222.4	18.6	4591.0	95.1	2.6	2.2
Lab 1	Stock5	128.2	0.388	203.1	10.5		98.6	1.4	
Lab 1	Stock6	115.5	0.354	176.4	18.2		96.4	3.6	
Lab 1	Stock7	146.0	0.370	234.3			100.0		
Lab 1	Stock8	143.2	0.321	211.1		1596.3	99.1		0.9
Lab 1	Stock9	147.6	0.345	215.0		3247.2	98.1		1.9
	Average	130.7	0.380	201.6	11.8	3671.5	97.4	2.0	2.7
	SD	23.2	0.037	38.7	6.4	1284.9	2.3	1.2	1.7
Lab 2	Stock1	54.4	0.299	81.4	8.0		94.9	5.1	
Lab 2	Stock2	54.0	0.310	80.9	7.8	4566.0	94.4	5.4	0.2
Lab 2	Stock3	64.1	0.420	103.8	10.6	4288.0	93.1	5.3	1.6
	Average	57.5	0.343	88.7	8.8	4427.0	94.1	5.3	0.9
	SD	5.7	0.067	13.1	1.6	196.6	0.9	0.2	1.0

Table S7 Size distribution of NM-300K diluted 1:100-1:10 in PBS, measured by DLS (by intensity) in two laboratories. A Zetasizer Ultra Red with measurement angle 174.4° was used at Lab 1, and a Zetasizer Nano ZS with measurement angle 173° was used at Lab 2. Results are average of 3-5 steps per sample. The stock ID corresponds to Table S4.

Laboratory	Stock ID	Z-Ave	PdI	Main peak	Smaller peak	Larger peak	Main peak	Smaller peak	Larger peak
		nm	a.u.	nm	nm	nm	%	%	%
Lab 1	Stock1	76.0	0.434	117.4	1653.2	2451.4	91.3	2.9	5.8
Lab 1	Stock8	144.5	0.359	224.0	0.0	1218.0	97.5	0.0	2.5
Lab 1	Stock9	151.4	0.368	230.3	1231.7	1572.3	96.7	2.5	0.7
Lab 2	Stock1	57.4	0.298	84.7	8.2	4694.0	96.0	3.8	0.2
Lab 2	Stock2	60.9	0.382	92.4	9.6	4285.0	97.2	1.4	1.2
Lab 2	Stock3	69.0	0.427	114.1	8.4	3591.0	93.9	2.2	3.9

S1.5. Stability of NM-300K in physiological buffers

To compare the stability of NM-300K in different buffers to use in the cloud system, the NM-300K was diluted 1:10 in pure water, PBS and HBSS with and without $CaCl_2$ and $MgCl_2$, before dilution 1:10 in pure water and measurement of hydrodynamic diameter by DLS. The NMs were stable in size upon dilution in different buffers (Table S8).

Table S8. Characterization of hydrodynamic diameter by DLS of NM-300K in different buffers (Lab 1). Results are shown as mean with SD of n=3 independent experiments. *n=2. PBS: Phosphate buffered saline. HBSS: Hank's balanced salt solution. -, without $CaCl_2$ and $MgCl_2$. +, with $CaCl_2$ and $MgCl_2$. PDI, polydispersity index.

	Pure water	**PBS -**	**PBS + (*)**	**HBSS -**	**HBSS +**
Z-ave (nm)	128.5 ± 30.7	123.9 ± 41.8	129.3 ± 33.7	120.6 ± 44.7	122.0 ± 42.9
PDI (nm)	0.359 ± 0.075	0.385 ± 0.037	0.294 ± 0.062	0.435 ± 0.150	0.388 ± 0.057

S1.6. AlamarBlue assay on cultures exposed to different physiological buffer solutions

The relative cell viability of A549 and EA.hy926 cells in cocultures after exposure to aerosolized buffers, was investigated by the AlamarBlue assay. Results are shown in Fig. S2 and explained in the main document.

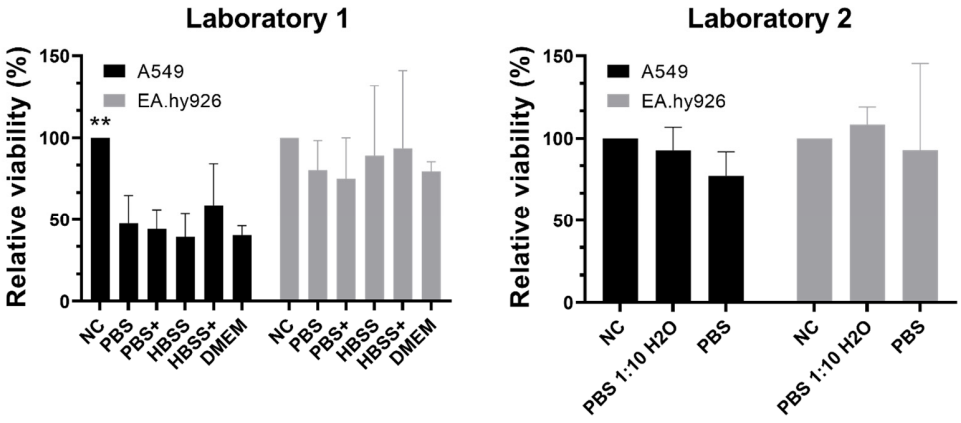

Figure S2. Relative viability measured by the AlamarBlue assay in A549/EA.hy926 cocultures exposed to buffer solutions at the air-liquid interface (ALI), performed at Lab 1 (left image) and Lab 2 (right image). The viability of A549 cells in cocultures was decreased after buffer exposure. Results are shown as mean with standard deviation (SD) of 3 independent experiments, each with duplicate cell culture inserts. Statistically significant differences compared to PBS were analyzed by ordinary one-way ANOVA with multiple comparisons post-test Dunnet´s, and are indicated by * p <0.5, ** p<0.1, and *** p<0.01. NC: negative control (incubator control), PBS: phosphate buffered saline, HBSS: Hanks' balanced saline solution, DMEM: Dulbecco's modified Eagle medium, +: with CaCl2/MgCl2.

II

III

nanomaterials

MDPI

Article

Different Sensitivity of Advanced Bronchial and Alveolar Mono- and Coculture Models for Hazard Assessment of Nanomaterials

Elisabeth Elje [1,2,*], Espen Mariussen [1,3], Erin McFadden [1], Maria Dusinska [1] and Elise Rundén-Pran [1,*]

[1] Health Effects Laboratory, Department for Environmental Chemistry, NILU—Norwegian Institute for Air Research, 2007 Kjeller, Norway
[2] Department of Molecular Medicine, Institute of Basic Medical Sciences, University of Oslo, 0372 Oslo, Norway
[3] Department of Air Quality and Noise, Norwegian Institute of Public Health, 0456 Oslo, Norway
* Correspondence: eel@nilu.no (E.E.); erp@nilu.no (E.R.-P.); Tel.: +47-63-89-81-98 (E.E.)

Abstract: For the next-generation risk assessment (NGRA) of chemicals and nanomaterials, new approach methodologies (NAMs) are needed for hazard assessment in compliance with the 3R's to reduce, replace and refine animal experiments. This study aimed to establish and characterize an advanced respiratory model consisting of human epithelial bronchial BEAS-2B cells cultivated at the air–liquid interface (ALI), both as monocultures and in cocultures with human endothelial EA.hy926 cells. The performance of the bronchial models was compared to a commonly used alveolar model consisting of A549 in monoculture and in coculture with EA.hy926 cells. The cells were exposed at the ALI to nanosilver (NM-300K) in the VITROCELL® Cloud. After 24 h, cellular viability (alamarBlue assay), inflammatory response (enzyme-linked immunosorbent assay), DNA damage (enzyme-modified comet assay), and chromosomal damage (cytokinesis-block micronucleus assay) were measured. Cytotoxicity and genotoxicity induced by NM-300K were dependent on both the cell types and model, where BEAS-2B in monocultures had the highest sensitivity in terms of cell viability and DNA strand breaks. This study indicates that the four ALI lung models have different sensitivities to NM-300K exposure and brings important knowledge for the further development of advanced 3D respiratory in vitro models for the most reliable human hazard assessment based on NAMs.

Keywords: NAMs—new approach methodologies; ALI—air–liquid interface; genotoxicity; BEAS-2B; A549; NM-300K; DNA damage; chromosomal damage; cytokines

Citation: Elje, E.; Mariussen, E.; McFadden, E.; Dusinska, M.; Rundén-Pran, E. Different Sensitivity of Advanced Bronchial and Alveolar Mono- and Coculture Models for Hazard Assessment of Nanomaterials. *Nanomaterials* **2023**, *13*, 407. https://doi.org/10.3390/nano13030407

Academic Editors: Saura Sahu and Jean-Marie Nedelec

Received: 25 November 2022
Revised: 3 January 2023
Accepted: 13 January 2023
Published: 19 January 2023

1. Introduction

The production and usage of nanomaterials (NMs) are rising, increasing the risk of human exposure. Inhalation is the most important exposure route for airborne nanomaterials (NMs) and particulate matter (PM) in humans, making the respiratory system a first-target organ [1]. The respiratory tract consists of the tracheobronchial region leading into the alveolar region, where gas exchange with blood occurs across the thin lung–blood barrier (0.4 µm) [1,2]. Besides gas exchange, a main function of the lower respiratory tract is defense against inhaled toxicants [1]. Interaction with and deposition of inhaled NMs are likely to occur in the bronchial and alveolar region. Particle deposition is dependent upon the NMs' physicochemical properties, such as size and solubility [2].

NMs and their dissolved compounds can cause primary effects in the respiratory system, or secondary circulatory effects after crossing the lung–blood barrier and taken up in the blood. A human study has shown the translocation of inhaled gold NM or its dissolved species into the circulatory system and accumulation at sites of vascular disease [3]. Gold was detected in blood and urine up to three months after inhalation

exposure to gold NMs [3,4]. Translocation of silver NMs has been seen in in vivo studies in rodents [5].

In order to comply with the 3R´s principle to reduce, refine and replace animal experiments, new advanced in vitro models are developed to better simulate the complexity of human lungs. Reliable in vitro models of the airway system are of critical importance for the risk assessment and governance of NMs and other environmental pollutants [6,7]. Human cells cultured on a microporous membrane at the air–liquid interface (ALI) with cell culture medium only at the basolateral side, represent a highly relevant model for inhalation toxicity studies [8]. Human lung cell lines such as A549 and BEAS-2B are commonly used as model cells in respiratory toxicology. A549 cells are alveolar type-II carcinoma cells, while BEAS-2B cells are immortalized cells from normal human bronchial epithelia. Both A549 and BEAS-2B cells form monolayers when cultivated at the ALI [9,10]. In order to further advance the models, cocultures with other cell types, such as macrophages, dendritic cells, or endothelial cells, can be established. The ALI exposure model aims to better mimic the physiology of the respiratory system and is regarded as a more relevant in vitro model compared to submerged exposure. Aerosolized exposure to the particles on top of the cells introduces less changes in the physicochemical properties of the test substance compared with submerged exposure [8].

Inhalation exposure to NMs, PM or other compounds may lead to adverse human effects. Genotoxicity is a critical endpoint in the hazard assessment of chemicals, including NMs, and should be assessed both at the level of DNA/genes and chromosomes. The comet assay is a widely used assay for determining DNA damage as DNA strand breaks (SBs), and as oxidized or alkylated bases by the inclusion of a repair enzyme such as formamidopyrimidine DNA glycosylase (Fpg) [11]. For the detection of chromosomal damage, the most-used test is the micronucleus assay (OECD test guideline 487), which detects the formation of micronuclei from chromosomes, chromatid fragments or whole chromosomes that lag behind in cell division [12,13]. So far, a very limited number of studies have addressed several genotoxicity endpoints in ALI models. Our approach, combining advanced and more physiologically relevant in vitro respiratory models and exposure systems with genotoxicity testing (by both comet and micronucleus assays), will support the hazard characterization of NMs for risk assessment and safe use.

NMs can induce DNA damage by direct contact with DNA, or indirectly via NM-induced oxidative stress or intermediate molecules and processes in cells (primary genotoxicity). Secondary genotoxicity can be driven by an inflammatory response [14]. The airway epithelium is an integrated part of the inflammatory defense response after inhalation exposure to toxicants. Pro-inflammatory cytokines are considered biomarkers of NM-induced toxicity and can be linked with adverse effects. The pro-inflammatory cytokines IL-6 and IL-8 are among the cytokines predominately secreted by monocytes, and both are coupled to lung injury and considered biomarkers of lung disease [15–17]. IL-8 can also act as a chemokine [17]. The bronchial epithelium serves as a first-line defense system against inhaled pathogens mainly by the release of chemokines, such as IL-8 [18]. The cytokines IL-6 and IL-8 have been shown to be secreted by airway epithelial, including BEAS-2B cells, and endothelial cells and be involved in lung inflammation responses [18–21]. IL-6 has been shown to be released from BEAS-2B cells after exposure to particulate matter below 1 µm in size (PM1), and both IL-6 and IL-8 were induced in BEAS-2B cells after exposure to the PM2.5 fraction [22,23]. Endothelial EA.hy926 cells were shown to release IL-6 and IL-8 after exposure to silica NMs [19].

The A549 cell line has frequently been used in coculture lung models and has been shown to be useful in a range of applications for hazard assessment of NMs [24–35]. The non-cancerous origin of BEAS-2B cells may make the cell line more relevant for use in risk governance of NMs, particularly as a bronchial respiratory model. Coculture models with BEAS-2B in ALI conditions for hazard assessment are, however, much less characterized than those with A549. The main aim of this study was to characterize an advanced respiratory model with BEAS-2B bronchial cells cultivated in ALI models,

after exposure to an aerosolized reference silver NM, NM-300K. The cells were cultivated both as monocultures and in cocultures with human endothelial EA.hy926 cells. Cells from ALI cultures were analyzed for cytokine secretion, cytotoxicity, barrier integrity, DNA damage by the comet assay and chromosomal damage by the cytokinesis-block micronucleus assay. Importantly, the responses obtained with the bronchial BEAS-2B model were compared with the A549 alveolar model. The experimental design brilliantly allows for the comprehensive analysis of several endpoints from the same sample, facilitating increased throughput, better comparability, reduced costs, and sustainability by design to support the development of new approach methodologies (NAMs) and next-generation risk assessment (NGRA) of NMs.

2. Materials and Methods

2.1. Experimental Design

An experimental design combining the analysis of several endpoints from the same sample was developed. The same inserts with cells at the ALI were used for the analysis of cytokine secretion in basolateral media (enzyme-linked immunosorbent assay, ELISA), Ag permeation (inductively coupled plasma mass spectrometry, ICP-MS), cell viability (alamarBlue assay), cell proliferation, DNA damage and oxidized base lesions (enzyme modified version of the comet assay), and chromosomal damage (micronucleus assay) (Figure 1). In parallel, additional experiments on ALI cultures were included to further characterize the models, and experiments with traditional submerged cultures were performed for comparisons. For each exposure condition, 1–2 culture inserts were included from both mono- and cocultures, and at least 3 independent experiments were performed, in order to allow for appropriate biological variation to be included in the results and analysis.

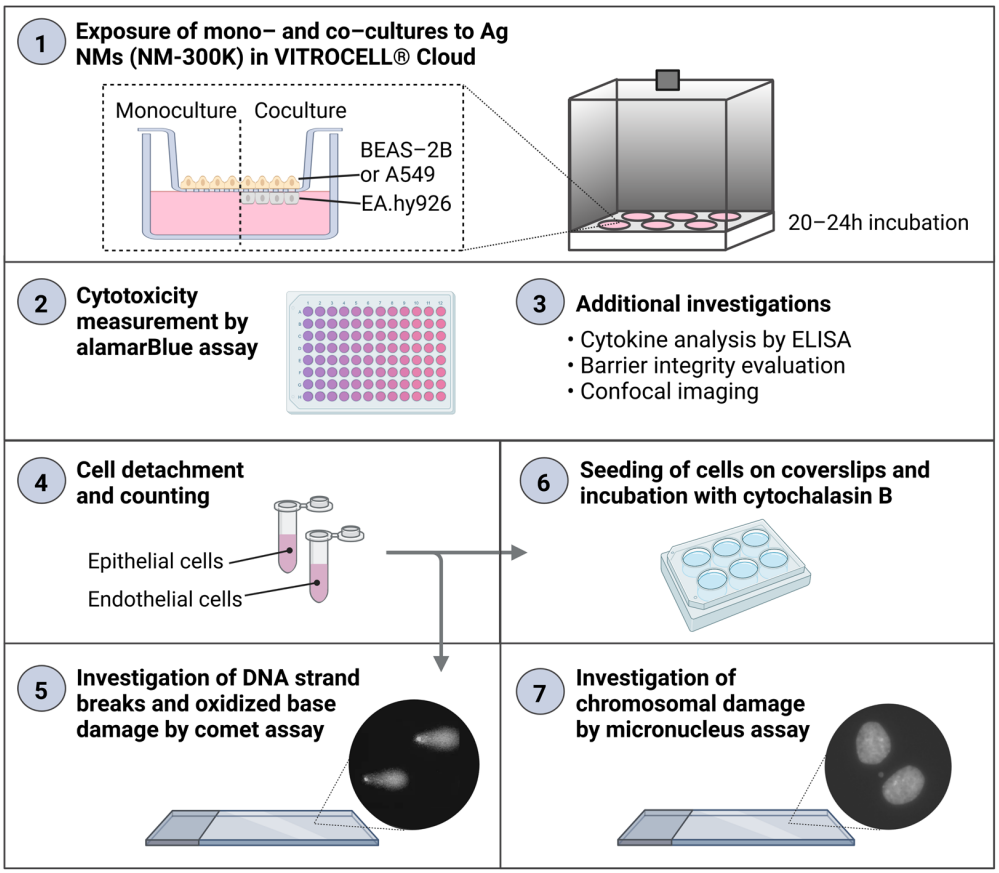

Figure 1. Experimental design for the four different respiratory models exposed at the air–liquid interface (ALI) in the VITROCELL® Cloud system. Created with BioRender.com.

2.2. Nanomaterials

The Ag NM NM-300K is listed on the representative manufactured NMs list of the European Commission Joint Research Centre (JRC, Brussels, Belgium) and was selected for this study based on its toxicity in our previous work [36–39]. NM-300K was provided by the Fraunhofer Institute for Molecular Biology and Applied Ecology (Schmallenberg, Germany). NM-300K is a silver colloidal dispersion with a nominal silver content of 10% *w*/*w*. The NMs were dispersed in an aqueous solution with stabilizing agents, consisting of 4% *w*/*w* each of polyoxyethylene glycerol trioleate and polyoxyethylene (20) sorbitan mono-laurate (Tween 20). The pristine diameter of NM-300K is about 15 nm, and the size distribution is narrow, where >99% of particles (by number) have a size below 20 nm. A second peak of smaller NMs of about 5 nm has also been reported. The majority of the NMs have a spherical shape [40].

Dispersed NMs were received in vials of approximately 2.0 g each, sealed under argon. The vials were stored at room temperature (RT) in the dark before use. The dispersion medium, NM-300K DIS, contained the aqueous solution with stabilizing agents at the same concentrations as NM-300K, but without Ag. This was used as a solvent control.

2.3. Nanomaterial Dispersion and Characterization

Stock dispersions of NM-300K were prepared in accordance with the Nanogenotox protocol [41]. The original vial of NM-300K was vortexed (>10 s), before approximately 1 g was added to a scintillation vial (Wheaton Industries, Millville, NJ, USA). To this, water with 0.05% bovine serum albumin (BSA) was added to yield a final nominal concentration of 10 mg/mL Ag-NMs, in order to obtain a high enough concentration of Ag-NMs in the ALI exposure system. The total Ag and dissolved Ag species (<3 kDa fraction) were measured from the same samples in Camassa and Elje et al. (2022), revealing a silver concentration of 7.2 ± 0.9 mg/mL with 3.6 ± 0.1% dissolved silver species [39].

The dispersion was sonicated in an ice bath using a calibrated Q500 sonicator with a 6 mm microtip probe (Qsonica L.L.C, Newtown, CT, USA), with amplitudes of 30–40% for 7–13 min. The energy output of the sample was 1030–1285 J/mL dispersion (n = 10), similarly to what is recommended by the Nanogenotox protocol (1176 J/mL [41]). Additional stock dispersions were sonicated using lower energy (95–720 J/mL, n = 5), and were included in the study as similar results were seen compared with the other dispersions. The NM stock dispersions were kept on ice for 10 min before use, to let the NMs settle. Before use, the vial was vortexed for approximately 10 s. The dispersion was kept on ice throughout the experiment. The dispersion medium NM-300K DIS (without Ag) was prepared following the same protocol as that for NM-300K.

The NMs were previously tested for endotoxins, with endotoxin contents below the limit of detection [39]. Stock dispersions for use in the submerged exposure experiments were diluted to 2.56 mg/mL in BSA-water before further dilution in culture medium (Section 2.4) in order to ensure consistency with other studies on the same NM.

2.4. Physicochemical Characterization of Nanomaterials in Dispersion

NM-300K was subjected to measurement of hydrodynamic diameter and zeta potential in a Zetasizer Ultra Red (Malvern Panalytical Ltd., Malvern, United Kingdom) immediately after preparation and after 24 h. The hydrodynamic diameter was determined using dynamic light scattering (DLS) by the particles in suspension. The measured particle size is the diameter of a sphere that diffuses at the same speed as the particle being measured, which is determined by measuring the Brownian motion of the particles by DLS and then interpreting the size using the Stokes–Einstein equation.

The NM stock dispersion was vortexed and diluted 1:100 in sterile filtered MilliQ water, and a 1 mL dispersion was transferred to a disposable cuvette (DTS0012) for size analysis. The hydrodynamic diameter was measured by non-invasive back scatter at 174.7° with 3–5 steps. Analysis was performed at 25 °C with 120 s equilibration time, automatic attenuation, and no pause between steps. Data were processed in the ZS Explorer software

(version 2.0.0.98, Malvern Panalytical Ltd.), using general purpose model, refractive index 1.59 and absorption 0.01.

Measurement of size distribution of NMs diluted in culture medium was performed directly after preparation and after 24 h incubation at 37 °C, 5% CO_2. First, the stock dispersion was vortexed, and mixed with serum-free LHC-9 medium (article no. 12680013, ThermoFisher Scientific, Waltham, MA, USA) to give the highest tested concentration (141 μg/mL or 100 μg/cm^2 in submerged exposure). Then, the sample was diluted 1:10 in sterile filtered MilliQ water, transferred to a disposable cuvette and measured as described above.

Results were presented as Z-average (Z-ave), which is the intensity-weighted mean hydrodynamic size of the ensemble collection of particles, the polydispersity index (PDI), and hydrodynamic diameter (by intensity) of individual peaks in the size distributions.

For zeta potential analysis, the NM stock dispersion was vortexed and diluted 1:100 in sterile filtered MilliQ water, and 1 mL dispersion was transferred to a pre-wetted disposable folded capillary cell (DTS1070). The zeta potential was measured at 25 °C using mixed-mode measurement phase analysis light scattering (M3-PALS).

2.5. Cell Culture

BEAS-2B cells, an Ad12-SV40 hybrid virus-transformed human bronchial epithelial cell line [42,43], were purchased from ATCC (Manassas, VA, USA) (SV40 immortalized, CRL-9609, LN: 62853911). The cells were cultured in serum-free LHC-9 medium without supplements, and they were maintained in an incubator with humidified atmosphere at 5% CO2 and at 37 °C. The cells were passaged two times a week at 80–85% confluency. To facilitate detachment, the cells were incubated with trypsin-EDTA (0.25%, Sigma-Aldrich, Saint-Louis, MO, USA) with polyvinylpyrrolidone (PVP, 0.5% wt/vol) for 3–5 min. Medium was added, and the suspension was centrifuged to remove the trypsin/PVP before cells were seeded at 1.3 × 10^4 cells/cm^2 in Corning CellBind® cell culture flasks (Corning, Corning, NY, USA). The cells were used at passages (P) 3–14 (details in Table S1).

The human alveolar type II lung epithelial A549 cells [44] were provided by ATCC, and they were cultured in Dulbecco's Modified Eagle's Medium, DMEM, with low glucose (D6046, Sigma-Aldrich) supplemented with 9% v/v fetal bovine serum, FBS (prod.no. 26140079, ThermoFisher Scientific), and 1% v/v penicillin–streptomycin (100 U/mL pen and 100 μg/mL strep) (catalog no. 15070063, ThermoFisher Scientific). Human endothelial EA.hy926 cells [45] were provided from ATCC and were cultured in DMEM with high glucose (catalog no. 11960, ThermoFisher Scientific), supplemented with 9% v/v FBS, 1% v/v penicillin-streptomycin, sodium pyruvate (1 mM) and L glutamine (4 mM). The cells were maintained in an incubator with a humidified atmosphere at 5% CO_2 and at 37 °C. The cell lines were passaged two or three times a week at 85–90% confluency, using phosphate-buffered saline (PBS, catalog no. 14190094, ThermoFisher Scientific) for washing and semi-dry trypsinization using trypsin-EDTA (0.25%) incubation at 37 °C for 3 min. The cells were seeded at 1.3 × 10^4 cells/cm^2 in standard cell culture flasks. A549 cells were used at P2–15 and EA.hy926 cells were used at P3–19 (details in Table S1). All cell lines were regularly tested for mycoplasma contamination and found negative.

2.6. Cell Cultures at the Air–Liquid Interface

The seeding of mono- and cocultures were performed in a similar manner as previously described [46,47] with some modifications. All cell types, epithelial A549 (P3–15) and BEAS-2B (P3–14), and endothelial EA.hy926 (P3–16) (details on p numbers in Table S1), were seeded at a density of 1.1 × 10^5/cm^2. Mono- and cocultures were cultivated on permeable cell culture inserts in 6-well plates with a porous membrane of polyethylene terephthalate (PET) with a 1 μm pore diameter. Two insert types were used, with similar properties and cell attachment results: Millicell (catalog no. MCRP06H48, Sigma-Aldrich) or ThinCert™ (catalog no. 392-0128, Greiner Bio-One, Kremsmünster, Austria). The same insert type was used for all samples within an experiment.

First, the basolateral side of the membrane was pre-wetted (dipped in media), and the insert was placed upside down in the lid of a Falcon 6-well plate for inserts (catalog no. 353502, Corning). Then, 250 µL of EA.hy926 cell suspension was added to the basolateral side to reach a cell density of $1.1 \times 10^5/cm^2$. The lid with inserts was gently tilted to all sides to ensure even distribution of the cell suspension to the whole membrane surface before incubation for 3.5 h at 37 °C, 5% CO_2. After incubation, the plate was turned in a quick movement back to the original position, and 3 mL media (for EA.hy926 cells) was added to the basolateral side. To the apical side, 1 mL of A549 or BEAS-2B cell suspension (in their own media) was added to reach a cell density of $1.1 \times 10^5/cm^2$. Monocultures of BEAS-2B or A549 were prepared in the same way, where the basolateral compartment was filled with 3 mL of media without cells. The medium volumes were optimized in pilot experiments in order to avoid too great a pressure on the cells and the insert. The cultures were incubated for 2–3 days (48–72 h) to let the cells grow to confluency. Two days' incubation was performed only for A549 mono- and cocultures for alamarBlue and comet assay.

Epithelial and endothelial cells were seeded in their respective media. After 2–3 days of incubation of mono- and cocultures, the basolateral medium was replaced by 1.5 mL of fresh media, and the apical media was removed to place the cells in ALI conditions. For BEAS-2B/EA.hy926 a 1:1 mixture of LHC-9 and DMEM high glucose with supplements was used in the basolateral compartment, and for A549/EA.hy926 a 1:4 mixture of DMEM low glucose and DMEM high glucose with supplements was used (Table S2). The mono- and cocultures were incubated for 20–24 h in order to let the cells adapt to ALI conditions before exposure (Section 2.7).

2.7. Exposure of ALI Cultures in the VITROCELL® Cloud System

The VITROCELL® Cloud system (6-well format) (VITROCELL®Systems GMBH, Waldkirch, Germany), was used for the aerosol exposure of mono- and cocultures at ALI conditions to NM-300K and controls. A small volume of NM dispersion or control solution was added to the Aeroneb Pro® vibrating membrane nebulizer, which generates a dense cloud of droplets with a median aerodynamic diameter of 4–6 µm inside an exposure chamber. After some minutes, the humid aerosol will deposit at the bottom of the exposure chamber (area 145 cm^2) with cell inserts [48].

Aerosol exposure was performed by aerosolizing 2 × 150 µL of sample, followed by 150 µL PBS (details below), to the mono- and cocultures positioned at ALI in the VITROCELL® Cloud system at 37 °C. After 8 min, the aerosol cloud had settled, and the chamber was opened to transfer the cell inserts to 6-well plates (Falcon) with 1.5 mL fresh culture media (for mono- or cocultures). The exposure of ALI cultures was performed in the same sample order for all experiments: PBS (2 × 150 µL), NM-300K dispersion medium (2 × 150 µL), NM-300K low concentration (2 × 150 µL of stock dispersion diluted 10× in PBS or NM-300K dispersion medium), and NM-300K high concentration (2 × 150 µL of stock dispersion). In order to reduce the amount of NMs left in the nebulizer, all samples were immediately exposed to additional 150 µL PBS. Thus, all samples were exposed to a cloud with a total volume of 450 µL. All solutions and dispersions were vortexed directly before use. The nebulizer was rinsed with PBS between all exposures, and the cloud system and chamber were wiped with a tissue with ethanol.

The relative amount of nebulized solution that is deposited on top of the cells, the deposition efficiency, can be measured by comparing the amount of deposited substance on the insert to the original solution, either by using a fluorescent compound or elemental analysis. As the deposition efficiency can vary between different nebulizers, the same nebulizer was used for all experiments in this study. We previously measured the deposition efficiency of this nebulizer to be 53% [39]. Additionally, the deposition of Ag in NM-300K was measured giving similar results [39]. This information was used to choose the exposure volumes needed for achieving the intended nominal concentrations for cell exposure.

2.8. Positive Control Exposures

Exposure of ALI cultures to positive controls were performed via the basolateral culture media below the inserts in 6-well plates, for 20–24 h. First, stock solutions were prepared and stored for use within all experiments before being diluted in sterile filtered H_2O directly before use and further diluted in culture medium. Chlorpromazine hydrochloride (catalog no. C8138, Sigma-Aldrich) was used as a positive control for cytotoxicity in the alamarBlue assay, with a stock solution at 5 mM in H_2O stored at 4 °C and exposure concentration of 50–100 μM. Mitomycin-C (catalog no. A2190.0002, PanReac AppliChem [VWR/Avantor]) was used as a positive control for micronuclei induction in the micronucleus assay, with stock solution at 0.2 mg/mL in dimethyl sulfoxide (DMSO) stored at −20 °C, and exposure concentration at 0.15 μg/mL, similarly to Reference [49]. In one experiment with A549/EA.hy926 and BEAS-2B/EA.hy926 cocultures, a higher concentration (0.30 μg/mL) was additionally included.

2.9. Characterization of the ALI Cultures by Microscopy Analysis

Daily evaluation of cell density and proliferation was performed with a Leica DM-IL microscope. More detailed characterization was performed by confocal microscopy. For confocal microscopy, cells in separate culture inserts were stained, fixed, and mounted between two glass coverslips, as described in Reference [39]. In brief, the plasma membranes were stained with CellMask Deep Red Plasma Membrane Stain (Invitrogen, 1:750 dilution in serum-free medium, 15 min at 37 °C), and the cells were fixed in formaldehyde (4%, 15 min, RT), before the nuclei were counterstained with DAPI (4′,6-diamidino-2-phenylindole, ProLong Gold Antifade reagent with DAPI, ThermoFischer Scientific). Confocal microscopy was performed using a Zeiss LSM 700 (lasers 405 and 639 nm; objective 40×). Image acquisition and processing were performed with the Zeiss Software ZEN. Z-stack acquisition was performed with 12–52 μm thickness with 7–53 images for each stack.

2.10. Barrier Function of the ALI Cultures by Elemental Analysis and Fluorescence

The barrier function of the BEAS-2B monocultures and BEAS-2B/EA.hy926 cocultures at the ALI, simulating the human lung–blood barrier, was tested by measuring the permeation of Ag or a fluorescent hydrophilic molecule into the basolateral medium. The procedures were performed similarly to as described in Reference [39] for A549 and A549/EA.hy926 cultures.

The permeation of Ag through the barrier was measured by analyzing the total Ag in the basolateral medium of the ALI cultures after 20–24 h exposure, and it was compared with the deposited Ag on empty culture inserts. The basolateral medium was collected in Eppendorf tubes, stored at −20 °C, and used for cytokine analysis by ELISA (Section 2.11) and Ag analysis by inductively coupled plasma mass spectrometry (ICP-MS). Culture medium was thawed on ice, vortexed for 10 s and 250–500 μL was transferred to a Teflon container (18 mL) vial. Sample preparation and ICP-MS analysis was performed as described in our recent study [39]. The ICP-MS results were analyzed to give the total Ag mass per insert, which was then divided by the deposited mass (low: 0.8 $\mu g/cm^2$, high: 6.0 $\mu g/cm^2$ [39], multiplied by insert area), and multiplied by 100% to give the percentage of Ag permeation through the ALI cultures.

Breakthrough of fluorescein sodium salt was measured on separate cell cultures in order to avoid interference between fluorescein and alamarBlue solution. After exposure to PBS (Section 2.7), 150 μL of fluorescein sodium salt (10 μg/mL in PBS) was nebulized and deposited on top of the cells for 3.5 min. In parallel, fluorescein was deposited on empty inserts in order to estimate the maximum leakage through the insert without cells and on inserts filled with 1 mL PBS in order to measure the maximum deposited fluorescein in the apical side. The leakage samples were transferred to 6-well plates with 1.5 mL medium on the basolateral side, and samples for deposition efficiency were transferred to empty wells. After 22–24 h of incubation, the fluorescence of fluorescein was measured in the basolateral medium or in apical PBS, related to a seven-point fluorescein standard

curve (1.6–50 ng/mL) and blank in the respective medium or PBS. Fluorescence was read in triplicate (90 µL/well) in a black 96-well plate on a FLUOstar OPTIMA microplate reader (BMG Labtech, Ortenberg, Germany) with excitation 480 nm and emission 525 nm. Two independent experiments (n = 2) were performed, each with 1–2 culture inserts for deposition and breakthrough.

2.11. Cytokine Measurement

The basolateral medium from the exposed mono- and cocultures were transferred to Eppendorf tubes and frozen at −20 °C. The amounts of cytokines present in the basolateral media was measured by the enzyme-linked immunosorbent assay (ELISA), which is a commonly used colorimetric immunological assay. The target molecule in the sample will bind to a specific antibody immobilized at the bottom of the microplate well. Through the addition of the second antibody, a sandwich complex is formed. A substrate solution binds to this complex and produces a measurable signal, which is directly proportional to the concentration of target present in the original sample.

ELISA was performed using kits for the human cytokines IL-6 (prod.no. 88-7066, Invitrogen) and IL-8 (prod.no. 88-8086, Invitrogen). The manufacturer's recommended procedures were followed. The samples were thawed on ice and vortexed before use and diluted 1–200 times in the assay buffer to fit within the measurement region. A standard curve was included in all plates. Duplicate measurements from each sample were performed. Plate washing was performed on a Hydroflex (TECAN, Grödig, Austria) microplate washer. Absorbance was read at 450 nm on an Infinite 200 Pro M Nano (TECAN) plate reader.

Potential interference between NM-300K and the performance of the ELISA was investigated. NM-300K was prepared as described above and diluted in cell culture media for BEAS-2B cells, A549 cells, or EA.hy926 cells, in order to achieve concentrations of 30, 3 and 0.3 µg/mL. The NMs in media were added to the ELISA plate in duplicates and mixed with reagent buffer or standard (final concentrations 25 pg/mL IL-6 or 31 pg/mL IL-8) provided in the kit. Further steps in the assay were run as described for the other samples.

2.12. Cell Viability Assessed by alamarBlue Assay

Cell viability was determined by the alamarBlue assay, which is based on the metabolic activity of cells and is commonly used for the quantitative analysis of cell viability and proliferation. The active ingredient in alamarBlue reagent (Sigma-Aldrich) is resazurin, which is a blue non-toxic, cell-permeable compound with low fluorescence. In living cells, resazurin is reduced to resorufin which is red and highly fluorescent, and the color change is detected on a plate reader.

AlamarBlue assay was performed 20–24 h after cell exposure. First, the basolateral media of ALI cultures was removed and saved for cytokine analysis. For monocultures, 1 mL alamarBlue reagent 10% v/v in cell culture media was added to the apical compartment, and 1.5 mL alamarBlue-free media was added to the basolateral compartment. For ALI cocultures, coculture media with alamarBlue 10% v/v was used in both compartments with the same volumes as for the monocultures. The plates were incubated for approximately 1 h. The plates were gently swirled to ensure even distribution of the alamarBlue solution, and 40 µL aliquots were transferred in triplicate to black 96-well plates, before fluorescence (excitation 530 nm, emission 590 nm) was measured on a FLUOstar OPTIMA microplate reader. Blank values (alamarBlue medium without cells present) were subtracted from the fluorescence intensity, which was further normalized by the average measurement of negative control (incubator control) set to 100% relative viability. Potential interference of NM-300K with the alamarBlue assay was investigated as described in Supplementary Materials.

2.13. Cell Detachment and Counting

Directly after performing the alamarBlue assay (Section 2.11), both sides of the insert were washed with PBS. Cells were detached by trypsin-EDTA incubation and subsequent

mixing/washing of insert. For the apical compartment with BEAS-2B or A549 cells, 300 µL trypsin-EDTA was used (with PVP for BEAS-2B). For the basolateral compartment, PBS was used for monocultures and 1–1.5 mL trypsin-EDTA 0.05% (Sigma-Aldrich) was used for EA.hy926 cells. Inserts were trypsinized for 3–5 min at 37 °C, and the apical suspension was mixed with a pipet to facilitate detachment before medium for each cell type was added (1 mL in apical side, 3 mL in basolateral side). BEAS-2B cells were centrifuged at 200 g for 5 min and resuspended in 1 mL fresh culture medium to remove trypsin-EDTA/PVP which was not neutralized by the serum-free cell culture medium.

The cell suspension was mixed 1:1 with trypan blue (0.4%, Invitrogen) for the staining of cells with compromised cell membrane. The cells were counted in an automated cell counter (Countess® C10227, Invitrogen) in order to determine the total number of live cells and viability (%). The cell density was calculated by dividing the total number of live cells by the membrane insert area. Immediately after counting, the cell suspensions were further diluted to approximately 200,000 live cells/mL and used for genotoxicity studies (Sections 2.14 and 2.15).

2.14. DNA Damage Assessed by the Comet Assay

Cell suspensions from ALI and submerged cultures (Section 2.16) were subjected to DNA damage evaluation by the enzyme-modified version of the comet assay. Briefly, in the comet assay, cells are embedded in gels, lysed, and the remaining nucleoids are subjected to an electrophoretic field. The movement of damaged DNA causes comet formations, wherein the relative amount of DNA in the comet tail is proportional to the number of DNASBs.

Reagents used for the comet assay were provided by Sigma-Aldrich unless otherwise stated. A cell suspension with approximately 10,000 cells in 50 µL was mixed with 200 µL low melting point (LMP) agarose (0.8% in PBS) in a 96-well plate, yielding a final concentration 0.64% LMP agarose. Mini-gels (10 µL) were placed on coded microscopy slides precoated with 0.5% standard melting point agarose, and the slides were submerged in lysis solution (2.5 M NaCl, 0.1 M EDTA, 10 mM Tris, 1% *v*/*v* Triton X-100, pH 10, 4 °C) overnight.

For the detection of oxidized bases, the bacterial repair enzyme formamidopyrimidine DNA glycosylase (Fpg, gift from NorGenoTech, Oslo, Norway), which converts oxidized bases to SBs, was used [11]. After lysis, gels for Fpg treatment were washed twice for 8 min in buffer F (40 mM HEPES, 0.1 M KCl, 0.5 mM EDTA, 0.2 mg/mL BSA, pH 8, 4 °C), before being placed in a humid box and covered with Fpg (200 µL/slide) and polyethylene foil. Fpg incubation was performed for 30 min at 37 °C.

All slides were placed in the tank and submerged with electrophoresis solution (0.3 M NaOH, 1 mM EDTA, pH > 13, 4 °C), and DNA was allowed to unwind for 20 min. The electrophoresis was run for 20 min (25 V, 1.25 V/cm, Consort EV202). Gels were neutralized in PBS, washed in ultrapure H_2O, and air-dried overnight. Staining of DNA was performed with SYBR gold (1:2000), and scored in Leica DMI 6000 B (Leica Microsystems), equipped with a SYBR® photographic filter (ThermoFischer Scientific) using the software Comet assay IV 4.3.1 (Perceptive Instruments, Bury St Edmunds, UK). Comets were scored semi-blindly by two operators, where all slides within one experiment were scored by the same operator. Median DNA tail intensity was calculated from 50 comets per gel as a measure of DNA SBs. Medians were averaged from 2–6 gels per sample per n = 3–7 independent experiments.

Hydrogen peroxide (H_2O_2) was used as a positive control for DNA SBs. Cells from negative control inserts were embedded in gels and submerged in 13–100 µM H_2O_2 in PBS for 5 min at 4 °C. The samples were washed twice for 2 min in PBS (4 °C) and then submerged in a separate Coplin jar of lysis solution. The short time between H_2O_2 treatment and lysis limits the process of damage repair. The H_2O_2 exposure experiments with BEAS-2B ALI mono- and cocultures were conducted by placing all cell types (BEAS-2B from monoculture, BEAS-2B from coculture, and EA.hy926 cells from coculture) on the same slide in order to minimize variation. For experiments with submerged cultures (Section 2.16), all cell types and exposure conditions were placed on the same slide. As a

negative control for the H_2O_2 exposure experiments, a separate slide with gels was exposed to PBS in parallel with H_2O_2 exposure.

As a positive control for the function of the Fpg enzyme, A549 cells were exposed to a photosensitizer, Ro 19–8022 (Hoffmann La Roche, Switzerland), and irradiated with visible light before embedding in gels, as described in Elje et al. 2019 [50]. The photosensitizer Ro 19-8022 induces with light oxidized purines, mainly 8-oxoG, which is detected by the Fpg [11]. The function of Fpg was controlled on a regular basis and was not included in all experiments. The positive control had an expected effect compared to the historical control data, with a net Fpg (level of SBs + Fpg minus level of SBs) of >20% DNA in tail.

2.15. Chromosomal Damage Assessed by the Cytokinesis-Block Micronucleus Assay

In parallel to the comet assay, cells from ALI cultures were seeded for detection of chromosomal damage by the cytokinesis-block micronucleus assay. The micronucleus assay measures the ability of the test substance to induce structural chromosome damage (clastogenic effect) or numerical chromosome alterations (aneugenic effect). Micronuclei are formed from chromosome or chromatid fragments or from whole chromosomes that lag behind in cell division. The addition of the active polymerization inhibitor cytochalasin B allows for analysis of the micronuclei frequency in cells that have completed one mitosis after treatment with the test substance, as such cells which are binucleated because the cytochalasin B prevents the separation of daughter cells after mitosis [13,51].

After the treatment and detachment of cells from ALI cultures, approximately 0.5–1 $\times$ 10^5 cells were seeded on flame-sterilized coverslips placed in 6-well plates with 1.5 mL media to a final concentration of 6 µg/mL cytochalasin B (prod.no. C6762, Sigma-Aldrich). The coverslips were incubated with culture media for 1–3 h before adding cells in order to facilitate cell adhesion. Coverslips and plates used for BEAS-2B cells were first coated with collagen IV (prod.no. 804592, Sigma-Aldrich). To each well with a coverslip, 1 mL collagen IV (30 µg/mL) diluted in Hanks' Balanced Salt solution (HBSS) (prod.no. 14175046, ThermoFisher Scientific) was added, before overnight incubation at 4 °C. The coated plates were washed with PBS before medium with cells was added. Cells were incubated at 37 °C and 5% CO_2 for 26–33 h (1–2 cell cycles). The same incubation time was used for all samples within the same experiment.

Cells were washed with PBS and fixed with methanol and acetic acid (3:1) in two steps, first for 15 min at RT, and then for up to 4 days at 4 °C. Coverslips were dried in the fume hood for 3–5 min and mounted on coded standard microscopy slides cleaned with ethanol, with a drop of the mounting medium ProLong Gold Antifade reagent with DAPI (ThermoFischer Scientific).

Cells were imaged in Zeiss Imager-Z2 microscope with a Metafer camera (MetaSystems Hard & Software GmbH, Altlussheim, Germany) and analysis system for micronuclei scoring. Scoring was performed in a semi-automatic manner, using 10$\times$ and 40$\times$ objectives. More details on the system and settings used for scoring can be seen in Section S1.2 in the Supplementary Materials, including the percentages of analyzed binucleated cells (Figure S1). The selected settings for scoring and analysis did not identify all binucleated cells with micronuclei, giving some false negative and false positive cells. Thus, to avoid this, all identified binucleated cells were manually accepted or rejected, and cells with possible micronuclei were checked with a 40$\times$ objective.

2.16. Statistical Analysis

At least three independent experiments were performed for each test method, unless otherwise stated. In each experiment, 1–2 parallel culture inserts were included (Table S4). Results are presented as mean with standard deviation (SD) calculated from the average results from *n* experiments. Normal distribution of data was assumed. In order to evaluate the statistical significance of the results, one-way ANOVA was performed followed by Dunnett's multiple comparisons test using GraphPad Prism version 9.3.1 for Windows (GraphPad Software, San Diego, CA, USA). Results were compared to the PBS control for

ALI cultures and unexposed control for submerged cells. Fluorescein permeation results were compared to empty inserts with no cells. Ag permeation results were analyzed by one-way ANOVA with post-test Sidak to allow for multiple comparisons between low and high concentrations and between models and empty inserts (16 comparisons in total). The level of significance was set to $p < 0.05$. Calculation of EC_{50} values, the concentration giving 50% response, was performed using non-linear regression analysis with the Hill equation, in GraphPad Prism. Mathematical calculations were performed in Excel (Microsoft 365).

3. Results

3.1. Nanomaterial Dispersion Quality and Physicochemical Characterization

The hydrodynamic diameter of NM-300K in stock dispersion and diluted in LHC-9 culture medium was measured by DLS directly after preparation and after 24 h (Table 1). The NMs in stock dispersion had a hydrodynamic diameter (Z-ave) of 149 nm and were stable in dispersion for 24 h. The size distribution of the NMs had two or three peaks, where most particles were within the peak with mean size 110–265 nm, and with some smaller (5–40 nm) and larger (>3000 nm) particles. The zeta potential was −17.1 ± 2.8 mV, indicating that the NM dispersions were semi-stable.

Table 1. Characterization of NM-300K directly after preparation (T0) and after 24 h (T24h). The stock dispersion (10 mg/mL) was used for aerosolized exposure and was diluted in LHC-9 culture medium to make a medium dispersion (141 µg/mL, 100 µg/cm^2) for submerged exposure. Results are presented as mean ± standard deviation or interval (lower value–higher value) from n = 3–15 independent experiments. PDI: polydispersity index, h: hours.

Sample	Time	Z-Ave (nm)	PDI (a.u.)	Main Peak (nm)	*n*
Stock dispersion	T0	149.3 ± 42.5	0.331 ± 0.062	110–265	15
	T24h	129.6 ± 15.4	0.347 ± 0.022	130–147	3
Stock diluted in medium	T0	378.2 ± 109.8	0.393 ± 0.032	148–280	5
	T24h	1838.8 ± 2344.2	0.884 ± 0.739	60–150	5

NM-300K diluted in LHC-9 culture medium had a higher hydrodynamic diameter than the stock dispersion, with a Z-ave of 378 nm and main peak with slightly higher size as for stock dispersion. After 24 h, larger NMs were detected in some of the measurements, giving a Z-ave between 119–5180 nm and a high PDI. Medium without NM-300K had a Z-ave of 15.4 ± 1.0 nm with PDI 0.349 ± 0.054 (n = 2).

3.2. Characterization of the Advanced Models

The advanced models of BEAS-2B/EA.hy926 and A549/EA.hy926 cells, cultured at the ALI, were characterized for cell density, viability and barrier integrity. The ALI-cultured apical cells were moist with a shiny surface, though some cultures occasionally showed a drier appearance (Figure S2). BEAS-2B cells were grown in dense structures on the porous membranes, as seen by confocal microscopy (Figure 2A,B). Higher density was observed for BEAS-2B in coculture with EA.hy926 cells compared to monocultures. Some holes in the apical cell layers of both mono- and cocultures were observed, and the fewest holes were seen in A549 cocultures (details not shown). The confocal images of BEAS-2B cells also indicated slightly higher thickness of the apical cell layer in cocultures, with cells growing in multilayers, compared to the BEAS-2B cells in monocultures (Figure 2 and Figure S3). Cell counting after detachment of cells confirmed a higher density of BEAS-2B cells in coculture compared to BEAS-2B in monocultures, indicating a higher proliferation of the cells in this condition (Table 2). The opposite result was seen for A549 cells, where the density was higher in monoculture compared to coculture with EA.hy926 cells. The endothelial cells had a similar density of both types of cocultures (Table 2) and were growing in a confluent monolayer (Figure 2C). The collected cells had high viability, though some cells were lost

during the detachment process and during washing before trypsinization, and some cells still remained on the insert.

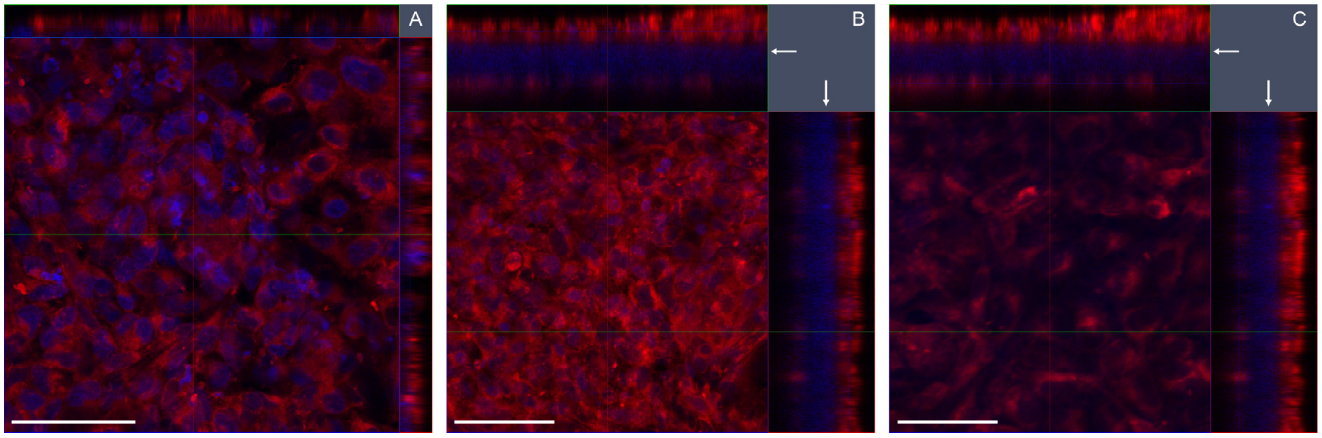

Figure 2. Confocal images of advanced bronchial BEAS-2B models. Z-stack image series (2D x–y view and respective side views) showing the distribution of BEAS-2B and EA.hy926 cells on the opposite sides of a transwell membrane insert (arrow). (**A**) BEAS-2B cells in monocultures (z-stack thickness 12 µm). (**B**) BEAS-2B cells in cocultures (z-stack thickness 52 µm). (**C**) EA.hy 926 cells in cocultures (z-stack thickness 52 µm). Red: cellular membranes stained with Cell Mask red dye; blue: nuclei counterstained with DAPI. Magnification: 40×. Scale bars 50 µm.

Table 2. Number of live cells, cell density and cell viability from ALI cultures at the end of the cultivation period, evaluated by cell counting with trypan blue staining after detaching the cells from the inserts. Results are presented as mean with standard deviation (SD) from 2–3 independent experiments (*n*) and 2–7 replica culture inserts in each experiment. ALI: air–liquid interface.

ALI Model		Cell Line	Live Cells ($\times 10^6$)	Cell Density ($\times 10^5/cm^2$)	Viability (%)	*n*
BEAS-2B	Monoculture	BEAS-2B	2.9 ± 0.3	6.8 ± 0.8	95 ± 2	2
	Coculture	BEAS-2B	4.7 ± 0.6	11.1 ± 1.4	97 ± 1	2
		EA.hy926	0.9 ± 0.3	1.6 ± 0.4	83 ± 15	3
A549	Monoculture	A549	2.4 ± 0.7	5.7 ± 1.5	97 ± 2	2
	Coculture	A549	1.4 ± 0.8	3.3 ± 1.9	94 ± 4	2
		EA.hy926	0.8 ± 0.1	1.8 ± 0.1	93 ± 3	2

The barrier integrity of the advanced models was investigated by measuring the permeation of the water-soluble fluorescein sodium salt and Ag (NMs or dissolved species) from NM-300K after aerosol exposure through the cellular layer by quantification in the basolateral media after 24 h (Table 3). A high permeation of fluorescein, at the same level as empty inserts without cells, was found in BEAS-2B/EA.hy926 cocultures (70%) (Table 3). Strongly reduced fluorescein permeation was seen in BEAS-2B monocultures (20%) and in A549/EA.hy926 cocultures (9%). No difference was seen in the permeation of fluorescein between incubator control and PBS-exposed cultures.

Table 3. Comparison of the barrier integrity of mono- and cocultures of BEAS-2B/EA.hy926 and A549/EA.hy926 cells, by measurement of fluorescein sodium salt and Ag permeation. Results are presented as mean permeation with SD of n = 2–3 independent experiments with single or duplicate inserts. Permeation is presented as the basolateral concentration (µM) and as the basolateral concentration relative to the deposited apical concentration (%). Results for A549/EA.hy926 cultures are based on our previous publication [39]. NC: negative control. PBS: phosphate-buffered saline, NM-300K DIS: dispersant control, NM-300K low: nominal 1 µg/cm^2, NM-300K high: nominal 10 µg/cm^2.

		Fluorescein or Ag Permeation				
Experiment Type	**Treatment**	**BEAS-2B/EA.hy926 Cultures**		**A549/EA.hy926 Cultures ***		**Empty Inserts**
		Monoculture	**Coculture**	**Monoculture**	**Coculture**	
Fluorescein (% of deposited apical concentration)	NC	21 ± 2% (n = 2) [a]	69 ± 2% (n = 2)	-	-	74 ± 11% (n = 2)
	PBS	22 ± 1% (n = 2) [a]	71 ± 7% (n = 2)	-	9 ± 5% (n = 3) [a]	
Ag (µM and % of deposited apical concentration) [b]	NM-300K DIS	0.017 ± 0.003 µM (n = 2)	0.026 ± 0.013 µM (n = 2)	0.069 ± 0.025 µM (n = 2)	0.030 ± 0.017 µM (n = 2)	-
	NM-300K low	11.9 ± 1.5 µM 57.1% (n = 3) [c,d]	7.7 ± 1.3 µM 37.1% (n = 3) [e]	1.9 ± 0.6 µM 8.1% (n = 2) [f]	3.3 ± 0.6 µM 14.3% (n = 2) [f]	-
	NM-300K high	11.9 ± 0.4 µM 7.7% (n = 3)	8.3 ± 2.2 µM 5.3% (n = 3) [e]	14.5 ± 1.4 µM 8.7% (n = 3)	15.4 ± 1.3 µM 9.2% (n = 2)	11.40 ± 0.03 µM 7% (n = 2)

* Results on A549/EA.hy926 cultures are based on [39]. [a] Statistically significant difference from empty inserts, evaluated by one-way ANOVA with post-test Dunnett ($p < 0.05$). [b] Ag permeation results were analyzed by one-way ANOVA with post-test Sidak ($p < 0.05$). A total of 16 comparisons were made: between low and high concentration for each model, low and low concentration for BEAS-2B and A549 monocultures, high and high concentration for BEAS-2B and A549 monocultures, low and low concentration for BEAS-2B and A549 cocultures, high and high concentration for BEAS-2B monocultures and A549 cocultures, and high concentration for all models and empty inserts. [c] Statistically significant difference from BEAS-2B coculture at the same concentration. [d] Statistically significant difference from A549 monoculture at the same concentration. [e] Statistically significant difference from A549 coculture at the same concentration. [f] Statistically significant difference from the same model at high concentration.

The permeation of Ag was higher in BEAS-2B monocultures compared with cocultures (Table 3). This difference was highest after exposure to the low concentration of NM-300K, giving a permeation of 57% in monocultures and 37% in cocultures. In the basolateral medium of cultures exposed to the high concentration of NM-300K, the Ag concentrations of both mono- and cocultures were similar to the maximum permeation through empty inserts (11 µM) (no statistically significant difference by one-way ANOVA with post-test Sidak, $p > 0.05$). The barrier integrity of A549 cultures differed from the BEAS-2B cultures. A slightly higher Ag permeation was seen after exposure to low concentration of NM-300K in A549 cocultures (14%) compared to monocultures (8%) although the difference was not statistically significant. However, the permeability of both A549 mono- and cocultures was lower than for BEAS-2B mono- and cocultures ($p < 0.05$). After exposure to the high concentration of NM-300K, similar results were seen for both A549 and BEAS-2B models, where the permeability was about the same as for the maximum permeation through empty inserts ($p > 0.05$). A low concentration of Ag was found in the basolateral medium of cultures exposed to NM-300K DIS, and the concentration was similar for all models.

3.3. Toxic Responses after NM-300K Exposure in Advanced Respiratory BEAS-2B or A549 Models

3.3.1. Cytotoxicity

The mono- and cocultures of BEAS-2B/EA.hy926 or A549/EA.hy926 cells were exposed to aerosolized NM-300K and control solutions in the VITROCELL® Cloud. After 20–24 h, cytotoxicity was investigated by the alamarBlue assay following the experimental

design in Figure 1. The measured deposited concentrations of NM-300K (low and high), with nominal concentrations 1 and 10 μg/cm^2, were measured in our recent study to be 0.8 and 6.0 μg/cm^2, respectively [39].

Cell viability is presented relative to incubator control (NC, set to 100%) and statistically analyzed against the PBS control. A reduction in the relative cell viability was seen after NM-300K exposure at high concentration in BEAS-2B monocultures (57%, Figure 3A), but not in the cocultures compared with the PBS exposure control. The viability of BEAS-2B cells in cocultures was significantly reduced after aerosol exposure to PBS, with a relative viability of 67%, compared with the incubator control. This effect of PBS was not seen in the monocultures (Figure 3B). The viability of cells exposed to NM-300K DIS was similar to that of cells exposed to PBS, in both models. The viability of EA.hy926 cells was not affected by aerosol exposure to NM-300K or PBS. The positive control, 50–100 μM chlorpromazine hydrochloride in basolateral media, strongly reduced the viability in all cultures, as expected.

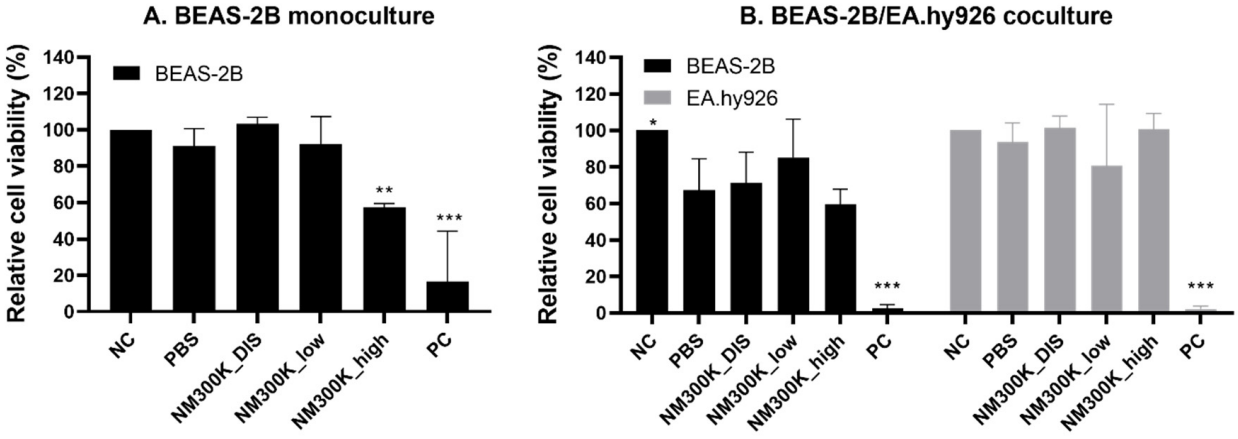

Figure 3. Relative cell viability of BEAS-2B and EA.hy926 cells after exposure to aerosolized NM-300K and control solutions at the air–liquid interface, evaluated by alamarBlue assay. The response of cells in monocultures (**A**) was different compared to cocultures (**B**). Cell viability is presented relative to NC, which is set to 100%. Results are presented as the mean with standard deviation from n= 5–7 (**A**) and n = 4 (**B**) independent experiments (where the results from each experiment are averaged in the case of two replica inserts). Statistically significant different effects on cell viability compared to control inserts with PBS-exposed cells were analyzed by one-way ANOVA followed by Dunnett´s post-hoc test (* $p < 0.05$, ** $p < 0.01$, *** $p < 0.001$). NC: negative control, PBS: phosphate-buffered saline, NM-300K DIS: dispersant control, NM-300K low: nominal 1 μg/cm^2, NM-300K high: nominal 10 μg/cm^2, PC: positive control (chlorpromazine hydrochloride 50–100 μM in basolateral medium for 24 h).

Similar results as with the BEAS-2B models were seen with A549 monocultures and A549/EA.hy926 cocultures after NM-300K exposure (Table 4, details in [39]). The viability of EA.hy926 cells was reduced after aerosol exposure when in coculture with A549 but not with BEAS-2B (Table 4).

Table 4. Comparison of the relative cell viability in bronchial BEAS-2B and alveolar A549 advanced models after aerosol exposure to PBS and NM-300K. Results are presented as the mean relative cell viability (compared to NC, set to 100%) with standard deviation from 4–9 independent experiments (*n*), each with 1–2 replica culture inserts. Statistically significant differences compared to control exposed to PBS were analyzed by one-way ANOVA with Dunnett´s multiple comparisons post-test, and they are indicated by * $p < 0.05$. Data for A549 mono- and cocultures are based on our results from [39]. NC: negative control, PBS: phosphate-buffered saline, NM-300K low: nominal 1 µg/cm^2, NM-300K high: nominal 10 µg/cm^2.

	Relative Cell Viability (%)					
	BEAS-2B/EA.hy926 Cultures			**A549/EA.hy926 Cultures [a]**		
	Monoculture	**Coculture**		**Monoculture [a]**	**Coculture [a]**	
Treatment	**BEAS-2B**	**BEAS-2B**	**EA.hy926**	**A549 [a]**	**A549 [a]**	**EA.hy926 [a]**
NC	100 ± 0	100 ± 0 *	100 ± 0	100 ± 0	100 ± 0	100 ± 0
PBS	91 ± 9	67 ± 17	94 ± 10	93 ± 23	62 ± 22	69 ± 19
NM-300K low	92 ± 15	85 ± 21	81 ± 34	72 ± 13	57 ± 20	67 ± 21
NM-300K high	57 ± 2 *	60 ± 8	100 ± 9	59 ± 26	59 ± 29	68 ± 21
n	5–8	4	4	6–9	4–5	4–5

[a] Data based on the results from [39].

For the comparison of the new advanced models with the corresponding traditional cell models, the cytotoxicity of NM-300K was also tested with submerged exposure of monocultured cells by alamarBlue assay. NM-300K was cytotoxic in BEAS-2B cells at concentrations above 10 µg/cm^2 and at 10 µg/cm^2 for submerged and ALI exposure, respectively (Figure 3 and Figure S4). BEAS-2B cells were more sensitive to NM-300K exposure compared to A549 and EA.hy926 cells in submerged conditions (Figure S4 and Table S5, [52,53]). No interference with the alamarBlue assay was detected for NM-300K (Figure S5).

3.3.2. Secretion of Pro-Inflammatory Cytokines IL-6 and IL-8

Upon NM exposure, pro-inflammatory cytokines can be secreted by the airway epithelium and endothelium in order activate the immune system. The concentrations of the pro-inflammatory cytokines IL-6 and IL-8 secreted from the ALI cultures into the basolateral medium during exposure were measured by ELISA. The results are presented as absolute concentrations (Figure 4 and Tables S6 and S7) and relative to NC (Figure S6).

An apparent trend towards increased levels of IL-8 was seen after NM-300K exposure in all cell models; however, a statistically significant increase was measured only for BEAS-2B in mono- and coculture for the lowest concentration of NM-300K compared with untreated incubator control. A similar effect was seen on IL-6 levels in BEAS-2B cocultures only. In BEAS-2B mono- and cocultures, the concentrations of both IL-6 and IL-8 were higher for low-concentration NM-300K compared with the high concentration. There was a significant effect of PBS exposure on the levels of IL-6 in monocultures of BEAS-2B compared to NC (Figure 4 and Figure S6).

IL-6 and IL-8 concentrations were found to be higher (3× and 9×, respectively) in cocultures of BEAS-2B/EA.hy926 compared with BEAS-2B monocultures (Figure 4 and Tables S6 and S7). For the monocultures, the increase in IL-6 was about the same for low-concentration NM-300K and NM-300K DIS. However, no increase was detected after exposure to the high concentration of NM-300K, for which the concentrations of NM-300K DIS was matching. For the A549 models, the level of IL-8 was about 4× higher in monocultures than in cocultures. For IL-6 level, there was no difference between mono- and cocultures of A549 cells. No interference between the NM-300K and the assay was found (Figure S7).

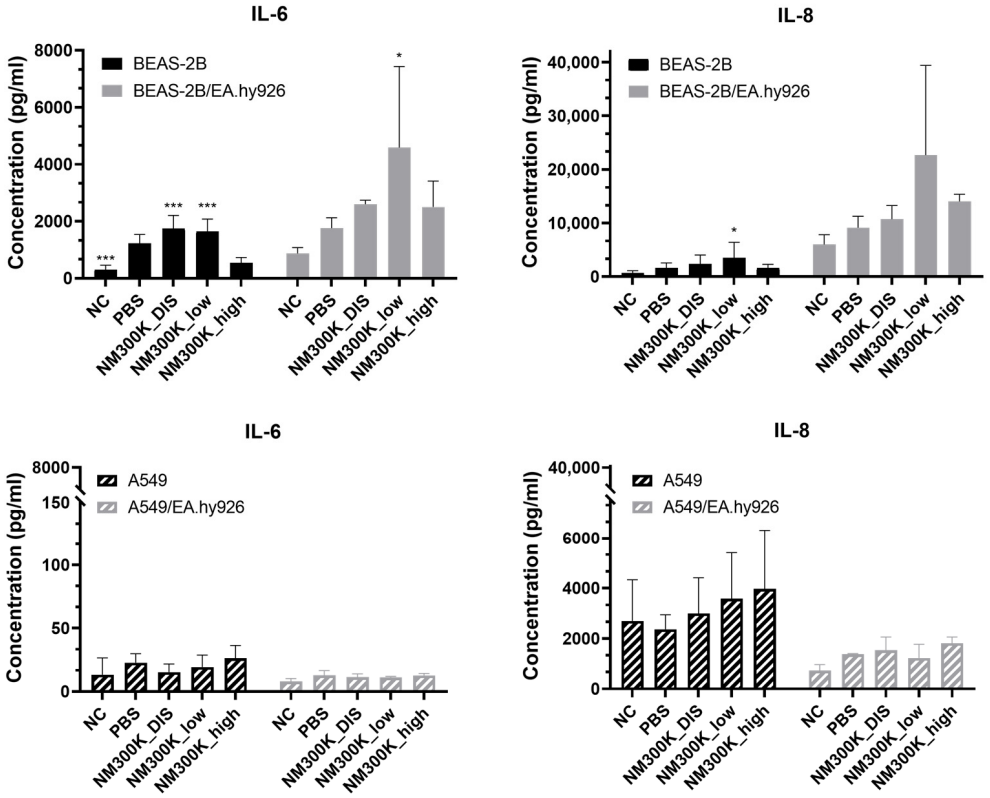

Figure 4. Concentrations of IL-6 and IL-8 in mono- and cocultures of BEAS-2B/EA.hy926 cells (top panel) and A549/EA.hy926 cells (bottom panel) after exposure to aerosolized NM-300K and control solutions at the air–liquid interface, evaluated by ELISA. Results are presented as the mean with standard deviation from single or duplicate inserts from n = 2–6 independent experiments (n = 6 for BEAS-2B monocultures, n = 3 for BEAS-2B/EA.hy926 cocultures and A549 monocultures, and n = 2 for A549/EA.hy926 cocultures). Statistically significant different effects on cytokine concentration compared to the negative control inserts with PBS-exposed cells (PBS) were analyzed by one-way ANOVA followed by Dunnett´s post-hoc test (* $p < 0.05$, *** $p < 0.001$). NC: negative control, PBS: phosphate-buffered saline, NM-300K DIS: dispersant control, NM-300K low: nominal 1 μg/cm^2, NM-300K high: nominal 10 μg/cm^2.

3.3.3. Genotoxicity by DNA and Chromosomal Damage in ALI Cultures

After viability analysis by alamarBlue assay and cytokine secretion analysis by ELISA, cells from the same samples were analyzed for DNA damage by the comet assay and cytokinesis-block micronucleus assay.

Different sensitivities on induction of DNA SBs and oxidized base lesions after exposure to NM-300K were measured by the enzyme-modified comet assay when comparing the different cell types and models. NM-300K exposure at low concentrations induced an increase in DNA SBs and SBs + Fpg in BEAS-2B cells in monoculture, with 26 ± 18% DNA in the tail (Figure 5A), but no effect in cocultures (Figure 5B). No significant effect was measured in BEAS-2B or in EA.hy926 cells (Figure 5) after exposure to high-concentration NM-300K. The levels of DNA SBs were similar in the incubator control (NC) and in samples exposed to PBS. No effect of NM-300K DIS was seen. However, the background of DNA SBs (in NC) was slightly higher in BEAS-2B cells from cocultures (5.9 ± 3.6% DNA in tail, n = 3) compared with monocultures (1.4 ± 1.6% DNA in tail, n = 6). For comparison, submerged NM300-K exposure of BEAS-2B cells did not induce any genotoxicity, as an increase in SBs was detected only at cytotoxic concentrations (from 10 μg/cm^2) (Figure S8).

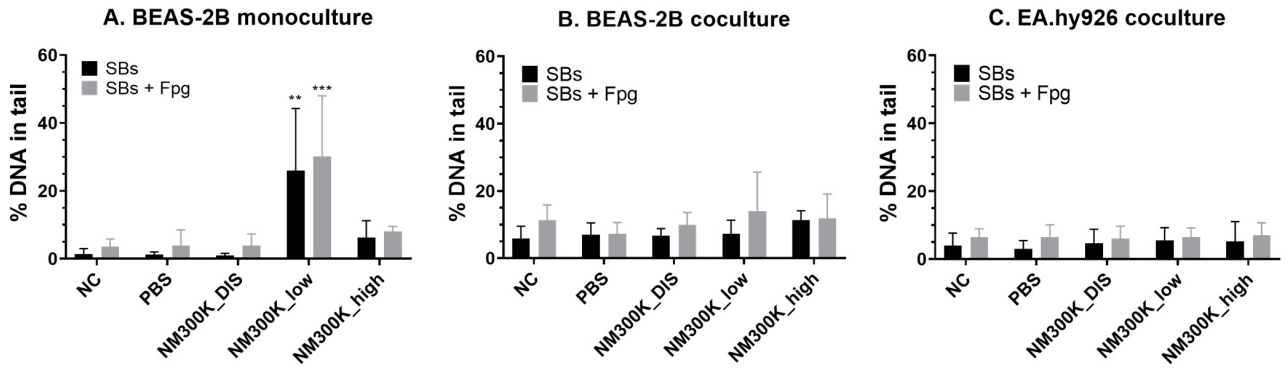

Figure 5. DNA damage by strand breaks (SBs) and oxidized base lesions (Fpg) of BEAS-2B and EA.hy926 cells after exposure to aerosolized NM-300K and control solutions at the air–liquid interface, evaluated by the comet assay. The response of cells in monocultures (**A**) was different compared with cocultures (**B**,**C**). Results are presented as the mean with standard deviation from single or duplicate inserts from n = 3–6 (**A**), n = 3 (**B**), and n = 4 (**C**) independent experiments. Statistically significant different effects on DNA damage compared to control inserts with PBS-exposed cells (PBS) were analyzed by one-way ANOVA followed by Dunnett´s post-hoc test (** $p < 0.01$, *** $p < 0.001$). NC: negative control, PBS: phosphate-buffered saline, NM-300K DIS: dispersant control, NM-300K low: nominal 1 μg/cm^2, NM-300K high: nominal 10 μg/cm^2.

H_2O_2 exposure induced a concentration-related induction of SBs in BEAS-2B cells from monocultures and EA.hy926 cells from cocultures (Figure 6 and Table 5). BEAS-2B cells in cocultures were found to be more sensitive, with a high level of SBs also at the lowest concentrations of H_2O_2 (80 ± 11% DNA in tail at 13 μM H_2O_2). Different media compositions were used in the BEAS-2B monocultures (LHC-9) and in the BEAS-2B/EA.hy926 cocultures (DMEM and LHC-9, 1:1). In submerged cells, which showed less sensitivity to H_2O_2 exposure than ALI cultures, the different media compositions did not affect the viability (Figure S9) or H_2O_2 sensitivity (Table 5 and Figure S10). Cells from A549 mono- and cocultures had a high response to 100 μM H_2O_2, as expected, and only one concentration was tested.

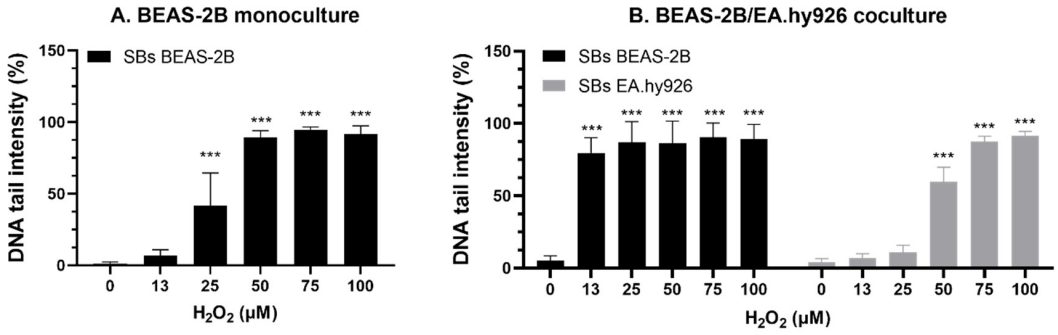

Figure 6. DNA damage by strand breaks (SBs) in BEAS-2B and EA.hy926 cells after exposure to H_2O_2 in gels, evaluated by the comet assay. Cells from unexposed inserts of (**A**) BEAS-2B monocultures and (**B**) BEAS-2B/EA.hy926 cocultures were embedded in gels before H_2O_2 exposure. Results are presented as the mean with standard deviation from single or duplicate inserts from n = 7 (**A**) and n = 3 (**B**) independent experiments. Statistically significant different effects of DNA damage compared to negative control cells without H_2O_2 exposure (0 μM in PBS) were analyzed by one-way ANOVA followed by Dunnett´s post-hoc test (*** $p < 0.001$). NC: negative control; H_2O_2: hydrogen peroxide; PBS: Phosphate-buffered saline.

Table 5. DNA damage response after the hydrogen peroxide (H_2O_2) exposure of BEAS-2B cells from different culturing conditions. Results are presented as the mean with standard deviation from $n = 3$ independent experiments (except ALI monocultures with $n = 6$), each with 1–2 culture inserts or culture wells per treatment. Medium type is presented as the ratio of medium for BEAS-2B cells (LHC-9) and medium for EA.hy926 cells (DMEM). ALI: air–liquid interface, SBs: strand breaks.

Culture Conditions			H_2O_2 Treatment			
			DNA SBs (% DNA in Tail)			EC_{50} (μM)
Culture Type	**Cell Line**	**LHC-9:DMEM**	**12.5 μM**	**25 μM**	**50 μM**	
ALI monoculture	BEAS-2B	1:0	7 ± 4	41 ± 23	89 ± 5	28 ± 6
ALI coculture	BEAS-2B	1:1	80 ± 11	87 ± 14	86 ± 15	4 ± 5
	EA.hy926	1:1	7 ± 3	11 ± 5	60 ± 10	45 ± 5
Submerged monoculture	BEAS-2B	1:0	7 ± 3	24 ± 12	84 ± 14	33 ± 6
		1:1	7 ± 3	18 ± 6	77 ± 10	37 ± 6
		0:1	4 ± 3	27 ± 6	85 ± 5	31 ± 1
	EA.hy926	1:0	18 ± 7	20 ± 5	42 ± 17	70 ± 31
		1:1	16 ± 1	19 ± 2	46 ± 19	>100
		0:1	19 ± 3	12 ± 6	34 ± 5	>100

No significant effect on micronuclei induction was found after exposure to PBS, NM-300K DIS, or NM-300K, on any of the cultures, compared to the PBS control (Figure 7). A high level of micronuclei was induced by the positive control (0.15 μg/mL mitomycin-C in basolateral media) in BEAS-2B and EA.hy926 cells from mono- and cocultures (Figure 7A,B), and slightly lower for A549 in mono- and cocultures (Figure 7C,D). The effect of mitomycin-C in A549 monocultures was significantly different from that of the unexposed NC control only ($p = 0.04$), and the increase in micronuclei formation was not statistically significant from the PBS control ($p = 0.08$). The proportion of binucleated cells in the samples for micronuclei investigation was estimated to be 21% for BEAS-2B and 19% for EA.hy926 cells. Corresponding numbers for A549/EA.hy926 cocultures were about 21% for A549 and 8% for EA.hy926 cells (Figure S1).

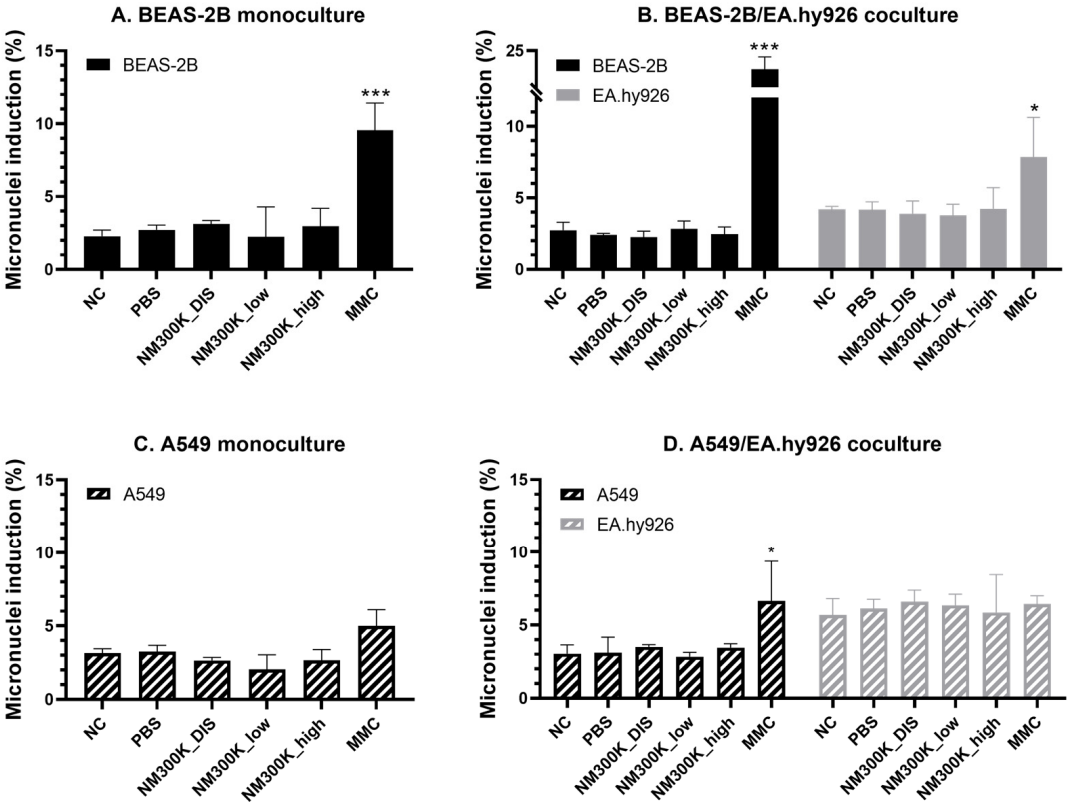

Figure 7. Micronuclei induction in BEAS-2B, EA.hy926 and A549 cells after exposure to aerosolized NM-300K and control solutions at the air–liquid interface, evaluated by the cytokinesis block micronuclei assay. Micronuclei induction was analyzed in cells from BEAS-2B monoculture (**A**), BEAS-2B/EA.hy926 coculture (**B**), A549 monoculture (**C**), and A549/EA.hy926 coculture (**D**). Results are presented as the mean with standard deviation from single or duplicate inserts from $n = 3$ independent experiments. Statistically significant different effects on micronuclei induction compared to control inserts with PBS-exposed cells (PBS) were analyzed by one-way ANOVA followed by Dunnett´s post-hoc test (* $p < 0.05$, *** $p < 0.001$). NC: negative incubator control, PBS: phosphate-buffered saline, NM-300K DIS: dispersant control, NM-300K low: nominal 1 μg/cm^2, NM-300K high: nominal 10 μg/cm^2, MMC: mitomycin-C at 0.15 μg/mL in basolateral medium for 24 h.

4. Discussion

An important part of NAMs, which are essential for NGRA, is the development and characterization of advanced in vitro models. Advanced respiratory in vitro models are of high importance for the hazard assessment of NMs after inhalation exposure. Cells cultured and exposed at the ALI represent a more physiological scenario than cells in submerged conditions. In order to develop the most realistic NAMs, the characterization, testing and validation of models is needed. Of importance to this is comparison of the effects of reference NMs on different advanced models for the same target, as well as to benchmark the effects of the tested NMs against the effects in traditional 2D in vitro models. This study focused on the characterization and application of the immortalized human bronchial epithelial cell line BEAS-2B cultivated at ALI in monoculture or in cocultures with endothelial EA.hy926 cells for the testing of different toxicity endpoints. It is, to our knowledge, the first study to successfully apply several genotoxicity endpoints, including the micronucleus assay, in advanced BEAS-2B cocultures at the ALI, and to perform a comparison of the effects of a reference NM in mono- and cocultures, and also with the more extensively used human alveolar epithelial cell line A549. Further, effects on the

advanced models at the ALI were compared with responses in traditional corresponding submerged cultures in monocultures.

Cell growth, barrier integrity, and confluency differed between mono- and cocultures of BEAS-2B cells. In cocultures with EA.hy926, the BEAS-2B cells had lower confluency compared with monocultures, and they showed a multilayer growth, which was not seen with the A549 cells. Thus, more holes were seen under confocal microscopy in the BEAS-2B epithelial layer, which was also thicker. We found a higher density of BEAS-2B cells in cocultures compared with monocultures, indicating higher cellular growth and stimulated cell proliferation in the cocultures. The opposite was found with A549 cells, where the cells had lower density in cocultures compared to monocultures. The stimulated proliferation of BEAS-2B cells in cocultures with EA.hy926 cells was found not to be due to different media compositions of mono- and cocultures. Rather, the increased proliferation of BEAS-2B cells in coculture might be related to cell signaling from the endothelial cells. The multilayer growth of BEAS-2B cells in coculture indicates that the advanced model facilitates conditions similar to tissue physiology in the lungs, as has been shown also in previous studies [10,54].

In monoculture, BEAS-2B and A549 had similar cell numbers at the end of the cultivation period, despite the longer doubling time (4 h) of BEAS-2B cells compared to A549 [55,56]. The endothelial cells showed a similar density and appearance in both coculture types, with BEAS-2B and A549, respectively.

The barrier function appeared to be less in BEAS-2B cocultures than in monocultures, as indicated by the higher permeability of fluorescein, which was measured in the basolateral medium. This finding is in line with the higher frequency of observed holes in the apical cell layers of cocultures of BEAS-2B. In contrast, Ag permeation was higher in BEAS-2B monocultures than in cocultures. It is known that Ag has a high affinity for sulfur and that it may form toxic complexes with sulfur-containing proteins in the cells [57]. The lower permeation of Ag in the coculture may be explained by the additional barrier constituted by the endothelial cells and the measured higher epithelial cell density in cocultures, and thus increased interaction with or dissolution of the NMs. Ag permeation after exposure to NM-300K at high concentrations was in all culture types similar to the permeation through empty inserts. As total silver was measured, it included both particles and dissolved Ag-ions diffusing from the apical side down the concentration gradient. However, the permeation of Ag was similar after exposure to low and high concentrations, and it was not increased as may be expected by the larger gradient. This low permeability might be due to the agglomeration/aggregation of the nanoparticles at high density, making them less likely to penetrate into the pores of the insert membrane, the pores being blocked, a saturation of the medium, or a combination of these factors.

A549 mono- and cocultures showed less permeation of fluorescein and also of Ag after exposure to low-concentration NM-300K, than BEAS-2B cultures. This is in accordance with previous studies showing that A549 cells form tight junctions [39,46] and thus a stronger barrier, measured as trans-epithelial resistance (TEER), at an earlier stage than BEAS-2B cells [54]. Different bronchial cell lines, including BEAS-2B, cultivated at ALI, were evaluated for barrier functions by He et al., (2021), and only Calu-3 cells were found to sustain a strong TEER for up to 21 days. Also, the immortalized cell line 16HBE formed tight junctions and developed a strong TEER, though the TEER dropped considerably in ALI conditions [10].

In order to compare the responses of the different models to a toxic insult, the cells were exposed to Ag NM-300K, which is a reference NM commonly used in many projects related to the safety of NMs (such as the European Commission FP7 project NanoReg, and H2020 projects NanoReg2, PATROLS and RiskGONE). The relative cell viability of BEAS-2B monocultures at the ALI was reduced by NM-300K exposure at the highest concentration. This is similar to what we observed for A549 monocultures [39]. The viability was reduced at lower concentrations after ALI exposure compared with submerged exposure, which may indicate higher sensitivity of the ALI models. However, direct comparisons between

the models are difficult due to large differences in the experimental conditions including aerosol or submerged exposure, cell number, and cell density.

Significant reduction in cell viability was only measured after exposure to high concentrations of NM-300K in monocultures. In cocultures, we observed that PBS aerosol exposure reduced cell viability of the BEAS-2B cells, compared with incubator control, and thus no significant difference in viability could be detected between PBS and NM exposures. The same effect of PBS was also seen previously with A549 cocultures [39]. This indicates that the coculture conditions at the ALI sensitize the apical epithelial cells to the aerosol exposure both of non-toxic and toxic compounds. One could speculate that the lack of direct basolateral contact with the cell culture media in the cocultures could influence this, due to the confluent layer of the endothelial cells. Additionally, the interaction and interplay between the endothelial cells in itself may play a role. Interestingly, the viability of the endothelial cells was not reduced after PBS exposure in coculture with BEAS-2B but with A549 [39], despite the demonstrated stronger barrier of the A549 epithelial layer.

When genotoxicity was tested, the models showed different sensitivities. Genotoxicity measured as DNA SBs was found only in BEAS-2B monocultures at low concentrations of NM-300K. The lack of genotoxic effects at high concentrations could be due to loss of damaged cells during the washing steps, as cytotoxicity was measured at this concentration. No genotoxic effect was seen in BEAS-2B or in the EA.hy926 cells in coculture. The lack of an effect in the BEAS-2B cells in coculture may be due to the higher cell density and thereby relatively lower number of particles per cell. One may also speculate as to whether the co-cultivation with the endothelial cells may increase the emergency preparedness of the BEAS-2B cells towards toxic insults. The increased level of pro-inflammatory cytokines in the cocultures (Figure 4) may support such a theory, and it has been suggested previously that increased expression of cytokines, such as IL-6, can promote DNA repair [58]. In cocultures of A549 and EA.hy926, genotoxicity measured as SBs was only found in the endothelial cells. However, we previously showed that in triculture with addition of differentiated THP-1 cells, no SBs were detected [39]. These results are not false negative, as NMs were internalized in the A549 cells [39]. A genotoxic response can be secondary due to the induction of an inflammatory response. Thus, we measured IL-6 and IL-8 levels in mono- and cocultures. No significant increase in IL-6 or IL-8 levels was detected in the A549 models after NM-300K exposure. In general, there was a trend towards increased levels after ALI exposure. However, the basal level of IL-8 was much higher in A549 cocultures than in monocultures, which was the opposite as seen with BEAS-2B. For BEAS-2B cocultures, the level of both IL-6 and IL-8 was increased after exposure to low concentration of NM-300K, although statistical significance was reached only for IL-6. The level of IL-6 was also increased in BEAS-2B monocultures at low concentrations of NM-300K, but it was about 9× lower than for cocultures. In contrast, significant induction of SBs was measured only in monocultures at low concentrations of NM-300K. As the toxic response was changed when coculturing different cell types, as compared with monocultures, further studies are merited to elucidate the interplay between the cell types and the importance of coculturing multiple cell types for hazard identification.

Genotoxicity was further tested at the chromosomal level by the micronucleus assay. Few studies have applied the micronucleus assay on advanced human lung models at the ALI; at the time of writing, we found only one publication on monocultured A549 [49], one on monocultured BEAS-2B and other bronchial cell types [59], and four studies on nasal epithelial cells from donors [60–63]. We successfully employed this assay to both mono- and cocultures of BEAS-2B cells exposed at the ALI. The effect of the positive control mitomycin-C (0.15 µg/mL in basolateral medium) was found to be more pronounced in the cocultures. The effect of mitomycin-C on A549 mono- and cocultures was lower than on BEAS-2B, and the effect in A549 monocultures was only significantly different from the unexposed control and not from the PBS control. Mitomycin-C also induced micronuclei in the underlying endothelial cells in coculture with the BEAS-2B-cells, but not with A549 cells, and the proportion of binucleated cells was lower when cocultured

with A549 cells. The epithelial and endothelial cells were cultured with cytochalasin B for the same duration; however, a longer incubation time was used for BEAS-2B/EA.hy926 cocultures compared to A549/EA.hy926 cocultures due to the differences in cell doubling times. Further investigations are needed in order to determine whether the differences in response are due to lower sensitivity towards mitomycin-C when in coculture with A549 or if experimental optimization is needed to produce a higher proportion of binucleated cells.

No aneugenic or clastogenic effects were detected after NM-300K exposure at the ALI, which is in contrast to previous studies with significant micronuclei induction by NM-300K in submerged BEAS-2B cells [64,65]. ALI exposure was performed when the cells had developed a confluent cell layer, which may have affected the cell cycle and proliferation rate. In our study the cells from ALI cultures were directly seeded with cytochalasin B on coverslips after NM treatment, at a lower density to initiate DNA replication and MN formation, before the cell fixation and analysis of MN in binucleated cells. The discrepancy in the effects between submerged and ALI may, therefore, be due to their different stages in division cycles during NM exposure, which merits further experiments to optimize the method. The agglomeration state of the NMs would also influence their toxicity, and this might differ between submerged and ALI exposure. A previous study on titanium dioxide NMs in BEAS-2B cells showed that changes in the composition of exposure medium affected the induction of MN due to differential states of agglomeration [66].

The experimental design presented in this study, enabling several endpoints to be measured from each insert, allows for increased throughput, reduced costs, time and materials and thus better sustainability, compared to measuring all endpoints in separate inserts. This is an important aspect of the NAMs and crucial for an integrated approach to testing and assessment (IATA) in NGRA. Further, more direct comparisons are enabled, as the different endpoints are measured from the same exposure, thus reducing the variability induced by distinct exposures. This is an essential issue, as variability may be expected to increase with the increasing complexity of the model, in line with variability in human responses between individuals. Our results, which showed the toxicity of PBS at the ALI in cocultures compared with an incubator control not exposed at the ALI, point to the importance of always including an incubator control in ALI experiments.

The higher complexity of the advanced models makes them more laborious and maybe less applicable for screening purposes. However, this is significantly improved by the efficient experimental design we here present, which also contributes to more robust mechanistical data, as several endpoints are measured from the same insert. One argument that has been used for the application of more complex cell models is that they may increase the sensitivity towards toxic insults. An approach to test the sensitivity towards the induction of SBs is to expose cells with H_2O_2 on gels directly before lysis. A striking observation was that the BEAS-2B cells in coculture appeared to be much more sensitive to H_2O_2 exposure. Cells in monoculture at ALI showed slightly higher sensitivity to H_2O_2 exposure compared to cells in submerged conditions. Also, the endothelial cells showed higher sensitivity to H_2O_2 when in coculture with BEAS-2B than as submerged monoculture. The culture media formulation appeared to have no influence on the outcome either in terms of viability or sensitivity towards SBs. The reasons for the higher sensitivity to H_2O_2 in coculture are not known and merits further investigations, but it may be related to the above-mentioned interaction between cells in coculture making the DNA more prone to damage.

The higher sensitivity of the BEAS-2B cells in coculture to NM-300K was observed in cell viability by the alamarBlue assay but not on SBs by the comet assay. NM-300K has a high cytotoxic potential and a quite narrow concentration window between non-cytotoxic and cytotoxic effects. During the technical procedure in the sample preparation for comet assay, the cells go through several washing steps, and there are reasons to believe that the more damaged cells are less attached to the insert and can be lost. In the MN assay, the effect of mitomycin-C was most pronounced in the cells from the coculture, which could be an indication that the BEAS-2B cells in coculture may be a more

sensitive model for the hazard assessment of genotoxic compounds, and thus a promising advanced model to be adapted for risk assessment based on in vitro data and an IATA approach. The differences in sensitivity between mono- and cocultures, and between the application of lung epithelial A549 cells or bronchial BEAS-2B cell models, for the various endpoints measured emphasizes the importance of carrying out proper characterization of the emerging advanced models, as well as developing robust SOPs. Further, it points to the importance of developing advanced coculture in vitro models, allowing for intercellular signaling, to better mimic tissue organization and enhance the prediction of human hazard.

5. Conclusions

An important step in finding the best predictive model for human adverse effects is to increase complexity and thereby obtain more tissue- and organ-like structures, use human cells, characterize the models, and compare responses in different models. This work indicates that the bronchial mono- and coculture models of BEAS-2B and EA.hy926 cells have different sensitivities to NM-300K exposure as measured by cytotoxicity and genotoxicity at DNA and chromosomal levels, and they are different from the alveolar models of A549 and EA.hy926 cells. This is important knowledge to provide more robust reproducible and reliable results, for the further development of advanced 3D respiratory in vitro models relevant to inhalation exposure, and to obtain the most reliable hazard identification and prediction of effects on humans based on non-animal studies. This study provides important knowledge for the further development of advanced 3D respiratory in vitro models for the most reliable hazard identification and prediction of the effects from inhalation on human-based NAMs for NGRA.

Supplementary Materials: The following supporting information can be downloaded at: https://www.mdpi.com/article/10.3390/nano13030407/s1, Figure S1: Percentage of binucleated cells in the samples for micronucleus assay; Figure S2: Images of A549/EA.hy926 cocultures at the ALI; Figure S3: Confocal images of advanced bronchial models; Figure S4: Relative cell viability of submerged BEAS-2B cells after exposure to NM-300K and NM-300K DIS; Figure S5: AlamarBlue interference test; Figure S6: Relative concentrations of IL-6 and IL-8 in ALI mono- and cocultures; Figure S7: ELISA interference test of NM-300K in cell culture media; Figure S8: DNA damage by strand breaks and oxidized base lesions in submerged BEAS-2B cells after exposure to NM-300K evaluated by Fpg-modified comet assay; Figure S9: Relative cell viability of submerged BEAS-2B cells after exposure to DMEM and LHC-9 culture media; Figure S10: DNA strand breaks evaluated by the comet assay after exposure to hydrogen peroxide of submerged monocultures of BEAS-2B and EA.hy926 cells with different media compositions. Table S1: Passage numbers; Table S2: Medium types used in mono- and cocultures; Table S3: NM-300K concentrations applied for exposure; Table S4: Number of cell culture inserts per experiment; Table S5: EC50 values for cytotoxic effect of NM-300K on submerged monocultures; Table S6: Concentrations of interleukin 6; Table S7: Concentrations of interleukin 8.

Author Contributions: Conceptualization, E.E., E.M. (Espen Mariussen) and E.R.-P.; formal analysis, E.E. and E.M. (Erin McFadden); investigation, E.E. and E.M. (Erin McFadden); writing—original draft preparation, E.E.; writing—review and editing, E.E., E.M. (Erin McFadden), E.M. (Espen Mariussen), M.D. and E.R.-P.; visualization, E.E.; supervision, E.M. (Espen Mariussen), M.D. and E.R.-P.; project administration, E.M. (Espen Mariussen), M.D. and E.R.-P.; funding acquisition, E.M. (Espen Mariussen), M.D. and E.R.-P. All authors have read and agreed to the published version of the manuscript.

Funding: This research was funded by The Norwegian Research Council, NanoBioReal project: 288768; The Norwegian Research Council Ph.D. project (E.E.): 272412/F40; TEPCAN project funded by the Program "Applied research" under the Norwegian Financial Mechanisms 2014–2021/POLNOR 2019 (EEA and Norway Grants), Thematic areas: welfare, health and care: NCBR Funding No. NOR/POLNOR/TEPCAN/0057/2019-00; European Union's Horizon 2020 research and innovation program RiskGONE: 814425; European Union's Horizon 2020 research and innovation program TWINALT: 952404—H2020-WIDESPREAD-2020-5.

Data Availability Statement: Data are available from the researchers on request.

Acknowledgments: The authors would like to thank Mihaela R. Cimpan and Ivan Rios Mondragon (University of Bergen, Norway) for the loan of LHC-9 medium, Marit Vadset (NILU) for performing ICP-MS analysis, Tatiana Honza (NILU) for assistance with comet scoring, Rudolf Dreschler (Metasystems) and Naouale El Yamani (NILU) for training on/assistance with the use of the Metafer system and expert opinions, Andrew Collins and Sergey Shaposhnikov (NorGenoTec AS, Norway) for providing the Fpg, and Reidun Torp (University of Oslo, Norway) for a critical revision of the manuscript. The graphical abstract was created with BioRender.com.

Conflicts of Interest: The authors declare no conflict of interest.

References

1. Bonner, J.C. Molecular Mechanisms of Respiratory Toxicity. In *Molecular and Biochemical Toxicology*; Smart, R.C., Hodgson, E., Eds.; Wiley: Hoboken, NJ, USA, 2018.
2. Oberdörster, G.; Oberdörster, E.; Oberdörster, J. Nanotoxicology: An Emerging Discipline Evolving from Studies of Ultrafine Particles. *Environ. Health Perspect.* **2005**, *113*, 823–839. [CrossRef] [PubMed]
3. Miller, M.R.; Raftis, J.B.; Langrish, J.P.; McLean, S.G.; Samutrtai, P.; Connell, S.P.; Wilson, S.; Vesey, A.T.; Fokkens, P.H.B.; Boere, A.J.F.; et al. Inhaled Nanoparticles Accumulate at Sites of Vascular Disease. *ACS Nano* **2017**, *11*, 4542–4552. [CrossRef] [PubMed]
4. Raftis, J.B.; Miller, M.R. Nanoparticle Translocation and Multi-Organ Toxicity: A Particularly Small Problem. *Nano Today* **2019**, *26*, 8–12. [CrossRef] [PubMed]
5. Hadrup, N.; Sharma, A.K.; Loeschner, K.; Jacobsen, N.R. Pulmonary Toxicity of Silver Vapours, Nanoparticles and Fine Dusts: A Review. *Regul. Toxicol. Pharmacol.* **2020**, *115*, 104690. [CrossRef]
6. Zavala, J.; Freedman, A.N.; Szilagyi, J.T.; Jaspers, I.; Wambaugh, J.F.; Higuchi, M.; Rager, J.E. New Approach Methods to Evaluate Health Risks of Air Pollutants: Critical Design Considerations for In Vitro Exposure Testing. *Int. J. Environ. Res. Public Health* **2020**, *17*, 2124. [CrossRef]
7. Pfuhler, S.; van Benthem, J.; Curren, R.; Doak, S.H.; Dusinska, M.; Hayashi, M.; Heflich, R.H.; Kidd, D.; Kirkland, D.; Luan, Y.; et al. Use of in Vitro 3D Tissue Models in Genotoxicity Testing: Strategic Fit, Validation Status and Way Forward. Report of the Working Group from the 7th International Workshop on Genotoxicity Testing (IWGT). *Mutat. Res. Genet. Toxicol. Environ. Mutagen.* **2020**, *850–851*, 503135. [CrossRef]
8. Lacroix, G.; Koch, W.; Ritter, D.; Gutleb, A.C.; Larsen, S.T.; Loret, T.; Zanetti, F.; Constant, S.; Chortarea, S.; Rothen-Rutishauser, B.; et al. Air-Liquid Interface in Vitro Models for Respiratory Toxicology Research: Consensus Workshop and Recommendations. *Appl. In Vitro Toxicol.* **2018**, *4*, 91–106. [CrossRef]
9. Heijink, I.H.; Brandenburg, S.M.; Noordhoek, J.A.; Postma, D.S.; Slebos, D.J.; van Oosterhout, A.J.M. Characterisation of Cell Adhesion in Airway Epithelial Cell Types Using Electric Cell-Substrate Impedance Sensing. *Eur. Respir. J.* **2010**, *35*, 894–903. [CrossRef]
10. He, R.W.; Braakhuis, H.M.; Vandebriel, R.J.; Staal, Y.C.M.; Gremmer, E.R.; Fokkens, P.H.B.; Kemp, C.; Vermeulen, J.; Westerink, R.H.S.; Cassee, F.R. Optimization of an Air-Liquid Interface in Vitro Cell Co-Culture Model to Estimate the Hazard of Aerosol Exposures. *J. Aerosol Sci.* **2021**, *153*, 105703. [CrossRef]
11. Collins, A.R. The Use of Bacterial Repair Endonucleases in the Comet Assay. In *Methods in Molecular Biology*; Humana Press Inc.: Totowa, NJ, USA, 2017; Volume 1641, pp. 173–184. [CrossRef]
12. Kohl, Y.; Rundén-Pran, E.; Mariussen, E.; Hesler, M.; el Yamani, N.; Longhin, E.M.; Dusinska, M. Genotoxicity of Nanomaterials: Advanced In Vitro Models and High Throughput Methods for Human Hazard Assessment—A Review. *Nanomaterials* **2020**, *10*, 1911. [CrossRef]
13. OECD. Test No. 487: In Vitro Mammalian Cell Micronucleus Test. In *OECD Guidelines for the Testing of Chemicals, Section 4*; OECD Publishing: Paris, France, 2016. [CrossRef]
14. Magdolenova, Z.; Collins, A.; Kumar, A.; Dhawan, A.; Stone, V.; Dusinska, M. Mechanisms of Genotoxicity. A Review of in Vitro and in Vivo Studies with Engineered Nanoparticles. *Nanotoxicology* **2014**, *8*, 233–278. [CrossRef]
15. Butt, Y.; Kurdowska, A.; Allen, T.C. Acute Lung Injury: A Clinical and Molecular Review. *Arch. Pathol. Lab. Med.* **2016**, *140*, 345–350. [CrossRef] [PubMed]
16. Ekstrand-Hammarström, B.; Akfur, C.M.; Andersson, P.O.; Lejon, C.; Österlund, L.; Bucht, A. Human Primary Bronchial Epithelial Cells Respond Differently to Titanium Dioxide Nanoparticles than the Lung Epithelial Cell Lines A549 and BEAS-2B. *Nanotoxicology* **2012**, *6*, 623–634. [CrossRef] [PubMed]
17. Borish, L.C.; Steinke, J.W. 2. Cytokines and Chemokines. *J. Allergy Clin. Immunol.* **2003**, *111*, S460–S475. [CrossRef]
18. Zou, J.; Zhou, L.; Hu, C.; Jing, P.; Guo, X.; Liu, S.; Lei, Y.; Yang, S.; Deng, J.; Zhang, H. IL-8 and IP-10 Expression from Human Bronchial Epithelial Cells BEAS-2B Are Promoted by Streptococcus Pneumoniae Endopeptidase O (PepO). *BMC Microbiol.* **2017**, *17*, 187. [CrossRef]
19. Napierska, D.; Thomassen, L.C.J.; Vanaudenaerde, B.; Luyts, K.; Lison, D.; Martens, J.A.; Nemery, B.; Hoet, P.H.M. Cytokine Production by Co-Cultures Exposed to Monodisperse Amorphous Silica Nanoparticles: The Role of Size and Surface Area. *Toxicol. Lett.* **2012**, *211*, 98–104. [CrossRef] [PubMed]

20. Khair, O.A.; Davies, R.J.; Devalia, J.L. Bacterial-Induced Release of Inflammatory Mediators by Bronchial Epithelial Cells. *Eur. Respir. J.* **1996**, *9*, 1913–1922. [CrossRef]
21. Adler, K.B.; Fischer, B.M.; Wright, D.T.; Cohn, L.A.; Becker, S. Interactions between Respiratory Epithelial Cells and Cytokines: Relationships to Lung Inflammation. *Ann. N. Y. Acad. Sci.* **1994**, *725*, 128–145. [CrossRef]
22. Longhin, E.; Holme, J.A.; Gualtieri, M.; Camatini, M.; Øvrevik, J. Milan Winter Fine Particulate Matter (WPM2.5) Induces IL-6 and IL-8 Synthesis in Human Bronchial BEAS-2B Cells, but Specifically Impairs IL-8 Release. *Toxicol. In Vitro* **2018**, *52*, 365–373. [CrossRef]
23. Tian, G.; Wang, J.; Lu, Z.; Wang, H.; Zhang, W.; Ding, W.; Zhang, F. Indirect Effect of PM 1 on Endothelial Cells via Inducing the Release of Respiratory Inflammatory Cytokines. *Toxicol. In Vitro* **2019**, *57*, 203–210. [CrossRef]
24. Herzog, F.; Loza, K.; Balog, S.; Clift, M.J.D.; Epple, M.; Gehr, P.; Petri-Fink, A.; Rothen-Rutishauser, B. Mimicking Exposures to Acute and Lifetime Concentrations of Inhaled Silver Nanoparticles by Two Different in Vitro Approaches. *Beilstein J. Nanotechnol.* **2014**, *5*, 1357–1370. [CrossRef]
25. Klein, S.G.; Cambier, S.; Hennen, J.; Legay, S.; Serchi, T.; Nelissen, I.; Chary, A.; Moschini, E.; Krein, A.; Blömeke, B.; et al. Endothelial Responses of the Alveolar Barrier in Vitro in a Dose-Controlled Exposure to Diesel Exhaust Particulate Matter. *Part. Fibre Toxicol.* **2017**, *14*, 7. [CrossRef]
26. Di Ianni, E.; Erdem, J.S.; Møller, P.; Sahlgren, N.M.; Poulsen, S.S.; Knudsen, K.B.; Zienolddiny, S.; Saber, A.T.; Wallin, H.; Vogel, U.; et al. In Vitro-in Vivo Correlations of Pulmonary Inflammogenicity and Genotoxicity of MWCNT. *Part. Fibre Toxicol.* **2021**, *18*, 25. [CrossRef]
27. Meindl, C.; Öhlinger, K.; Zrim, V.; Steinkogler, T.; Fröhlich, E. Screening for Effects of Inhaled Nanoparticles in Cell Culture Models for Prolonged Exposure. *Nanomaterials* **2021**, *11*, 606. [CrossRef]
28. Barosova, H.; Karakocak, B.B.; Septiadi, D.; Petri-Fink, A.; Stone, V.; Rothen-Rutishauser, B. An In Vitro Lung System to Assess the Proinflammatory Hazard of Carbon Nanotube Aerosols. *Int. J. Mol. Sci.* **2020**, *21*, 5335. [CrossRef] [PubMed]
29. Cappellini, F.; di Bucchianico, S.; Karri, V.; Latvala, S.; Malmlöf, M.; Kippler, M.; Elihn, K.; Hedberg, J.; Wallinder, I.O.; Gerde, P.; et al. Dry Generation of CeO2 Nanoparticles and Deposition onto a Co-Culture of A549 and THP-1 Cells in Air-Liquid Interface—Dosimetry Considerations and Comparison to Submerged Exposure. *Nanomaterials* **2020**, *10*, 618. [CrossRef] [PubMed]
30. Wang, Y.; Adamcakova-Dodd, A.; Steines, B.R.; Jing, X.; Salem, A.K.; Thorne, P.S. Comparison of in Vitro Toxicity of Aerosolized Engineered Nanomaterials Using Air-Liquid Interface Mono-Culture and Co-Culture Models. *NanoImpact* **2020**, *18*, 100215. [CrossRef] [PubMed]
31. Loret, T.; Peyret, E.; Dubreuil, M.; Aguerre-Chariol, O.; Bressot, C.; le Bihan, O.; Amodeo, T.; Trouiller, B.; Braun, A.; Egles, C.; et al. Air-Liquid Interface Exposure to Aerosols of Poorly Soluble Nanomaterials Induces Different Biological Activation Levels Compared to Exposure to Suspensions. *Part. Fibre Toxicol.* **2016**, *13*, 58. [CrossRef]
32. Herzog, F.; Clift, M.J.D.; Piccapietra, F.; Behra, R.; Schmid, O.; Petri-Fink, A.; Rothen-Rutishauser, B. Exposure of Silver-Nanoparticles and Silver-Ions to Lung Cells in Vitro at the Air-Liquid Interface. *Part. Fibre Toxicol.* **2013**, *10*, 11. [CrossRef]
33. Friesen, A.; Fritsch-Decker, S.; Hufnagel, M.; Mülhopt, S.; Stapf, D.; Weiss, C.; Hartwig, A. Gene Expression Profiling of Mono- and Co-Culture Models of the Respiratory Tract Exposed to Crystalline Quartz under Submerged and Air-Liquid Interface Conditions. *Int. J. Mol. Sci.* **2022**, *23*, 7773. [CrossRef]
34. Kaur, K.; Mohammadpour, R.; Ghandehari, H.; Reilly, C.A.; Paine, R.; Kelly, K.E. Effect of Combustion Particle Morphology on Biological Responses in a Co-Culture of Human Lung and Macrophage Cells. *Atmos. Environ.* **2022**, *284*, 119194. [CrossRef] [PubMed]
35. Friesen, A.; Fritsch-Decker, S.; Hufnagel, M.; Mülhopt, S.; Stapf, D.; Hartwig, A.; Weiss, C. Comparing α-Quartz-Induced Cytotoxicity and Interleukin-8 Release in Pulmonary Mono- and Co-Cultures Exposed under Submerged and Air-Liquid Interface Conditions. *Int. J. Mol. Sci.* **2022**, *23*, 6412. [CrossRef] [PubMed]
36. Gábelová, A.; el Yamani, N.; Alonso, T.I.; Buliaková, B.; Srančíková, A.; Bábelová, A.; Pran, E.R.; Fjellsbø, L.M.; Elje, E.; Yazdani, M.; et al. Fibrous Shape Underlies the Mutagenic and Carcinogenic Potential of Nanosilver While Surface Chemistry Affects the Biosafety of Iron Oxide Nanoparticles. *Mutagenesis* **2017**, *32*, 193–202. [CrossRef] [PubMed]
37. El Yamani, N.; Collins, A.R.; Rundén-Pran, E.; Fjellsbø, L.M.; Shaposhnikov, S.; Zielonddiny, S.; Dusinska, M. In Vitro Genotoxicity Testing of Four Reference Metal Nanomaterials, Titanium Dioxide, Zinc Oxide, Cerium Oxide and Silver: Towards Reliable Hazard Assessment. *Mutagenesis* **2017**, *32*, 117–126. [CrossRef]
38. Elje, E.; Mariussen, E.; Moriones, O.H.; Bastús, N.G.; Puntes, V.; Kohl, Y.; Dusinska, M.; Rundén-Pran, E. Hepato(Geno)Toxicity Assessment of Nanoparticles in a HepG2 Liver Spheroid Model. *Nanomaterials* **2020**, *10*, 545. [CrossRef]
39. Camassa, L.M.A.; Elje, E.; Mariussen, E.; Longhin, E.M.; Dusinska, M.; Zienolddiny-Narui, S.; Rundén-Pran, E. Advanced Respiratory Models for Hazard Assessment of Nanomaterials—Performance of Mono-, Co- and Tricultures. *Nanomaterials* **2022**, *12*, 2609. [CrossRef]
40. Klein, C.L.; Comero, S.; Stahlmecke, B.; Romazanov, J.; Kuhlbusch, T.A.J.; van Doren, E.; De Temmerman, P.-J.; Mast, T.J.; Wick, P.; Krug, H.; et al. *NM-Series of Representative Manufactured Nanomaterials NM-300 Silver Characterisation, Stability, Homogeneity*; Publications Office of the European Union: Luxembourg, 2011. [CrossRef]
41. Jensen, K.A.; Clausen, P.A.; Birkedal, R.; Kembouche, Y.; Christiansen, E.; Jacobsen, N.R.; Levin, M.; Koponen, I.; Wallin, H.; de Temmerman, P.-J.; et al. Towards a Method for Detecting the Potential Genotoxicity of Nanomaterials. Deliverable 3. Final Protocol for Producing Suitable Manufactured Nanomaterial Exposure Media. The Generic NANOGENOTOX Dispersion

Protocol. Standard Operating Procedure (SOP) and Background Documentation. Available online: https://www.anses.fr/en/system/files/nanogenotox_deliverable_5.pdf (accessed on 17 June 2022).
42. Ke, Y.; Reddel, R.R.; Gerwin, B.I.; Miyashita, M.; McMenamin, M.; Lechner, J.F.; Harris, C.C. Human Bronchial Epithelial Cells with Integrated SV40 Virus T Antigen Genes Retain the Ability to Undergo Squamous Differentiation. *Differentiation* **1988**, *38*, 60–66. [CrossRef]
43. Reddel, R.R.; Ke, Y.; Kaighn, M.E.; Malan-Shibley, L.; Lechner, J.F.; Rhim, J.S.; Harris, C.C. Human Bronchial Epithelial Cells Neoplastically Transformed by V-Ki-Ras: Altered Response to Inducers of Terminal Squamous Differentiation. *Oncogene Res.* **1988**, *3*, 401–408.
44. Lieber, M.; Todaro, G.; Smith, B.; Szakal, A.; Nelson-Rees, W. A Continuous Tumor-Cell Line from a Human Lung Carcinoma with Properties of Type II Alveolar Epithelial Cells. *Int. J. Cancer* **1976**, *17*, 62–70. [CrossRef]
45. Suggs, J.E.; Madden, M.C.; Friedman, M.; Edgell, C.J.S. Prostacyclin Expression by a Continuous Human Cell Line Derived from Vascular Endothelium. *Blood* **1986**, *68*, 825–829. [CrossRef]
46. Rothen-Rutishauser, B.M.; Kiama, S.C.; Gehr, P. A Three-Dimensional Cellular Model of the Human Respiratory Tract to Study the Interaction with Particles. *Am. J. Respir. Cell. Mol. Biol.* **2005**, *32*, 281–289. [CrossRef] [PubMed]
47. Klein, S.G.; Serchi, T.; Hoffmann, L.; Blömeke, B.; Gutleb, A.C. An Improved 3D Tetraculture System Mimicking the Cellular Organisation at the Alveolar Barrier to Study the Potential Toxic Effects of Particles on the Lung. *Part. Fibre Toxicol.* **2013**, *10*, 31. [CrossRef] [PubMed]
48. Ding, Y.; Weindl, P.; Lenz, A.G.; Mayer, P.; Krebs, T.; Schmid, O. Quartz Crystal Microbalances (QCM) Are Suitable for Real-Time Dosimetry in Nanotoxicological Studies Using VITROCELL®Cell Exposure Systems. *Part. Fibre Toxicol.* **2020**, *17*, 44. [CrossRef] [PubMed]
49. Binder, S.; Cao, X.; Bauer, S.; Rastak, N.; Kuhn, E.; Dragan, G.C.; Monsé, C.; Ferron, G.; Breuer, D.; Oeder, S.; et al. In Vitro Genotoxicity of Dibutyl Phthalate on A549 Lung Cells at Air–Liquid Interface in Exposure Concentrations Relevant at Workplaces. *Environ. Mol. Mutagen.* **2021**, *62*, 490–501. [CrossRef]
50. Elje, E.; Hesler, M.; Rundén-Pran, E.; Mann, P.; Mariussen, E.; Wagner, S.; Dusinska, M.; Kohl, Y. The Comet Assay Applied to HepG2 Liver Spheroids. *Mutat. Res. Genet. Toxicol. Environ. Mutagen.* **2019**, *845*, 403033. [CrossRef] [PubMed]
51. Dusinska, M.; Mariussen, E.; Rundén-Pran, E.; Hudecova, A.M.; Elje, E.; Kazimirova, A.; el Yamani, N.; Dommershausen, N.; Tharmann, J.; Fieblinger, D.; et al. In Vitro Approaches for Assessing the Genotoxicity of Nanomaterials. In *Methods in Molecular Biology*; Humana Press Inc.: Totowa, NJ, USA, 2019; Volume 1894, pp. 83–122. [CrossRef]
52. El Yamani, N.; Mariussen, E.; Gromelski, M.; Wyrzykowska, E.; Grabarek, D.; Puzyn, T.; Tanasescu, S.; Dusinska, M.; Rundén-Pran, E. Hazard Identification of Nanomaterials: In Silico Unraveling of Descriptors for Cytotoxicity and Genotoxicity. *Nano Today* **2022**, *46*, 101581. [CrossRef]
53. Rundén-Pran, E. Hazard assessment of spherical and rod-shaped silver nanomaterials by an advanced lung model at the air-liquid interface. Manuscript in Preparation. 2023.
54. Schlinkert, P.; Casals, E.; Boyles, M.; Tischler, U.; Hornig, E.; Tran, N.; Zhao, J.; Himly, M.; Riediker, M.; Oostingh, G.J.; et al. The Oxidative Potential of Differently Charged Silver and Gold Nanoparticles on Three Human Lung Epithelial Cell Types. *J. Nanobiotechnol.* **2015**, *13*, 1. [CrossRef]
55. A549—CCL-185 | ATCC. Available online: https://www.atcc.org/products/ccl-185 (accessed on 10 October 2022).
56. Haniu, H.; Saito, N.; Matsuda, Y.; Tsukahara, T.; Maruyama, K.; Usui, Y.; Aoki, K.; Takanashi, S.; Kobayashi, S.; Nomura, H.; et al. Culture Medium Type Affects Endocytosis of Multi-Walled Carbon Nanotubes in BEAS-2B Cells and Subsequent Biological Response. *Toxicol. In Vitro* **2013**, *27*, 1679–1685. [CrossRef]
57. Le Ouay, B.; Stellacci, F. Antibacterial Activity of Silver Nanoparticles: A Surface Science Insight. *Nano Today* **2015**, *10*, 339–354. [CrossRef]
58. Centurione, L.; Aiello, F.B. DNA Repair and Cytokines: TGF-β, IL-6, and Thrombopoietin as Different Biomarkers of Radioresistance. *Front. Oncol.* **2016**, *6*, 175. [CrossRef]
59. Platel, A.; Privat, K.; Talahari, S.; Delobel, A.; Dourdin, G.; Gateau, E.; Simar, S.; Saleh, Y.; Sotty, J.; Antherieu, S.; et al. Study of in Vitro and in Vivo Genotoxic Effects of Air Pollution Fine (PM2.5-0.18) and Quasi-Ultrafine (PM0.18) Particles on Lung Models. *Sci. Total Environ.* **2020**, *711*, 134666. [CrossRef] [PubMed]
60. Koehler, C.; Ginzkey, C.; Friehs, G.; Hackenberg, S.; Froelich, K.; Scherzed, A.; Burghartz, M.; Kessler, M.; Kleinsasser, N. Aspects of Nitrogen Dioxide Toxicity in Environmental Urban Concentrations in Human Nasal Epithelium. *Toxicol. Appl. Pharmacol.* **2010**, *245*, 219–225. [CrossRef]
61. Koehler, C.; Ginzkey, C.; Friehs, G.; Hackenberg, S.; Froelich, K.; Scherzed, A.; Burghartz, M.; Kessler, M.; Kleinsasser, N. Ex Vivo Toxicity of Nitrogen Dioxide in Human Nasal Epithelium at the WHO Defined 1-h Limit Value. *Toxicol. Lett.* **2011**, *207*, 89–95. [CrossRef] [PubMed]
62. Koehler, C.; Thielen, S.; Ginzkey, C.; Hackenberg, S.; Scherzed, A.; Burghartz, M.; Paulus, M.; Hagen, R.; Kleinsasser, N.H. Nitrogen Dioxide Is Genotoxic in Urban Concentrations. *Inhal. Toxicol.* **2013**, *25*, 341–347. [CrossRef] [PubMed]
63. Wiest, F.; Scherzad, A.; Ickrath, P.; Poier, N.; Hackenberg, S.; Kleinsasser, N. Studies on Toxicity and Inflammatory Reactions Induced by E-Cigarettes: In Vitro Exposure of Human Nasal Mucosa Cells to Propylene Glycol at the Air–Liquid Interface. *HNO* **2021**, *69*, 952–960. [CrossRef] [PubMed]

64. Cervena, T.; Rossnerova, A.; Zavodna, T.; Sikorova, J.; Vrbova, K.; Milcova, A.; Topinka, J.; Rossner, P. Testing Strategies of the in Vitro Micronucleus Assay for the Genotoxicity Assessment of Nanomaterials in Beas-2b Cells. *Nanomaterials* **2021**, *11*, 1929. [CrossRef]
65. García-Rodríguez, A.; Kazantseva, L.; Vila, L.; Rubio, L.; Velázquez, A.; Ramírez, M.J.; Marcos, R.; Hernández, A. Micronuclei Detection by Flow Cytometry as a High-Throughput Approach for the Genotoxicity Testing of Nanomaterials. *Nanomaterials* **2019**, *9*, 1677. [CrossRef]
66. Prasad, R.Y.; Wallace, K.; Daniel, K.M.; Tennant, A.H.; Zucker, R.M.; Strickland, J.; Dreher, K.; Kligerman, A.D.; Blackman, C.F.; Demarini, D.M. Effect of Treatment Media on the Agglomeration of Titanium Dioxide Nanoparticles: Impact on Genotoxicity, Cellular Interaction, and Cell Cycle. *ACS Nano* **2013**, *7*, 1929–1942. [CrossRef]

nanomaterials

MDPI

Supplementary materials

Different sensitivity of advanced bronchial and alveolar mono- and coculture models for hazard assessment of nanomaterials

Elisabeth Elje [1,2,*], Espen Mariussen [1,3], Erin McFadden [1], Maria Dusinska [1] and Elise Rundén-Pran [1,*]

[1] NILU—Norwegian Institute for Air Research, Department for Environmental Chemistry, Health Effects Laboratory, 2007 Kjeller, Norway

[2] University of Oslo, Institute of Basic Medical Sciences, Department of Molecular Medicine, 0372 Oslo, Norway

[3] Norwegian Institute of Public Health, FHI, 0456 Oslo, Norway

* Correspondence: eel@nilu.no (E.E.) ; erp@nilu.no (E.R.P.); Tel.: +47 63 89 81 98

S1. Cell cultures

The passage numbers for BEAS-2B, A549 and EA.hy926 cells used in this study is summarized in Table S1. The culture medium and supplements are summarized in Table S2.

Table S1. Passage numbers for BEAS-2B, A549 and EA.hy926 cells.

Culture	BEAS-2B	A549	EA.hy926
ALI monocultures	3,6,8,9,10,12,13,14	3,5,6,8,9,11,13,15	-
ALI cocultures	8,10,12,14	2,3,9,11,13,15	Coculture with BEAS-2B: 9,11,13,16. Coculture with A549: 3,5,7,9,10.
Submerged monocultures	3,5,7,8,9,13	3,5,9,12	4,7,8,12,19

Table S2. Medium types used in mono- and cocultures, with supplements. DMEM: Dulbecco's modified Eagle's medium, with low glucose or high glucose; FBS: Fetal bovine serum; PS: penicillin-streptomycin. 1% PS equals 100 U/mL penicillin and 100 μg/mL streptomycin. % given as vol/vol.

Cell type	Medium	Serum	Supplement
Monocultures			
BEAS-2B	100 % LHC-9	-	-
A549	90 % DMEM low glucose	9 % FBS	1 % PS
EA.hy926	90 % DMEM high glucose	9 % FBS	1 % PS
			4 mM L-glutamine
			1 mM Sodium pyruvate
Co-cultures			
BEAS-2B/EA.hy926	50 % LHC-9	4.5 % FBS	0.5 % PS
	45 % DMEM high glucose		2 mM L-glutamine
			0.5 mM Sodium pyruvate
A549/EA.hy926	18 % DMEM low glucose	9 % FBS	1 % PS
	72 % DMEM high glucose		3.5 mM L-glutamine
			0.9 mM Sodium pyruvate

S1. Cytokinesis-block micronucleus assay

The semi-automatic scoring system identified mono- and binucleated cells. A minimum of 500 binucleated cells was scored for micronuclei of most samples, however, this was not possible for all samples due to low number of cells possible to score. The selected settings for scoring and analysis did not identify all binucleated cells with micronuclei, giving some false negative and false positive cells. Thus, all identified binucleated cells were manually accepted or rejected, and cells with possible micronuclei were checked with a 40x objective.

The percentage of binucleated cells in the populations used for micronucleus assay, was estimated by dividing the number of binucleated cells by the total number of analyzed cells. This is a minimum estimate, because the total numbers of analyzed cells were not checked in detail for all samples and thus may include some false positives/artefacts. Results are summarized in Figure S1. About 20% of the BEAS-2B and A549 cells were binucleated. EA.hy926 cells had about 19% binucleated cells when in coculture with BEAS-2B, and about 8% when in coculture with A549 cells.

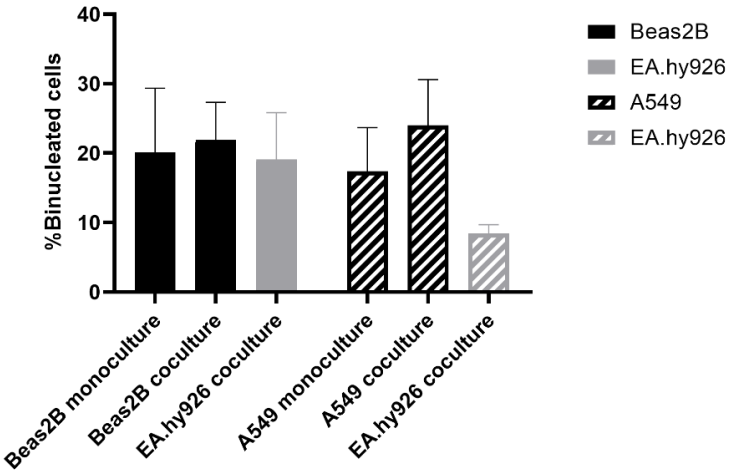

Figure S1. Percentage of binucleated cells in the samples for micronucleus assay. The numbers are minimum estimates.

S3. NM-300K concentrations for exposure

The concentrations of NM-300K applied for air-liquid interface exposure and submerged exposure are summarized in Table S3, with metrics mass per culture area and mass per volume of medium. The concentrations were corrected to measured Ag concentration in the stock dispersion by dividing the concentration by nominal stock concentration (10 mg/ml) and multiplying with corrected concentration (7.2 mg/ml).

Table S3. NM-300K concentrations applied for exposure, given as metrics mass per culture area and mass per volume of medium. ALI: air-liquid interface. *Corrected based on analysis of total Ag in the stock dispersion and on cell-free culture inserts, in our previous paper Camassa & Elje et al, 2022 [1].

	Nominal concentrations		**Corrected concentrations***	
	µg/cm²	**µg/ml**	**µg/cm²**	**µg/ml**
Submerged	0.1	0.1	0.1	0.1
	0.3	0.4	0.2	0.3
	1.0	1.4	0.7	1.0
	3.0	4.2	2.2	3.1
	10.0	14.1	7.2	10.2
	30.0	42.4	21.6	30.5
	75.0	106.0	54.0	76.3
	100.0	141.4	72.0	101.8
ALI low conc.	1	-	0.8	-
ALI high conc.	10	-	6.0	-

S4. Number of replica inserts and experiments

The number of cell culture inserts (= technical replica) per experiment for each test method is summarized in Table S4.

Table S4. Number of cell culture inserts per experiment. Models are described by cell types present; BEAS-2B (monoculture), BEAS-2B/EA.hy926 (coculture), A549 (monoculture), and A549/EA.hy926 (coculture). ELISA: enzyme-linked immunosorbent assay. MMC: mitomycin-C. CHLO: chlorpromazine hydrochloride.
* From our previous paper [1].

Test method	Model	Compartment	Exp	Number of inserts							Ref
				NC	PBS	NM-300K DIS	NM-300K low	NM-300K high	MMC	CHLO	
Fluorescein permeation	BEAS-2B	Basolateral	Exp1	2	2						
			Exp2	1	1						
	BEAS-2B/EA.hy926	Basolateral	Exp1	1	2						
			Exp2	1	1						
	Empty insert	Basolateral	Exp1	2							
			Exp2	2							
Ag permeation	BEAS-2B	Basolateral	Exp1			1	1	1			
			Exp2			1	1	1			
			Exp3				1	1			
	BEAS-2B/EA.hy926	Basolateral	Exp1			1	1	1			
			Exp2			1	1	1			
			Exp3				1	1			
	A549	Basolateral	Exp1			1	2	2			*
			Exp2			1		1			*
			Exp3				2	2			*
	A549/EA.hy926	Basolateral	Exp1			1		1			*
			Exp2			2	2	2			*
			Exp3				1				*
	Empty insert	Basolateral	Exp1					1			*
			Exp2					1			*
ELISA	BEAS-2B	Basolateral	Exp1	2	2	2	2	2			
			Exp2	2	2	1	2	2			
			Exp3	1	1	1	1	1			
			Exp4	1	1	1	1	0			
			Exp5	2	2	0	2	0			
			Exp6	2	0	0	0	0			
	BEAS-2B/EA.hy926	Basolateral	Exp1	2	1	1	1	1			
			Exp2	1	1	1	1	1			
			Exp3	2	1	1	1	1			

Table S4 continued.

ELISA	A549	Basolateral	Exp1	1	1	1	1	1		
			Exp2	2	2	2	2	2		
			Exp3	2	1	1	1	1		
	A549/EA.hy926	Basolateral	Exp1	2	2	2	2	2		
			Exp2	2	2	2	2	2		
alamarBlue	BEAS-2B	Apical	Exp1	2	2					2
			Exp2	2	2		2			1
			Exp3	2	2	2	2	2	2	1
			Exp4	2	2	1	2	2		
			Exp5	2	1	1	1	1	1	1
			Exp6	1	1	1	1	1	1	1
			Exp7	2	1	1	1	1	1	1
	BEAS-2B/EA.hy926	Apical	Exp1	2	1	1	1	1	1	1
			Exp2	1	1	1	1	1	1	1
			Exp3	2	1	1	1	1	2	1
			Exp4	2	1	1	1	1	0	1
		Basolateral	Exp1	2	1	1	1	1	1	1
			Exp2	1	1	1	1	1	1	1
			Exp3	2	1	1	1	1	2	1
			Exp4	2	1	1	1	1	0	1
Comet assay	BEAS-2B	Apical	Exp1	2	2	2	2	2		
			Exp2	2	2	1	2	2		
			Exp3	1	1	1	1	1		
			Exp4	1	1	1	1	0		
			Exp5	2	2	0	2	0		
			Exp6	2	0	0	0	0		
	BEAS-2B/EA.hy926	Apical	Exp1	2	1	1	1	1		
			Exp2	1	1	1	1	1		
			Exp3	2	1	1	1	1		
		Basolateral	Exp1	2	1	1	1	1		
			Exp2	1	1	1	1	1		
			Exp3	2	1	1	1	1		
			Exp4	2	1	1	1	1		

Table S4 continued.

Micronucleus	BEAS-2B	Apical	Exp1	2	1	1	1	1	1
			Exp2	1	1	1	1	1	1
			Exp3	2	1	1	1	1	1
	BEAS-2B/EA.hy926	Apical	Exp1	2	1	1	1	1	1
			Exp2	1	1	1	1	1	1
			Exp3	2	1	1	1	1	1
		Basolateral	Exp1	2	1	1		1	1
			Exp2	1	1	1	1	1	1
			Exp3	2	1	1	1	1	1
	A549	Apical	Exp1	1		1	1	1	1
			Exp2	2	2	2	2	2	2
			Exp3	2	1	1	1	1	1
	A549/EA.hy926	Apical	Exp1	2	2	2	2	2	1
			Exp2	2	2	2	2	2	2
			Exp3	2	2	2	2	2	2
		Basolateral	Exp1	2	2	2	2	2	2
			Exp2	2	2	2	2	2	2
			Exp3	2	2	2	2	2	2

S5. Advanced models

The advanced models of epithelial and endothelial cells cultured on permeable inserts were moist with a shiny surface when cultured in ALI. However, occasionally a lack of moisture/shine was seen (Figure S2). The parts with more dry appearance were located in variable positions on the insert. This was occasionally seen in all types of cultures and was not systematically investigated. Confocal microscopy of the BEAS-2B/EA.hy926 cocultures, indicated that the BEAS-2B cells were growing in multilayers (Figure S3).

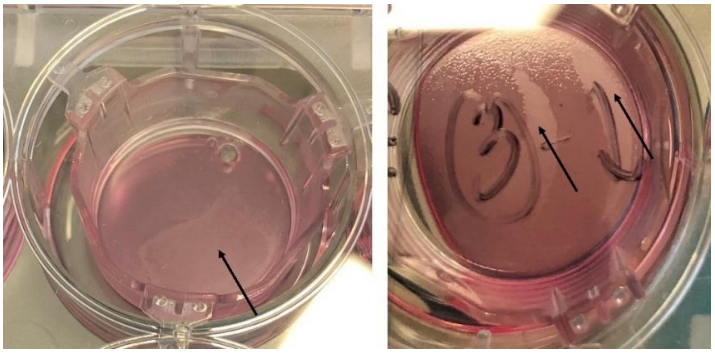

Figure S2. Images of A549/EA.hy926 cocultures at the ALI, cultured on permeable 1 μm 6 well inserts. Occasionally, a lack of moisture/shine was seen, marked by black arrows in the images.

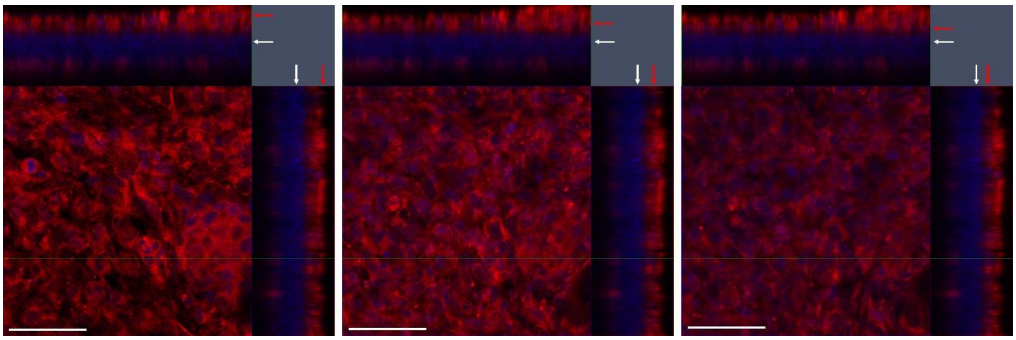

Figure S3. Confocal images of advanced bronchial models. Z-stack image series (2D x-y view and respective side views) showing the distribution of BEAS-2B on the apical side sides of a transwell insert (white arrows), at different heights from the insert (red arrows). The distance from the insert is decreasing from left to right. Z-stack thickness 52 μm. Red: cellular membranes stained with Cell Mask red dye, blue: nuclei counterstained with DAPI. Magnification: 40x. Scale bars 50 μm.

S6. AlamarBlue assay on submerged cells after NM-300K exposure

For comparison of the new advanced models with corresponding traditional cell models, the cytotoxicity of NM-300K was tested also with submerged exposure of monocultured cells by alamarBlue assay. BEAS-2B cells (P5-13) were seeded at a density of 15.000 cells/well (5.3x10^4 cells/cm^2) in 96-well plates pre-coated with Collagen IV. Precoating was performed for BEAS-2B only, with 40 μl of 30 μg/ml Collagen IV overnight at 4 °C, and plates were washed with PBS and used immediately. A549 (P3-12) were seeded in 96-well plates at 10.000 cells/well (3.5 x10^4 cells/cm^2), and EA.hy926 (P4-19) at 10.000 cells/well (3.5 x10^4 cells/cm^2) or 15.000 cells/well (5.3x10^4 cells/cm^2). Equal cell density was used for all samples within each experiment. The cells were incubated overnight at 37 °C and 5 % CO_2. The next day, the cells were exposed to nominal concentrations 0.1-100 μg/cm^2 NM-300K diluted in culture medium (200 μl/well) for 24 h. For corresponding mass/volume and corrected concentrations, see Table S3. BEAS-2B cells were also exposed to corresponding concentrations of NM-300K DIS (solvent control), diluted in cell culture medium. Negative control was exposed to culture medium only. Positive control chlorpromazine hydrochloride was prepared as described in main article and exposed to the cells in the apical media (200 μl/well) for 24 h. Cells were exposed in duplicates or triplicates.

AlamarBlue assay was performed on submerged cultures as described in section 2.11 in the main article, except with smaller volumes and longer incubation time. After exposure, the cells were washed twice with 100 μl PBS before 200 μl alamarBlue solution (10 % v/v) was added to each well. Aliquots were taken in triplicates (40 μl/well) for fluorescence reading after 3 h incubation at 37 °C and 5 % CO_2. Negative control was cells exposed to culture media only.

The viability of BEAS-2B, A549 and EA.hy926 cells, relative to cells exposed to culture medium only (set to 100 %), was affected by NM-300K (Figure S4 and Table S5) and NM-300K DIS (Figure S4). BEAS-2B cells were more sensitive to NM-300K exposure compared to A549 and EA.hy926 cells. The effective concentration giving 50 % cytotoxicity (EC_{50}) was 16.4 μg/cm^2 for BEAS-2B and about the double for A549 (Table S5, [2, 3]). The positive control chlorpromazine hydrochloride reduced the viability as expected (by >80 %, not shown). NM-300K DIS was cytotoxic at concentrations equivalent to 37 μg/cm^2 NM-300K, and no effect was seen at the concentration equivalent to about 10 μg/cm^2 (Figure S4).

To test if the NM-300K interfered with the readout of the AB assay, separate cell-free samples with NM-300K and AB solution were analyzed. NMs were diluted in LHC-9 culture medium to concentrations 0.1-100 μg/cm^2 and mixed with 10% (v/v) AB solution,

including blank sample (AB-medium without NMs), to a final volume of 200 µl per well in a 96 well plate. The plates were incubated at 37 °C and 5 % CO_2 for approximately 3h. The solution was mixed by pipet, and 40 µl aliquots were transferred in duplicate to black 96 well plates, before fluorescence (excitation 530 nm, emission 590 nm) was measured on a FLUOstar OPTIMA microplate reader. Results were averaged and compared to blank. Three independent experiments were performed, each with 1 well per concentration and at least 2 blanks. No difference was seen in fluorescence intensity from samples with NMs compared to blank, which indicate no interference between the NM-300K and the AB assay (Figure S5).

Table S5. Calculated EC_{50} (effective concentration giving 50 % cytotoxicity) values for cytotoxic effect of NM-300K on submerged monocultures of BEAS-2B, A549 and EA.hy926 cells measured by the alamarBlue assay after 24h exposure. Values are given with dose metrics mass per surface (µg/cm²) and mass per volume (µg/ml) ± standard deviation, based on nominal concentrations. Results are calculated from at least 2 independent experiments (n=2) and presented with standard deviation (BEAS-2B, EA.hy926) or standard error of the mean (A549).

Cell line	EC_{50} µg/cm²	EC_{50} µg/ml	Reference
BEAS-2B	16.4 ± 6.0	23.2 ± 8.4	-
A549	37 ± 15	59 ± 43	[2]
EA.hy926	22.5 ± 8.2	36.0 ± 13.1	[3]

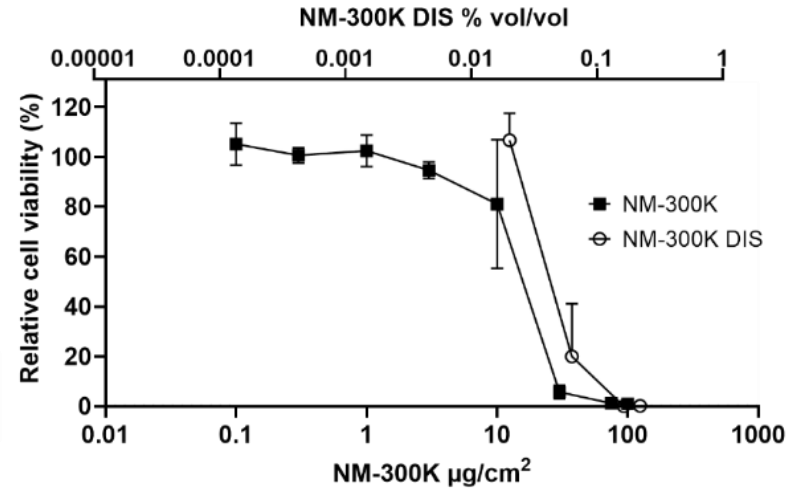

Figure S4. Relative cell viability of BEAS-2B cells after 24h submerged exposure to NM-300K (black squares) and NM-300K DIS (open circles), evaluated by alamarBlue assay. Results are presented as mean with SD from duplicate culture wells from n=4 independent experiments. Positive control (chlorpromazine hydrochloride 50-100 µM for 24h) gave a relative viability of <20 % (not shown in figure). Statistically significant different effects on cell viability compared to negative control cultures with cells exposed to medium (0 µg/cm²) were analyzed by one-way ANOVA followed by Dunnett´s post-hoc test (*P<0.05, **P<0.01, *** P<0.001). SD: standard deviation.

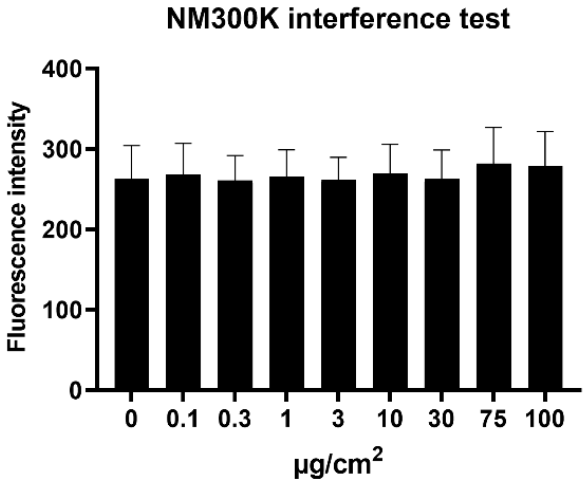

Figure S5. Alamarblue interference test, n=3 with single wells. No statistically significant different from blank (0 µg/cm^2), tested by one-way ANOVA followed by Dunnett´s post-hoc test. Nominal concentrations are shown. Please see Table S1 for concentrations as mass/volume and corrected after ICP-MS analysis.

S7. Enzyme-linked immunosorbent assay (ELISA)

The concentrations of IL-6 and IL-8 measured by ELISA are summarized in Table S6 and S7, and relative concentrations (relative to NC) in Figure S6. Potential interference between NM-300K and the performance of the ELISA was investigated. NM-300K was prepared as described in the main document, and diluted in cell culture media for BEAS-2B cells, A549 cells, or EA.hy926 cells, to achieve the concentrations 30, 3 and 0.3 µg/ml. The NMs in media were added to the ELISA plate in duplicates and mixed with reagent buffer or standard (25 pg/ml IL-6 or 31 pg/ml IL-8) provided in the kit. Further steps in the assay were run as described for the other samples (in main document). The results showed no interference between the NM-300K and the assay. The culture medium with and without NM-300K had similar absorbance as the blank samples of the kit. The combination of IL-6 or IL-8 and NM-300K had similar measured interleukin concentration as the NM-free control samples (Figure S7).

Table S6. Concentrations of interleukin 6 (IL-6) by the enzyme-linked immunosorbent assay (ELISA). Mean ± standard deviation (n independent experiments).

Treatment	BEAS-2B	BEAS-2B/EA.hy926	A549	A549/EA.hy926
NC	304 ± 158 (n=6)	875 ± 203 (n=3)	13 ± 13 (n=3)	8 ± 2 (n=2)
PBS	1229 ± 313 (n=6)	1758 ± 364 (n=3)	23 ± 7 (n=2)	13 ± 4 (n=2)
NM-300K_DIS	1744 ± 461 (n=5)	2604 ± 138 (n=3)	15 ± 6 (n=3)	11 ± 2 (n=2)
NM-300K_low	1647 ± 432 (n=6)	4595 ± 2842 (n=3)	19 ± 9 (n=3)	11 ± 1 (n=2)
NM-300K_high	542 ± 189 (n=5)	2501 ± 910 (n=3)	26 ± 10 (n=3)	13 ± 2 (n=2)

Table S7. Concentrations of interleukin 8 (IL-8) by the enzyme-linked immunosorbent assay (ELISA). Mean ± standard deviation (n independent experiments).

Treatment	BEAS-2B	BEAS-2B/EA.hy926	A549	A549/EA.hy926
NC	660 ± 444 (n=6)	5991 ± 1838 (n=3)	2695 ± 1637 (n=3)	725 ± 238 (n=2)
PBS	1640 ± 921 (n=6)	9140 ± 2135 (n=3)	2366 ± 579 (n=2)	1377 ± 27 (n=2)
NM-300K_DIS	2354 ± 1693 (n=5)	10728 ± 2541 (n=3)	2996 ± 1416 (n=3)	1534 ± 525 (n=2)
NM-300K_low	3500 ± 2903 (n=5)	22672 ± 16736 (n=3)	3580 ± 1830 (n=3)	1227 ± 545 (n=2)
NM-300K_high	1618 ± 692 (n=5)	14053 ± 1308 (n=3)	3969 ± 2360 (n=3)	1816 ± 246 (n=2)

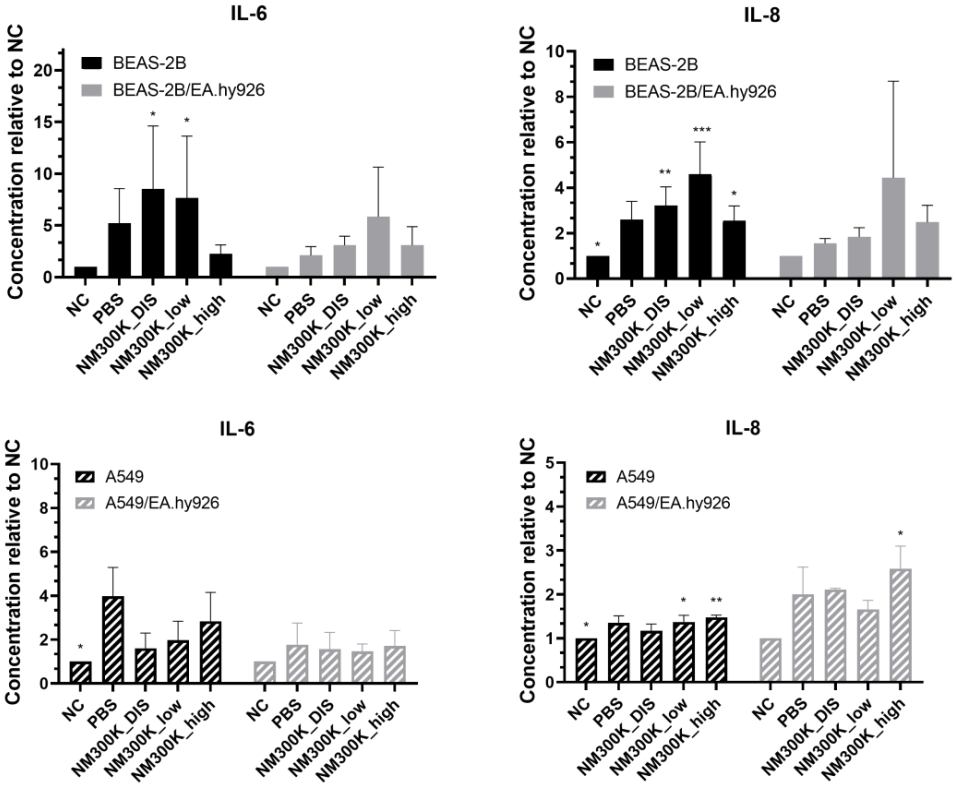

Figure S6. Relative concentrations of IL-6 and IL-8 in mono- and co-cultures of BEAS-2B/EA.hy926 cells (top panel) and A549/EA.hy926 cells (bottom panel) after exposure to aerosolized NM-300K and control solutions at the air-liquid interface, evaluated by ELISA. Results are presented as mean with SD from single or duplicate inserts from n=2-6 independent experiments (n=6 for BEAS-2B monocultures, n=3 for BEAS-2B/EA.hy926 cocultures and A549 monocultures, and n=2 for A549/EA.hy926 cocultures). Statistically significant different effects on cell viability compared to negative control inserts with non-exposed cells (NC) were analyzed by one-way ANOVA followed by Dunnett´s post-hoc test (*P<0.05, **P<0.01, *** P<0.001). NC: negative control; PBS: Phosphate buffered saline; SD: standard deviation.

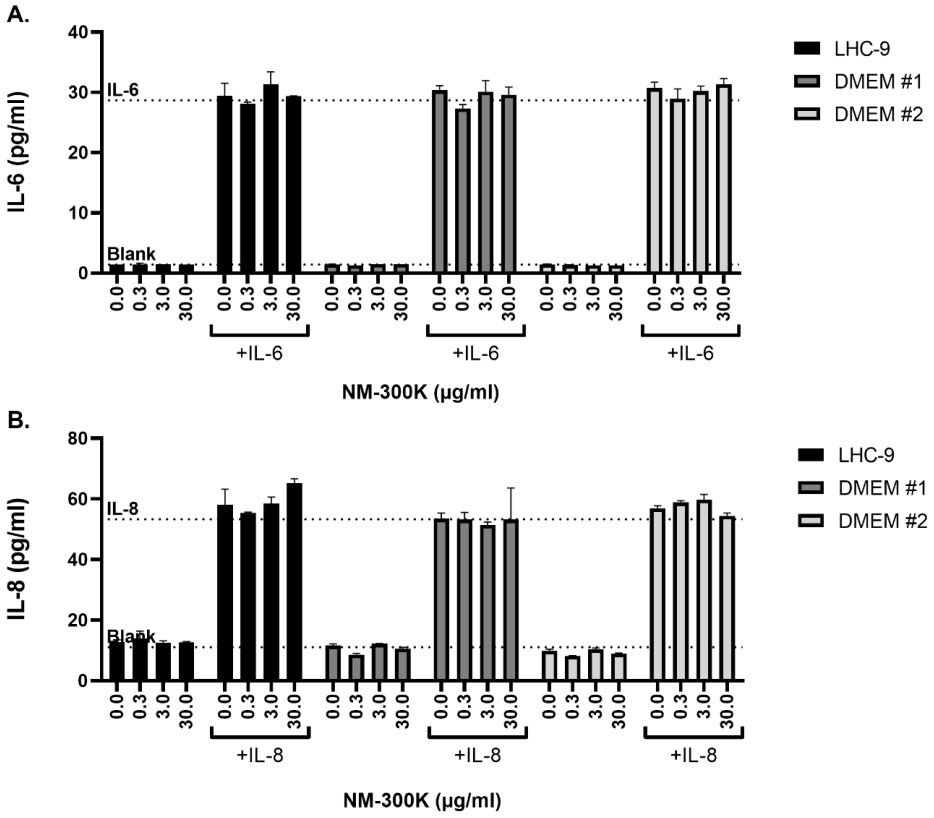

Figure S7. ELISA interference test of NM-300K in cell culture media. No interference of NM-300K with the ELISA was found, as the measured concentrations of interleukin 6 (A) and 8 (B) in samples with mixture of NM-300K, cell culture medium, and interleukins were in the same range as the corresponding controls. The test was run with duplicate samples. LHC-9 (black): medium for BEAS-2B cells, DMEM #1 (dark grey): medium for A549 cells, DMEM #2 (light grey): medium for EA.hy926 cells.

S7. Comet assay on submerged cells after NM-300K exposure

The induction of DNA damage after exposure to NM-300K was measured by the comet assay. Cells were exposed as described above for alamarBlue assay on submerged cultures. Comet assay was performed as described in section 2.13 in the main article. First, cells were washed twice with 100 µl PBS, and detached by dry trypsinization for 3-5 min at 37 °C and 5 % CO_2. Cells were resuspended in 150 µl medium. Immediately after, 50 µl cell suspension was mixed with 200 µl LMP-agarose. Separate cell cultures were used for alamarBlue and comet assays. Potential interference between NM-300K and the readout of the comet assay was investigated as described in [39].

NM-300K caused increased levels of DNA SBs and oxidized base lesions at cytotoxic concentrations only (Figure S8). A slight increase in SBs was seen at 10 µg/cm^2. However, no effect was seen at 1 µg/cm^2, corresponding to the concentration giving DNA damage after ALI exposure of BEAS-2B monocultures. No interference was seen (not shown).

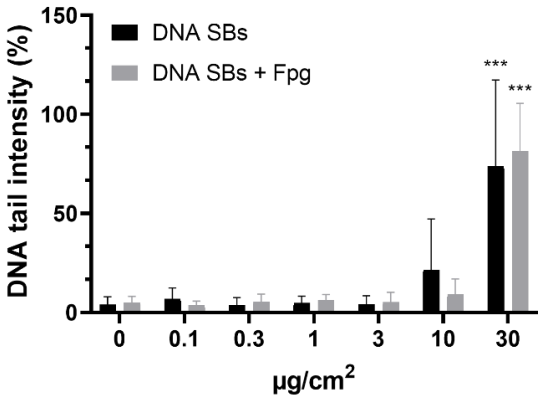

Figure S8. DNA damage by strand breaks (SBs) and oxidized base lesions (SBs + Fpg) in BEAS-2B cells after 24 hours submerged exposure to NM-300K (nominal concentrations) evaluated by Fpg-modified comet assay. Results are presented as mean with SD from n=3 independent experiments, each with duplicate exposure wells, except for DNA SBs + Fpg 10 and 30 µg/cm² where n=2. Statistically significant different effects on DNA damage compared to negative control cultures with cells exposed to medium (0 µg/cm²) were analyzed by one-way ANOVA followed by Dunnett´s post-hoc test (*p<0.05, **p<0.01, ***p<0.001). SBs: strand breaks; SD: standard deviation.

S7. Effect of medium composition on cyto- and genotoxicity in BEAS-2B and EA.hy926 cells

Different media compositions were used in the BEAS-2B monocultures (LHC-9) and in the BEAS-2B/EA.hy926 cocultures (DMEM and LHC-9, 1:1), and we wanted to investigate if this could influence on the different sensitivity in the measured cyto- and genotoxicity of the cells. Thus, the relative viability and DNA damage responses of submerged BEAS-2B or EA.hy926 cells were evaluated after 24 h exposure to LHC-9 and DMEM media at different ratios (10-100 %).

No difference in relative viability (Figure S9) or background levels of DNA SBs or Fpg sites (not shown) was seen on either of the cell types with the different media compositions, compared to cells cultured in the cells' respective media. Induction of DNA damage by H_2O_2 exposure in the gels was similar for the submerged cells with different media compositions (Figure S10). The submerged BEAS-2B cells had less sensitivity to H_2O_2 compared to BEAS-2B cells from mono- or cocultures at ALI conditions (Table 5 in article). Rather high background of DNA SBs was seen in EA.hy926 cells, and less sensitivity to H_2O_2 compared to BEAS-2B cells, independently on the culture media (Figure S10).

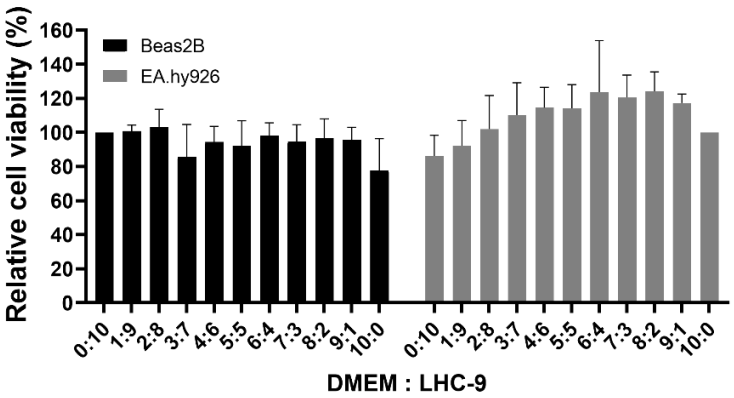

Figure S9. Relative cell viability of BEAS-2B cells after 24h submerged exposure to DMEM and LHC-9 culture media, evaluated by AlamarBlue assay. Results are presented as mean with SD from triplicate culture wells from n=3 independent experiments. Positive control (chlorpromazine hydrochloride 100 μM for 24h) gave a relative viability of <5 % (not shown in figure). Statistically significant different effects on cell viability compared to negative control cultures with cells exposed to the respective culture medium (LHC-9 for BEAS-2B, DMEM for EA.hy926) were analyzed by one-way ANOVA followed by Dunnett´s post-hoc test. No statistically significant results were found (P>0.05). SD: standard deviation.

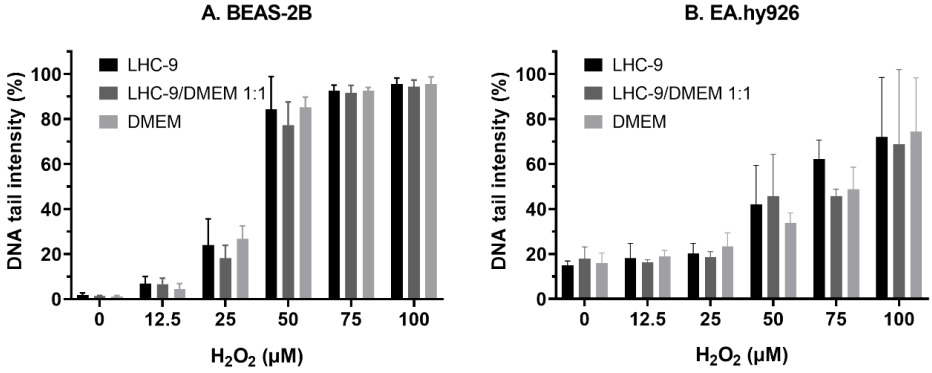

Figure S10. DNA strand breaks (SBs) evaluated by the comet assay after exposure to hydrogen peroxide (H_2O_2) of monocultures of BEAS-2B (A) and EA.hy926 (B) cells cultivated at submerged conditions with different media compositions. Results are presented as mean with SD from duplicate culture wells from n=3 independent experiments. SBs: strand breaks, SD: standard deviation.

References

1. Camassa, L. M. A.; Elje, E.; Mariussen, E.; Longhin, E. M.; Dusinska, M.; Zienolddiny-Narui, S.; Rundén-Pran, E. Advanced Respiratory Models for Hazard Assessment of Nanomaterials—Performance of Mono-, Co- and Tricultures. Nanomaterials 2022, Vol. 12, Page 2609 2022, 12 (15), 2609. https://doi.org/10.3390/NANO12152609.

2. El Yamani, N.; Mariussen, E.; Gromelski, M.; Wyrzykowska, E.; Grabarek, D.; Puzyn, T.; Tanasescu, S.; Dusin-ska, M.; Rundén-Pran, E. Hazard Identification of Nanomaterials: In Silico Unraveling of Descriptors for Cytotoxicity and Genotoxicity. Nano Today 2022, 46, 101581. https://doi.org/10.1016/J.NANTOD.2022.101581.

3. Rundén-Pran, E. Manuscript in Preparation. 2023.

IV

Mutat Res Gen Tox En 845 (2019) 403033

Contents lists available at ScienceDirect

Mutat Res Gen Tox En

journal homepage: www.elsevier.com/locate/gentox

The comet assay applied to HepG2 liver spheroids

Elisabeth Elje[a], Michelle Hesler[b], Elise Rundén-Pran[a], Pascal Mann[b], Espen Mariussen[a], Sylvia Wagner[b], Maria Dusinska[a], Yvonne Kohl[b,*]

[a] NILU – Norwegian Institute for Air Research, Department for Environmental Chemistry, Health Effects Laboratory, Instituttveien 18, 2007 Kjeller, Norway
[b] Fraunhofer Institute for Biomedical Engineering IBMT, Department Bioprocessing & Bioanalytics, Joseph-von-Fraunhofer-Weg 1, 66280 Sulzbach, Germany

ARTICLE INFO

Keywords:
Liver spheroids
Advanced *in vitro* model
Genotoxicity
Comet assay
2D and 3D culture

ABSTRACT

In accordance with the 3 Rs to reduce *in vivo* testing, more advanced *in vitro* models, moving from 2D monolayer to 3D cultures, should be developed for prediction of human toxicity of industrial chemicals and environmental pollutants. In this study we compared cytotoxic and genotoxic responses induced by chemicals in 2D and 3D spheroidal cultures of the human liver cancer cell line HepG2.

HepG2 spheroids were prepared by hanging drop technology. Both 3D spheroids and 2D monolayer cultures were exposed to different chemicals (colchicine, chlorpromazine hydrochloride or methyl methanesulfonate) for geno- and cytotoxicity studies. Cytotoxicity was investigated by alamarBlue assay, flow cytometry and confocal imaging. DNA damage was investigated by the comet assay with and without Fpg enzyme for detection of DNA strand breaks and oxidized or alkylated base lesions.

The results from the cyto- and genotoxicity tests showed differences in sensitivity comparing the 2D and 3D HepG2 models. This study shows that human 3D spheroidal hepatocellular cultures can be successfully applied for genotoxicity testing by the comet assay and represent a promising advanced *in vitro* model for toxicity testing.

1. Introduction

In experimental toxicology, there is an ongoing shift towards increased use of *in vitro* models in compliance with the 3 Rs to reduce, replace and refine animal experiments. The importance of developing new advanced *in vitro* models, that decrease the costs and time for hazard characterization and risk assessment but still provide reliable results, is stressed in the Regulation made by the EU Registration, Evaluation, Authorization and restriction of Chemicals (REACH) (EC No 1907/2006) [1]. Also, *in vitro* models allow utilization of human cells, which might better reflect human effects than *in vivo* rodent models [2–4]. For standard *in vitro* models, the cells are grown in two dimensions. Compared to the *in vivo* situation, these models comprise limited intercellular signaling, which is an important aspect in cellular responses and cell survival after exposure to chemical compounds [3,4]. Thus, *in vitro* models with cells arranged in a three-dimensional (3D) structure, resembling cell organization of tissues and organs, are likely to better mimic responses in humans. The development of advanced 3D models has gained increased attention within the last two decades [5,6]. Models for the assessment of toxicity must reflect the *in vivo* situation as closely as possible. The existing 3D cell models vary widely due to the diverse requirements of different cell lines and applications, and each model has its own advantages and limitations [7–9].

Liver models are important for toxicity testing, as the liver is a main target organ for substances reaching systemic circulation and plays a central role in metabolism as well as the toxification and de-toxification of substances. Liver 3D models can be prepared by hydrogel, scaffold based technologies or spheroidal culture techniques [4,6,9]. Hepatocytes growing in spheroids have become a highly used 3D model, where monodispersed cells self-organize themselves into a spherical conformation as the adhesion to the culture substrate is prevented [4]. Cultures of primary human hepatocytes are considered as the gold standard for studying metabolism and toxicity [4,9,10]. However, because of difficulties associated with isolating and culturing of cells, costs and inter-donor variation, much research has been directed towards using alternatives, such as hepatic-derived cell lines [4,11].

The human hepatocellular carcinoma cell line HepG2 is frequently used in early safety assessment because of availability, unlimited cell

Abbreviations: 2D, two-dimensional; 3D, three-dimensional; ALT, alanine transaminase; AST, aspartate aminotransferase; CHLO, chlorpromazine hydrochloride; COL, colchicine; FDA, fluorescein diacetate; FPG, formamidopyrimidine DNA glycosylase; ECM, extracellular matrix; GDH, glutamate dehydrogenase; MMS, methyl methanesulfonate; PBS, phosphate buffered saline; PI, propidium iodide; SEM, standard error of the mean; SBs, strand breaks

* Corresponding author.
E-mail address: yvonne.kohl@ibmt.fraunhofer.de (Y. Kohl).

https://doi.org/10.1016/j.mrgentox.2019.03.006
Received 21 November 2018; Received in revised form 6 March 2019; Accepted 15 March 2019
Available online 29 March 2019

growth and high reproducibility of results [12,13]. The HepG2 cell line has many liver-specific functions [14–16] and is used as a screening model for cytotoxic substances and to study the metabolism of xenobiotics [17]. The cells are highly differentiated and reflect the liver activity of human parenchymal liver cells [17,18], such as synthesis and secretion of plasma proteins and cell surface receptors [17,19]. However, the HepG2 cell line has limited hepatocyte functionality in 2D culture [9]. Spheroids of HepG2 cells have been shown to comprise enhanced liver-like functionality compared to 2D cultures by upregulation of genes involved in liver-specific xenobiotic and lipid metabolism [4,20], and formation of bile canalicular-like structures and tight cell-cell interactions [4,21,22], making it a more realistic liver model. Compared to the 2D HepG2 cultures, HepG2 spheroids are described as cultures with a high activity of liver-specific functions, e.g. albumin [23–25], urea synthesis [23,24] and CYP expression [24–26].

3D cultures can be applied for different toxicological endpoints [3,5]. An important endpoint in hazard characterization is genotoxicity. The micronucleus assay has successfully been applied on HepG2 spheroids to detect chromosomal damage [26]. The comet assay is a very useful technique for screening of genotoxic potential of compounds. Several genotoxic endpoints can be detected, such as DNA strand breaks (SBs) and oxidized or alkylated base lesions [27–33], and the comet assay can provide an early prediction of a compound's mutagenic and carcinogenic potential [34,35]. Thus, the development of protocols for application of 3D cultures for genotoxicity assessment (via e.g. the comet assay) is needed for a better and more precise prediction of adverse effects on human health after environmental exposure.

The current study is, to our knowledge, the first study on the application of the comet assay to spheroidal HepG2 cultures. Colchicine (COL), chlorpromazine hydrochloride (CHLO), and methyl methanesulfonate (MMS) were used for cytotoxicity evaluation, and MMS and hydrogen peroxide (H_2O_2) were used for evaluating potential differences in response and sensitivity of genotoxicity in 2D and 3D HepG2 cultures.

2. Materials and methods

2.1. Cultivation of HepG2 cells

HepG2 cells, provided from the ECACC-European Collection of Authenticated Cell Cultures (cell line no. 85011430, Salisbury, United Kingdom) and Leibniz-Institut DSMZ-Deutsche Sammlung von Mikroorganismen und Zellkulturen GmbH (cell line no. ACC-180, Braunschweig, Germany), were cultured in Dulbecco's modified Eagle's medium (DMEM D6046 with low glucose and 4 mM L-glutamine, Sigma-Aldrich) or Roswell Park Memorial Institute medium (RPMI 1640, R8758, Sigma-Aldrich) supplemented with 10% v/v fetal bovine serum (FBS, 26140-079 ThermoFisher Scientific), 100 U/ml penicillin and 100 µg/ml streptomycin (5070-63, ThermoFisher Scientific). Experiments were performed in two independent laboratories. For experiments at NILU (Laboratory 1) with cells from ECACC DMEM was used, and RPMI was used at Fraunhofer IBMT (Laboratory 2) for cells from DSMZ. Cells were passaged two times a week using phosphate buffered saline (PBS, 14190094, ThermoFisher) for washing and dry trypsinization with trypsin-EDTA 0.25% (59429C, Sigma-Aldrich) or wet trypsinization with trypsin-EDTA 0.05% (25-052-CI, Corning).

2.2. Preparation of 3D spheroid cultures

Drops (20 µl) of HepG2 cells were pipetted to the inside of a lid of a petri dish (312, 625, 1250, 2500, 5000 cells per 20 µl; 65 drops per dish), and carefully placed on top of the dish filled with 5 ml cell culture medium. After 4 days incubation at 37 °C 5% CO_2, the spheroids (one spheroid formed per drop) were transferred by pipetting to a 96-well spheroid culture plate (Corning). One spheroid was placed per well. The spheroids were further incubated for additional 21 days for size and circularity measurements, with medium renewal (4/5 vol) every two days. For all exposure studies, conditions with 2500 cells per drop, 4 days in hanging drop and one week in low adhesion plate were selected. Day 1 of the presented results is the day after transfer of the spheroids to plates. For trypsinization, the spheroids were washed twice with PBS, incubated with 50 µl 0.25% trypsin-EDTA for 10 min and neutralized in 150 µl fresh medium. The whole content of the well was transferred to an Eppendorf tube and centrifuged for 5 min at 200 *g*. The supernatant was removed, and the pellet re-suspended, before 30 µl medium was added for samples for cell counting and 70 µl medium was added for samples used for the comet assay.

2.3. Preparation of 2D cultures

Parallel to experiments with spheroids, standard *in vitro* 2D cultures were used. HepG2 cells were seeded at 20,000 cells/well in a standard flat 96-well plate for the comet assay and alamarBlue assay, 10,000 cells/well for measuring metabolic capacity of cells, and 200,000 cells/well in flat 24-well plate for flow cytometry analysis. The 2D cultures were then incubated overnight prior to exposure to test substances or fresh medium. For trypsinization, 2D cultures were washed twice with PBS, dry trypsinized for 4 min and re-suspended in cell culture medium.

2.4. Cell counting

The cells were counted in automated cell counter Countess® (C10227, Invitrogen). The cell suspension was mixed 1:1 with trypan-blue (0.4%, Invitrogen) for staining of cells with compromised cell membrane.

2.5. Evaluation of metabolic status of 2D and 3D cultures

The levels of albumin, alanine transaminase (ALT), aspartate aminotransferase (AST) and glutamate dehydrogenase (GDH) in 2D and 3D cultures were measured after 8 days in culture. Albumin was measured with kit BCG Albumin Assay Kit (Cell Biolabs, USA), ALT with Alanine Aminotransferase (ALT or SGPT) Activity Colori-metric/Fluorometric Assay Kit (Biovision, USA), AST with Aspartate Aminotransferase (AST) Activity Colorimetric Assay Kit (Biovision), and GDH with Glutamate Dehydrogenase (GDH) Activity Colorimetric Assay Kit (Biovision). All assays were performed according to the manufacturers' protocols. For the albumin assay, FBS-free medium was used. Values were normalized to the number of cells per 2D or 3D culture on day of measurement.

2.6. Size measurements of the spheroids

For measuring the size (diameter and area) of the spheroids, images were acquired in the bright field microscope Leica DM-IL microscope with camera (Moticam) and the software Motic Images (Laboratory 1), and Olympus IX70 microscope with CC-12 camera (Olympus) and the software i-cell (Laboratory 2). The images of 8–18 spheroids per experiment were analyzed with the software Fiji Is Just ImageJ (Fiji) [36] using the same settings for all images. Also the circularity of the spheroids was analyzed via Fiji.

2.7. Fluorescence imaging of the spheroids

The spheroids were stained with fluorescein diacetate (FDA, Invitrogen) and propidium iodide (PI, Invitrogen) to allow for visualization of live and dead cells, respectively. The spheroids were incubated in dark at room temperature with 30 µg/ml FDA and 40 µg/ml PI for up to 10 min, before washing with PBS and imaging in PBS in confocal microscope Zeiss LSM 700 with the software ZEN2010 (Zeiss). At least three spheroids were imaged per sample in two independent experiments (n = 2).

2.8. Test substances and exposure

HepG2 cells in 2D and 3D culture were exposed in 96-well plates to COL, CHLO or MMS (1–750 μM) for 24 h, using at least two (2D) or three (3D) parallel wells per experiment, each with one culture or spheroid. As negative control complete chemical-free culture medium was used, with at least four (2D) or five (3D) parallel wells per experiment. For both 2D and 3D cultures the same volumes and concentrations were used. Stock solutions of COL (cat.no. A13240.03, VWR International), MMS (cat. no. 129925, Sigma-Aldrich), and CHLO (cat. no. C8138, Sigma-Aldrich) were freshly prepared before all experiments. COL was dissolved in sterile PBS (10 mM), MMS was dissolved in dimethyl sulfoxide (DMSO) and sterile PBS at a ratio of 1:1.8:9 (1 M) before dilution in PBS (10 mM), and CHLO was dissolved in sterile filtered ultrapure water (5 mM). Working solutions were prepared by serial dilution in cell culture medium.

HepG2 cells in 2D and 3D cultures were exposed also to H_2O_2 (7722841, Sigma-Aldrich). 2D and 3D cultures were exposed both as cells in culture in 96-well plates and as disintegrated single cells, to 12.5–250 μM H_2O_2 in PBS for 5 min on ice. See Section 2.11 for further details.

2.9. Viability measured by alamarBlue assay

Spheroids or cells in 2D culture were washed twice with PBS, and alamarBlue diluted in cell culture medium (10% v/v) was added (100 μl/well for 3D, 200 μl/well for 2D). Samples were incubated at 37 °C, 5% CO_2 in dark for 3–4 h before the supernatant was transferred to a new 96-well plate (40 μl/well). Fluorescence (excitation 530 nm, emission 590 nm) was determined on a FLUOstar OPTIMA microplate reader. Per exposure well, four 2D samples and two 3D samples were measured in parallel, and at least two 2D or three 3D exposure wells were used per experiment. Blank values (alamarBlue without cells present) were subtracted from the measured fluorescence intensity, which was further normalized by the average measurement of the unexposed samples, giving the relative viability of the exposed samples.

2.10. Viability measured by flow cytometry

The exposure medium was removed and the cells were washed with PBS. Cells of the 2D model were detached with trypsin and transferred into tubes. Cells of two parallel culture wells treated with the same conditions were transferred into the same tube. In case of the 3D model, three spheroids treated with the same conditions were transferred in one tube and trypsinized. Cells were centrifuged at 200 *g* for 3 min and washed again with PBS. Cells were stained with 30 μg/ml FDA solution for 1 min. After an additional washing step with PBS the cells were fixed in fixing solution (1% paraformaldehyde, 0.85% NaCl in PBS, pH 7.4) and analyzed with a FACS Calibur (BD Biosciences, USA) at 488 nm. Viability measurement by flow cytometry were performed with internal duplicates (2D) or triplicates (3D).

2.11. DNA damage measured by the comet assay

The miniaturized 12-gel comet assay was performed as described by El Yamani et al. (2017) [37]. Briefly, exposed 2D and 3D cultures were disaggregated with trypsin as described above, and re-suspended in 150 μl and 70 μl fresh medium, respectively. For embedding of cells in gels, 50 μl cell suspension was mixed 1:3 with low melting point-agarose (0.8% w/v, A9414, Sigma-Aldrich, 37 °C) in a 96-well plate, giving a final agarose concentration of 0.6% w/v. Mini-gels (10 μl) were made on microscope slides pre-coated with 0.5% standard melting point agarose (05066, Sigma-Aldrich), and submerged in lysis solution (2.5 M NaCl, 0.1 M EDTA, 10 mM Tris, 10% v/v Triton X-100, pH 10, 4 °C) for at least 1 h.

In addition to the alkylating agent MMS, H_2O_2 was used as a positive control for DNA SBs. 2D and 3D cultures were exposed both as cells in culture and as disintegrated single cells. For cells in culture, the 2D and 3D cultures were exposed to 12.5–250 μM H_2O_2 for 5 min on ice, washed in PBS, trypsinized and embedded in gels as described above. For exposure of single cells from 2D and 3D cultures, control, non-treated cells were embedded into gels on slides and the gels were submerged in 12.5–100 μM H_2O_2 in PBS for 5 min at 4 °C, washed twice for 5 min in PBS (4 °C) and then submerged in a separate coplin jar of lysis solution.

For detection of oxidized or alkylated bases, the modified comet assay was used with the bacterial repair enzyme formamidopyrimidine DNA glycosylase (Fpg, gift from Professor Andrew Collins, University of Oslo, Norway), which converts oxidized or alkylated bases to SBs [33]. After lysis, slides with cells embedded in gels were washed twice for 8 min in buffer F (40 mM HEPES, 0.1 M KCl, 0.5 mM EDTA, 0.2 mg/ml BSA, pH 8, 4 °C), added Fpg enzyme diluted in buffer F, and covered with a polyethylene foil and incubated at 37 °C for 30 min in a humid box. As positive control for function of Fpg enzyme, HepG2 cells were exposed to a photosensitizer Ro 19–8022 (2 μM, kindly provided by Hoffmann La Roche, Switzerland) and irradiated with visible light (30 cm distance from cells, 250 W) on ice for 4 min, before embedding into gels. The photosensitizer Ro 19-8022 with light induces oxidized purines, mainly 8-oxoG, which is detected by the Fpg enzyme [38,33].

For electrophoresis, the slides were placed in the tank, submerged in electrophoresis solution (0.3 M NaOH, 1 mM EDTA, pH > 13, 4 °C), to let the DNA unwind for 20 min, before running electrophoresis for 20 min (25 V, 1.25 V/cm, Consort EV202). The gels were neutralized in PBS, washed in ultrapure H_2O and left to dry overnight. Comets were visualized after staining with SYBR gold (1:2000, S11494, Sigma-Aldrich), and scored in Leica DMI 6000 B (Leica Microsystems), equipped with a SYBR®photographic filter (Thermo Fischer Scientific) using the software Comet assay IV 4.3.1 (Perceptive Instruments, Bury St Edmunds, UK). Median DNA tail intensity was calculated from approximately 50 comets per spheroid/sample as a measure of DNA SBs. For 3D cultures, medians were averaged from six parallel control spheroids and three parallel exposed spheroids per experiment. For 2D culture, medians were averaged from 4 parallel control samples and 2 parallel exposed samples per experiment.

2.12. Statistical analysis

Results are presented as mean with standard error of the mean (SEM) of 3 independent experiments (n = 3), unless otherwise mentioned. Effects were compared to non-treated cells, and statistical analysis by one-way ANOVA, multiple comparisons and post-test Dunnett performed in Prism/GraphPad 7. Two-way ANOVA was used for comparison between 2D and 3D cultures, with multiple comparisons and post-test Sidak. P-values are marked by * as $p < 0.05$, ** as $p < 0.01$, *** as $p < 0.001$ and **** as $p < 0.0001$. EC50 values were calculated in Prism using linear regression.

3. Results

3.1. Formation, growth and metabolic status of HepG2 spheroids

To find optimal conditions for spheroid formation via hanging drop technique and growth, different cell numbers per droplet (312–5000 cells per droplet) were studied. Spheroids were formed with all cell numbers. Spheroid area increased time-dependently until reaching a plateau after one week culture of the spheroids in a 96-well plate (after 4 days hanging drop culture) (Fig. 1). The circularity was high and stable for the spheroids seeded with lower cell numbers, and increasing over time for spheroids with higher cell numbers (Fig. 1). Based on these results, conditions with 2500 cells per drop and 4 day hanging drop culture and one week culture of the spheroids in a 96-well plate were selected for the cyto- and genotoxicity experiments.

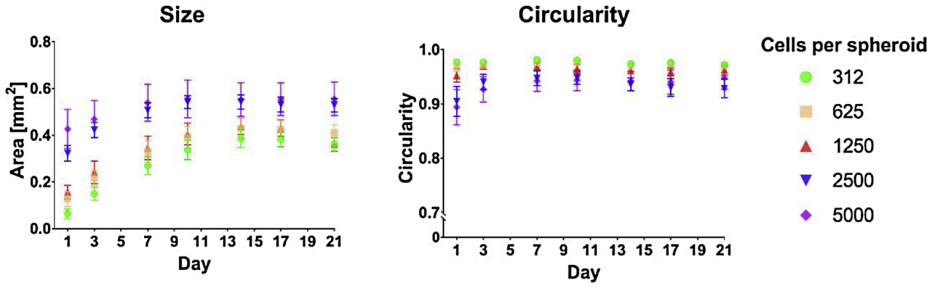

Fig. 1. Size and circularity of HepG2 spheroids. 312–5000 cells were seeded as hanging drops and cultured for 4 days before transferred to a spheroid culture plate. Size, measured as area, and circularity of the individual spheroids were measured over 21 days. Spheroid area and circularity determined by image analysis, show a time-dependent increase in spheroid size before reaching a plateau with a stable size and circularity. Mean with SEM (n = 3).

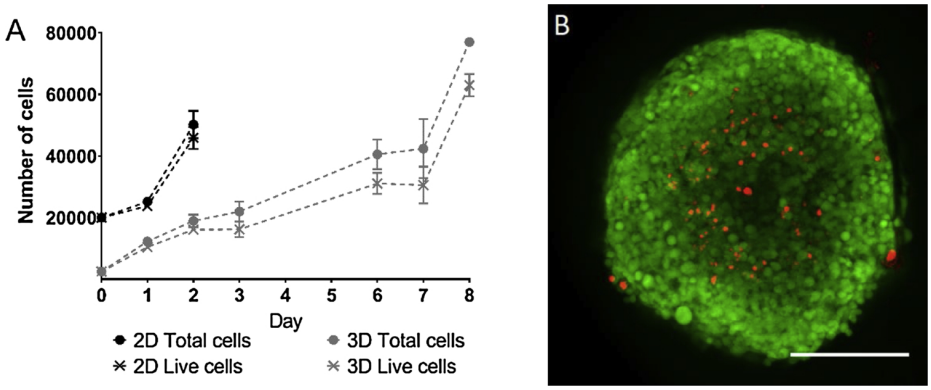

Fig. 2. Cell proliferation and viability of HepG2 cells in 2D and 3D cultures. A) The cell number in the spheroids increased over time after seeding 2500 cells, with a relatively constant viability. The number of cells in 2D cultures cultured in parallel (20.000 seeded cells) is shown as comparison. Day 0: Cell number at seeding of cells. Day 1: One day after transfer to spheroid plate (3D). Mean with SEM (n = 3). B) Representative confocal image of a spheroid at day 1, showing viable cells stained with FDA in green and a necrotic core stained with PI in red. The image is a merged image of 10 images of the spheroids cross section. A shadow is removed from the image in Fiji. Scale bar 200 µm.

Growth of the spheroids over time was investigated by measuring the diameter and counting the number of cells per spheroid. The number of cells increased in consistency with enlarged spheroid size and time (Fig. 2A). Average cell viability over time was 79% ± 2% in the 3D cultures, and 92% ± 2% in the 2D cultures, determined by the trypan blue assay. The visual analysis of the HepG2 spheroids via confocal laser scanning microscopy verified the viability of the cells in the 3D culture (Fig. 2B). The distribution of live and dead cells in the spheroids was investigated by FDA/PI staining. A small necrotic core was seen, and the viability was stable over time. A representative image of the HepG2 spheroid at day 1 is shown in Fig. 2B, with a high presence of viable cells.

An inter-laboratory comparison for investigating reproducibility and reliability of the development and cultivation of HepG2 liver spheroids was performed. The spheroids were cultured in laboratory 1 and laboratory 2 using the same protocol. Spheroid diameter was determined over 8 days. The growth rate was found to differ slightly, but the spheroid diameter was found to be similar both at start of culture and at time of exposure, increasing from 630 µm to 800 µm (Fig. 3).

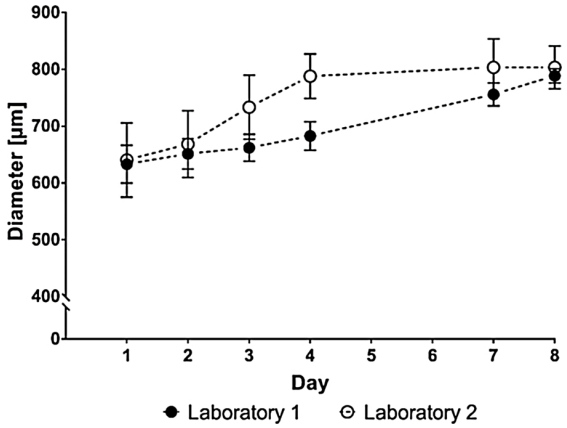

Fig. 3. Inter-laboratory comparison of HepG2 spheroid diameter. Both laboratories used the same protocol for culturing the spheroids, and achieved an increasing spheroid size, with approximately the same diameter at day 8, the end of the culture period. Day 1: One day after the transfer to spheroid plate. Mean with SEM (n = 3). No statistical differences were found between the results from the two laboratories, using two-way ANOVA with multiple comparisons and post-test Sidak.

To compare the metabolic status of the 2D and 3D HepG2 cultures, the albumin production as well as the activity of the liver-specific enzymes AST, ALT and GDH were measured (Fig. 4). Albumin concentration (2D: 7.6 µg/10^9 cells, 3D: 1.7 µg/10^9 cells) and ALT activity (2D: 27.0 units/10^9 cells, 3D: 8.5 units µg/10^9 cells), measured at day 8, was significantly increased in cultures grown as monolayers compared to spheroidal HepG2 cultures. In contrast GDH (2D: 3.4 units/10^9 cells, 3D: 9.3 units/10^9 cells) was significantly increased in the spheroidal HepG2 cultures. No significant difference was seen comparing the AST activity in 2D and 3D HepG2 cultures (Fig. 4).

3.2. Cytotoxicity studies in 2D and 3D HepG2 cultures

To investigate and compare toxicological responses of 2D and 3D HepG2 cultures, the monolayer and the spheroidal culture were exposed to COL, CHLO or MMS. Cytotoxicity was determined both by alamarBlue assay which measures metabolic activity and by flow cytometry which measures cell vitality/membrane damage (Fig. 5). Cell viability of HepG2 2D cultures, measured by alamarBlue assay, was reduced by exposure to COL. Already at 10 µM, COL induced a significant decrease in relative cell viability, whereas in 3D liver cultures an exposure with the highest tested concentration (750 µM) did not result in a significant decrease in relative cell viability (Fig. 5A). Statistically significant differences were found between 2D and 3D cultures for 5 and 10 µM COL where the relative cell viability of 3D cultures were high. By flow cytometry, no effect of COL was seen in either 2D or 3D cultures (Fig. 5D). In contrast, CHLO induced in both models (2D and 3D) a concentration dependent decrease in relative cell viability, but with different sensitivity (Fig. 5B). EC50 values were calculated for CHLO in 2D culture to be 93 µM (alamarBlue assay) and 177 µM (flow cytometry analysis), respectively. For 3D cultures the EC50 values were

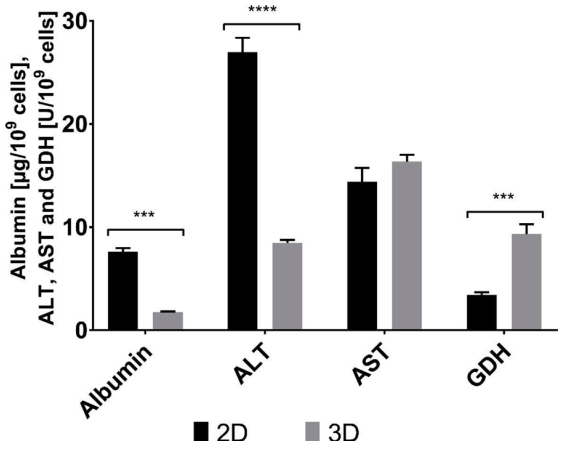

Fig. 4. Metabolic status of 2D and 3D HepG2 cultures at day 8. Amounts of released albumin, AST, ALT and GDH from HepG2 cells are dependent on culture conditions. Numbers are normalized to number of live cells per culture at time of measurement. Similar results would be seen if presented as mass or unit per volume. Mean with SEM (n = 3). Two-way ANOVA with multiple comparisons and post-test Sidak was performed to compare 2D and 3D results. *** $p < 0.001$; **** $p < 0.0001$.

higher; 227 µM measured by alamarBlue assay and > 750 µM by flow cytometry (Fig. 5B and 5E, Table 1). MMS was cytotoxic at the highest tested concentrations in 2D culture, with an EC50 value of 417 µM by alamarBlue assay (Fig. 5C, Table 1). No significant reduction in relative cell viability was observed at the highest concentration for 3D culture (Fig. 5F, Table 1).

Confocal imaging of exposed spheroids showed an increase in the amount of dead cells by PI staining after exposure to 750 µM MMS and 300 µM CHLO, but no effect after COL exposure (Fig. 6). The staining was successful for cells mainly at the surface of the spheroid (Fig. A.1 and A.2). In summary, all three compounds induced cytotoxicity to HepG2 cells in 2D cultures, measured by alamarBlue assay (Fig. 5A–C). Only CHLO and MMS were cytotoxic for 3D cultures, determined by alamarBlue assay (Fig. 5E) and confocal imaging (Fig. 6).

3.3. Genotoxicity measured in 2D and 3D cultures by the comet assay

The background level of damage in non-treated 3D cultures was 5.1% ± 1.3% DNA in tail for DNA SBs and 8.7% ± 1.6% for DNA SBs plus Fpg sites. Corresponding values for 2D cultures were 4.8% ± 0.6% and 5.1% ± 1.4%. The background levels for 2D and 3D cultures are in the same range. The control for function of Fpg (Ro 19-8022) was within the expected range, as the Fpg treated control had an increase of at least 20% DNA in tail compared to the control without Fpg (data not shown). For genotoxicity studies by the comet assay only MMS and H_2O_2 were selected because they are direct acting mutagens and the most common positive controls in the comet assay. When exposing 2D and 3D cultures to H_2O_2 in the culture wells, before trypsinization, the induction of SBs in 2D cultures was significant at a concentration of 50 µM and above (Fig. 7A). A smaller increase in SBs was seen for 3D cultures treated with H_2O_2 as spheroids before trypsinization. When exposing disaggregated single cells after trypsinization, both 2D and 3D cultured cells had high levels of DNA SBs at all tested concentrations (Fig. 7B).

HepG2 monolayer and spheroids were treated with MMS for 24 h before disaggregation of cells and DNA damage investigation. A concentration related response was seen after the MMS exposure, both for DNA SBs and DNA SBs + Fpg (Fig. 8). In 3D cultures, significantly increased DNA damage relative to control was found already at 50 µM MMS. The responses of 2D and 3D cultures were significantly different from each other at 100 µM and 300 µM, where a higher induced damage was seen in 3D cultures.

4. Discussion

In this study a liver spheroid model was established and the suitability for genotoxicity studies by the comet assay was investigated. HepG2 2D cultures are commonly used for evaluating toxicity of chemicals, drugs and nanoparticles [9,44–46]. They are easy to handle and are frequently used for high-throughput toxicity screening, but have also disadvantages. The adherent monolayer cell culture is far removed from the *in vivo* morphology, and this could account for the altered metabolism compared to 3D tissue structure. 3D cell models, such as spheroids, represent a much more *in vivo*-like morphology and behavior and are thus a more realistic model. Ramaiahgari et al. concludes that the 3D model better is more sensitive than monolayer cultures and better predicts potential hepatotoxicity, especially when increasing the exposure time from 24 h to repeated exposures [22]. Therefore, the development of a new liver spheroid model combined with the comet assay is in-line with the 3R concept and meets the strong need for new *in vitro* models for genotoxicity screening under realistic *in vivo*-like conditions. Kermanizadeh et al. used the commercialized InSphero liver spheroids for comet assay studies [39]. Our study is, to the best of our knowledge, the first to focus on the application of the comet assay to HepG2 liver spheroids cultured in a simple and reproducible manner. The protocol used here for the spheroid preparation and cultivation has not yet been published before. Published protocols differ in cell numbers, culture conditions and durations, and droplet volumes [26].The implementation of the developed protocol in two independent laboratories, using HepG2 cells from different sources and with different cell culture media, confirmed a high reproducibility, in contrast to a study by Hurrell et al. [40]. The background levels of DNA SBs in 2D and 3D cultures were similar and within the recommended range for human cells [27,41].

The increase in number of cells during the first week of spheroid culture is consistent with other studies on HepG2 and primary hepatocytes [40,42]. The plateau of the spheroid area after about one week in culture (Fig. 1) could indicate a reduced proliferation index of the spheroidal cells [40], and/or a decreased level of the proliferation marker Ki67 [22]. The observed necrotic core in the spheroids is characteristic of cultures with diameters > 300 µm [4].

The metabolic status of HepG2 cells cultured in 2D and 3D was measured by the presence of different proteins and enzyme activity. The production of albumin is an indicator for metabolic activity [43], ALT, AST and GDH are *in vivo* liver functionality biomarkers. Upon liver injury, the serum concentrations of ALT, AST and GDH increase [43,44]. In contrast to published studies [4,22,26], the albumin production in HepG2 spheroids was lower than in 2D monolayers (Fig. 4). Shah et al. reported a higher albumin secretion in hanging spheroids on day 4 compared to day 7 [26]. One reason for the low albumin concentration could be the late time point (day 8) in our study. Additionally, the albumin secretion could depend on the spheroid size. Nishikawa et al. determined the highest albumin level in the smallest spheroids (200 µm), and albumin levels similar to ours were found in larger spheroids and monolayers [45]. One can speculate over the possibility of the cells in the spheroids being packed too tightly for the albumin to pass through to the surface, resulting in a lower albumin concentration in the supernatant where the quantification takes place. Comparing the results of the 2D and 3D HepG2 cultures, ALT decreased, AST remained relatively constant and GDH increased in the spheroidal model, suggesting a difference in the metabolic status of the cells. In the 3D spheroid culture approach, all cells are in contact with other cells but not with an artificial matrix. The spheroid approach supports much more the maintenance of *in vivo*-like cell morphology and behavior than 2D approaches.

After characterizing the HepG2 liver spheroids, the cytotoxicity in 2D and 3D cultures was evaluated to determine the concentrations for

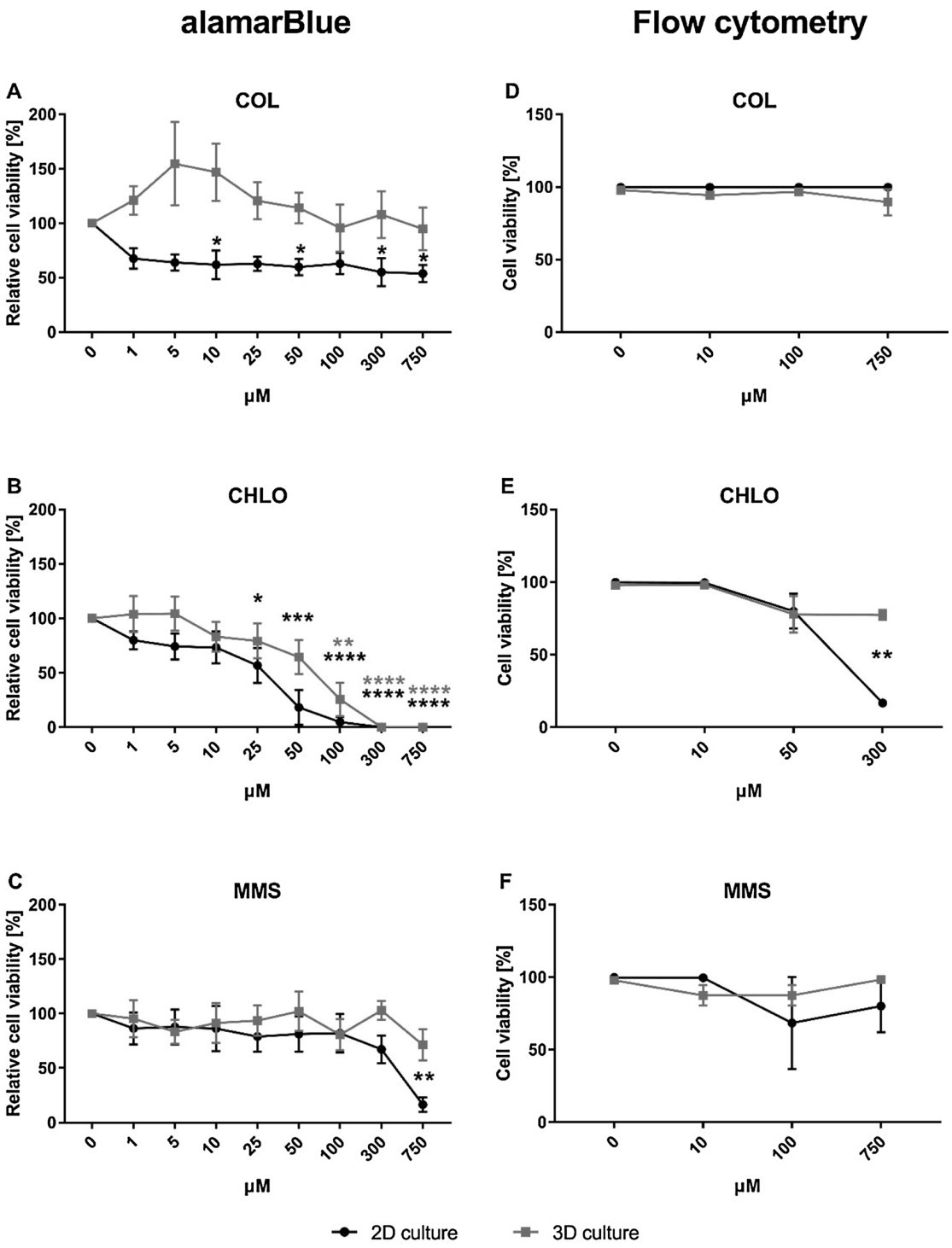

Fig. 5. Effect of COL, CHLO and MMS on cell viability of 2D and 3D HepG2 cultures, measured by alamarBlue assay (endpoint: metabolic activity) (A–C) and flow cytometry (endpoint: cell vitality/ membrane damage) (D–F) after 24 h exposure. COL reduced the relative cell viability of 2D cultures in the alamarBlue assay but no viability reduction was seen by flow cytometry analysis after FDA/PI staining. CHLO was cytotoxic for both 2D and 3D cultures. MMS was cytotoxic at high concentrations for 2D culture in alamarBlue assay. Mean with SEM and n = 3, except for 3D cultures in alamarBlue assay where n = 5. One-way ANOVA with multiple comparisons and post-test Dunnett was performed to compare effect to negative control. * $p < 0.05$; ** $p < 0.01$; *** $p < 0.001$; **** $p < 0.0001$. Statistically significant differences were seen between 2D and 3D results only for COL 5 µM and 10 µM ($p < 0.05$), using two-way ANOVA with multiple comparisons and post-test Sidak.

the comet assay. Three different cytotoxicity assays (alamarBlue assay, live/dead staining with flow cytometry, confocal imaging) were applied. The alamarBlue assay showed an effect of COL, CHLO and MMS in 2D cultures, but only with CHLO on 3D cultures. Confocal imaging showed however that MMS induced cytotoxic effects in 3D cultures. The cell viability assay with flow cytometry showed a smaller effect or

Table 1
EC50 values of the test compounds COL, CHLO and MMS.

	alamarBlue		Flow cytometry	
	2D	3D	2D	3D
COL	> 750 µM	> 750 µM	> 750 µM	> 750 µM
CHLO	93 µM	227 µM	177 µM	> 750 µM
MMS	417 µM	> 750 µM	> 750 µM	> 750 µM

no effect. The differences in the effects between the methods may reflect differences in their modes of action. The alamarBlue assay measures the cells' ability to metabolize the substrate resazurin, PI stains DNA in cells that have lost their membrane integrity, whereas FDA is hydrolyzed to the fluorescent fluorescein in viable cells. The smaller or no effect on the viability measured by flow cytometry may in addition be due to the loss of dead cells during the washing steps which are not performed with the other cytotoxicity assays. This illustrates the importance of including more than one assay or endpoint to evaluate the cytotoxicity of a substance. A statistically significant difference in induced cytotoxicity when comparing 2D and 3D cultures, was seen only for low concentrations of COL evaluated by alamarBlue assay. Greater variation, however, was seen for 3D cultures than 2D cultures with alamarBlue (Fig. 5), possibly related to variations in spheroid size.

In vivo and *in vitro* studies have shown that CHLO, a tricyclic antidepressant, is intrinsically toxic to the liver as it can induce cholestasis and hepatic necrosis [46]. The concentration-related cytotoxicity after exposure to CHLO (Fig. 5, Table 1) was similar to that reported by Xuan et al. [47]. Similar EC50 values were obtained for 2D and 3D cultures in a study on HepaRG cells [11]. However, Mueller et al. used spheroids of HepG2 and HepaRG cells, and found lower CHLO EC50 values for 2D cultures compared to 3D cultures after 72 h exposure [48].

COL, a drug for treatment of acute gout, binds to tubulin and inhibits cell division [49] leading to decreased metabolism of the cell culture. Consistent with this, COL was cytotoxic in 2D cultures (Fig. 5) – but not in 3D culture, possibly owing to differences in cellular metabolism in the spheroid or poor penetration of the compound into the spheroid.

MMS is a mutagenic compound [50] that methylates DNA bases, leading to SBs, chromosome breaks, micronucleus formation, and finally cell death [51,52]. The effect of MMS on cell viability (Figs. 5, 6) was seen mainly at the highest test concentrations. MMS was, in addition, able to induce genotoxicity in HepG2 2D and 3D cultures in a concentration related manner (Fig. 8) at non-cytotoxic concentrations. There was slightly more DNA damage after MMS exposure of 3D compared to 2D cultures. A similar HepG2 spheroid model, tested with other chemicals, had a higher sensitivity to micronucleus formation [26].

H_2O_2 exposure of disaggregated cells from 3D cultures induced elevated levels of DNA SBs at lower concentrations than in cells from 2D cultures. Exposure of intact 2D and 3D cultures to non-cytotoxic concentrations of H_2O_2 [53,54] (Fig. 7A) led to fewer DNA SBs compared with exposure of disaggregated single cells in the gel (Fig. 7B). One reason for this difference could be the fast repair of SBs during

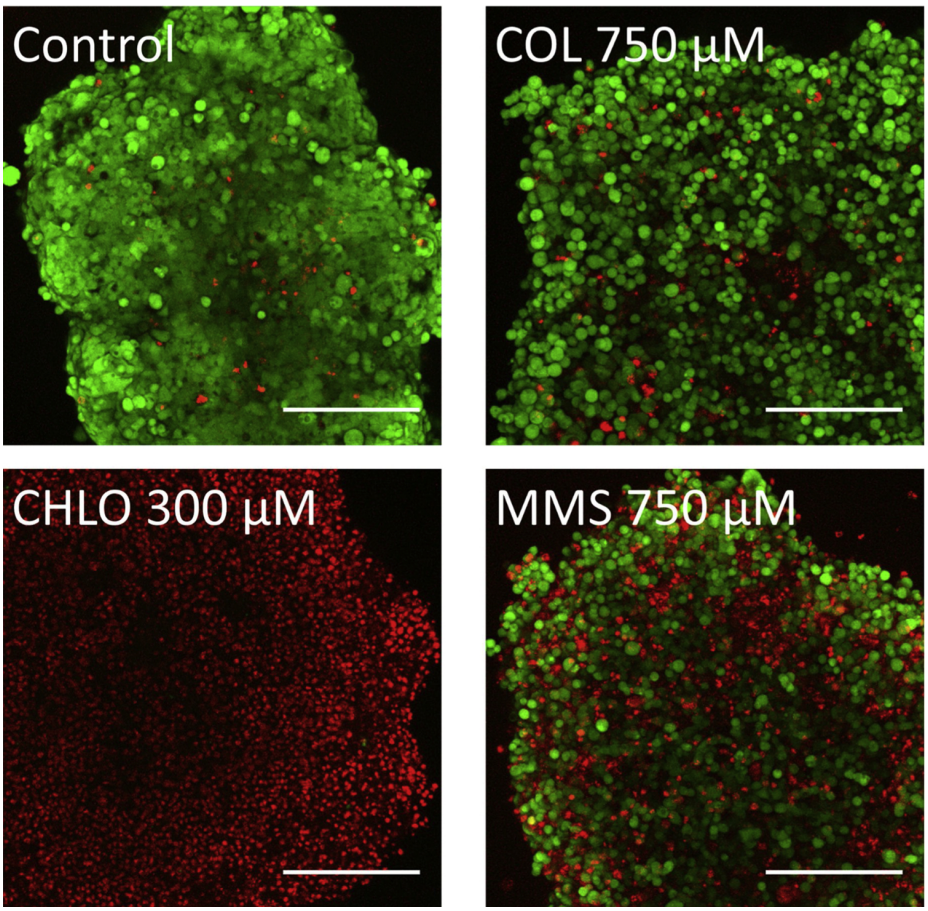

Fig. 6. Representative images from confocal microscopy of exposed HepG2 spheroids. Spheroids were exposed to COL, CHLO and MMS for 24 h before viable (green) and dead (red) cells were stained with FDA (green) and PI (red). The images are z-stack projections from the spheroid surface to approximately 150 µm towards the spheroid core. Scale bar 200 µm.

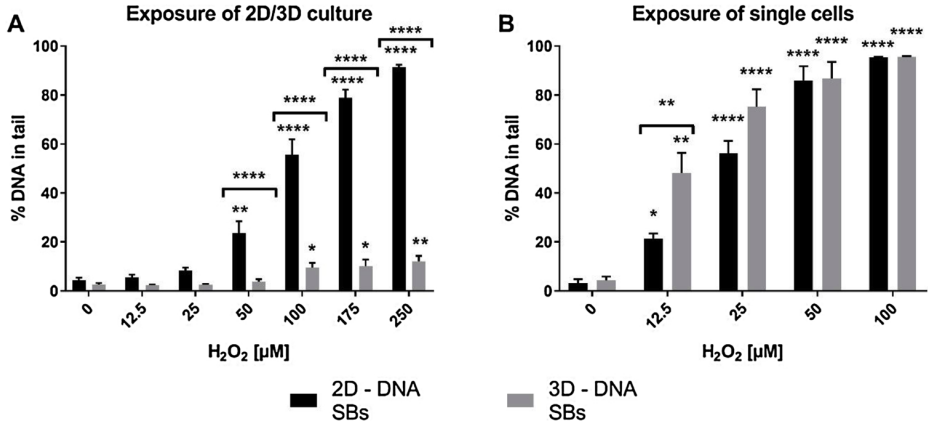

Fig. 7. DNA damage in H_2O_2 exposed HepG2 2D and 3D culture measured by the comet assay. H_2O_2 induced DNA SBs in HepG2 cells exposed either in (A) 2D or 3D culture where the cultures were treated with H_2O_2 for five minutes before disaggregation of the cells and embedding of cells in gel, and (B) as single cells where the cells were incubated with H_2O_2 for five minutes after trypsinization and embedding of cells in gel. The level of DNA SBs was higher for single cell exposure than for monolayer/spheroid exposure. Mean with SEM (n = 3). One-way ANOVA with multiple comparisons and post-test Dunnett was performed to compare effect to negative control. Two-way ANOVA with multiple comparisons and post-test Sidak was performed to compare 2D and 3D results. * $p < 0.05$; ** $p < 0.01$; *** $p < 0.001$; **** $p < 0.0001$.

disaggregation of cells after exposure [54]. 3D cultures required longer time for disaggregation of cells, compared to 2D cultures, resulting in a higher level of damage in 2D cultures. Also, it has been reported that the incubation time and concentration of trypsin and EDTA can affect the background level of SBs in HepG2 cells [55]. Additionally, it is possible that the tested compounds in this study did not fully diffuse inside the spheroid, thus accounting for differences in the observed results between 2D and 3D cultures. Concentration gradients of oxygen, proteins, waste and other solutes have been shown to be present in tissues or 3D cultures [6,9]. However, in a study by Gaskell et al. the exposure of autofluorescent doxorubicin was found to be homogenous throughout the spheroid volume in a C3A liver spheroid [56]. In contrast, limited fluorescence of dyes was found in the middle of the center of breast cancer spheroids [57]. A similar effect was observed in our study with PI and FDA at the end of the culture period, where the dyes stained mainly the outer parts of the spheroid and did not reach the center and so measuring cytotoxicity in this way may not be completely reliable.

Cell density, incubation time, pH, spheroid size, the surrounding extracellular matrix (ECM), and factors involved with bioaccumulation, such as lipophilicity, could potentially be important for the chemical's distribution in the spheroid [58]. However, heterogeneous exposure of spheroids can possibly also be closer to *in vivo* exposure, with the cellular arrangements and metabolic zonation through the acinus. The investigation of the influence of the location of the cells in the spheroid on the genomic damage could give more detailed information [59].

5. Conclusions

The present study demonstrates the successful application of the comet assay to HepG2 liver spheroids, bridging the gap between *in vivo* studies and assays based on 2D monolayers. We tested a liver spheroid model in two independent laboratories, with successful application for both genotoxicity studies via the comet assay and several cytotoxicity assays. Compared to traditional 2D monolayer culture, spheroidal cultures can have higher variability; however, due to the different geometrical arrangements of the cells, they reflect much better the *in vivo* situation. Depending on the objective of the study, it should be considered which cell model is best suited for the investigations. Time- and cost-efficient 2D models are usually sufficient for pre-screening in the field of pharmaceutical drug development. However, if effects in complex systems or the interaction of several cell responses or different cell types should be considered, 3D spheroids are more realistic models that comply with the 3Rs policy to reduce *in vivo* testing. Our study is a positive contribution to the development of advanced *in vitro* models. Future studies with HepG2 spheroids should focus on increasing the relevance towards the human liver, by including co-cultures of hepatocytes with macrophages and longer or repeated exposure.

Conflicts of interest

The authors declare that there are no conflicts of interest.

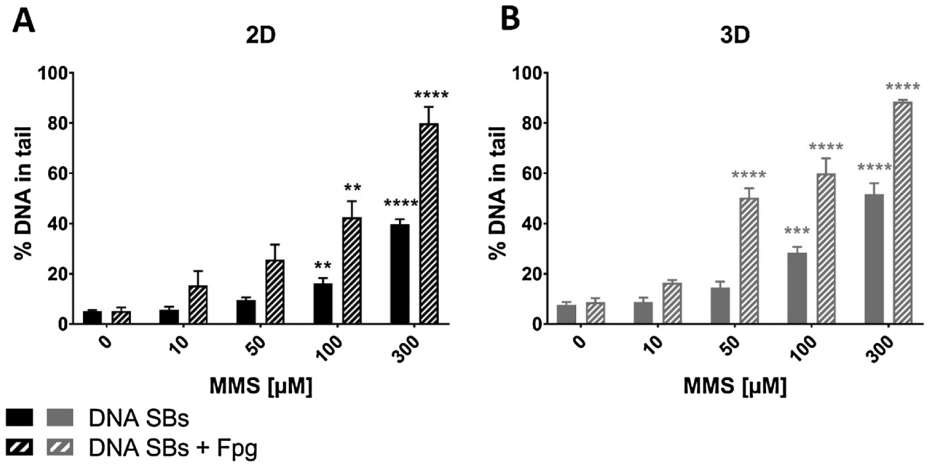

Fig. 8. DNA damage in MMS exposed HepG2 2D and 3D cultures measured by the comet assay. HepG2 monolayer (A) and spheroids (B) were treated with MMS for 24 h before disaggregation of cells and DNA damage investigation. The % DNA in tail is increasing with increasing MMS concentration, for both 2D and 3D cultures. Mean with SEM (n = 3). In 3D culture significant difference from control was found already at 50 µM MMS. 2D (A) and 3D cultures (B) were significantly different from each other ($P < 0.01$) at 100 µM and 300 µM, using two-way ANOVA with multiple comparisons and post-test Sidak. One-way ANOVA with multiple comparisons and post-test Dunnett was performed to compare effect to negative control. ** $p < 0.01$; *** $p < 0.001$; **** $p < 0.0001$.

Acknowledgments

The authors would like to thank Iren E. Sturtzel for technical assistance, Hoffmann La Roche for providing the Ro 19-8022, and Andrew Collins for providing the Fpg enzyme.

Funding

This work was supported by the European Commission under the Horizon2020 program (grant agreement no 685817, HISENTS), the hCOMET project (COST Action, CA 15132), and the Norwegian Research Council (272412/F40).

Appendix A. Supplementary data

Supplementary material related to this article can be found, in the online version, at doi:https://doi.org/10.1016/j.mrgentox.2019.03.006.

References

[1] E. Commission, Regulation (EC) No. 1907/2006 of the European Parliament and the Council of 18 December 2006 Concerning the Registration, Evaluation, Authorisation and Restriction of Chemicals (REACH), Establishing a European Chemical Agency, (1999), pp. 451–849.
[2] S.S. Bale, et al., In vitro platforms for evaluating liver toxicity, Exp. Biol. Med. (Maywood) 239 (9) (2014) 1180–1191, https://doi.org/10.1177/1535370214531872.
[3] S.J. Evans, et al., Critical review of the current and future challenges associated with advanced in vitro systems towards the study of nanoparticle (secondary) genotoxicity, Mutagenesis 32 (1) (2017) 233–241, https://doi.org/10.1093/mutage/gew054.
[4] J.A. Kyffin, et al., Impact of cell types and culture methods on the functionality of in vitro liver systems - A review of cell systems for hepatotoxicity assessment, Toxicol. In Vitro 48 (2018) 262–275, https://doi.org/10.1016/j.tiv.2018.01.023.
[5] C. Calitz, et al., Recent advances in three-dimensional cell culturing to assess liver function and dysfunction: from a drug biotransformation and toxicity perspective, Toxicol. Mech. Methods 28 (5) (2018) 369–385, https://doi.org/10.1080/15376516.2017.1422580.
[6] L.G. Griffith, M.A. Swartz, Capturing complex 3D tissue physiology in vitro, Nat. Rev. Mol. Cell Biol. 7 (3) (2006) 211–224, https://doi.org/10.1038/nrm1858.
[7] S. Breslin, L. O'Driscoll, Three-dimensional cell culture: the missing link in drug discovery, Drug Discov. Today 18 (5–6) (2013) 240–249, https://doi.org/10.1016/j.drudis.2012.10.003.
[8] A. Astashkina, D.W. Grainger, Critical analysis of 3-D organoid in vitro cell culture models for high-throughput drug candidate toxicity assessments, Adv. Drug Deliv. Rev. 69-70 (2014) 1–18, https://doi.org/10.1016/j.addr.2014.02.008.
[9] P. Godoy, et al., Recent advances in 2D and 3D in vitro systems using primary hepatocytes, alternative hepatocyte sources and non-parenchymal liver cells and their use in investigating mechanisms of hepatotoxicity, cell signaling and ADME, Arch. Toxicol. 87 (8) (2013) 1315–1530, https://doi.org/10.1007/s00204-013-1078-5.
[10] A.J. Harris, S.L. Dial, D.A. Casciano, Comparison of basal gene expression profiles and effects of hepatocarcinogens on gene expression in cultured primary human hepatocytes and HepG2 cells, Mutat. Res. 549 (1-2) (2004) 79–99, https://doi.org/10.1016/j.mrfmmm.2003.11.014.
[11] Z. Wang, et al., HepaRG culture in tethered spheroids as an in vitro three-dimensional model for drug safety screening, J. Appl. Toxicol. 35 (8) (2015) 909–917, https://doi.org/10.1002/jat.3090.
[12] Z.H. Jiao, et al., Hormesis effects of silver nanoparticles at non-cytotoxic doses to human hepatoma cells, PLoS One 9 (7) (2014) e102564, https://doi.org/10.1371/journal.pone.0102564.
[13] S. Wilkening, F. Stahl, A. Bader, Comparison of primary human hepatocytes and hepatoma cell line Hepg2 with regard to their biotransformation properties, Drug Metab. Dispos. 31 (8) (2003) 1035–1042, https://doi.org/10.1124/dmd.31.8.1035.
[14] K. Nakamura, et al., Expression of albumin and cytochrome P450 enzymes in HepG2 cells cultured with a nanotechnology-based culture plate with micro-fabricated scaffold, J. Toxicol. Sci. 36 (5) (2011) 625–633.
[15] T. Anada, et al., An oxygen-permeable spheroid culture system for the prevention of central hypoxia and necrosis of spheroids, Biomaterials 33 (33) (2012) 8430–8441, https://doi.org/10.1016/j.biomaterials.2012.08.040.
[16] N.B. Javitt, Hep G2 cells as a resource for metabolic studies: lipoprotein, cholesterol, and bile acids, FASEB J. 4 (2) (1990) 161–168, https://doi.org/10.1096/fasebj.4.2.2153592.
[17] A. Nowrouzi, et al., Cytotoxicity of subtoxic AgNP in human hepatoma cell line (HepG2) after long-term exposure, Iran. Biomed. J. 14 (1-2) (2010) 23–32.
[18] S.C. Sahu, et al., Comparative cytotoxicity of nanosilver in human liver HepG2 and colon Caco2 cells in culture, J. Appl. Toxicol. 34 (11) (2014) 1155–1166, https://doi.org/10.1002/jat.2994.
[19] F. Faedmaleki, et al., Toxicity effect of silver nanoparticles on mice liver primary cell culture and HepG2 cell line, Iran. J. Pharm. Res. 13 (1) (2014) 235–242.
[20] T.T. Chang, M. Hughes-Fulford, Monolayer and spheroid culture of human liver hepatocellular carcinoma cell line cells demonstrate distinct global gene expression patterns and functional phenotypes, Tissue Eng. Part A 15 (3) (2009) 559–567, https://doi.org/10.1089/ten.tea.2007.0434.
[21] J.M. Kelm, et al., Method for generation of homogeneous multicellular tumor spheroids applicable to a wide variety of cell types, Biotechnol. Bioeng. 83 (2) (2003) 173–180, https://doi.org/10.1002/bit.10655.
[22] S.C. Ramaiahgari, et al., A 3D in vitro model of differentiated HepG2 cell spheroids with improved liver-like properties for repeated dose high-throughput toxicity studies, Arch. Toxicol. 88 (5) (2014) 1083–1095, https://doi.org/10.1007/s00204-014-1215-9.
[23] M. Bokhari, et al., Culture of HepG2 liver cells on three dimensional polystyrene scaffolds enhances cell structure and function during toxicological challenge, J. Anat. 211 (4) (2007) 567–576, https://doi.org/10.1111/j.1469-7580.2007.00778.x.
[24] L. Meli, et al., Influence of a three-dimensional, microarray environment on human cell culture in drug screening systems, Biomaterials 33 (35) (2012) 9087–9096, https://doi.org/10.1016/j.biomaterials.2012.08.065.
[25] Y. Miki, et al., The advantages of co-culture over mono cell culture in simulating in vivo environment, J. Steroid Biochem. Mol. Biol. 131 (3-5) (2012) 68–75, https://doi.org/10.1016/j.jsbmb.2011.12.004.
[26] U.K. Shah, et al., A three-dimensional in vitro HepG2 cells liver spheroid model for genotoxicity studies, Mutat. Res. 825 (2018) 51–58, https://doi.org/10.1016/j.mrgentox.2017.12.005.
[27] M. Dusinska, A.R. Collins, The comet assay in human biomonitoring: gene-environment interactions, Mutagenesis 23 (3) (2008) 191–205, https://doi.org/10.1093/mutage/gen007.
[28] A.R. Collins, et al., High throughput toxicity screening and intracellular detection of nanomaterials, Wiley Interdiscip. Rev. Nanomed. Nanobiotechnol. 9 (1) (2017), https://doi.org/10.1002/wnan.1413.
[29] M. Dusinska, A. Collins, Detection of oxidised purines and UV-induced photoproducts in DNA, by inclusion of lesion-specific enzymes in the comet assay (single cell gel electrophoresis), Alta- Altern. Lab. Anim. 24 (1996) 405–411.
[30] S. Boiteux, et al., Homogeneous Escherichia coli FPG protein. A DNA glycosylase which excises imidazole ring-opened purines and nicks DNA at apurinic/apyrimidinic sites, J. Biol. Chem. 265 (7) (1990) 3916–3922.
[31] S. Boiteux, et al., Substrate specificity of the Escherichia coli Fpg protein (formamidopyrimidine-DNA glycosylase): excision of purine lesions in DNA produced by ionizing radiation or photosensitization, Biochemistry 31 (1) (1992) 106–110.
[32] G. Speit, et al., Sensitivity of the FPG protein towards alkylation damage in the comet assay, Toxicol. Lett. 146 (2) (2004) 151–158.
[33] A.R. Collins, The use of bacterial repair endonucleases in the comet assay, in: J.-C. Gautier (Ed.), Drug Safety Evaluation: Methods and Protocols, Springer New York, New York, NY, 2017, pp. 173–184.
[34] S.H. Kang, et al., Recent advances in in vivo genotoxicity testing: prediction of carcinogenic potential using comet and micronucleus assay in animal models, J. Cancer Prev. 18 (4) (2013) 277–288.
[35] Y.H. Hong, et al., Assessment of the predictive capacity of the optimized in vitro comet assay using HepG2 cells, Mutat. Res. 827 (2018) 59–67, https://doi.org/10.1016/j.mrgentox.2018.01.010.
[36] J. Schindelin, et al., Fiji: an open-source platform for biological-image analysis, Nat. Methods 9 (7) (2012) 676–682, https://doi.org/10.1038/nmeth.2019.
[37] N. El Yamani, et al., In vitro genotoxicity testing of four reference metal nanomaterials, titanium dioxide, zinc oxide, cerium oxide and silver: towards reliable hazard assessment, Mutagenesis 32 (1) (2017) 117–126, https://doi.org/10.1093/mutage/gew060.
[38] A. Azqueta, et al., Comet assay to measure DNA repair: approach and applications, Front. Genet. 5 (2014) 288, https://doi.org/10.3389/fgene.2014.00288.
[39] A. Kermanizadeh, et al., Hepatic toxicology following single and multiple exposure of engineered nanomaterials utilising a novel primary human 3D liver microtissue model, Part. Fibre Toxicol. 11 (1) (2014) 56, https://doi.org/10.1186/s12989-014-0056-2.
[40] T. Hurrell, et al., Characterization and reproducibility of HepG2 hanging drop spheroids toxicology in vitro, Toxicol. In Vitro 50 (2018) 86–94, https://doi.org/10.1016/j.tiv.2018.02.013.
[41] P. Moller, The alkaline comet assay: towards validation in biomonitoring of DNA damaging exposures, Basic Clin. Pharmacol. Toxicol. 98 (4) (2006) 336–345, https://doi.org/10.1111/j.1742-7843.2006.pto_167.x.
[42] C.C. Bell, et al., Characterization of primary human hepatocyte spheroids as a model system for drug-induced liver injury, liver function and disease, Sci. Rep. 6 (2016) 25187, https://doi.org/10.1038/srep25187.
[43] X. Yang, et al., Chapter 13: hepatic toxicity biomarkers, in: R. Gupta (Ed.), Biomarkers in Toxicology, Elsevier, USA, 2014.
[44] J. Ozer, et al., The current state of serum biomarkers of hepatotoxicity, Toxicology 245 (3) (2008) 194–205, https://doi.org/10.1016/j.tox.2007.11.021.
[45] T. Nishikawa, et al., Optimization of albumin secretion and metabolic activity of cytochrome P450 1A1 of human hepatoblastoma HepG2 cells in multicellular spheroids by controlling spheroid size, Biol. Pharm. Bull. 40 (3) (2017) 334–338, https://doi.org/10.1248/bpb.b16-00833.
[46] J.P. Buchweitz, et al., Underlying endotoxemia augments toxic responses to chlorpromazine: is there a relationship to drug idiosyncrasy? J. Pharmacol. Exp. Ther. 300 (2) (2002) 460–467.
[47] J. Xuan, et al., Development of HepG2-derived cells expressing cytochrome P450s for assessing metabolism-associated drug-induced liver toxicity, Chem. Biol.

Interact. 255 (2016) 63–73, https://doi.org/10.1016/j.cbi.2015.10.009.
[48] D. Mueller, et al., 3D organotypic HepaRG cultures as in vitro model for acute and repeated dose toxicity studies, Toxicol. In Vitro 28 (1) (2014) 104–112, https://doi.org/10.1016/j.tiv.2013.06.024.
[49] Y. Finkelstein, et al., Colchicine poisoning: the dark side of an ancient drug, Clin. Toxicol. (Phila) 48 (5) (2010) 407–414, https://doi.org/10.3109/15563650.2010.495348.
[50] World Health Organization, I.A.f.R.o.C.I, IARC Monographs on the Evaluation of Carcinogenic Risks to Humans, (1999).
[51] M.D. Wyatt, D.L. Pittman, Methylating agents and DNA repair responses: Methylated bases and sources of strand breaks, Chem. Res. Toxicol. 19 (12) (2006) 1580–1594, https://doi.org/10.1021/tx060164e.
[52] M.Y. Lee, et al., Alkylating agent methyl methanesulfonate (MMS) induces a wave of global protein hyperacetylation: implications in cancer cell death, Biochem. Biophys. Res. Commun. 360 (2) (2007) 483–489, https://doi.org/10.1016/j.bbrc.2007.06.084.
[53] D. Slamenova, et al., Carboxymethyl chitin-glucan (CM-CG) protects human HepG2 and HeLa cells against oxidative DNA lesions and stimulates DNA repair of lesions induced by alkylating agents, Toxicol. In Vitro 24 (7) (2010) 1986–1992, https://doi.org/10.1016/j.tiv.2010.08.015.
[54] M. Dusinska, A. Collins, Detection of oxidised purines and UV-induced photo-products in DNA, by inclusion of lesion-specific enzymes in the comet assay (single cell gel electrophoresis), Atla- Altern. Lab. Anim. 24 (1996) 405–411.
[55] M. Uhl, C. Helma, S. Knasmuller, Single-cell gel electrophoresis assays with human-derived hepatoma (Hep G2) cells, Mutat. Res. 441 (2) (1999) 215–224.
[56] H. Gaskell, et al., Characterization of a functional C3A liver spheroid model, Toxicol. Res. (Camb) 5 (4) (2016) 1053–1065, https://doi.org/10.1039/c6tx00101g.
[57] S. Lemmo, et al., Optimization of Aqueous biphasic tumor spheroid micro-technology for anti-cancer drug testing in 3D culture, Cell. Mol. Bioeng. 7 (3) (2014) 344–354, https://doi.org/10.1007/s12195-014-0349-4.
[58] D.J. Kerr, et al., The effect of adriamycin and 4'-deoxydoxorubicin on cell survival of human lung tumour cells grown in monolayer and as spheroids, Br. J. Cancer 54 (3) (1986) 423–429.
[59] A. Nagelkerke, P.N. Span, Staining against phospho-H2AX (gamma-H2AX) as a marker for DNA damage and genomic instability in cancer tissues and cells, Adv. Exp. Med. Biol. 899 (2016) 1–10, https://doi.org/10.1007/978-3-319-26666-4_1.

The comet assay applied to HepG2 liver spheroids – Appendix A. Supplementary data

Elisabeth Elje [1], Michelle Hesler [2], Elise Rundén-Pran [1], Pascal Mann [2], Espen Mariussen [1], Sylvia Wagner [2], Maria Dusinska [1], Yvonne Kohl [2 *]

[1] NILU – Norwegian Institute for Air Research, Department for Environmental Chemistry, Health Effects Laboratory, Instituttveien 18, 2007 Kjeller, Norway
[2] Fraunhofer Institute for Biomedical Engineering IBMT, Joseph-von-Fraunhofer-Weg 1, 66280 Sulzbach, Germany
*Corresponding author: yvonne.kohl@ibmt.fraunhofer.de

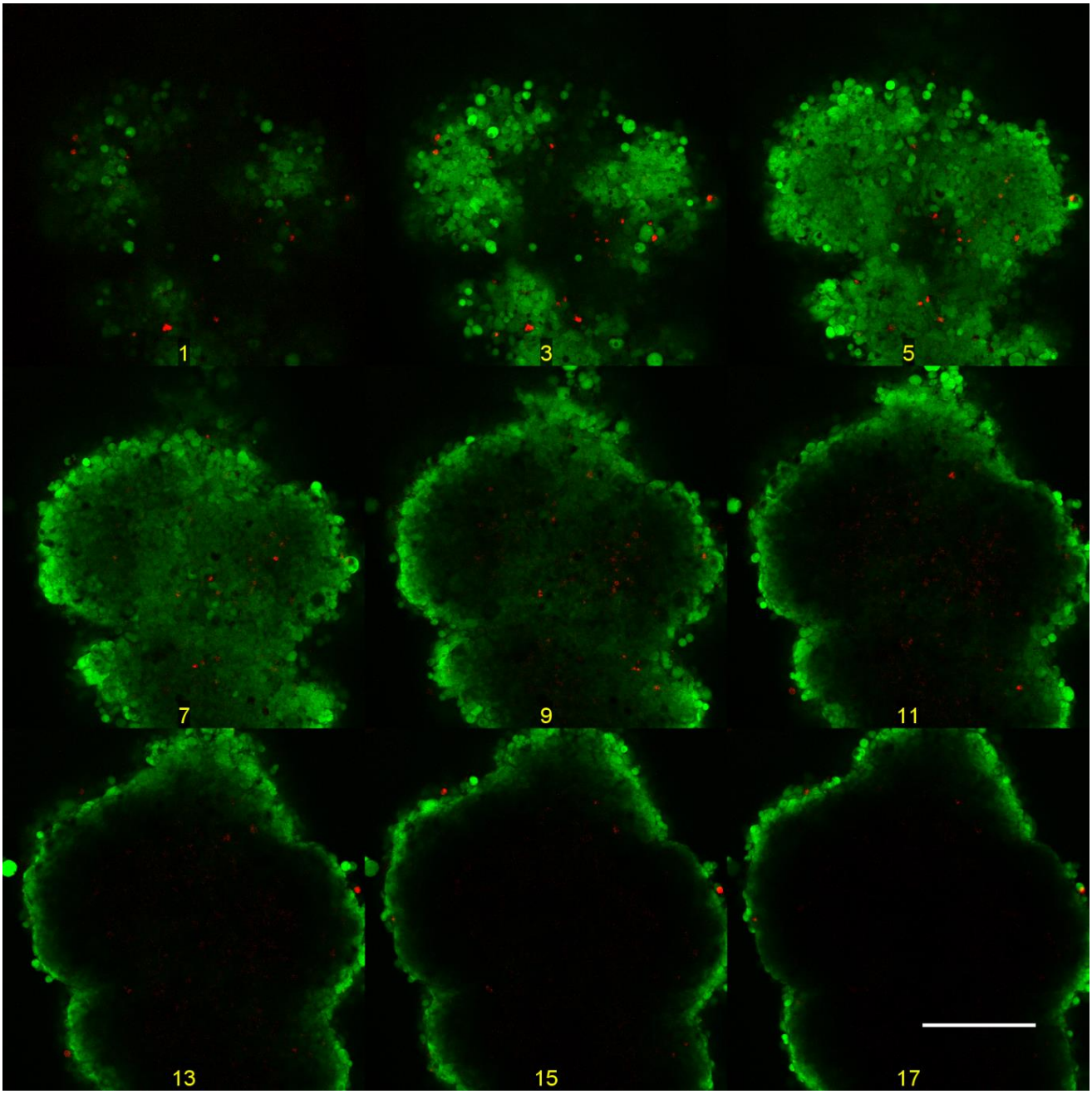

Fig. A.1: Z-stack of confocal images of a non-exposed HepG2 spheroid. The cells were stained with the fluorescent dyes fluorescein diacetate (green) and propidium iodide (red). The images from the z-stack show a low number of dead cells (red) and a large number of viable cells (green). Nine of 20 images are shown, where the first image (1) is at the surface of the spheroid. Images were collected at 5.45 µm intervals. Scale bar 200 µm.

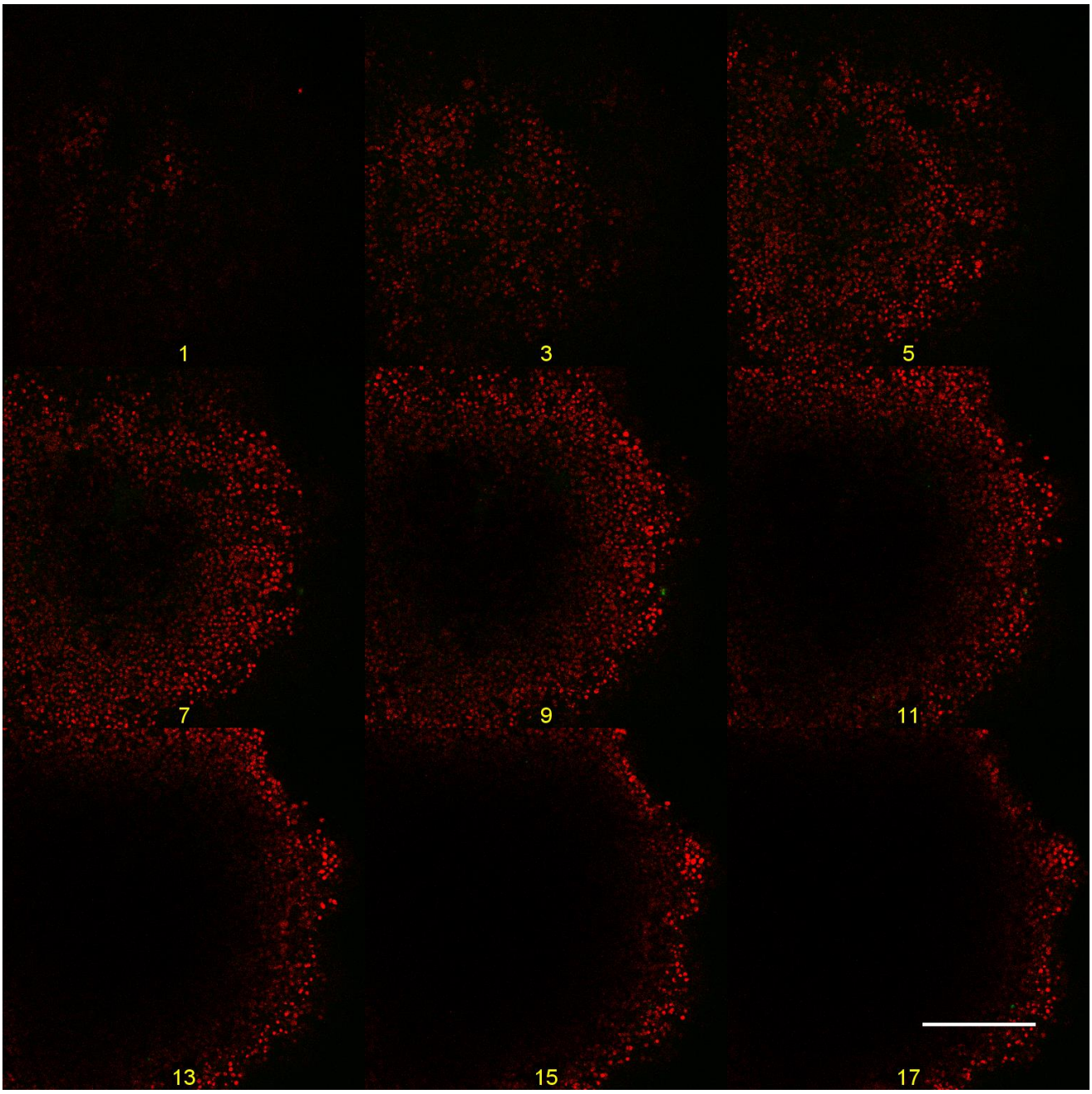

Fig. A.2: Z-stack of confocal images of a HepG2 spheroid exposed to 300 µM CHLO for 24h. After the CHLO-exposure the cells were stained with the fluorescent dyes fluorescein diacetate (green) and propidium iodide (red). The images from the z-stack show a low number of viable cells (green) and a large number of dead cells (red). Nine of 28 images are shown, where the first image (1) is at the surface of the spheroid. Images were collected at 5.45 µm intervals. Scale bar 200 µm.

nanomaterials

MDPI

Article

Hepato(Geno)Toxicity Assessment of Nanoparticles in a HepG2 Liver Spheroid Model

Elisabeth Elje [1,2], Espen Mariussen [1], Oscar H. Moriones [3,4], Neus G. Bastús [3], Victor Puntes [3,5,6], Yvonne Kohl [7], Maria Dusinska [1] and Elise Rundén-Pran [1,*]

1 Health Effects Laboratory, Department for Environmental Chemistry, NILU—Norwegian Institute for Air Research, Instituttveien 18, 2007 Kjeller, Norway; eel@nilu.no (E.E.); ema@nilu.no (E.M.); mdu@nilu.no (M.D.)
2 Department of Molecular Medicine, Institute of Basic Medical Sciences, Faculty of Medicine, University of Oslo, Sognsvannsveien 9, 0372 Oslo, Norway
3 Institut Català de Nanociència y Nanotecnologia (ICN2-UAB-CSIC-BIST), Campus UAB, Bellaterra, 08193 Barcelona, Spain; oscarhernando.moriones@icn2.cat (O.H.M.); neus.bastus@icn2.cat (N.G.B.); victor.puntes@icn2.cat (V.P.)
4 Universitat Autonòma de Barcelona (UAB), Campus UAB, Bellaterra, 08193 Barcelona, Spain
5 Vall d'Hebron Institut de Recerca (VHIR), 08035 Barcelona, Spain
6 Institució Catalana de Recerca i Estudis Avançats (ICREA), 08010 Barcelona, Spain
7 Fraunhofer Institute for Biomedical Engineering IBMT, Joseph-von-Fraunhofer-Weg 1, 66280 Sulzbach, Germany; yvonne.kohl@ibmt.fraunhofer.de
* Correspondence: erp@nilu.no

Received: 31 January 2020; Accepted: 11 March 2020; Published: 18 March 2020

Abstract: (1) In compliance with the 3Rs policy to reduce, refine and replace animal experiments, the development of advanced in vitro models is needed for nanotoxicity assessment. Cells cultivated in 3D resemble organ structures better than 2D cultures. This study aims to compare cytotoxic and genotoxic responses induced by titanium dioxide (TiO_2), silver (Ag) and zinc oxide (ZnO) nanoparticles (NPs) in 2D monolayer and 3D spheroid cultures of HepG2 human liver cells. (2) NPs were characterized by electron microscopy, dynamic light scattering, laser Doppler anemometry, UV-vis spectroscopy and mass spectrometry. Cytotoxicity was investigated by the alamarBlue assay and confocal microscopy in HepG2 monolayer and spheroid cultures after 24 h of NP exposure. DNA damage (strand breaks and oxidized base lesions) was measured by the comet assay. (3) Ag-NPs were aggregated at 24 h, and a substantial part of the ZnO-NPs was dissolved in culture medium. Ag-NPs induced stronger cytotoxicity in 2D cultures (EC_{50} 3.8 μg/cm^2) than in 3D cultures (EC_{50} > 30 μg/cm^2), and ZnO-NPs induced cytotoxicity to a similar extent in both models (EC_{50} 10.1–16.2 μg/cm^2). Ag- and ZnO-NPs showed a concentration-dependent genotoxic effect, but the effect was not statistically significant. TiO_2-NPs showed no toxicity (EC_{50} > 75 μg/cm^2). (4) This study shows that the HepG2 spheroid model is a promising advanced in vitro model for toxicity assessment of NPs.

Keywords: advanced in vitro model; comet assay; genotoxicity; hepatotoxicity; liver spheroids; nanoparticles; 3D culture; HepG2

1. Introduction

During the last decades, concerns have been raised about the potential human health risk of nanoparticles (NPs) due to the increased development and production of NPs with novel properties [1,2]. NPs are produced in a huge variety of forms and in large volumes, and they are used in a broad range of applications in everyday life. For example, NPs of titanium dioxide (TiO_2) are used as a pigment in paint, food and cosmetics [3]; zinc oxide (ZnO) is used in cosmetics due to its UV-blocking properties [4];

and silver (Ag) is used as a disinfection agent in medical equipment and consumer products, on account of its antimicrobial activity [5]. Thus, humans are likely to be exposed to NPs, either intentionally or accidentally, during production and usage [6]. Transport of NPs across biological barriers has been observed by elemental analysis in both rodents and humans [7–11]. As an example, gold NPs have been reported to reach the systemic circulation in humans, after inhalation, and translocate to other organs [8,9].

Several *in vivo* studies show that NPs accumulate in the liver, which is an important target organ for NPs and other xenobiotics due to its metabolic activity [12–18]. Induction of hepatotoxicity is one of the most common reasons for a medicine to be rejected or removed from the market [19,20]. Therefore, there is a need for sensitive hepatotoxicity screening methods for drug development and hazard assessment of chemicals or new materials, such as NPs. When considering the 3Rs—replacement, reduction and refinement—to minimize the use of animal experiments, hepatotoxicity should be assessed by reliable in vitro models. A great advantage of in vitro hepatocellular models for studying hepatotoxicity is the possibility of using human cells, either as primary cells or cell lines. The use of human hepatocyte cell lines, such as HepG2, C3A, Huh7 and HepaRG, has many advantages compared to primary cells. They are relatively easy to culture and have an unlimited life span, a relatively stable phenotype, high availability and low costs; moreover, inter-donor variations are avoided [21]. However, when comparing in vitro cell culture models in standard two-dimensional (2D) monolayers with complex organs, the cell lines in 2D culture display a limited hepatocytic functionality [21].

The liver-like functionality of the human hepatocellular carcinoma cell line HepG2 is enhanced when the cells are cultured in a three-dimensional (3D) arrangement. This increases the cell-to-cell contacts and intercellular communication [22] and changes the protein expression and metabolic status of the cells [21–23]. HepG2 cells in 3D cultures show upregulation of genes involved in liver-specific xenobiotic and lipid metabolism, whereas genes related to the extracellular matrix, cytoskeleton and cell adhesion have higher expression in 2D cultures [22,24].

The use of spheroids as 3D cultures in hepatotoxicity assessment is an increasing field of interest, and HepG2 spheroids, prepared with and without using scaffolds, have been applied for toxicity experiments with both NPs [6,25,26] and chemicals [27,28]. However, the differences in toxic responses between cells cultured in 2D and 3D are not yet clear. The scaffold-free HepG2 spheroid model was characterized in [27], where we demonstrated its applicability for testing genotoxicity of standard chemicals by the modified enzyme-linked comet assay, which measures DNA strand breaks (SBs) and oxidized DNA lesions. Interestingly, we found differences in sensitivity between the 2D and 3D models [27]. The comet assay has also been performed with Ag-, ZnO- and TiO_2-NPs and carbon nanotubes on a commercialized spheroid model with primary liver cells [6], and it has been shown to work well with different 3D models [6,27,29,30]. However, the comet assay has—to our knowledge—not yet been applied in HepG2 spheroids for genotoxicity testing of NPs. By using the miniaturized version of the comet assay, the throughput is increased. High-throughput methods are needed to reduce and replace animal experiments and to align with the increasing amounts of NPs being produced [31]. HepG2 spheroids have also been applied in the micronucleus test for chromosomal aberration testing, showing higher sensitivity than a standard 2D model to exposure to benzo(a)pyrene and 2-amino-1-methyl-6-phenylimidazo(4,5-b)pyridine [28]. In contrast, Dubiak-Szepietowska et al. (2016) found that liver 3D cultures are more resistant than 2D to cytotoxicity induced by NPs of Ag, SiO_2 and ZnO [25].

This study aimed to evaluate cytotoxicity and genotoxicity in HepG2 2D and 3D cultures after 24 h exposure to TiO_2-, Ag- and ZnO-NPs and to identify any differences in responses in 2D and 3D cultures. The tested NPs were selected on the basis of high production volumes and applications in consumer and medical products.

2. Materials and Methods

2.1. Cultivation of HepG2 Cells and Preparation of Spheroidal Cultures

HepG2 cells, provided from the ECACC (European Collection of Authenticated Cell Cultures) (cell line no. 85011430, Salisbury, United Kingdom) were cultured in 2D and 3D arrangements, as previously explained in detail [27]. In brief, HepG2 cells were cultured in Dulbecco's modified Eagle's medium (DMEM D6046 with low glucose and 4 mM L-glutamine, Sigma-Aldrich, Oslo, Norway) supplemented with 10% *v/v* fetal bovine serum (FBS, 26140-079, Thermo Fisher Scientific, Oslo, Norway), 100 U/mL penicillin and 100 µg/mL streptomycin (5070-63, Thermo Fisher Scientific, Oslo, Norway). Spheroid generation was performed, using the hanging drop technique, with 2500 cells per 20 µL drop. After four days of incubation of the cells at 37 °C with 5% CO_2 as hanging drop, the spheroids were transferred to a low adhesion plate. After one week, the spheroids had a diameter of approximately 800 µm [27] and were exposed to NPs as explained below. In parallel, 2D cultures were seeded in a 96-well plate with 20000 cells/well the day before exposure.

2.2. Nanoparticle Dispersions and Preparation for Toxicity Studies

TiO_2-NPs were provided by Catalan Institute of Nanoscience and Nanotechnology (ICN2, Spain) in colloidal dispersion and stored at 4 °C. TiO_2-NPs, of a mean size of approximately 4 nm in diameter, were prepared by a precipitation method following and adapting the method of Pottier et al. [32]. The stock solution of Ti^{4+} (0.7 M) was prepared by dissolving the Titanium (IV) isopropoxide (TTIP, Fluka Chemika) precursor in an HCl (3 mol/L) solution. For the production of TiO_2 anatase NPs, an aqueous Ti^{4+} stock solution (50 mL) was diluted in Milli-Q water (350 mL), at room temperature. The pH of the mixture was fixed at 11 by the addition of NaOH (3 M). Suspensions were aged at 70 °C for 24 h, and the solid was collected by centrifugation. Samples were further purified by 3 centrifuging cycles and re-suspended in an aqueous solution of tetramethylammonium hydroxide (TMAOH, Sigma-Aldrich) (100 M). Samples were characterized by transmission electron microscopy, dynamic light scattering and UV-Vis spectroscopy. The former was used to determine the particle size and size distribution. On the day of exposure, the TiO_2-NPs were diluted in FBS (1:1), and thereafter diluted 1:9 in cell culture medium, without FBS, to a concentration of 455 µg/mL (stock dispersion).

Ag-NPs (NM300K) were provided by Fraunhofer Institute for Molecular Biology and Applied Ecology (IME, Schmallenberg, Germany) and ZnO-NPs (NM110, JRCNM01100a) by the Joint Research Centre (Ispra, Italy). Stock dispersions of Ag- and ZnO-NPs were prepared according to the NANOGENOTOX protocol [33]. Briefly, the Ag- or ZnO-NPs were mixed with a bovine serum albumin (BSA) water solution (0.05% *m/v*, product nr A9418, Sigma-Aldrich), in a 20 mL scintillation vial (Wheaton Industries, Millville, NJ, USA), to a final concentration of 2.56 mg/mL (stock dispersion). To the ZnO-powder, 30 µL 100% ethanol (product nr 600068, Antibac AS, Asker, Norway) per 15.4 mg NP powder was added before BSA-water, to facilitate dispersion. The NP/BSA–water mixtures were sonicated on ice with a sonicator probe Labsonic®P Probe 3 mm (853 5124, Sartorius Stedim Biotech, Göttingen, Germany) and Labsonic®P (Sartorius Stedim Biotech), at 50% amplitude for 15 min (100% cycle, 100 watts), or with an ultrasound homogenizer Sonopuls (Bandelin, Germany), at 50% amplitude for 15 min (100% cycle). The dispersion solution of NM300K (NM300K DISP) was not included in the study, based on negative results from other studies on cytotoxicity and DNA damage [34–36].

Working concentrations of all the NPs were prepared by serial dilution of the stock dispersion in the culture medium. HepG2 cells in 2D and 3D culture were exposed for 24 h to TiO_2-NPs, Ag-NPs or ZnO-NPs (1–75 µg/cm^2 in 2D system, corresponding to 3–212 µg/mL in both systems; see Supplementary Tables S1 and S2 for details). As a negative control, complete NP-free culture medium was used. The same volumes (100 µL per well) and concentrations of NPs were used for both 2D and 3D cultures. NP dispersions were prepared, at most, two hours before cell exposure and NP characterization.

For characterization purposes (next sections), the NP stock solutions were also prepared in water dispersions, without proteins present, as described above, but in water instead of FBS/medium and BSA-water.

2.3. Size and Morphology Measurements of the NPs by Electron Microscopy

TiO_2-NP diameters were obtained from the analysis of transmission electron microscopy (TEM) images acquired with a FEI Tecnai G2 F20 S-TWIN HR(S) TEM equipped with an energy-dispersive X-ray spectroscopy (EDX) detector, operated at an accelerated voltage of 200 kV. Microliters of the samples were prepared by drop-casting 10 µL of the sample on a carbon-coated copper TEM grid and leaving to dry at room temperature. In addition, scanning electron microscopy was done with a FEI Magellan 400L XHR SEM, in scanning mode, operated at 1 kV, and in transmission mode, operated at 20 kV/STEM, for bigger sizes. The average size and size distribution of the samples were measured by using ImageJ software, by counting at least 300 particles from different regions of the grid. TEM images of Ag- and ZnO-NPs were acquired, but the size distribution was not measured.

2.4. Hydrodynamic Diameter and Zeta Potential Measurements of the NPs

The hydrodynamic size and surface charge of the NPs were determined by Dynamic Light Scattering and Laser Doppler Anemometry, respectively, using a Zetasizer Nano ZS (Malvern Instruments, Malvern, UK) instrument equipped with a light source wavelength of 532 nm and a fixed scattering angle of 173°. Aliquots of one milliliter of the colloidal NP dispersions at a concentration of 10% (*v*/*v*) were placed into specific plastic cuvettes, and the software was arranged with the parameters of refractive index and absorption coefficient, and the solvent viscosity at 25 °C. Each value was the average of at least 3 independent measurements. All measurements used the Smoluchowski model.

2.5. UV-Vis Measurements of the NP Dispersions

UV-visible spectra were acquired with an Agilent Cary 60 UV-Vis spectrophotometer. A 10% (*v*/*v*) colloidal NP dispersion was placed in a cell, and the spectral analysis was performed in the 200–800 nm wavelength range, at room temperature.

2.6. Analysis of Silver and Zinc Ions in NP Dispersions

Samples for analysis of dissolved silver and zinc and potential dissolution of the NPs were taken from cell-free exposure medium parallel to the start of exposure. The concentrations 1, 10, 30 and 100 µg/cm^2 were selected, corresponding to 2.8–283 µg/mL. Medium without NPs was used as control. The samples were transferred to Amicon Ultra centrifugal filter unit tubes (Millipore, product no UFC900324) containing a 3 KDa filter unit [37]. The tubes were preconditioned before use with ultrapure water at 3900 g for 10 min. The samples were centrifuged at 3900 g for 30 min, to let the particles remain in the filter and the dissolved Ag and Zn to go through with the filtrate.

An aliquot of the filtrate containing released ions from the NPs was added to supra pure nitric acid, at a final concentration of 1% (*v*/*v*). The concentrations of dissolved zinc and silver (defined as <3 kDa fraction) were determined by the use of an inductively coupled plasma mass spectrometer (ICP-MS) type Agilent 7700× (Agilent, Santa Clara, CA, USA), using the method accredited according to requirements of NS-EN/IEC 17025 (NILU-U-110). Then, ^{115}In was added to all standards, blanks and samples, as internal standard, and detection limits were 0.006 ng/mL Ag and 0.6 ng/mL Zn. Certified reference material (1640a Trace Elements in Natural Water, NIST) were analyzed in every run. One sample per concentration was used in three independent experiments (n = 3).

2.7. Fluorescence Imaging of the Spheroids

After NP exposure, the spheroids were washed with PBS before live and dead cells were stained by fluorescein diacetate (FDA, Invitrogen, Thermo Fisher Scientific, Oslo, Norway) and propidium iodide (PI, Invitrogen, Thermo Fisher Scientific), respectively. After incubation with 30 µg/mL FDA and 40 µg/mL PI for 10 min in the dark, at room temperature, the spheroids were washed with PBS and transferred to a glass-bottomed culture slide (µ-slide 8-well glass bottom, Ibidi) for imaging with confocal microscope Zeiss LSM 700, using the software ZEN2010 (Zeiss). Excitation and emissions peaks were 535 and 617 nm for PI and 498 and 517 nm for FDA. At least three spheroids were imaged from each sample in two independent experiments (n = 2). Z-stack images were captured from the spheroid surface and approximately 150 µm inside, toward the center of the spheroid, as described in [27]. The images were merged by using maximum intensity in ImageJ [38].

2.8. Viability Measurements by AlamarBlue Assay

The alamarBlue assay measures the ability of the cells to metabolize resazurin by reducing it to the fluorescent molecule resorufin. The metabolic capacity represents the viability of the cell culture relative to the control sample. The assay was performed to evaluate the cell viability in the 3D and 2D cultures after NP exposure, as described in [27]. In brief, 2D and 3D cultures were washed with PBS and incubated with alamarBlue solution (10% *w*/*v*) for 3 h, before fluorescence was measured quantitatively on a plate reader (excitation = 530 nm; emission = 590 nm). Chlorpromazine hydrochloride (Sigma-Aldrich, Oslo, Norway), 100 µM, was included as positive control for the assay, based on results from [27], giving cell viability below 30% for both 2D and 3D cultures after 24 h exposure. At least two and three parallel culture wells were used per concentration for 2D and 3D cultures, respectively, and at least two wells per culture well were used for determining average fluorescence. To control for potential interference between the NPs and the alamarBlue solution, cell-free control samples, with and without NPs, were included.

To compare potential cytotoxic effects of NPs with their corresponding salts, HepG2 cells in 2D configuration were exposed to solutions of silver nitrate ($AgNO_3$) and zinc chloride ($ZnCl_2$). Both $AgNO_3$ (product nr 319430, Fluka) and $ZnCl_2$ (product nr 793523, Sigma-Aldrich, Oslo, Norway) were dissolved in complete cell culture medium (5 mM) before being further diluted upon cell exposure (1–5000 µM). Cells (2D) were exposed in 96-well plates, with at least 3 parallel exposure wells, for 24 h.

2.9. DNA Damage Measured by the Comet Assay

The enzyme-linked alkaline comet assay with inclusion of formamidopyrimidine DNA glycosylase (Fpg, gift from NorGenoTec AS Professor Andrew Collins and Dr. Sergey Shaposhnikov, Norway) was used to measure the level of DNA SBs and oxidized bases in 2D and 3D cultures. Fpg measures oxidized and ring open purines and DNA alkylated bases [39,40] and converts these lesions to SBs. The detailed procedure of the modified comet assay in 2D and 3D models is described in [27]. In brief, disaggregated cultures were embedded in low-melting-point agarose on precoated slides, before being submerged in lysis solution (2.5 M NaCl, 0.1 M EDTA, 10 mM Tris, 10% *v*/*v* Triton X-100, pH 10, 4 °C) for at least 1 h. The miniaturized version of the comet assay was used, with 12 mini-gels on each slide, similarly to [36]. Slides with samples for Fpg incubation were washed twice for 8 min in buffer F (40 mM HEPES, 0.1 M KCl, 0.5 mM EDTA, 0.2 mg/mL BSA, pH 8, 4 °C), Fpg diluted in buffer F was added, covered with a polyethylene foil and incubated at 37 °C for 30 min, in a humid box. All slides with cells embedded in gels were placed in the electrophoresis tank with electrophoresis solution (0.3 M NaOH, 1 mM EDTA, pH > 13, 4 °C), to let the DNA unwind for 20 min before running electrophoresis for 20 min (25 V, 1.25 V/cm, Consort EV202). Slides were neutralized in PBS and H_2O and dried horizontally, before staining with SYBR®gold (Sigma-Aldrich, Oslo, Norway). Comets were imaged using a Leica DMI 6000 B microscope (Leica Microsystems), equipped with a SYBR®photographic filter (Thermo Fischer Scientific, Oslo, Norway), and scored using the software Comet Assay IV 4.3.1

(Perceptive Instruments, Bury St Edmunds, UK). Median % DNA in tail from around 50 comets per gel was used as a measure of DNA SBs. Oxidized DNA lesions were calculated as net Fpg-sensitive sites, i.e., as the difference in % DNA in tail between samples with Fpg incubation and samples without incubation. Hydrogen peroxide, H_2O_2 (50 μM, Sigma-Aldrich, Oslo, Norway), and the photosensitizer Ro 19-8022 (2 μM, kindly provided by Hoffmann La Roche) with light irradiation were included as positive controls for DNA SBs and Fpg activity, respectively. The photosensitizer with light induces oxidized purines, mainly 8-oxoGuanine, which is detected by the Fpg [39,41]. At least 2 and 3 gels were prepared for each concentration, for 2D and 3D cultures, respectively, in each experiment.

2.10. Statistical Analysis

Results are presented as mean with standard error of the mean (SEM) of 3 independent experiments ($n = 3$), unless otherwise mentioned. Effects were compared to nontreated cells, and statistical analysis by one-way ANOVA, multiple comparisons and post-test Dunnett were performed in GraphPad Prism 7. Comparison of 2D and 3D cultures were performed by two-way ANOVA, multiple comparisons and post-test Sidak. The *p*-values are marked by * as $p < 0.05$, ** as $p < 0.01$, *** as $p < 0.001$ and **** as $p < 0.0001$. EC_{50} values were calculated in Prism, using nonlinear regression analysis (Hill function).

3. Results

3.1. Characterization of the NPs

Characterization of the NPs was performed in water (TiO_2-NPs 455 μg/mL, Ag- and ZnO-NPs 2.56 mg/mL), stock dispersions (TiO_2-NPs 455 μg/mL in TMAOH and culture medium with FBS, Ag- and ZnO-NPs 2.56 mg/mL in BSA-water) and working dispersions (212 μg/mL in medium), at 0 and 24 h after preparation. A summary of the physical and chemical characteristics of the pristine NPs used is shown in Table 1.

3.1.1. Electron Microscopy Analysis for Size and Shape of the NPs

The primary size and shape of the NPs in water were determined by electron microscopy imaging (Figure 1). The TiO_2-NPs were quasi-spherical, with a mean diameter of 5.54 ± 0.98 nm (Figure 1A), the Ag-NPs were spherical (Figure 1B) and the ZnO-NPs were aggregated with irregular shapes (Figure 1C).

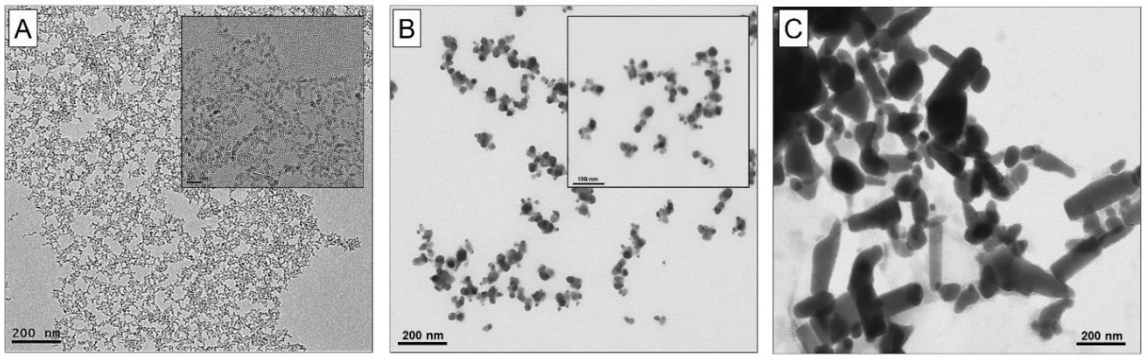

Figure 1. Representative transmission electron microscopy (TEM) images of (**A**) quasi-spherical TiO_2-NPs, and representative scanning transmission electron microscopy (STEM) images of (**B**) spherical Ag-NPs and (**C**) irregular ZnO-NPs in pure water. Scale bar = 200 nm. Scale bar in inserts: (**A**) 20 nm and (**B**) 100 nm.

Table 1. Characterization of pristine nanoparticles (NPs). TiO_2-NPs were provided by ICN2, Ag-NPs by Fraunhofer IME and ZnO-NPs by JRC. TMAOH: tetramethylammonium hydroxide. PGT: polyoxyethylene glycerol trioleate. PEG: polyethylene glycol, TEM: transmission electron microscopy. NA: not available.

NP	Code	Product Type	Solvent	Polymorph	Morphology	Surface Functionali-zation	TEM Diameter (nm)	Surface Area (m^2/g)	Ref.
TiO_2	-	Dispersion	TMAOH	Anatase	Quasi-sphere	TMAOH	5.54 ± 0.98	NA	
Ag	NM300K	Dispersion	PGT (4%), Tween 20 (4%)	Metallic	Sphere	PEG	<20 nm	NA	[42]
ZnO	NM110/JRCNM01100a	Powder	-	Zincite	Variable	Uncoated	147 ± 149	12.4 ± 0.2	[43]

3.1.2. UV-Vis Spectroscopy for Analysis of Particle Stability

UV−vis spectra of the NP dispersions prepared in pure water (t = 0 h), as stock dispersions (t = 0 and 24 h) and as working dispersions (t = 0 and 24 h) are shown in Figure 2. When comparing Ag-NPs diluted in pure water and in water with BSA (stock), no red-shift is observed (Figure 2A,B). The red-shift is indicative of the formation of a dense dielectric layer onto the NP surface consistent with the absorption of proteins on their surface, and no stable protein corona formation was thus measured for Ag-NPs, which can be ascribed to the presence of polyethylene glycol at their surface. The UV-vis spectra of Ag-NPs working dispersions have an increased absorbance signal at high wavelengths and a decrease in the peak intensity, indicative of aggregation. The UV-vis spectra of TiO_2- and ZnO-NPs (Figure 2C–F) lack absorption peaks in the visible region, and no changes in time were observed. The small peak that appears in the visible region around 500 nm, as shown in Figure 2B,D,F, is due to the presence of phenol red in the culture medium.

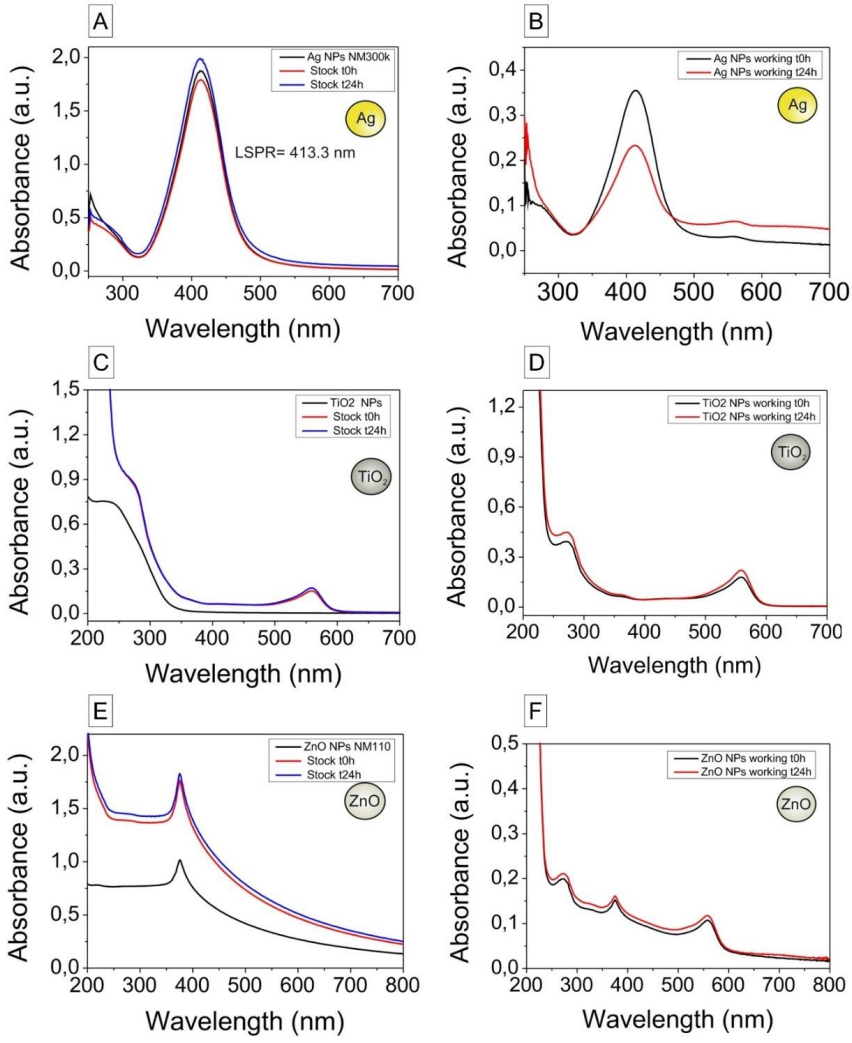

Figure 2. UV−vis spectra of the nanoparticle dispersions diluted in pure water (t = 0 h), as stock dispersions (t = 0 and 24 h) and as working dispersions (t = 0 and 24 h). Samples were diluted 1:200 (Ag), 1:10 (TiO_2) and 1:20 (ZnO) in pure water for analysis. (**A**) Ag-NPs in pure water and stock dispersion (2.56 mg/mL). (**B**) Ag-NPs working dispersion (212 μg/mL, t = 0 and 24 h). (**C**) TiO_2-NPs in water and stock dispersion (455 μg/mL, t = 0 and 24 h). (**D**) TiO_2-NPs working dispersion (212 μg/mL, t = 0 and 24 h). (**E**) ZnO-NPs in pure water and stock dispersion (2.56 mg/mL, t = 0 and 24 h). (**F**) ZnO-NPs working dispersion (212 μg/mL, t = 0 and 24 h). The peak at 560 nm can be ascribed to the presence of phenol red in the culture medium.

3.1.3. Hydrodynamic Diameter and Zeta Potential

The hydrodynamic diameter and zeta potential of the Ag-, ZnO- and TiO_2-NPs in pure water (t = 0 h only) are summarized in Supplementary Table S3; NP stock dispersions are in Table 2, and NP working dispersions are in Table 3. Representative size distribution curves are shown in Supplementary Figures S1 and S2.

Table 2. Hydrodynamic diameter and zeta potential (ZP) of nanoparticle (NP) stock dispersions (concentrations: TiO_2 455 µg/mL; Ag and ZnO 2.56 mg/mL). For analysis, samples were diluted 1:10 in pure water. Numbers are given as mean ± standard deviation (SD) (n = 3). PDI: polydispersity index, a.u.: arbitrary unit.

NP	Time (h)	Hydrodynamic Diameter (nm), by Intensity	PDI (a.u.)	ZP (mV)
TiO_2-NPs	0	193.6 ± 6.2	0.262 ± 0.013	−16.1 ± 1.80
	24	207.4 ± 43.1	0.242 ± 0.008	−14.3 ± 0.61
Ag-NPs (NM300K)	0	54.2 ± 3.48	0.364 ± 0.023	−9.84 ± 3.94
	24	57.5 ± 1.50	0.459 ± 0.026	−8.79 ± 2.41
ZnO-NPs (NM110)	0	373.8 ± 21.5	0.199 ± 0.046	−15.8 ± 0.70
	24	400.1 ± 11.9	0.166 ± 0.032	−14.8 ± 0.30

Table 3. Hydrodynamic diameter and zeta potential (ZP) of nanoparticle (NP) working dispersions (concentration 212 µg/mL, corresponding to 75 µg/cm^2). For analysis, samples were diluted 1:10 in pure water. Numbers are given as mean ± standard deviation (SD) (n = 3). PDI: polydispersity index; a.u.: arbitrary unit.

NP	Time (h)	Hydrodynamic Diameter (nm), by Intensity	PDI (a.u.)	ZP (mV)
TiO_2-NPs	0	217.3 ± 27.3	0.285 ± 0.013	−5.73 ± 1.62
	24	189.8 ± 16.2	0.235 ± 0.022	−7.49 ± 2.63
Ag-NPs (NM300K)	0	37.3 ± 0.04	0.283 ± 0.065	−14.4 ± 1.99
	24	508.8 ± 29.5	0.452 ± 0.095	−20.1 ± 1.45
ZnO-NPs (NM110)	0	346.1 ± 9.6	0.258 ± 0.020	−23.8 ± 0.30
	24	338.0± 21.7	0.281 ± 0.032	−24.9 ± 0.25

The hydrodynamic diameter (by intensity) was for all NPs higher than the pristine NP size. At the start of the experiment, the mean hydrodynamic diameter (by intensity) was 54.2 nm for Ag-NPs, 373.8 nm for ZnO-NPs and 193.6 nm for TiO_2-NPs. The hydrodynamic diameter of the TiO_2- and ZnO-NPs increased slightly between 0 and 24 h, for both the stock and working dispersions. In contrast, the increase in hydrodynamic diameter of the Ag-NPs was strong between 0 and 24 h, and the polydispersity index (PDI) was relatively high at 24 h, indicating a broader size distribution. The mean hydrodynamic diameter of samples without NPs showed the presence of proteins in the dispersions, measured with high variations (BSA-water 152.7 nm ± 43.0 nm with PDI 0.406 ± 0.003; medium 120.2 nm ± 59.9 nm with PDI 0.299 ± 0.128).

The zeta potential measurements also showed an evolution of the NPs' surface charge. A drop in the surface charge, toward the average value of proteins, was observed when comparing the dispersions without proteins (Supplementary Table S3) with stock (Table 2) and working dispersions (Table 3). Zeta potential curves are shown in Supplementary Figure S3. The zeta potential of NP free BSA-water was −2.15 ± 1.01 mV, and the corresponding value of medium was −5.77 ± 2.49 mV.

3.1.4. ICP-MS Analysis of Dissolved Ag and Zn in NP Dispersions

The concentrations of dissolved Ag and Zn in the <3 kDa filtrates were analyzed by ICP-MS. Medium without NPs had a Zn concentration of 25.7 µg/L (25.4–150.9 µg/L) or 0.4 µM (0.2–2.3 µM) whereas the Ag concentration was below the detection limit (<0.006 µg/L). A substantial amount of Zn was measured in the filtrate of the medium with added ZnO-NPs, ranging from 8 to 87 µM. In the filtrates from medium with added Zn-NPs (10–100 µg/cm^2), the Zn concentration was nearly the same (79 to 87 µM) (Table 4). The concentrations of dissolved Ag in the filtrate of the medium with added Ag-NPs ranged from 0.00008 to 0.014 µM (Table 4).

Table 4. Concentrations of dissolved Ag and Zn in dispersions of Ag- and ZnO-nanoparticles (NPs) in cell culture medium. Zn concentrations in medium without NPs was 25.7 µg/L (25.4–150.9 µg/L) or 0.4 µM (0.2–2.3 µM). Ag content was below the limit of detection (<0.006 µg/L). Numbers are given as median (interquartile range) (n = 3). * Theoretical concentration of total Ag or Zn in the dispersion (not ZnO).

NP	Nominal Concentration			Measured Dissolved Ag/Zn Concentration (<3 kDa)		
	µg/cm^2	µg/L *	µM *	µg/L	µM	% of Nominal
Ag-NPs (NM300K)	1	2827.4	26.2	0.0090 (0.0089–0.0399)	0.00008 (0.00008–0.00037)	0.0003
	10	28274.3	262.1	0.0920 (0.0804–1.2723)	0.001 (0.001–0.012)	0.0003
	30	84823.0	786.3	1.49 (0.88–4.08)	0.014 (0.008–0.038)	0.0018
	100	282743.3	2621.1	0.20 (0.12–6.98)	0.002 (0.001–0.065)	0.00007
ZnO-NPs (NM110)	1	2271.5	34.7	519.7 (428.0–611.3)	7.9 (6.5–9.4)	22.9
	10	22715.0	347.5	5166.9 (4998.8–5693.0)	79.0 (76.5–87.1)	22.7
	30	68144.9	1042.4	5177.1 (4898.0–5436.3)	79.2 (74.9–83.2)	7.6
	100	227149.6	3474.8	5700.5 (5627.4–6057.8)	87.2 (86.1–92.7)	2.5

3.2. Cytotoxicity of Ag-NPs, ZnO-NPs and TiO_2-NPs in 2D and 3D Cultures

Effects of Ag-NPs, ZnO-NPs and TiO_2-NPs on the viability of HepG2 cells in 2D and 3D cultures were measured after 24 h exposure, using alamarBlue assay and confocal imaging. No interference of NPs with the alamarBlue assay was found (results not shown). The relative cell viability decreased in a concentration-dependent manner after exposure to ZnO- and Ag-NPs, but not for TiO_2-NPs, in both 2D and 3D cultures (Figure 3). For ZnO-NPs, calculated EC_{50} values were in the same range for 2D and 3D cultures: 10.1 and 16.2 µg/cm^2, respectively (Table 5). The induced cytotoxicity of Ag-NP was higher in 2D cultures compared to 3D cultures, with EC_{50} values of 3.8 and >30 µg/cm^2, respectively (Table 5).

Table 5. EC_{50} values from alamarBlue assay in HepG2 2D and 3D cultures after 24 h exposure to TiO_2-NPs, Ag-NPs or ZnO-NPs. EC_{50} values of metal compartments are given in parentheses.

Substance	2D			3D		
	EC_{50} (µg/cm^2)	EC_{50} (µg/mL)	EC_{50} (µM)	EC_{50} (µg/cm^2)	EC_{50} (µg/mL)	EC_{50} (µM)
TiO_2-NP	>75.0 (>45.0)	>212.1 (>127.1)	>2655.2	>75.0 (>45.0)	>212.1 (>127.1)	>2655.2
Ag-NP	3.8	10.7	99.2	>30.0	>84.8	>786.4
ZnO-NP	10.1 (8.1)	28.5 (22.9)	350.4	16.2 (13.0)	45.7 (36.7)	561.4
$AgNO_3$	1.2 (0.8)	3.4 (2.2)	20.1	-	-	-
$ZnCl_2$	17.5 (8.4)	49.4 (23.7)	362.7	-	-	-

To investigate the distribution of viable and dead cells in the spheroid culture after exposure to Ag- and ZnO-NPs, confocal microscopy and imaging was performed on exposed spheroids with live and dead cell staining by FDA and PI, respectively. Increased numbers of dead cells on the spheroid surface were seen after exposure to Ag- and ZnO-NPs at the highest concentration, and correspondingly, fewer viable cells were detected. Limited fluorescence could be detected from the spheroid core, and the viability of cells in this region could therefore not be determined. Representative images show a projection of z-stack images from the spheroid surface to approximately 150 µm into the spheroid

(Figure 4). The confocal microscopy analysis showed a clear induction of cell death on the spheroid surface after exposure of Ag- and ZnO-NPs.

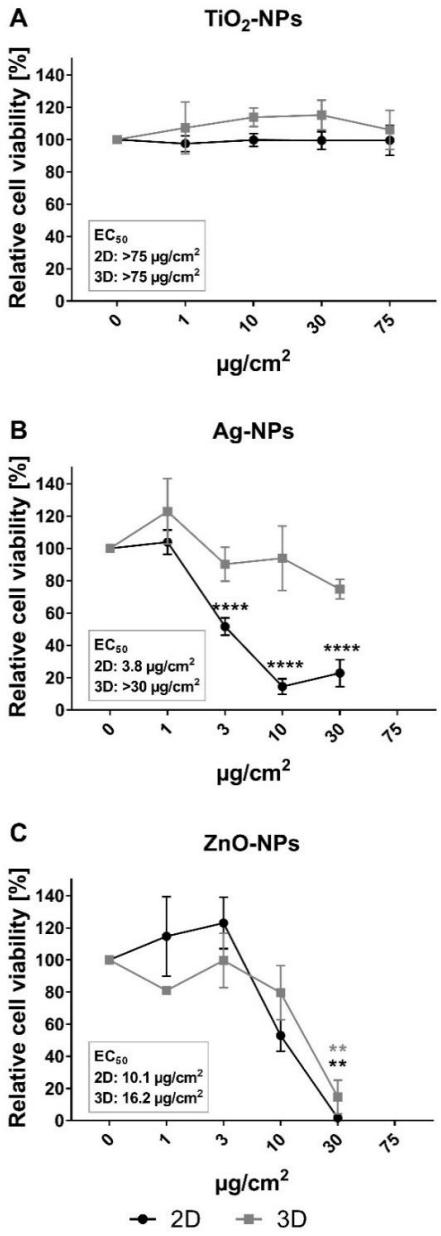

Figure 3. Cytotoxicity of TiO_2-, Ag- and ZnO-NPs measured by alamarBlue assay in 2D and 3D HepG2 cultures. Cell viability was measured as metabolic capacity and calculated relative to negative control cultures (set to 100%). (**A**) No significant effects were seen on the viability of 2D (black curve) and 3D (gray curve) cultures after 24 h exposure to TiO_2-NPs. The cell viability was reduced after 24 h incubation with (**B**) Ag-NP and (**C**) ZnO-NP for both 2D and 3D cultures. The effect of the exposure was significantly different in 2D and 3D cultures after exposure to Ag-NP at concentrations 10 and 30 µg/cm^2, evaluated by two-way ANOVA with post-test Sidak. Values are presented as mean ± SEM of 2–6 independent experiments: (**A**) n = 2, 3, (**B**) n = 4–6 and (**C**) n = 3. The concentration 75 µg/cm^2 was excluded for testing of Ag-NP and ZnO-NP (b and c) because of high cytotoxicity in previously published experiments [36]. ** $p < 0.01$; **** $p < 0.0001$.

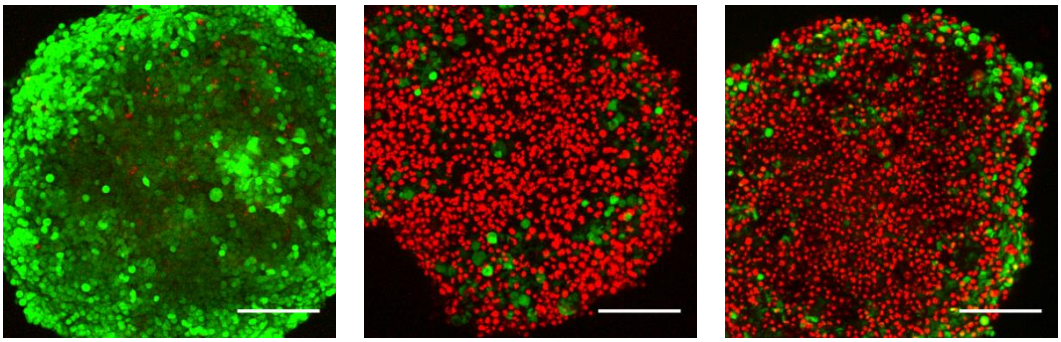

(**a**) (**b**) (**c**)

Figure 4. Representative confocal images of HepG2 spheroids exposed for 24 h to (**a**) culture medium, (**b**) Ag-NPs and (**c**) ZnO-NPs. Spheroids were exposed to 30 μg/cm^2 (85 μg/mL) of Ag- and ZnO-NPs for 24 h, before staining. Dead cells were stained with propidium iodide (PI) (**red**) and viable cells with fluorescein diacetate (FDA) (**green**). The images are z-stack projections from the spheroid surface and approximately 150 μm down toward the core. An increase in number of dead cells on the surface of the spheroids was seen after exposure to Ag-NPs and ZnO-NPs. Scale bar = 200 μm. Representative images from two independent experiments (n = 2), each with at least three parallel spheroids.

3.3. Cytotoxicity of Zn^{2+} and Ag^{+} Ion Solutions in 2D and 3D Cultures

To compare the cytotoxicity of Ag- and ZnO-NPs with corresponding salts, the alamarBlue assay was performed after exposure of HepG2 cells in the 2D model to $AgNO_3$ and $ZnCl_2$ solutions. Some precipitation was seen upon mixing the $AgNO_3$ solution into the cell culture medium, most likely due to precipitation of AgCl due to a high presence of Cl^- in the medium. The relative cell viability of the HepG2 cells after $AgNO_3$ and $ZnCl_2$ exposure decreased in a concentration-related manner (Supplementary Figure S4). The EC_{50} values were 20.1 μM for $AgNO_3$ and 362.7 μM for $ZnCl_2$ (Table 5), which are higher than the amounts of dissolved Ag and Zn measured in the NP dispersions (Section 3.1.4). If we used the same concentration units as the NPs, the EC_{50} values of $AgNO_3$ and $ZnCl_2$ would correspond to 0.8 μg/cm^2 (2.2 μg/mL) Ag^+ ions, and 8.4 μg/cm^2 (23.7 μg/mL) Zn^{2+} ions, assuming the compounds were freely dissolved in the solution. The EC_{50} values after exposure to ZnO-NPs and $ZnCl_2$ were similar. The EC_{50} value for Ag-NPs exposure was higher than for $AgNO_3$, showing higher cytotoxicity of the salt solution than the NPs in this test system.

3.4. Genotoxicity in 2D and 3D Cultures Measured by the Comet Assay

The levels of DNA SBs and oxidized base lesions were measured by the enzyme-linked comet assay after 24 h exposure with NPs. In both 2D and 3D cultures, a trend with a concentration-dependent increasing level of DNA SBs was seen after exposure to Ag-NPs and ZnO-NPs; however, a statistically significant increase was found only at cytotoxic concentrations in the 2D cultures (from exposure of 3 μg/cm^2 Ag-NPs and at 10 μg/cm^2 ZnO-NPs in 2D cultures). No effect on the level of DNA damage was observed after exposure to TiO_2-NPs in either 2D or 3D cultures (Figure 5). The background level of DNA damage was measured in unexposed HepG2 cells from 2D and 3D cultures and found to be similar for DNA SBs, with 5.0 ± 0.8 (2D, n = 9) and 6.2 ± 1.0 (3D, n = 7) % DNA in tail as average in all experiments (Supplementary Figure S5). For oxidized DNA base lesions, the background level was higher in 3D cultures compared to 2D, with levels of net Fpg sites at 3.7 ± 0.7 (2D, n = 9) and 7.6 ± 2.1 (3D, n = 7) % DNA in tail (Supplementary Figure S5). As a positive control for DNA SBs, cells were treated for 5 min with 50 μM H_2O_2; this induced a high level of DNA damage in both 2D and 3D cultures (Supplementary Figure S5). The control sample for Fpg enzyme activity, cells treated with Ro 19-8022 plus light, showed DNA damage within the expected range; the % DNA in tail was increased by at least 20 percentage points compared to without Fpg incubation (results not shown).

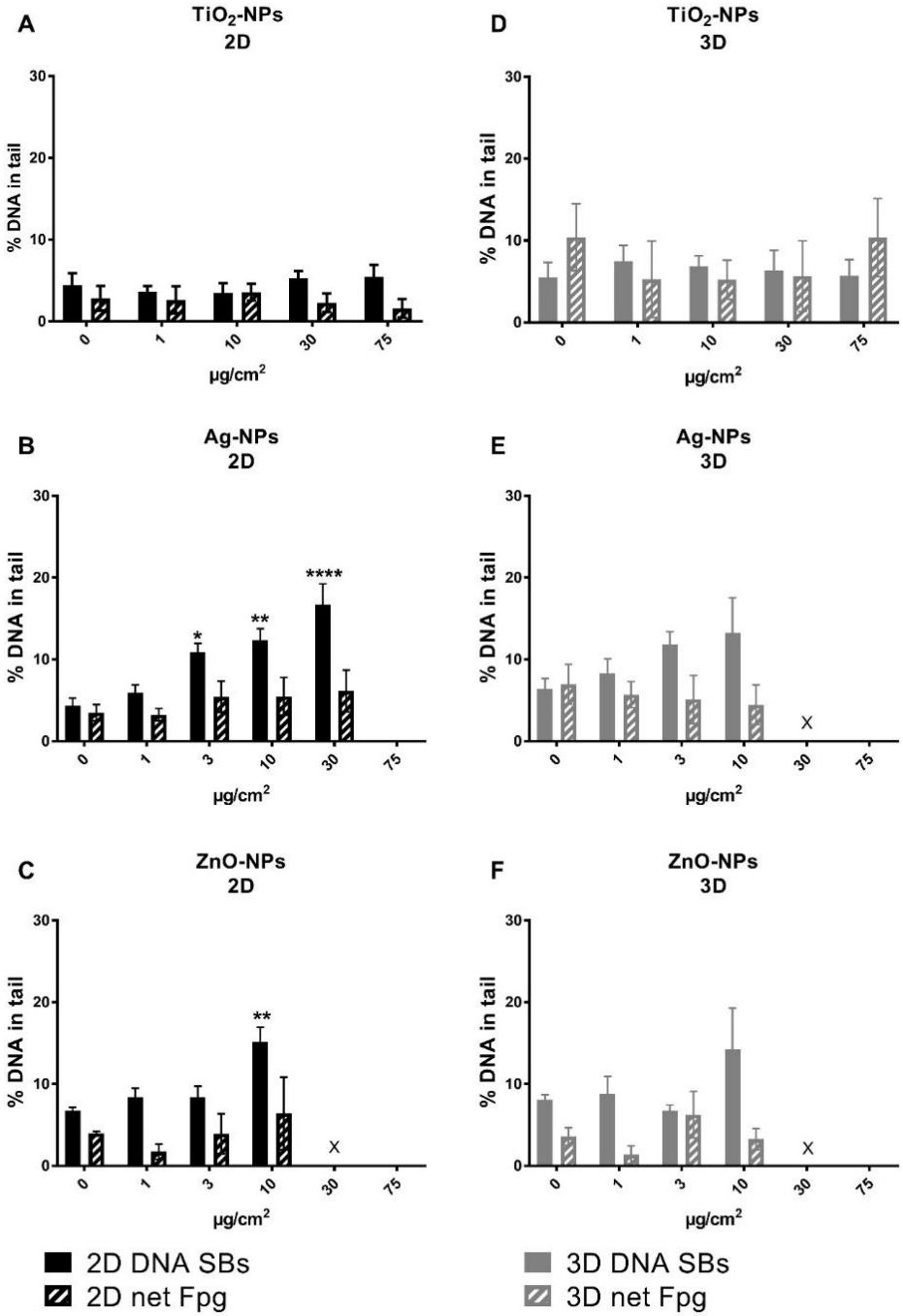

Figure 5. DNA damage in 2D and 3D cultures after exposure to TiO_2-, Ag- and ZnO-NPs measured by the comet assay. The 2D (**A**–**C**) and 3D (**D**–**F**) cultures were exposed to TiO_2-, Ag- and ZnO-NPs for 24 h. No increase in DNA damage was seen after exposure to TiO_2-NPs. Ag- and ZnO-NPs induced an increase in DNA SBs; however, this was statistically significant only at cytotoxic concentrations. Moreover, $n = 3$ for TiO_2- and ZnO-NPs, and $n = 6$ for Ag-NPs except at 3 µg/cm^2, where $n = 4$. X: not measured due to cytotoxicity and too low cell number. The concentration 75 µg/cm^2 was excluded in the experiments with Ag-NPs and ZnO-NPs (**B**,**C** and **E**,**F**) because of high cytotoxicity in previously published experiments [36]. * $p < 0.05$, ** $p < 0.01$, *** $p < 0.001$ and **** $p < 0.0001$.

4. Discussion

There is a huge demand to develop in vitro models that more closely resemble the *in vivo* situation, for toxicity assessment of NPs and chemicals. These models should be standardized in regard to critical toxicity endpoints. Here, we have focused on the liver spheroid model and evaluated it for reliability in detecting cytotoxicity and genotoxicity of NPs.

This study investigated potential differences in induction of cell death and DNA damage, depending on whether the liver cells were cultured in 2D or 3D arrangements, by applying the enzyme-linked comet assay, accompanied with cytotoxicity tests, on HepG2 spheroids and monolayers exposed to TiO_2-, Ag- and ZnO-NPs. HepG2 spheroids were prepared with a reproducible scaffold-free technique described in detail in Elje et al. (2019). Levels of DNA SBs in unexposed cells were found to be similar to the previous study [27]. However, 3D cultures had a higher background level of oxidized DNA lesions than 2D cultures, which can indicate a higher basal level of oxidative stress in the 3D model. This should be investigated further.

As toxicity of NPs is highly dependent upon physicochemical properties, it is important to characterize NP behavior under the given experimental conditions. The strong increase in the hydrodynamic size and the high PDI value for Ag-NPs indicate that the working dispersion of Ag-NPs had aggregated after 24 h of exposure. These results are in accordance with the UV-vis spectra, in which a decrease in intensity of the silver plasmon band, along with the increased absorbance at higher wavelengths, is shown. Ag-NP absorption is highly sensitive to the aggregation state of the NPs, due to strong surface plasmon resonance interactions between close NPs (at distances about their diameter) [44]. The UV-vis results, combined with the changes in size distribution and zeta potential, suggest that the amount of BSA protein per Ag-NP was too low to form a homogenous and dense coating, and that the stabilization of the NPs was likely to be electrostatic. Consequently, the ionic strength of the culture medium may contribute to the aggregation of the NPs. The increase in hydrodynamic diameter of TiO_2- and ZnO-NPs after 24 h can be explained by the formation of a loosely bound soft protein corona. In terms of NP stabilization by proteins, no significant information can be drawn from the UV-vis spectra of TiO_2- and ZnO-NPs. The wide band gap nature of these materials and their inability to absorb energy in the visible range explain the absence of absorption peaks in the visible region. Thus, the attenuation of transmitted light comes from the combination of absorption and Rayleigh scattering. Other studies using the same Ag-NPs (NM300K) and ZnO-NPs (NM110) have reported smaller hydrodynamic sizes and higher stability [6,36,43,45]. As NPs' behavior depends on their surroundings [46], this highlights the importance of performing NP characterization with the same conditions as used in the experiments.

Exposure of HepG2 cells to TiO_2-NPs did not induce any cytotoxicity or genotoxicity in 2D and 3D cultures. TiO_2-NPs have also been reported in other studies to be less toxic than other nano-metal oxides [47], and their toxicity is dependent on their physicochemical properties [48–50]. Toxic effects have been seen in both in vitro and *in vivo* studies [36,51,52] and are not related to dissolution of metal ions [47].

ZnO-NPs exposure induced cytotoxicity to a similar extent in both 2D and 3D HepG2 cultures. Elevated DNA damage was observed in 2D and 3D cultures at the highest concentrations; however, significant induction of DNA damage was found only in 2D cultures and at cytotoxic concentrations. Similarly, exposure to Ag-NPs induced cell death and a concentration-dependent increase in DNA damage, though statistically significant only at cytotoxic concentrations. The reduced viability seen with the alamarBlue assay was strongest in 2D cultures and did not reach statistical significance in the 3D cultures. However, when the spheroids were examined with confocal microscopy, many dead cells were seen at the surface of the exposed 3D cultures. As expected for a relatively complex model that closely resembles organ structure, higher variability was found in 3D cultures compared to 2D cultures. This can explain why statistically significant results were more difficult to achieve.

Significant induction of DNA SBs after ZnO- and Ag-NPs exposure was seen only at cytotoxic concentrations, in contrast to previously reported results for A549 and TK6 cells with the same NPs

and nearly identical comet assay protocols [36]. This can be explained by the cell lines used, as the HepG2 cells seem to be less sensitive to genotoxic compounds than A549 and TK6 cells. Cowie et al. studied genotoxic response to metal and polymeric NPs in human and mammalian cells of different origin and found large differences in sensitivity of cells, with TK6 cells giving one of the best concentration-dependent response [53]. The discrepancy can also be related to the differences in cell cycle and exposure times. As demonstrated in a study applying the comet assay with Fpg to spheroids of primary liver cells (InSphero model), the genotoxic effect of NPs increased after repeated or longer exposures [6]. This was shown using the same Ag- and ZnO-NPs as in the present study, in addition to TiO_2-NPs and carbon nanotubes. Ag- and ZnO-NPs were the most potent NPs for inducing DNA SBs in the spheroidal culture, showing similar effects as in 2D cultured C3A HepG2 derivative cells [6,54]. Ag-NPs also induce an increase in DNA oxidation [6]. The presence of non-parenchymal cells can possibly explain the higher response to the NPs in the InSphero model compared to the HepG2 spheroids. The HepG2 spheroids show relatively high metabolic capacity and appear to be a good advanced in vitro model for the liver [21–24]. The commercial primary cell InSphero co-culture model is more complex than the HepG2 spheroids. However, the HepG2 spheroids used in this study are easy to prepare, have low costs and high interlaboratory reproducibility [27], and are thus a convenient and reliable alternative to commercial models.

Underlying mechanisms of NP toxicity include oxidative stress and dissolution of the NPs. In the case of metal or metal oxide NPs, toxicity can be caused by dissolution of ions, direct action of the NPs or interaction between NPs and the cellular environment [1,47,55–57]. Both ZnO- and Ag-NPs are generally found to induce toxicity in 2D cultures, as well as liver damage *in vivo* [17,18,55,56]. For metal NPs, there is always a question of whether toxicity is due to direct effect of the NPs or to dissolved ions. We found that a substantial number of ions was released at the start of the exposure (Table 4), with dissolved Zn concentrations of 10–100 μg/cm^2. Increased intracellular Zn^{2+} levels resulting from dissolution of ZnO-NPs have been reported to be correlated with high levels of reactive oxygen species (ROS) and apoptosis [56]. However, Sharma et al. (2012) found that the released zinc ions were less important for the toxic effects of ZnO-NPs in HepG2 cells [58]. Other critical factors for cytotoxicity and genotoxicity of ZnO-NPs are size, shape, surface composition and semiconductor characteristics [55,56,58]. Other studies have showed that ZnO-NPs dissolve rapidly in cell culture medium DMEM, with a subsequent slow increase over time [59], and that the dissolution is dependent upon factors such as pH, ionic strength and HCO_3^- and HPO_4^{2-} concentrations, and less on the initial NP concentration [60]. That the level of dissolved Zn reached a plateau is most likely explained by a saturation of dissolved zinc in the medium. In the 2D model, $ZnCl_2$ and ZnO-NPs had similar EC_{50} values for cytotoxicity by alamarBlue assay. The level of dissolved Zn from the ZnO-NPs corresponded to a nontoxic concentration of $ZnCl_2$. These results indicate that the cytotoxic effect of ZnO-NP was caused by either by ZnO-NPs or the combination of ZnO-NPs and Zn^{2+} ions, and not only by released Zn^{2+} ions.

Dissolution and release of ions has been linked also with toxicity induced by Ag-NPs [47,55]. Oxidation of Ag(0) on the surface of the NPs, as well as other forms of interactions, will lead to particle corrosion and release of Ag^+ [61–64], which, after cellular uptake, can cause mitochondrial dysfunction [64,65]. In the present study, low levels of dissolved Ag were found in the Ag-NPs exposure dispersions shortly after exposure, and the amounts were lower than the measured EC_{50} for cytotoxicity of $AgNO_3$. Higher amounts of dissolved Ag have been found in other studies using the same Ag-NPs [6,37,54], and the differences may be related to distinct exposure media, different incubation times and sample preparation. However, most Ag^+ released from the NPs will not remain freely dissolved in the cell culture medium, due to the high ionic strength of cell culture media and presence of halides (0.12 M total dissolved Cl [66]), amino acids and proteins. Unbound Ag^+ will precipitate as AgCl and Ag_2S [62,65] or bind to proteins due to high affinity to thiol groups (SH-groups) [67]. Precipitation was observed when preparing $AgNO_3$, and a substantial part of the $AgNO_3$ solution was most likely precipitated AgCl (K_{SP} 1.77×10^{-10} M^2 [68]) and not freely dissolved

Ag^+ ions [69,70]. For the Ag-NPs dispersion, precipitated nano- and microcrystals may have been trapped in the filter during sample preparation for ion analysis and thus not detected as dissolved Ag. Consequently, the low level of freely dissolved Ag cannot be correlated with the persistence of the Ag-NPs in the presence of halides. Thus, it is unclear to what extent the Ag-NPs dissolve under the given experimental conditions. Oxidative stress is a likely underlying mechanism of Ag-NP-induced toxicity [64], as the corrosion of Ag-NPs is REDOX active and produces ROS [49,50]. A mechanism for induction of ROS production of Ag-NPs consists of interactions with proteins, subsequent altered protein function [71] and activation of signaling pathways involved in ROS production [64]. An increased intracellular level of ROS can activate cell-death-regulating pathways, such as p53, AKT and MAP kinase [72]. Thus, it is not clear if the toxicity of Ag-NPs in 2D and 3D cultures was caused by the ions released from the Ag-NPs, the Ag-NPs or both.

The differences in sensitivity to NP-induced toxicity on 2D and 3D cultures could possibly be related to the exposure scenarios. While the cells in the 2D cultures were growing on the bottom of flat wells, the spheroids were cultured slightly above the bottom of U-shaped wells. The cultures are most likely exposed to the same NP concentration (μg/mL) only if the exposure medium is a stable colloidal dispersion during the experimental time, which would be the case for TiO_2- and ZnO-NPs. The Ag-NPs were aggregated at the end of the exposure time, and sedimentation of the aggregates would increase the concentration of NPs reaching the cells in the 2D cultures, while decreasing it for the 3D cultures. Possibly this can explain the stronger effect on viability of the 2D cultures compared with 3D cultures. As spheroidal cultures are exposed directly only on the spheroid surface, the exposure of cells in the interior is dependent on penetration of the compound inside the spheroid. Toxicity to cells in the interior of the spheroid could also occur via cell signaling pathways activated in the cells on the surface of the spheroid. As shown in Elje et al., short exposure to H_2O_2 was not sufficient to induce the same levels of DNA SBs in HepG2 2D and 3D cultures. The induced damage was around ten times higher in the 2D cultures, possibly explained by too short a time for the compound to reach the cells in the interior of the spheroid [27]. Fleddermann et al. found that SiO_2-NPs were distributed through the whole HepG2 spheroid when the NPs were mixed with cells before spheroid formation. However, when exposing the already formed spheroids for 24 h, NPs were seen only to a depth of 20 μm [26]. Cell types, cell densities, physicochemical characteristics of the NPs (including size distribution) and ion release may influence the penetration inside the spheroid [73–77].

Several studies have shown differences in sensitivity to induced toxicity in 3D and 2D cultures [25,27–29,73,78]. We have previously found similar cytotoxicity in 2D and 3D HepG2 cultures, but higher sensitivity in the 3D culture for induced DNA damage by MMS [27]. Increased sensitivity in genotoxicity was also seen after exposure to 11 chemicals in a HepaRG spheroid model [29]. In agreement with this, benzo(a)pyrene and 2-amino-1-methyl-6-phenylimidazo(4,5-b)pyridine, which both require metabolic activation for induction of genotoxicity, induced a higher micronucleus frequency in HepG2 spheroids compared to monolayer cultures [28]. Other studies showed a greater resistance of the 3D cultures to toxicity of various drugs and chemicals [73,78]. Thus, the development of advanced 3D models for toxicity testing in vitro can give a more realistic model for human hazard and risk assessment. Slight modifications of experimental protocols may be needed for 3D cultures when comparing them to 2D cultures, to be able to control the concentration of the tested NPs or chemical that reaches the cells. Introduction of non-parenchymal cells, such as endothelial cells, stellate cells or macrophages, in co-cultures with hepatocytes, will make the model more complex and can further increase the relevance to the human liver.

5. Conclusions

With the increasing production of NPs and, thus, the risk of exposure to humans, the development of advanced in vitro models is especially important with respect to time, costs and the 3Rs. This study has shown that the HepG2 spheroid model can be applied successfully for the testing of NP-induced cytotoxic and genotoxic effects. The toxic responses in 2D and 3D cultures can be different, as seen

after exposure to Ag-NPs where the 3D cultures were more resistant, but also similar, as TiO_2-NPs induced no effect, and ZnO-NPs induced a strong cytotoxic effect in both models. The 2D cultures reflected concentration-dependent responses better; higher variability was seen in 3D cultures, and thus statistically significant results were more difficult to achieve. Ultimately, 3D cultures may be a more realistic model when compared to the human liver, as the spheroid model involves more complex cell arrangements and exposure scenario. The HepG2 spheroid model is thus a promising 3D model for use in nanotoxicology.

Supplementary Materials: The following are available online at http://www.mdpi.com/2079-4991/10/3/545/s1. Figure S1: DLS size distribution (by intensity) of nanoparticle dispersions. Figure S2: DLS size distribution (by number) of nanoparticle dispersions. Figure S3: Zeta potential of nanoparticle dispersions. Figure S4: Cytotoxicity results from alamarBlue assay on HepG2 2D model after $AgNO_3$ and $ZnCl_2$ exposure. Figure S5: Untreated and H_2O_2-exposed controls in the comet assay. Table S1: Theoretical nanoparticle concentrations applied to the 2D and 3D cultures during 24 h exposure. Table S2: Theoretical Ag and Zn content in the applied nanoparticle dispersions of Ag (NM300k) and ZnO (NM110). Table S3: Characterization of NPs in pure water.

Author Contributions: Conceptualization, E.E., M.D., E.M., E.R.-P. and Y.K.; methodology, E.E., M.D., E.M., E.R.-P., Y.K. and V.P.; software, M.D., E.M., E.E. and E.R.-P.; validation, M.D., E.M. and E.R.-P.; formal analysis, E.E., M.D., E.M., E.R.-P., V.P., O.H.M. and N.G.B.; investigation, E.E., E.M. and O.H.M.; resources, M.D., E.M., E.R.-P. and V.P.; data curation, E.E. and O.H.M.; writing—original draft preparation, E.E.; writing—review and editing, E.E., E.M., O.H.M., N.G.B., V.P., Y.K., M.D. and E.R.-P.; visualization, E.E. and O.H.M.; supervision, E.R.-P., E.M., M.D., Y.K. and V.P.; project administration, E.R.-P., E.M. and M.D.; funding acquisition, M.D., E.R.-P. and E.M. All authors have read and agreed to the published version of the manuscript.

Funding: This research was funded by the European Commission under the Horizon2020 program (grant agreement No. 685817, HISENTS, and grant agreement No. 814425, RiskGONE), the hCOMET project (COST Action, CA 15132) and the Norwegian Research Council (272412/F40).

Acknowledgments: The authors would like to thank Michelle Hesler (IBMT) and Iren E. Sturtzel (NILU) for technical assistance, Marit Vadset (NILU) for performing ICP-MS analysis, Hoffmann La Roche for providing the Ro 19-8022, Fraunhofer IME for providing the Ag-NPs, and JRC for providing the ZnO-NPs. Further, the authors thank Andrew Collins and Sergey Shaposhnikov at NorGenoTec AS, Norway, for providing the Fpg. Andrew Collins also kindly edited the manuscript with English corrections.

Conflicts of Interest: The authors declare no conflict of interest.

References

1. Nel, A.; Xia, T.; Mädler, L.; Li, N. Toxic potential of materials at the nanolevel. *Science* **2006**, *311*, 622–627. [CrossRef]
2. Donaldson, K.; Stone, V.; Kreyling, W.; Borm, P.J.A. Nanotoxicology. *Occup. Environ. Med.* **2004**, *61*, 727–728. [CrossRef]
3. Weir, A.; Westerhoff, P.; Fabricius, L.; Hristovski, K.; von Goetz, N. Titanium dioxide nanoparticles in food and personal care products. *Environ. Sci. Technol.* **2012**, *46*, 2242–2250. [CrossRef]
4. Vaseem, M.; Umar, A.; Hahn, Y. Chapter 4: ZnO Nanoparticles: Growth, Properties, and Application. In *Metal Oxide Nanostructures and Their Applications*; Umar, A., Hahn, Y., Eds.; American Scientific Publishers: Valencia, CA, USA, 2010; pp. 1–36.
5. Tran, Q.H.; Nguyen, V.Q.; Le, A.-T. Silver nanoparticles: Synthesis, properties, toxicology, applications and perspectives. *Adv. Nat. Sci. Nanosci. Nanotechnol.* **2013**, *4*. [CrossRef]
6. Kermanizadeh, A.; Løhr, M.; Roursgaard, M.; Messner, S.; Gunness, P.; Kelm, J.M.; Møller, P.; Stone, V.; Loft, S. Hepatic toxicology following single and multiple exposure of engineered nanomaterials utilising a novel primary human 3D liver microtissue model. *Part. Fibre Toxicol.* **2014**, *11*, 56. [CrossRef]
7. Choi, H.S.; Ashitate, Y.; Lee, J.H.; Kim, S.H.; Matsui, A.; Insin, N.; Bawendi, M.G.; Semmler-Behnke, M.; Frangioni, J.V.; Tsuda, A. Rapid translocation of nanoparticles from the lung airspaces to the body. *Nat. Biotechnol.* **2010**, *28*, 1300–1303. [CrossRef]
8. Miller, M.R.; Raftis, J.B.; Langrish, J.P.; McLean, S.G.; Samutrtai, P.; Connell, S.P.; Wilson, S.; Vesey, A.T.; Fokkens, P.H.B.; Boere, A.J.F.; et al. Correction to "Inhaled Nanoparticles Accumulate at Sites of Vascular Disease". *ACS Nano* **2017**, *11*, 10623–10624. [CrossRef]

9. Miller, M.R.; Raftis, J.B.; Langrish, J.P.; McLean, S.G.; Samutrtai, P.; Connell, S.P.; Wilson, S.; Vesey, A.T.; Fokkens, P.H.B.; Boere, A.J.F.; et al. Inhaled Nanoparticles Accumulate at Sites of Vascular Disease. *ACS Nano* **2017**, *11*, 4542–4552. [CrossRef]
10. Kafa, H.; Wang, J.T.; Rubio, N.; Klippstein, R.; Costa, P.M.; Hassan, H.A.; Sosabowski, J.K.; Bansal, S.S.; Preston, J.E.; Abbott, N.J.; et al. Translocation of LRP1 targeted carbon nanotubes of different diameters across the blood-brain barrier in vitro and in vivo. *J. Control. Release* **2016**, *225*, 217–229. [CrossRef]
11. Braakhuis, H.M.; Kloet, S.K.; Kezic, S.; Kuper, F.; Park, M.V.; Bellmann, S.; van der Zande, M.; Le Gac, S.; Krystek, O.; Peters, R.J.; et al. Progress and future of in vitro models to study translocation of nanoparticles. *Arch. Toxicol.* **2015**, *89*, 1469–1495. [CrossRef]
12. Sykes, E.A.; Dai, Q.; Tsoi, K.M.; Hwang, D.M.; Chan, W.C.W. Nanoparticle exposure in animals can be visualized in the skin and analysed via skin biopsy. *Nat. Commun.* **2014**, *5*, 3796. [CrossRef] [PubMed]
13. Choi, C.H.J.; Alabi, C.A.; Webster, P.; Davis, M.E. Mechanism of active targeting in solid tumors with transferrin-containing gold nanoparticles. *PNAS* **2010**, *107*, 1235–1240. [CrossRef] [PubMed]
14. Arami, H.; Khandhar, A.; Liggitt, D.; Krishnan, K.M. In vivo delivery, pharmacokinetics, biodistribution and toxicity of iron oxide nanoparticles. *Chem. Soc. Rev.* **2015**, *44*, 8576–8607. [CrossRef] [PubMed]
15. Wang, B.; He, X.; Zhang, Z.; Zhao, Y.; Feng, W. Metabolism of nanomaterials in vivo: Blood circulation and organ clearance. *Acc. Chem. Res.* **2013**, *46*, 761–769. [CrossRef]
16. Roy, R.; Kumar, S.; Tripathi, A.; Dwivedi, P.D. Interactive threats of nanoparticles to the biological system. *Immunol. Lett.* **2014**, *158*, 79–87. [CrossRef]
17. Wu, T.; Tang, M. Review of the effects of manufactured nanoparticles on mammalian target organs. *J. Appl. Toxicol.* **2018**, *38*, 25–40. [CrossRef]
18. Cao, Y.; Gong, Y.; Liao, W.; Luo, Y.; Wu, C.; Wang, M.; Yang, Q. A review of cardiovascular toxicity of TiO_2, ZnO and Ag nanoparticles (NPs). *Biometals* **2018**, *31*, 457–476. [CrossRef]
19. Fung, M.; Thornton, A.; Mybeck, K.; Wu, J.S.; Hornbuckle, K.; Muniz, E. Evaluation of the Characteristics of Safety Withdrawal of Prescription Drugs from Worldwide Pharmaceutical Markets-1960 to 1999 Therapeutic Innovation & Regulatory. *Science* **2001**, *35*, 293–317. [CrossRef]
20. Devarbhavi, H. An Update on Drug-induced Liver Injury. *J. Clin. Exp. Hepatol.* **2012**, *2*, 247–259. [CrossRef]
21. Godoy, P.; Hewitt, N.J.; Albrecht, U.; Andersen, M.E.; Ansari, N.; Bhattacharya, S.; Bode, J.G.; Bolleyn, J.; Borner, C.; Böttger, J.; et al. Recent advances in 2D and 3D in vitro systems using primary hepatocytes, alternative hepatocyte sources and non-parenchymal liver cells and their use in investigating mechanisms of hepatotoxicity, cell signaling and ADME. *Arch. Toxicol.* **2013**, *87*, 1315–1530. [CrossRef]
22. Kyffin, J.A.; Sharma, P.; Leedale, J.; Colley, H.E.; Murdoch, C.; Mistry, P.; Webb, S.D. Impact of cell types and culture methods on the functionality of in vitro liver systems—A review of cell systems for hepatotoxicity assessment. *Toxicology* **2018**, *48*, 262–275. [CrossRef] [PubMed]
23. Hurrell, T.; Ellero, A.A.; Masso, Z.F.; Cromarty, A.D. Characterization and reproducibility of HepG2 hanging drop spheroids toxicology in vitro. *Toxicology* **2018**, *50*, 86–94. [CrossRef] [PubMed]
24. Chang, T.T.; Hughes-Fulford, M. Monolayer and spheroid culture of human liver hepatocellular carcinoma cell line cells demonstrate distinct global gene expression patterns and functional phenotypes. *Tissue Eng. Part A* **2009**, *15*, 559–567. [CrossRef] [PubMed]
25. Dubiak-Szepietowska, M.; Karczmarczyk, A.; Jönsson-Niedziolka, M.; Winckler, T.; Feller, K.H. Development of complex-shaped liver multicellular spheroids as a human-based model for nanoparticle toxicity assessment in vitro. *Toxicol. Appl. Pharmacol.* **2016**, *294*, 78–85. [CrossRef] [PubMed]
26. Fleddermann, J.; Susewind, J.; Peuschel, H.; Koch, M.; Tavernaro, I.; Kraegeloh, A. Distribution of SiO_2 nanoparticles in 3D liver microtissues. *Int. J. Nanomed.* **2019**, *14*, 1411–1431. [CrossRef] [PubMed]
27. Elje, E.; Hesler, M.; Rundén-Pran, E.; Mann, P.; Mariussen, E.; Wagner, S.; Dusinska, M.; Kohl, Y. The comet assay applied to HepG2 liver spheroids. *Mutat. Res. Genet. Toxicol. Environ.* **2019**, *845*, 403033. [CrossRef]
28. Shah, U.K.; Mallia, J.O.; Singh, N.; Chapman, K.E.; Doak, S.H.; Jenkins, G.J.S. A three-dimensional in vitro HepG2 cells liver spheroid model for genotoxicity studies. *Mutat. Res.* **2018**, *825*, 51–58. [CrossRef]
29. Mandon, M.; Huet, S.; Dubreil, E.; Fessard, V.; Le Hegarat, L. Three-dimensional HepaRG spheroids as a liver model to study human genotoxicity in vitro with the single cell gel electrophoresis assay. *Sci. Rep.* **2019**, *9*, 10548. [CrossRef]

30. Reisinger, K.; Blatz, V.; Brinkmann, J.; Downs, T.R.; Fischer, A.; Henkler, F.; Hoffmann, S.; Krul, C.; Liebsch, M.; Luch, A. Validation of the 3D Skin Comet assay using full thickness skin models: Transferability and reproducibility. *Mutat. Res. Genet. Toxicol. Environ.* **2018**, *827*, 27–41. [CrossRef]
31. Collins, A.R.; Annangi, B.; Rubio, L.; Marcos, R.; Dorn, M.; Merker, C.; Estrela-Lopis, I.; Cimpan, M.R.; Ibrahim, M.; Cimpan, E. High throughput toxicity screening and intracellular detection of nanomaterials. *Wiley Interdiscip. Rev. Nanomed. Nanobiotechnol.* **2017**, *9*. [CrossRef]
32. Pottier, A.; Cassaignon, S.; Chaneac, C.; Villain, F.; Tronc, E.; Jolivet, J.-P. Size tailoring of TiO_2 anatase nanoparticles in aqueous medium and synthesis of nanocomposites. Characterization by Raman spectroscopy. *J. Mater. Chem.* **2003**, *13*, 877–882. [CrossRef]
33. The Generic NANOGENOTOX dispersion protocol—Standard Operation Procedure (SOP) and Background Documentation. Available online: https://www.anses.fr/en/system/files/nanogenotox_deliverable_5.pdf (accessed on 20 January 2020).
34. Kleiven, M.; Macken, A.; Oughton, D.H. Growth inhibition in Raphidocelis subcapita—Evidence of nanospecific toxicity of silver nanoparticles. *Chemosphere* **2019**, *221*, 785–792. [CrossRef] [PubMed]
35. Maria, V.L.; Ribeiro, M.J.; Guilherme, S.; Soares, A.M.V.M.; Scott-Fordsmand, J.J.; Amorim, M.J.B. Silver (nano)materials cause genotoxicity in Enchytraeus crypticus, as determined by the comet assay. *Environ. Toxicol. Chem.* **2018**, *37*, 184–191. [CrossRef] [PubMed]
36. El Yamani, N.; Collins, A.R.; Rundén-Pran, E.; Fjellsbø, L.M.; Shaposhnikov, S.; Zienolddiny, S.; Dusinska, M. In vitro genotoxicity testing of four reference metal nanomaterials, titanium dioxide, zinc oxide, cerium oxide and silver: Towards reliable hazard assessment. *Mutagenesis* **2017**, *32*, 117–126. [CrossRef]
37. Kleiven, M.; Rossbach, L.M.; Gallego-Urrea, J.A.; Brede, D.A.; Oughton, D.H.; Coutris, C. Characterizing the behavior, uptake, and toxicity of NM300K silver nanoparticles in Caenorhabditis elegans. *Environ. Toxicol. Chem.* **2018**, *37*, 1799–1810. [CrossRef]
38. Schindelin, J.; Arganda-Carreras, I.; Frise, E.; Kaynig, V.; Longair, M.; Pietzsch, T.; Preibisch, S.; Rueden, C.; Saalfeld, S.; Schmid, B. Fiji: An open-source platform for biological-image analysis. *Nat. Methods* **2012**, *9*, 676–682. [CrossRef]
39. Dusinska, M.; Collins, A. Detection of oxidised purines and UV-induced photoproducts in DNA, by inclusion of lesion-specific enzymes in the comet assay (single cell gel electrophoresis). *ALTA-Altern. Lab. Anim.* **1996**, *24*, 405–411.
40. Speit, G.; Schütz, P.; Bonzheim, I.; Trenz, K.; Hoffmann, H. Sensitivity of the FPG protein towards alkylation damage in the comet assay. *Toxicol. Lett.* **2004**, *146*, 151–158. [CrossRef]
41. Azqueta, A.; Slyskova, J.; Langie, S.A.S.; Gaivao, I.O.; Collins, A. Comet assay to measure DNA repair: Approach and applications. *Front. Genet.* **2014**, *5*, 288. [CrossRef]
42. Klein, C.L.; Comero, S.; Stahlmecke, B.; Romazanov, J.; Kuhlbusch, T.A.J.; Van Doren, E.; De Temmerman, P.-J.; Mast, J.; Wick, P.; Krug, H.; et al. *NM-Series of Representative Manufactured Nanomaterials, NM-300 Silver*; Publications Office of the European Union: Luxembourg, 2011.
43. Singh, C.; Friedrichs, S.; Levin, M.; Birkedal, R.; Jensen, K.A.; Pojana, G.; Wohlleben, W.; Schulte, S.; Wiench, K.; Turney, T.; et al. *NM-Series of Representative Manufactured Nanomaterials—Zinc Oxide NM-110, NM-111, NM-112, NM-113: Characterisation and Test Item Preparation*; Publications Office of the European Union: Luxembourg, 2011.
44. Piella, J.; Bastus, N.G.; Puntes, V. Size-Dependent Protein-Nanoparticle Interactions in Citrate-Stabilized Gold Nanoparticles: The Emergence of the Protein Corona. *Bioconj. Chem.* **2017**, *28*, 88–97. [CrossRef]
45. Safar, R.; Doumandji, Z.; Saidou, T.; Ferrari, L.; Nahle, S.; Rihn, B.H.; Joubert, O. Cytotoxicity and global transcriptional responses induced by zinc oxide nanoparticles NM 110 in PMA-differentiated THP-1 cells. *Toxicol. Lett.* **2019**, *308*, 65–73. [CrossRef] [PubMed]
46. Nel, A.E.; Mädler, L.; Velegol, D.; Xia, T.; Hoek, E.M.V.; Somasundaran, P.; Klaessig, F.; Castranova, V.; Thompson, M. Understanding biophysicochemical interactions at the nano–bio interface. *Nat. Mater.* **2009**, *8*, 543. [CrossRef]
47. Vimbela, G.V.; Ngo, S.M.; Fraze, C.; Yang, L.; Stout, D.A. Antibacterial properties and toxicity from metallic nanomaterials. *Int. J. Nanomed.* **2017**, *12*, 3941–3965. [CrossRef] [PubMed]
48. Wang, J.; Fan, Y. Lung injury induced by TiO_2 nanoparticles depends on their structural features: Size, shape, crystal phases, and surface coating. *Int. J. Mol. Sci.* **2014**, *15*, 22258–22278. [CrossRef] [PubMed]

49. Bastús, N.G.; Casals, E.; Vàzquez-Campos, S.; Puntes, S. Reactivity of engineered inorganic nanoparticles and carbon nanostructures in biological media. *Nanotoxicology* **2008**, *2*, 99–112. [CrossRef]
50. Casals, E.; Gonzalez, E.; Puntes, V.F. Reactivity of inorganic nanoparticles in biological environments: Insights into nanotoxicity mechanisms. *J. Phys. D Appl. Phys.* **2012**, *45*, 443001. [CrossRef]
51. Zhang, X.; Li, W.; Yang, Z. Toxicology of nanosized titanium dioxide: An update. *Arch. Toxicol.* **2015**, *89*, 2207–2217. [CrossRef]
52. Shi, H.; Magaye, R.; Castranova, V.; Zhao, J. Titanium dioxide nanoparticles: A review of current toxicological data. *Part. Fibre Toxicol.* **2013**, *10*, 15. [CrossRef]
53. Cowie, H.; Magdolenova, Z.; Saunders, M.; Drlickova, M.; Correia, S.C.; Halamoda, B.K.; Gombau, L.; Gaudagnini, R.; Lorenzo, Y.; Walker, L.; et al. Suitability of human and mammalian cells of different origin for the assessment of genotoxicity of metal and polymeric engineered nanoparticles. *Nanotoxicology* **2015**, *9* (Suppl. 1), 57–65. [CrossRef]
54. Kermanizadeh, A.; Pojana, G.; Gaiser, B.K.; Birkedal, R.; Bilanicova, D.; Wallin, H.; Jensen, K.A.; Sellergren, B.; Hutchison, G.R.; Marcomini, A.; et al. In vitro assessment of engineered nanomaterials using a hepatocyte cell line: Cytotoxicity, pro-inflammatory cytokines and functional markers. *Nanotoxicology* **2013**, *7*, 301–313. [CrossRef]
55. Ivask, A.; Juganson, K.; Bondarenko, O.; Mortimer, M.; Aruoja, V.; Kasemets, K.; Blinova, I.; Heinlaan, M.; Slaveykova, V.; Kahru, A. Mechanisms of toxic action of Ag, ZnO and CuO nanoparticles to selected ecotoxicological test organisms and mammalian cells in vitro: A comparative review. *Nanotoxicology* **2014**, *8* (Suppl. 1), 57–71. [CrossRef]
56. Krol, A.; Pomastowski, P.; Rafinska, K.; Railean-Plugaru, V.; Buszewski, B. Zinc oxide nanoparticles: Synthesis, antiseptic activity and toxicity mechanism. *Adv. Colloid Interface Sci.* **2017**, *249*, 37–52. [CrossRef]
57. Sirelkhatim, A.; Mahmud, S.; Seeni, A.; Kaus, N.H.M.; Ann, L.C.; Bakhori, S.K.M.; Hasan, H.; Mohamad, D. Review on Zinc Oxide Nanoparticles: Antibacterial Activity and Toxicity Mechanism. *Nano-Micro Lett.* **2015**, *7*, 219–242. [CrossRef]
58. Sharma, V.; Singh, P.; Pandey, A.K.; Dhawan, A. Induction of oxidative stress, DNA damage and apoptosis in mouse liver after sub-acute oral exposure to zinc oxide nanoparticles. *Mutat. Res.* **2012**, *745*, 84–91. [CrossRef]
59. Reed, R.B.; Ladner, D.A.; Higgins, C.P.; Westerhoff, P.; Ranville, J.F. Solubility of nano-zinc oxide in environmentally and biologically important matrices. *Environ. Toxicol. Chem.* **2012**, *31*, 93–99. [CrossRef]
60. Li, M.; Lin, D.; Zhu, L. Effects of water chemistry on the dissolution of ZnO nanoparticles and their toxicity to Escherichia coli. *Environ. Pollut.* **2013**, *173*, 97–102. [CrossRef]
61. McShan, D.; Ray, P.C.; Yu, H. Molecular toxicity mechanism of nanosilver. *J. Food Drug Anal.* **2014**, *22*, 116–127. [CrossRef]
62. Behra, R.; Sigg, L.; Clift, M.J.D.; Herzog, F.; Minghetti, M.; Johnston, B.; Petri-Fink, A.; Rothen-Ruthishauser, B. Bioavailability of silver nanoparticles and ions: From a chemical and biochemical perspective. *J. R. Soc. Interface* **2013**, *10*, 20130396. [CrossRef]
63. Adamczyk, Z.; Ocwieja, M.; Mrowiec, H.; Walas, S.; Lupa, D. Oxidative dissolution of silver nanoparticles: A new theoretical approach. *J. Colloid Interface Sci.* **2016**, *469*, 355–364. [CrossRef]
64. Akter, M.; Sikder, M.T.; Rahman, M.M.; Ullah, A.K.M.A.; Hossain, K.F.B.; Banik, S.; Hosokawa, T.; Saito, S.; Kurasaki, M. A systematic review on silver nanoparticles-induced cytotoxicity: Physicochemical properties and perspectives. *J. Adv. Res.* **2018**, *9*, 1–16. [CrossRef]
65. Reidy, B.; Haase, A.; Luch, A.; Dawson, K.A.; Lynch, I. Mechanisms of Silver Nanoparticle Release, Transformation and Toxicity: A Critical Review of Current Knowledge and Recommendations for Future Studies and Applications. *Materials* **2013**, *6*, 2295–2350. [CrossRef]
66. Product Information, Dulbecco's Modified Eagle's Medium (DME). Available online: https://www.sigmaaldrich.com/content/dam/sigma-aldrich/docs/Sigma/Formulation/d6046for.pdf (accessed on 20 January 2020).
67. Kędziora, A.; Speruda, M.; Krzyżewska, E.; Rybka, J.; Łukowiak, A.; Bugla-Płoskońska, G. Similarities and Differences between Silver Ions and Silver in Nanoforms as Antibacterial Agents. *J. Mol. Sci.* **2018**, *19*, 444. [CrossRef]
68. Solubility Product Constants. Available online: https://www.periodni.com/solubility_product_constants.htmL (accessed on 20 January 2020).

69. Kaiser, J.P.; Roesslein, M.; Diener, L.; Wichser, A.; Nowack, B.; Wick, P. Cytotoxic effects of nanosilver are highly dependent on the chloride concentration and the presence of organic compounds in the cell culture media. *J. Nanobiotechnol.* **2017**, *15*, 5. [CrossRef]
70. Loza, K.; Sengstock, C.; Chernousova, S.; Köller, M.; Epple, M. The predominant species of ionic silver in biological media is colloidally dispersed nanoparticulate silver chloride. *RSC Adv.* **2014**, *4*, 35290–35297. [CrossRef]
71. Saptarshi, S.R.; Duschl, A.; Lopata, A.L. Interaction of nanoparticles with proteins: Relation to bio-reactivity of the nanoparticle. *J. Nanobiotechnol.* **2013**, *11*, 26. [CrossRef]
72. Li, Y.; Guo, M.; Lin, Z.; Zhao, M.; Xiao, M.; Wang, C.; Xu, T.; Chen, T.; Zhu, B. Polyethylenimine-functionalized silver nanoparticle-based co-delivery of paclitaxel to induce HepG2 cell apoptosis. *Int. J. Nanomed.* **2016**, *11*, 6693–6702. [CrossRef]
73. Evans, S.J.; Clift, M.J.D.; Singh, N.; Mallia, J.O.; Burgum, M.; Wills, J.W.; Wilkinson, T.S.; Jenkins, G.J.S.; Doak, S.H. Critical review of the current and future challenges associated with advanced in vitro systems towards the study of nanoparticle (secondary) genotoxicity. *Mutagenesis* **2017**, *32*, 233–241. [CrossRef]
74. Konstantinova, V.; Ibrahim, M.; Lie, S.A.; Birkeland, E.S.; Neppelberg, E.; Marthinussen, M.C.; Costea, D.E.; Cimpan, M.R. Nano-TiO_2 penetration of oral mucosa: In vitro analysis using 3D organotypic human buccal mucosa models. *J. Oral Pathol. Med.* **2017**, *46*, 214–222. [CrossRef]
75. Hao, F.; Jin, X.; Liu, Q.S.; Zhou, Q.; Jiang, G. Epidermal Penetration of Gold Nanoparticles and Its Underlying Mechanism Based on Human Reconstructed 3D Episkin Model. *ACS Appl. Mater. Interfaces* **2017**, *9*, 42577–42588. [CrossRef]
76. England, C.G.; Priest, T.; Zhang, G.; Sun, X.; Patel, D.N.; McNally, N.R.; van Berkel, V.; Gobin, A.M.; Frieboes, H.B. Enhanced penetration into 3D cell culture using two and three layered gold nanoparticles. *Int. J. Nanomed.* **2013**, *8*, 3603–3617. [CrossRef]
77. Conte, C.; Mastrotto, F.; Taresco, V.; Tchoryk, A.; Quaglia, F.; Stolnik, S.; Alexander, C. Enhanced uptake in 2D- and 3D- lung cancer cell models of redox responsive PEGylated nanoparticles with sensitivity to reducing extra- and intracellular environments. *J. Control. Release* **2018**, *277*, 126–141. [CrossRef]
78. Ham, S.L.; Joshi, R.; Thakuri, P.S.; Tavana, H. Liquid-based three-dimensional tumor models for cancer research and drug discovery. *Exp. Biol. Med.* **2016**, *241*, 939–954. [CrossRef]

nanomaterials

MDPI

Supplementary Materials

Hepato(geno)toxicity assessment of nanoparticles in a HepG2 liver spheroid model

Elisabeth Elje [1,2], Espen Mariussen [1], Oscar H. Moriones [3,4], Neus G. Bastús [5], Victor Puntes [3,5,6], Yvonne Kohl [7], Maria Dusinska [1] and Elise Rundén-Pran [1,*]

[1] NILU – Norwegian Institute for Air Research, Department for Environmental Chemistry, Health Effects Laboratory, Instituttveien 18, 2007 Kjeller, Norway
[2] University of Oslo, Faculty of Medicine, Institute of Basic Medical Sciences, Department of Molecular Medicine, Sognsvannsveien 9, 0372 Oslo, Norway
[3] Institut Català de Nanociència y Nanotecnologia (ICN2-UAB-CSIC-BIST), Campus UAB, 08193, Bellaterra, Barcelona, Spain
[4] Universitat Autonòma de Barcelona (UAB), Campus UAB, 08193, Bellaterra, Barcelona, Spain
[5] Vall d'Hebron Institut de Recerca (VHIR), 08035, Barcelona, Spain
[6] Institució Catalana de Recerca i Estudis Avançats (ICREA), 08010, Barcelona, Spain
[7] Fraunhofer Institute for Biomedical Engineering IBMT, Joseph-von-Fraunhofer-Weg 1, 66280 Sulzbach, Germany
* Correspondence: erp@nilu.no

1. Nanoparticle concentrations

HepG2 2D and 3D cultures were exposed to three types of NPs with several concentrations (Table S-1). The total theoretical Ag and Zn content in the applied concentrations is shown in Table S-2.

Table S1. Theoretical nanoparticle (NP) concentrations applied to the 2D and 3D cultures during 24h exposure. The delivered amounts of NPs to the cells have not been determined. Cell numbers used are average of cell numbers at start and end of exposure of 2D and 3D cultures [27].

µg/cm²	*µg/ml*	*µg/well*	*NP mass per 2D culture: (µg/hepatocytes)*	*NP mass per 3D culture: (µg/hepatocytes)*
1	*3*	*0.3*	*8.1E-06*	*1.7E-10*
3	*9*	*0.8*	*2.4E-05*	*5.2E-10*
10	*28*	*2.8*	*8.1E-05*	*1.7E-09*
30	*85*	*8.5*	*2.4E-04*	*5.2E-09*
75	*212*	*21.2*	*6.1E-04*	*1.3E-08*

Table S2. Theoretical Ag and Zn content in the applied nanoparticle dispersions of Ag (NM300k) and ZnO (NM110).

NPs	*Ag*		*Zn*	
µg/cm²	*µg/well*	*µM*	*µg/well*	*µM*
1	*0.3*	*26.2*	*0.2*	*34.7*
3	*0.8*	*78.6*	*0.7*	*104.2*
10	*2.8*	*262.1*	*2.3*	*347.4*
30	*8.5*	*786.4*	*6.8*	*1042.3*
75	*21.2*	*1965.9*	*17.0*	*2605.8*
100	*28.3*	*2621.1*	*22.7*	*3474.8*

2. Additional nanoparticle characterization results

Table S3. Characterization of NPs in pure water. Samples in pure water were diluted 1:10 for analysis. TEM: Transmission electron microscopy. PDI: polydispersity index. ZP: zeta potential. NP: nanoparticle.

NP	*Diameter [nm], TEM*	*Hydrodynamic diameter [nm], intensity*	*Hydrodynamic diameter [nm], number*	*PDI [a.u.]*	*ZP [mV]*
Ag-NPs (NM300k)	*< 20 nm [42]*	81.3 ± 15.3	3.58 ± 1.96	0.467 ± 0.064	-12.7 ± 0.66
ZnO-NPs (NM110)	*147 ± 149 [43]*	577.8 ± 89.7	522.2 ± 67.0	0.435 ± 0.028	+17.1 ± 0.82
TiO_2-NPs	*5.54 ± 0.89*	111.5 ± 15.0	44.7 ± 14.1	0.306 ± 0.022	-30.8 ± 3.46

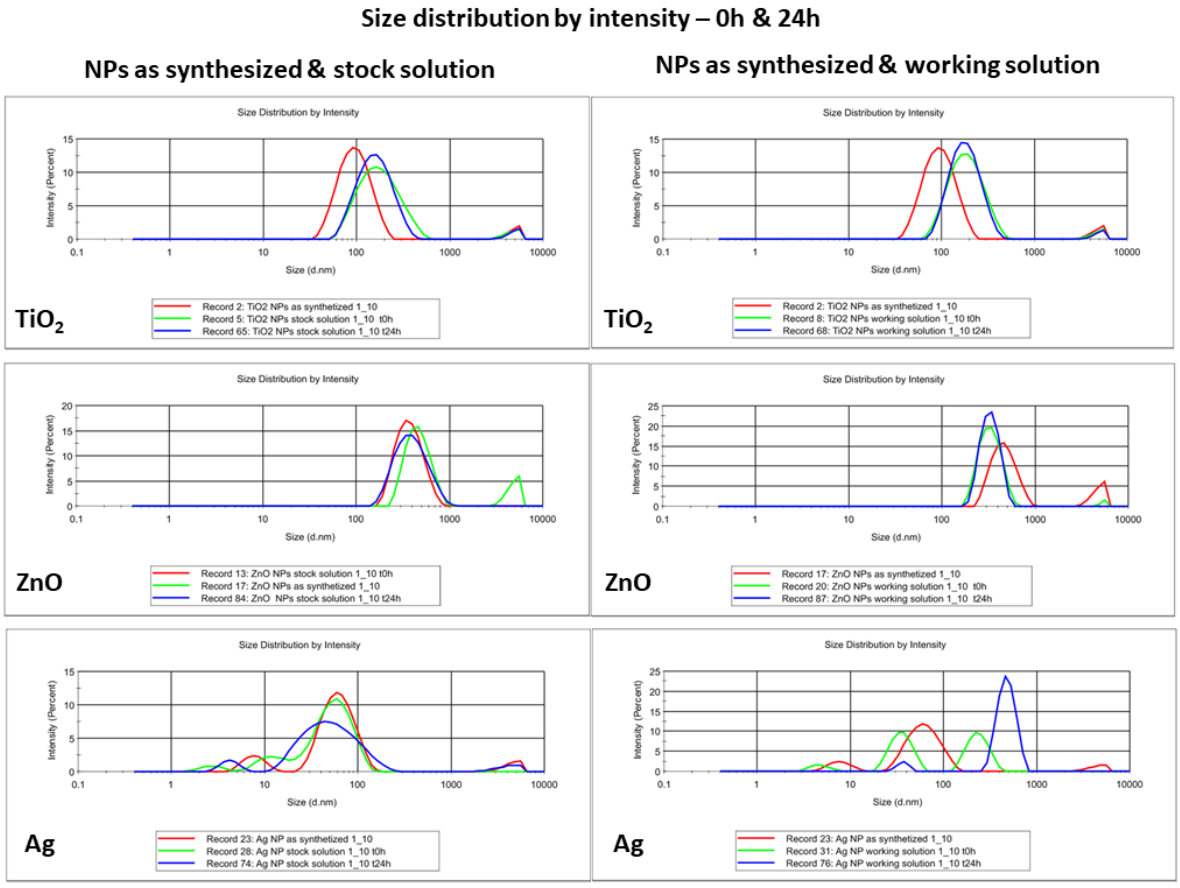

Figure S1. DLS size distribution (by intensity) of nanoparticle dispersions (as synthesized/pure water, stock dispersion and working dispersion).

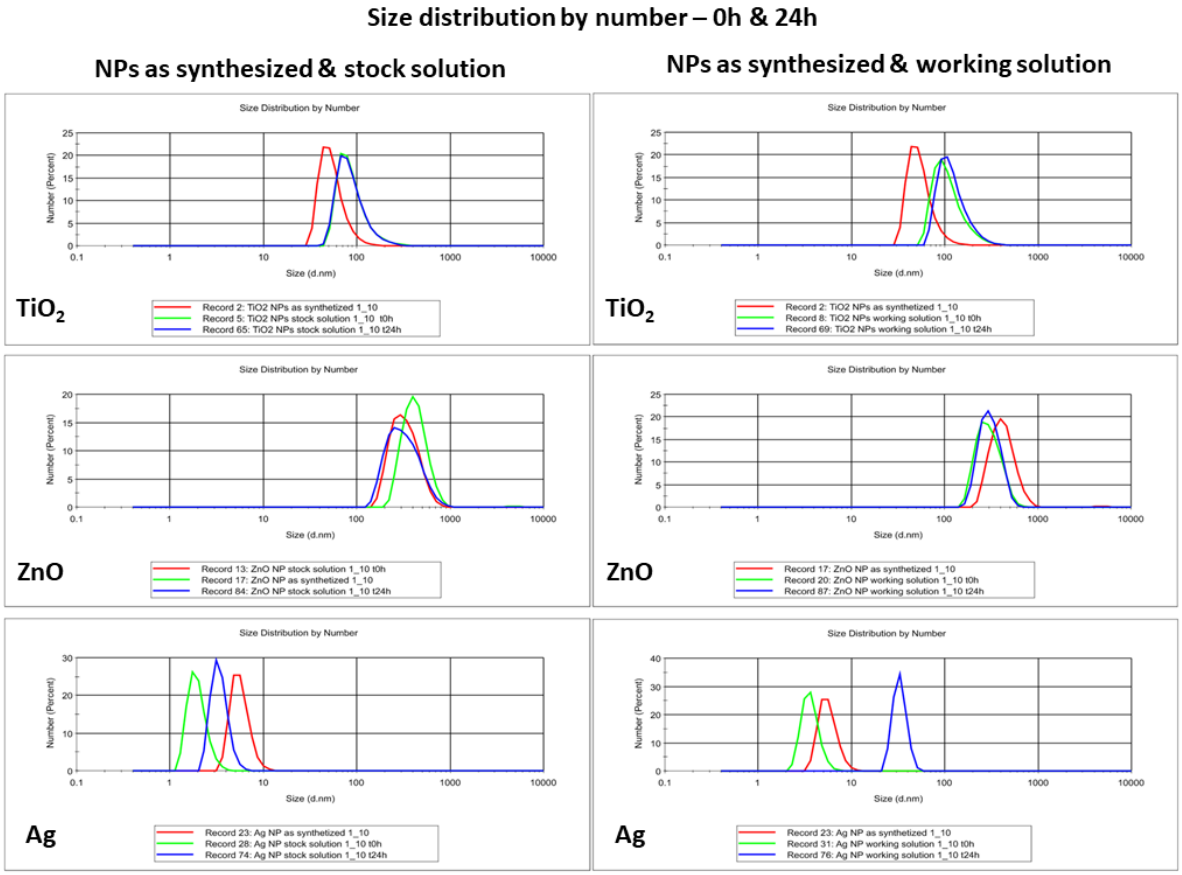

Figure S-2. DLS size distribution (by number) of nanoparticle dispersions (as synthesized/pure water, stock dispersion and working dispersion).

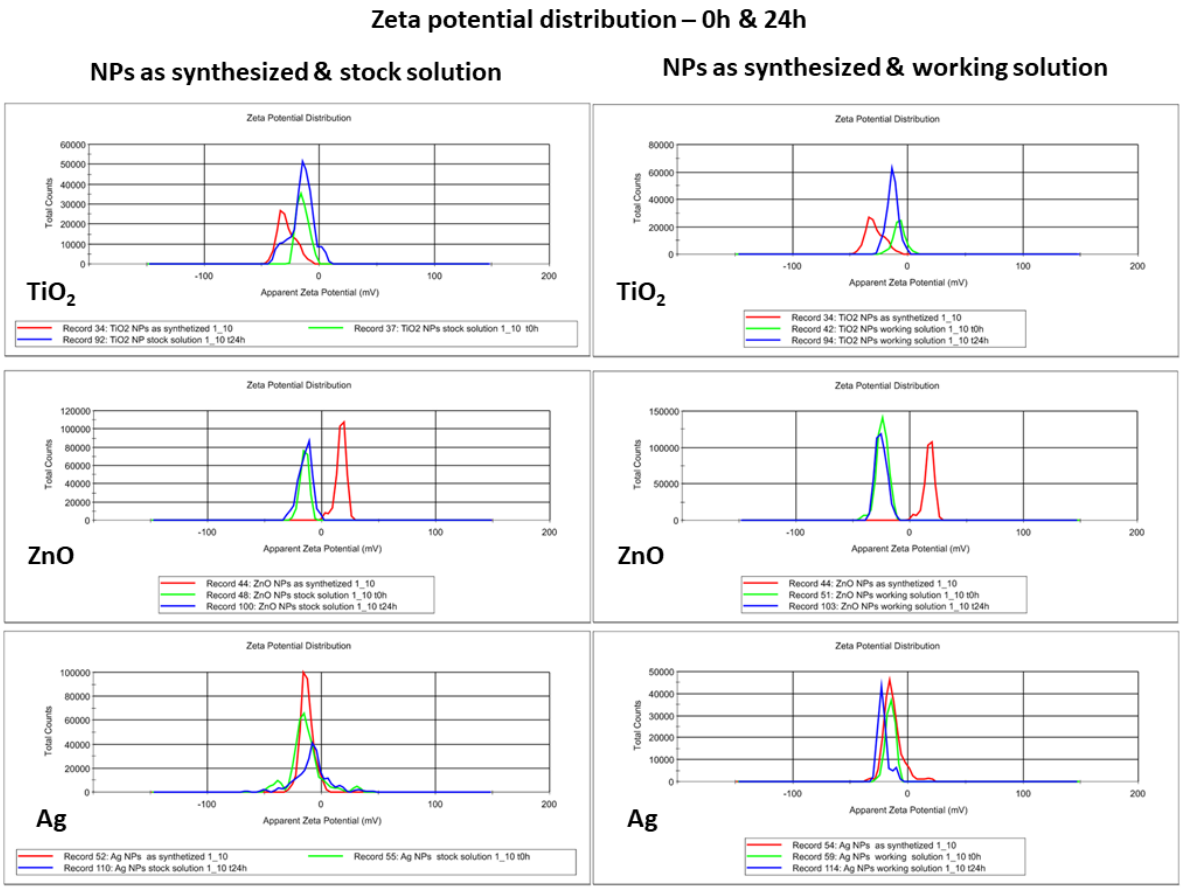

Figure S-3. Zeta potential of nanoparticle dispersions (as synthesized/pure water, stock dispersion and working dispersion).

3. Cytotoxicity of $AgNO_3$ and $ZnCl_2$ on HepG2 2D cultures

To compare the effects of Ag- and ZnO-NPs with metal salts, the cytotoxicity of $AgNO_3$ and $ZnCl_2$ on HepG2 2D cultures was measured by AlamarBlue assay after 24h exposure (Fig. S-4). EC_{50} values were 21.7 μM $AgNO_3$ and 280.5 μM $ZnCl_2$. Using the same concentration units as the NPs, these EC_{50} values would correspond to 0.8 μg/cm² (2.3 μg/ml) Ag^+ ions, and 6.5 μg/cm² (18.3 μg/ml) Zn^{2+} ions.

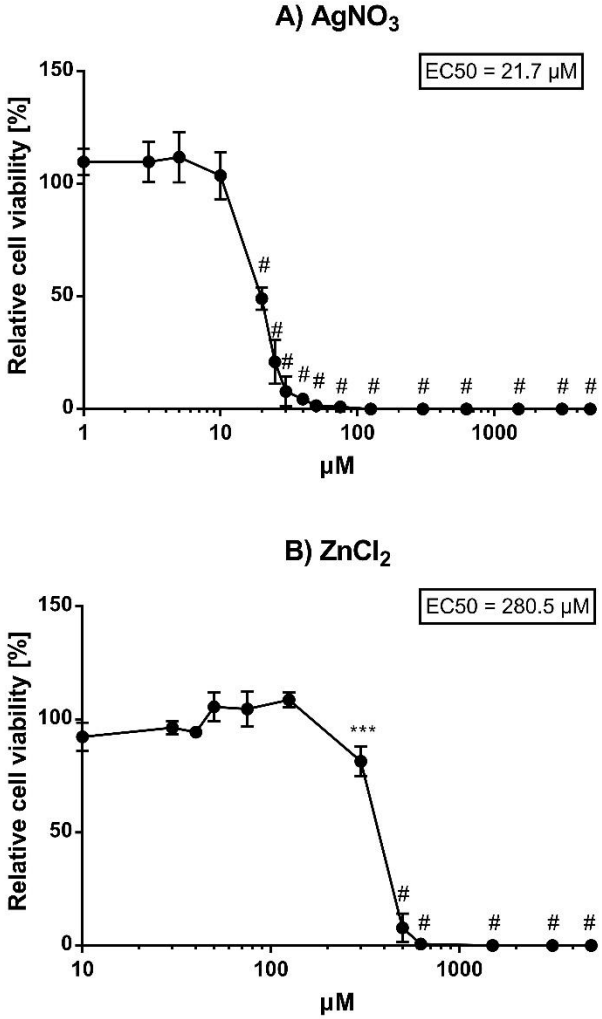

Figure S4. Cytotoxicity results from alamarBlue assay on HepG2 2D model after $AgNO_3$ and $ZnCl_2$ exposure. The viability of 2D cultures was significantly decreased in a concentration dependent way, after 24h exposure to (**a**) $AgNO_3$ and (**b**) $ZnCl_2$. Mean with SD of 3 independent experiments, except for 20, 30 and 40 μM (**a**) and 500 μM (**b**) where n=2. One-way ANOVA with multiple comparisons and post-test Dunnett, *** $p<0.001$, # $p < 0.0001$.

3. Control samples for comet assay on HepG2 2D and 3D cultures

Basal levels of DNA damage in untreated control cells are shown in Fig A-5, together with the positive control H2O2 (50 μM, 5 min). 3D cultures had a higher level of oxidized lesions measured as Fpg sites compared to 2D cultures.

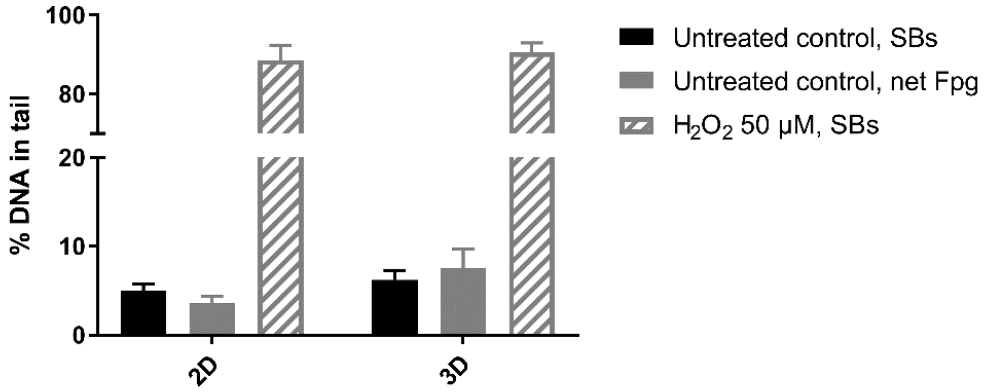

Figure S5. Untreated and H_2O_2-exposed controls in the comet assay. Untreated control cells from 2D and 3D cultures had a similar level of DNA SBs. 3D cultures had a higher level of oxidized lesions measured as Fpg sites. Short treatment of disaggregated cells from 2D and 3D cultures with 50 μM H_2O_2 for 5 minutes induced high levels of DNA SBs. Mean ± SEM (n=3 for H_2O_2 exposure, n=7 for 2D untreated control, n=9 for 3D untreated control).

References

27. Elje, E.; et al. The comet assay applied to HepG2 liver spheroids. *Mutat Res Gen Tox En* **2019**, 845, pp. 403033. DOI: 10.1016/j.mrgentox.2019.03.006
42. Klein, C.L., et al. *NM-Series of Representative Manufactured Nanomaterials, NM-300 Silver*. Publications Office of the European Union: Luxembourg, 2011. DOI: 10.2788/23079.
43. Singh, C., et al. NM-Series of Representative Manufactured Nanomaterials - Zinc Oxide NM-110, NM-111, NM-112, NM-113: Characterisation and Test Item Preparation. Publications Office of the European Union, Luxembourg, 2011. DOI: 10.2787/55008.